# Organofunctionalisation of Polyoxometalates for Photocatalysis

**Nicole Tsang**
A thesis submitted for the degree of Doctor of Philosophy
School of Chemistry, University of Nottingham

December 2023

## Declaration

The research presented in this thesis was conducted by the author within the School of Chemistry at the University of Nottingham, under the supervision of Professor Graham Newton and Professor Hon Wai Lam. This thesis has not been submitted for any degree or diploma at any institution. To the best of my knowledge, the content herein is original and has not been previously published or authored by anyone else, except where explicitly acknowledged. The candidate confirms that the appropriate credit has been given within the thesis where reference has been made to the work of others.

## Acknowledgements

I would first like to extend my gratitude to **Prof. Graham Newton** for his supervision throughout my PhD. I am incredibly grateful for the time and tremendous support he has given me. His kindness and constant positivity have motivated me to constantly drive forward. For this I am extremely grateful and thankful. Thank you to **Prof. Hon Wai Lam** for always being present, patient, and willing to help with all manner of things throughout my time in both the Lam group and the CDT. His hard work and dedication to Chemistry is truly inspiring.

I have been very lucky to count on the support of many people during my PhD but two names deserve a special mention. **Dr. Kieran Jones** has been a constant source of guidance through the unavoidable highs and lows of a PhD. I am so grateful for how talented he is, from his chemistry knowledge to his cooking skills, he never fails to surprise me at how he seems to excel at almost everything he does. **Dr. Alex Kibler** has been a constant rock since from day one, ready to answer any ridiculous question I throw at him. From making me feel so very welcome in the group, to working on a paper together, to going through a pandemic, to helping me read my thesis, I could not have asked for someone so incredibly kind, supportive, and encouraging to help me through the past few years. I would never have achieved the PhD without the both of them.

Thank you to the staff who have supported me through my research. From stores staff, technicians, analytical staff, and administrators who work so incredibly hard behind the scenes. Special mention to **Dr. Stephen Argent** for his superior crystal knowledge and the help he has provided with the crystallography of the POMs.

I would like to thank the EPRSC CDT in Sustainable Chemistry for funding my PhD, including the management team and directors for accepting me onto this programme and for the constant support and advice.

To my fellow NAMI, Lam, and CDT Cohort 6 members, it has been such a privilege to work with you all. Special mention to **Dr. Will Townsend**, **Adedayo Dada**, **Dr. Tom Butler**, **Jo Lee**, **Jack Castle**, **Dr. Luke O'Brien**, **Dr. Matt Bird**, **Dr. Cath Peake**, **Dr. Tom Barber**, **Lola Ogunyemi, Dr. Letizia Liirò Peluso** and the 'Battery Babies' for their incredible friendships throughout my PhD. Every single one of them has brought so much joy into my life, with all the laughs and cries, I wish them the all the best for the future.

I would like to thank my partner **Dr. Alister Davis**. Undertaking a PhD has been one of the hardest things I have ever done. His unwavering support throughout the personal ups and downs in the past few years is something I am so grateful for.

Finally, I would like to thank my family for their continued support throughout the years. **Yuet Chung**, **Tony Wade**, **Keri Tsang**, and **Jimmy Tsang** – I thank them for the unconditional love and support. I dedicate this thesis to them.

## Abbreviations

| | |
|---|---|
| Δ | Chemical Shift (parts per million) |
| µL | Microlitre |
| $^{o}$C | Degrees Celsius |
| Ar | Aromatic/Aryl (generic) |
| BDE | Bond Dissociation Energy |
| Calc. | Calculated |
| Cat. | Catalyst or catalytic |
| CHN | Carbon, Hydrogen and Nitrogen (Elemental Analysis) |
| CV | Cyclic Voltammetry/Voltammogram |
| d | Doublet in NMR Spectroscopy |
| DMF | Dimethylformamide |
| DMSO | Dimethyl sulphoxide |
| *e.g* | *Exempli gratia* (from Latin meaning "for example") |
| EDG | Electron-donating group |
| Equiv. | Equivalents |
| ESI-MS | Electron-spray Ionisation Mass Spectrometry |
| $Et_2O$ | Diethyl Ether |
| Et | Ethyl |
| $Et_2O$ | Diethyl Ether |
| *et al*. | *Et alii* (from Latin meaning "and the rest") |
| EtOH | Ethanol |
| eV | Electron Volt |
| EWG | Electron-withdrawing group |
| g | Gram(s) |
| h | Hour(s) |
| HAT | Hydrogen Atom Transfer |
| HOMO | Highest Occupied Molecular Orbital |
| HPOM | Heteropolyoxometalate |
| Hz | Hertz |
| IPOM | Isopolyoxometalate |
| IR | Infrared (Spectroscopy) |
| IVCT | Intervalence Charge Transfer |

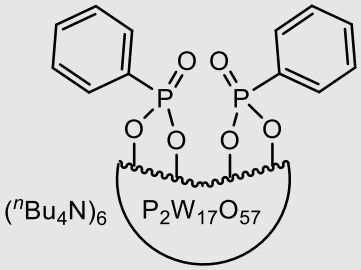
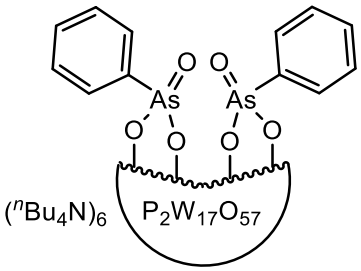
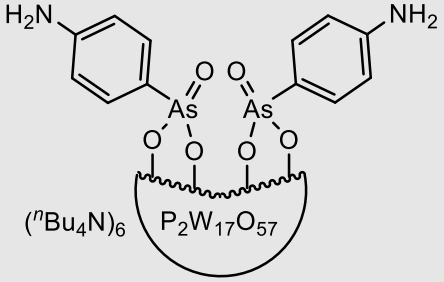
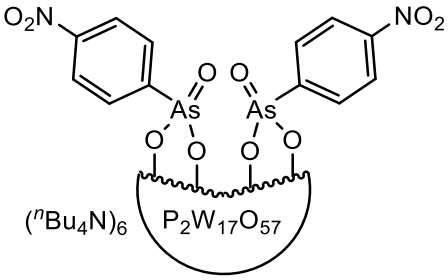
| | |
|---|---|
| *J* | Coupling constant in NMR Spectroscopy |
| KCl | Potassium Chloride |
| LMCT | Ligand-to-Metal Charge Transfer |
| LUMO | Lowest Unoccupied Molecular Orbital |
| M | Molar |
| *m*- | *Meta* |
| *m/z* | Mass-to-Charge Ratio |
| M+ | Molecular Ion |
| POM | Methyl |
| Me | Polyoxometalate |
| MeCN | Acetonitrile |
| MeOH | Methanol |
| mg | Milligrams |
| min | Minutes |
| mL | Millilitres |
| MLCT | Metal-to-Ligand Charge Transfer |
| mmol | Millimoles |
| NMR | Nuclear Magnetic Resonance |
| *o*- | *Ortho* |
| obs | Observed |
| *p*- | *Para* |
| PC | Photocatalyst |
| Ph | Phenyl |
| POM | Polyoxometalate |
| ppm | Parts per million |
| r.t | Room Temperature |
| RDS | Rate-Determining Step |
| s | Singlet in NMR Spectroscopy |
| SET | Single Electron Transfer |
| $^{n}Bu_4N$ | Tetra-*n*-butylammonium |
| $^{n}Bu_4NBr$ | Tetra-*n*-butylammonium bromide |
| t | Triplet in NMR Spectroscopy |
| TBME | *Tert*-butyl methyl ether |
| $^{t}Bu$ | *Tert*-butyl |

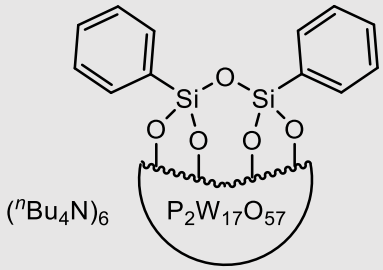
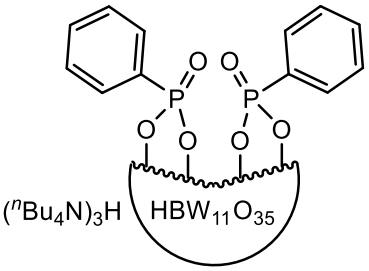
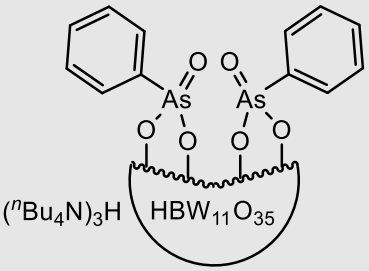
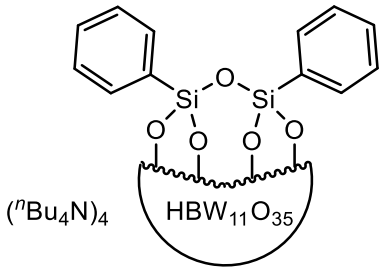
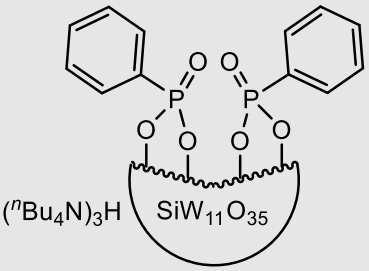
| | |
|---|---|
| Temp. | Temperature |
| UV | Ultra-violet |
| XRD | X-ray Diffraction |

## Polyoxometalate Notation

Throughout this thesis, an abbreviated notation for POM structures will be used, without oxygen atoms, charge, or brackets, and are given in **bold**.

The main compounds of focus in this thesis are listed below, including their molecular formula, and abbreviated names by which they are referred to in the text.

| **Hybrid Polyoxometalates** | |
|---|---|
| Schematic representation of the anionic structure | Full molecular formula<br>**Shorthand abbreviation** |
|  | ($^n$Bu$_4$N)$_6$[P$_2$W$_{17}$O$_{61}$(POC$_6$H$_5$)$_2$]<br>**PPhP$_2$W$_{17}$** |
|  | ($^n$Bu$_4$N)$_6$[P$_2$W$_{17}$O$_{61}$(AsOC$_6$H$_5$)$_2$]<br>**AsPhP$_2$W$_{17}$** |
|  | ($^n$Bu$_4$N)$_6$[P$_2$W$_{17}$O$_{61}$(AsOC$_6$H$_4$NH$_2$)$_2$]<br>**AsPhNH$_2$P$_2$W$_{17}$** |
|  | ($^n$Bu$_4$N)$_6$[P$_2$W$_{17}$O$_{61}$(AsOC$_6$H$_4$NO$_2$)$_2$]<br>**AsPhNO$_2$P$_2$W$_{17}$** |

| | |
|---|---|
|  | ($^n$Bu$_4$N)$_6$[P$_2$W$_{17}$O$_{61}$(Si$_2$O(C$_6$H$_5$)$_2$)]<br>**SiPhP$_2$W$_{17}$** |
|  | ($^n$Bu$_4$N)$_3$H[HBW$_{11}$O$_{39}$(POC$_6$H$_5$)$_2$]<br>**PPhBW$_{11}$** |
|  | ($^n$Bu$_4$N)$_3$H[HBW$_{11}$O$_{39}$(AsOC$_6$H$_5$)$_2$]<br>**AsPhBW$_{11}$** |
|  | ($^n$Bu$_4$N)$_4$[HBW$_{11}$O$_{39}$(Si$_2$O(C$_6$H$_5$)$_2$)]<br>**SiPhBW$_{11}$** |
|  | ($^n$Bu$_4$N)$_3$H[SiW$_{11}$O$_{39}$(POC$_6$H$_5$)$_2$]<br>**PPhSiW$_{11}$** |

## Publications

1. **“Electronic Structure and Photoactivity of Organoarsenic Hybrid Polyoxometalates”**, A. J. Kibler, N. Tsang, M. Winslow, S. P. Argent, H. Wai Lam, D. Robinson and G. N. Newton, *Inorg. Chem. 2023, 62, 8, 3585–359.*
2. **“Organofunctionalized Borotungstate Polyoxometalates as Tunable Photocatalysts for Oxidative Dimerization of Amines”**, N. Tsang, A. J. Kibler, S. P. Argent, H. Wai Lam, K. D. Jones, G. N. Newton, In preparation.

## Abstract

The organofunctionalisation of polyoxometalates (POMs) has emerged as a powerful strategy for enhancing the diversity of POM clusters, resulting in structures with tuneable electrochemical and photochemical properties. Despite notable progress, the integration of these functionalised POMs into organic photocatalysis remains limited. The work presented in this thesis aims to advance the scope of functionalised POMs beyond the current state-of-the-art and to gain a greater understanding of how structural variations influence the photochemical properties of POMs.

Chapter 2 of this thesis focuses on the synthesis of organic-inorganic phosphotungstate hybrid Wells-Dawson POMs. This involves the study of their electro- and photochemical properties through voltametric and spectroscopic analysis. Discussions in this chapter will encompass the impact of structural variation, organofunctionalisation, and heteroanion modulation, on the estimated frontier orbital energies of the POMs. Chapter 3 extends this study by detailing the synthesis and structural elucidation of novel borotungstate Keggin hybrids. This exploration delves into the distinctive characteristics of this family of POMs, contributing to the broader understanding of the impact of structural variation on their properties of hybrid POMs. The concluding chapter focuses the application of organofunctionalised hybrid POMs, with particular focus on borotungstate hybrids, as photocatalysts in organic synthesis. Specifically, their role as single electron transfer (SET) catalysts will be investigated, with application to the photooxidative coupling of amines.

In summary, this comprehensive study hopes to not only advance the current understanding of the intricate relationships between structural modifications of organofunctionalised hybrid POMs and their tuneable electro- and photochemical properties, but to also gain insight into their potential applicability in organic photocatalysis.

## Table of Contents


Declaration ..... i
Acknowledgements ..... ii
Abbreviations ..... iv
Polyoxometalate Notation ..... vii
Publications ..... ix
Abstract ..... x
Table of Contents ..... xi
1 General Introduction ..... 1
1.1 Polyoxometalates ..... 1
1.2 General POM Structure and Assembly ..... 1
1.2.1 POM Archetypes ..... 5
1.3 Organofunctionalisation of POMs ..... 11
1.3.1 General POM Functionalisation ..... 11
1.3.2 Covalent Organofunctionalisation Strategies ..... 12
1.3.3 Electronic Nature of POMs ..... 15
1.4 Application of POMs in Catalysis ..... 20
1.4.1 Introduction to POM Photocatalysis ..... 21
1.4.2 Photochemical Properties of POMs ..... 21
1.4.3 Decatungstate Photocatalysis ..... 24
1.5 Functionalised POM Photocatalysis ..... 26
1.5.1 Photosensitiser–Hybridisation in POM Photocatalysis ..... 26
1.5.2 Organofunctionalised POM Photocatalysis ..... 27
2 General Aims and Objectives ..... 31
3 Organofunctionalisation of Phosphotungstate Hybrid POMs ..... 32
3.1 Introduction ..... 32
3.2 POM Frontier Orbital Calculations ..... 33
3.2.1 LUMO Energy Level Calculations ..... 34
3.2.2 HOMO Energy Level Calculations ..... 36
3.3 Advancing Phosphotungstate Organic-Inorganic Hybrid POMs ..... 37
3.4 Aims and Objectives ..... 39
3.5 Results and Discussion ..... 40
3.5.1 Design and Synthesis ..... 40
3.5.2 Electronic Characterisation and Investigation ..... 45
3.5.3 POM HOMO–LUMO Determination ..... 50

3.5.4 POM Frontier Orbital Estimations Relative to Oxygen ..... 57
3.6 Conclusions ..... 58
4 Organofunctionalisation of Borotungstate Hybrid POMs ..... 59
4.1 Introduction ..... 59
4.1.1 Plenary and Lacunary Borotungstate POMs ..... 59
4.1.2 Organofunctionalised Borotungstate Hybrid POMs ..... 62
4.2 Aims and Objectives ..... 64
4.3 Results and Discussion ..... 65
4.3.1 Design, Synthesis & Structural Elucidation ..... 65
4.3.2 X-ray Crystallography ..... 80
4.3.3 Hydrolytic Stability ..... 86
4.4 Electronic Characterisation and Investigation ..... 91
4.5 Conclusions ..... 100
5 Photocatalytic Investigation of POMs ..... 101
5.1 TBADT Photocatalysis ..... 101
5.2 Photocatalytic Oxidative Coupling of Amines ..... 102
5.3 Aims and Objectives ..... 105
5.4 Results and Discussion ..... 106
5.4.1 Phosphotungstate Photocatalysis ..... 106
5.4.2 Borotungstate Photocatalysis ..... 109
5.4.3 Substrate Scope ..... 116
5.4.4 POM-Substrate Interactions ..... 118
5.5 Conclusion ..... 125
6 Summary ..... 126
7 Perspectives ..... 127
8 Future Work ..... 128
8.1 POM-Substrate Interactions Study A ..... 128
8.2 POM-Substrate Interactions Study B ..... 129
8.3 {$AsPhNH_2BW_{11}$} Crystallisation ..... 130
9 Experimental ..... 131
$K_6[P_2W_{18}O_{62}]$ ..... 135
$K_{10}[P_2W_{17}O_{61}]$ ..... 136
$(^nBu_4N)_6[P_2W_{17}O_{61}(POC_6H_5)_2]$ / {$PPhP_2W_{17}$} ..... 137
$(^nBu_4N)_6[P_2W_{17}O_{61}(AsOC_6H_5)_2]$ / {$AsPhP_2W_{17}$} ..... 139
$(^nBu_4N)_6[P_2W_{17}O_{61}(AsOC_6H_4NO_2)_2]$ / {$AsPhNO_2P_2W_{17}$} ..... 141

($^n$Bu$_4$N)$_6$[P$_2$W$_{17}$O$_{57}$(AsOC$_6$H$_4$NH$_2$)$_2$)] / {AsPhNH$_2$P$_2$W$_{17}$} ..... 142
($^n$Bu$_4$N)$_6$[P$_2$W$_{17}$O$_{61}$(SiC$_6$H$_5$)$_2$O)] / {SiPhP$_2$W$_{17}$} ..... 144
K$_5$[BW$_{12}$O$_{40}$] / {K•BW$_{12}$} ..... 145
($^n$Bu$_4$N)$_5$[BW$_{12}$O$_{40}$] / {BW$_{12}$} ..... 147
K$_8$[HBW$_{11}$O$_{39}$] / {K•BW$_{11}$} ..... 148
($^n$Bu$_4$N)$_8$[HBW$_{11}$O$_{39}$] / {BW$_{11}$} ..... 150
K$_3$H[HBW$_{11}$O$_{39}$(POC$_6$H$_5$)$_2$] / {K•PPhBW$_{11}$} ..... 151
(Bu$_4$N)$_3$H[HBW$_{11}$O$_{39}$(POC$_6$H$_5$)$_2$] / {PPhBW$_{11}$} ..... 152
K$_3$H[HBW$_{11}$O$_{39}$(AsOC$_6$H$_5$)$_2$] / {K•AsPhBW$_{11}$} ..... 154
($^n$Bu$_4$N)$_3$H[HBW$_{11}$O$_{39}$(AsOC$_6$H$_5$)$_2$] / {AsPhBW$_{11}$} ..... 156
K$_3$H[HBW$_{11}$O$_{39}$(AsOC$_6$H$_4$NO$_2$)$_2$] / {K•AsPhNO$_2$BW$_{11}$} ..... 157
($^n$Bu$_4$N)$_3$H[HBW$_{11}$O$_{39}$(AsOC$_6$H$_4$NO$_2$)] / {AsPhNO$_2$BW$_{11}$} ..... 158
K$_3$H[HBW$_{11}$O$_{39}$(AsOC$_6$H$_4$NH$_2$)$_2$] / {K•AsPhNO$_2$BW$_{11}$} ..... 159
($^n$Bu$_4$N)$_3$H[HBW$_{11}$O$_{39}$(AsOC$_6$H$_4$NH$_2$)$_2$] / {AsPhNH$_2$BW$_{11}$} ..... 160
($^n$Bu$_4$N)$_4$[HBW$_{11}$O$_{39}$(SiC$_6$H$_5$)$_2$O] / {SiPhBW$_{11}$} ..... 161
Photocatalysis – Substrate Scope ..... 162
10 References ..... 169
11 Appendix ..... 177
11.1 Additional Structural Analysis ..... 177
11.2 Additional CV and Spectroscopic Data ..... 179
11.3 Crystal Data and Structure Refinement for {K•AsPhBW$_{11}$} ..... 180
11.4 Crystal Images of {K•AsPhBW$_{11}$} ..... 182
11.5 Crystal Data and Structure Refinement for {K•PPhBW$_{11}$} ..... 183
11.6 Crystal Data and Structure Refinement for {AsPhNH$_2$BW$_{11}$} ..... 186
11.7 Crystal Images of {AsPhNH$_2$BW$_{11}$} ..... 188
11.8 Frontier Orbital Estimations ..... 189

# 1 General Introduction

## 1.1 Polyoxometalates

Polyoxometalates (POMs) are a remarkable class of anionic metal-oxo clusters, typically composed of early transition metals in their highest oxidation states.[1] For the past 200 years, the structure, versatility and unique self-assembly capabilities of POMs have captured the imagination of chemists and material scientists, driving their investigation into the synthesis of complex supramolecular architectures with tailored functionalities.[2,3] With each passing year, the understanding and utilisation of POMs continues to evolve, propelling scientific advancements in areas such as catalysis,[4] material science,[5,6] energy storage,[7–11] and medicine,[12–14] and opening up new avenues for innovation and discovery.[15]

## 1.2 General POM Structure and Assembly

In the general self-assembly of POMs, the individual components can be compared to 'Lego' building blocks, due to their modular nature and ability to interconnect in various ways to construct diverse structures. Starting with the smallest POM building block, this comprises of a metal centre (M) coordinated to oxo-ligands (O), which leads to the formation coordination polyhedra [$MO_y$] (where y = 4–7).[16,17] The most prominent metal centres found in POM chemistry include high-valent molybdenum (V/VI) and tungsten (V/VI), with a growing prevalence of structures involving vanadium (IV/V), niobium (V), and tantalum (V). These group V and VI transition metals, often referred to as 'addenda' atoms, are found in their highest oxidation state, possessing a $d^0$ and $d^1$ configuration. Exhibiting high positive charges, the radii of these metals fall within the suitable range for octahedral packing with oxygens. Furthermore, a crucial feature of these metals involves their capability to form terminal M=O bonds *via* dπ-pπ interactions, as illustrated in **Figure 1**.[3] The oxygen atoms found in polyoxometalates can be described as either bridging or terminal. A bridging oxygen is bound to two or more addenda atoms and can link anywhere between two and six addenda atoms. Alternatively, terminal oxo-ligands form

a double bond with a single metal centre and are positioned at the vertices of each polyhedral unit.[18]

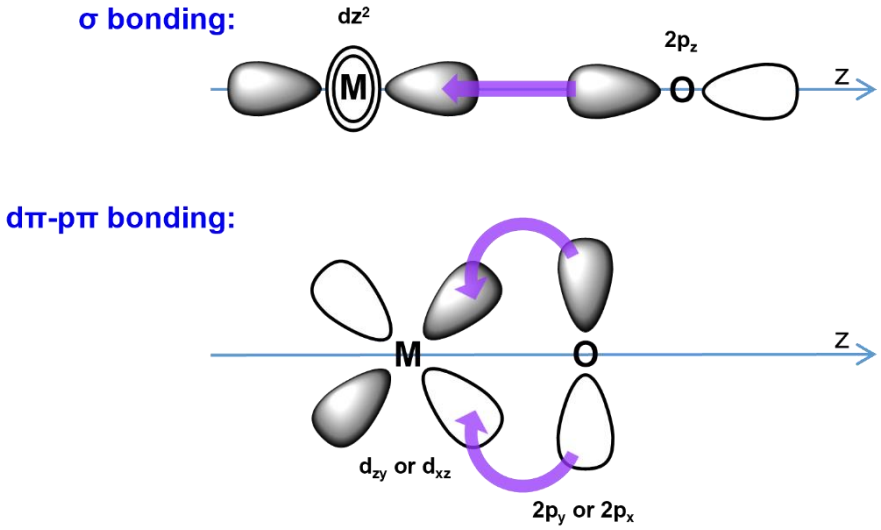



**Figure 1.** Graphical representation of the σ-donor and π-donor character of the oxo-ligand found in the terminal metal-oxo double bonds in POMs.

In the formation of octahedral polyhedra [$MO_6$], the presence of terminal oxo-ligands (M=O) causes a strong thermodynamic *trans*-effect, effectively weakening the metal-ligand bond (M–O) coordinated to the opposite side of the metal (**Figure 2** - a).[3] The electron-donating nature of the terminal M=O bonds, in comparison to the bridging oxygen ligands, induces a pronounced effect which leads to the shortening of the M=O bonds and distortion of the octahedral polyhedra.[19,20] This shortening effect is evident by the displacement and polarisation of the metal centre towards the terminal M=O bond. The resulting polarisation significantly reduces the basicity at the surface of these anions, preventing further protonation and polymerisation of the polyhedra. Subsequently, the growth of the metal-oxide structures is confined to the formation of discrete clusters, rather than infinite solid-state structures.[21]

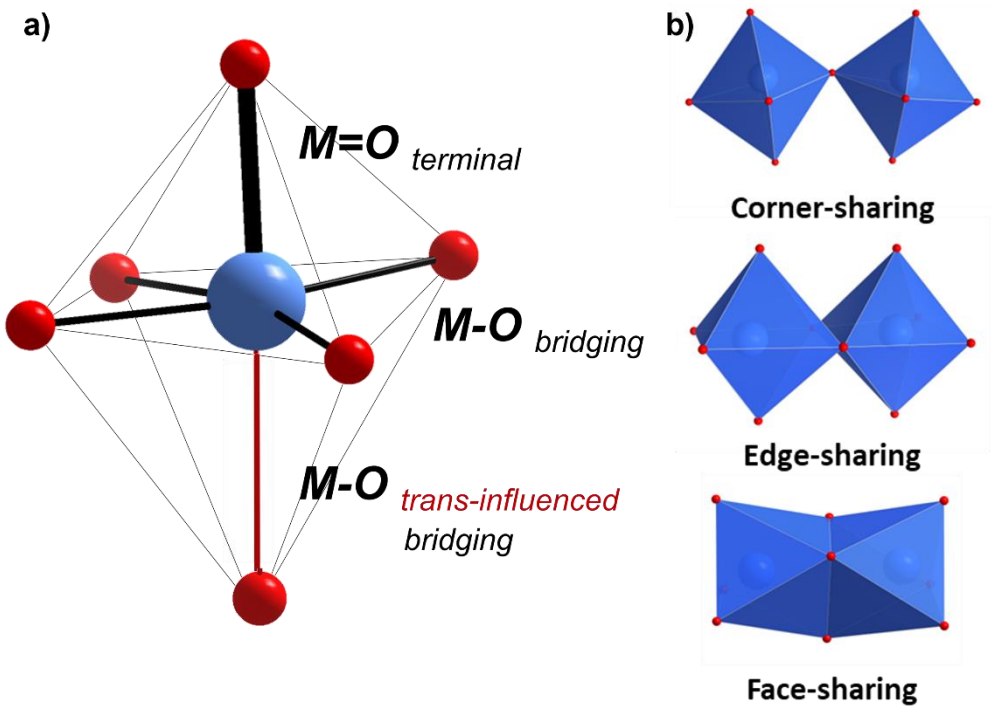



**Figure 2.** a) An [$MO_6$] octahedral unit. b) Binding modes of [$MO_x$] polyhedra after condensation, namely corner-, edge-, and face-sharing modes, respectively.

Occurring in aqueous solutions, the self-assembly process of POM clusters can be described as an acid-mediated condensation reaction between the polyhedra building blocks. The polyhedra link *via* corner-, edge-, or face-sharing modes (**Figure 2** – b) and follow "Lipscomb's Principle" whereby each metal unit must be connected to either one or two terminal oxo-ligands.[22,23] The self-assembly process can be influenced by various factors, including reagent variations (metal oxide starting material, reducing/oxidising agents, and additional heteroanions) and reaction conditions (solvent polarity and ionic strength, pH, temperature, time, pressure, and concentration).[24,25] These parameters shape the characteristics of the POM archetype. In addition to this, competing POM structures or isomers can also be synthesised under the same reaction conditions, with the formation and disassembly processes of various structures in a dynamic equilibrium in the solution.

As POMs are anionic in nature, they are often paired with charge-balancing countercations.[26,27] These counterions play a role in both the self-assembly process, solubility, and in some cases, the reactivity of the POMs. Furthermore, the choice of counterion can also influence the successful crystallisation of the POMs, which may be required for isolation, purification, and characterisation.[28] Examples include alkali metals ($Na^+$ and $K^+$) - often for aqueous phase reactions;[29] ammonium,[30] or organic tetraalkylammonium salts - typically chosen for organic phase reactions.[26]

### 1.2.1 POM Archetypes

As a large and structurally diverse class of compounds, one approach for categorising POMs is based on the presence of additional heteroatoms (**Figure 3**). Isopolyoxometalates (IPOMs), represented by the general formula $[M_mO_y]^{n-}$, exhibit a composition exclusively consisting of oxygen-bridged addenda atoms.[31] In contrast, the incorporation of one or more additional heteroatoms, often represented as $[XO_y]^{n-}$ (where X is often a main group p-block element) into the metal-oxide framework, results in the assembly of heteropolyoxometalates (HPOMs).[17]

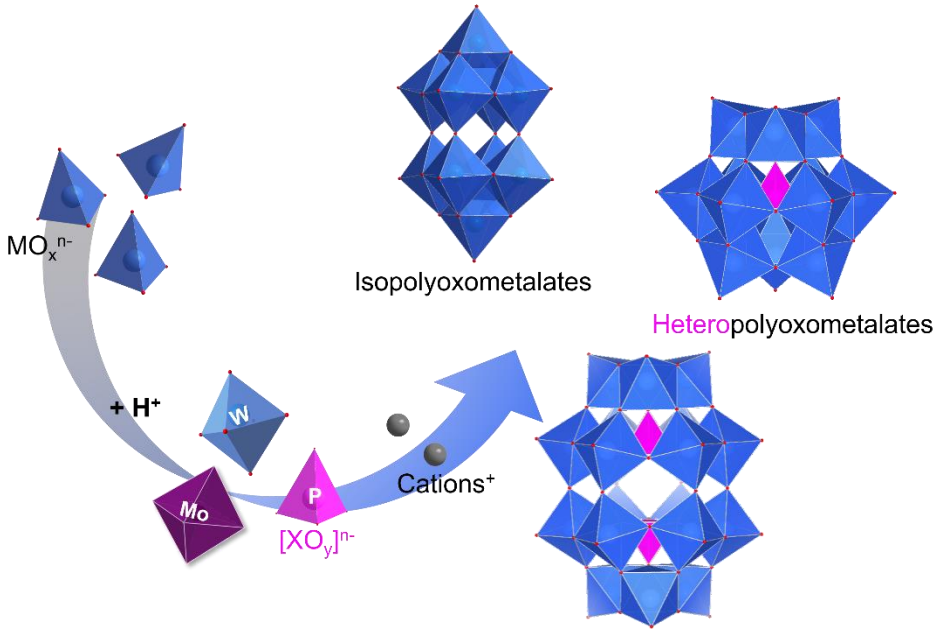



**Figure 3.** Schematic representation of the general POM self-assembly process by acid-mediated condensation of metal-oxo fragments.

Occupying both HPOM and IPOM classifications, the 'molybdenum blues/browns' are a family of POMs, characterised by their mixed-valence states, which give rise to their blue/brown colour. Formed through self-assembly processes around $\{Mo(Mo)_5\}$ units, these POMs typically exhibit large, curved topologies. Due to their impressive size and intricate structures, they are often referred to as 'big wheel' type clusters. An example can be seen in **Figure 4**.[32]

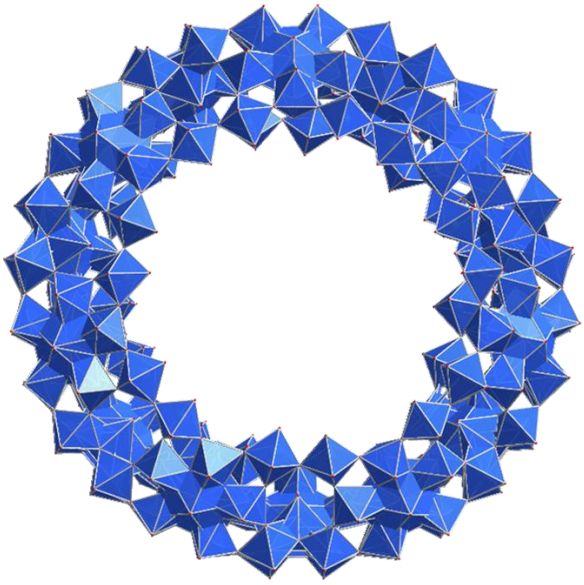


**Figure 4.** Polyhedral representation of the archetypical {$Mo_{152}$} 'molybdenum blue' nano-wheel structure.[32]

While the structure of IPOMs is primarily governed by the nature of the chosen addenda species, the assembly of HPOMs is largely influenced by the type, size, and chemistry of the heteroanion present. The heteroanion usually resides within the core of the POM and acts as a directing template around which the oxometallate framework can condense. Typical examples of central heteroanions include $SiO_4^{4-}$ or $PO_4^{3-}$.[19] Importantly, the incorporation of central templating heteroanions often significantly stabilises the overall cluster relative to IPOM species, especially in multi-electron reductions. Furthermore, it broadens the range of available structural variations compared to IPOMs, leading to the frequent study and attention of HPOMs in the synthetic field.[33]

With a general formula of $[W_{10}O_{32}]^{4-}$, the decatungstate anion is a well-established example of an IPOM.[31,34] The decatungstate archetype is comprising of a central belt containing eight [$MO_6$] units, capped by two [$MO_6$] units positioned at opposite ends (**Figure 5**).

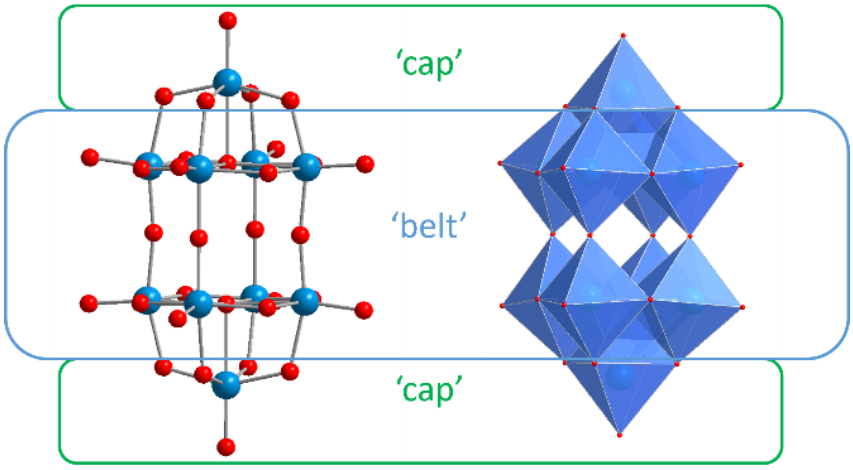



**Figure 5.** Ball and stick (left) and polyhedral (right) representations of the Decatungstate structure ($[W_{10}O_{32}]^{4-}$) indicating the two different metal environments: cap and belt.

The most known examples of HPOMs include the Keggin and the Dawson (otherwise known as Wells-Dawson) archetypes.[35,36] The Keggin structure has the general formula $[XM_{12}O_{40}]^{n-}$ and features a central tetrahedral anion $\{XO_4^{n-}\}$ surrounded by twelve $\{MO_6\}$ octahedral units, where M is commonly Mo or W.[37,38] In this structure, three $\{MO_6\}$ polyhedra units combine through edge-sharing modes to form a $\{M_3O_{13}\}$ triad. Subsequently, four $\{M_3O_{13}\}$ triads are further linked *via* corner-sharing modes. The arrangement of the triads allows for the existence of five isomers (α, β, γ, δ, and ε), depending on the orientation of the $\{M_3O_{13}\}$ units (**Figure 6**).[39] This is due to the 60° rotation movements of the triad units around a three-fold symmetry axis.

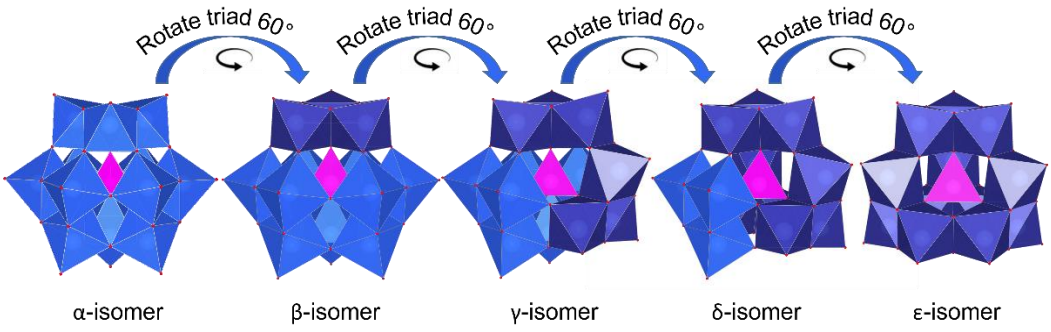



**Figure 6.** Five isomers of the Keggin anion, accessed by successive rotations of the four $\{M_3O_{13}\}$ units through 60°.

The Wells-Dawson structure is represented by the general formula $[X_2M_{18}O_{62}]^{n-}$.[40] The structure can be seen as derived from the Keggin through the removal of one $\{M_3O_{13}\}$ triad unit, resulting in the formation of a $[XM_9O_{34}]^{n-}$ cluster. In the Wells-Dawson POM, two of these $[XM_9O_{34}]^{n-}$ units are fused forming the POM with a central belt of twelve corner-sharing octahedral addenda, capped by two edge-sharing $[M_3O_{13}]$ units (**Figure 7**).[41] Similar to the Keggin, different orientations of the triad caps, combined with the rotation of the half-Dawson unit $[XM_9O_{34}]^{n-}$, can lead to the formation of six different Wells-Dawson isomers (α, α*, β, β*, γ, and γ*).[42] To date, only α, β, γ, and γ* have been synthetically isolated.[42]

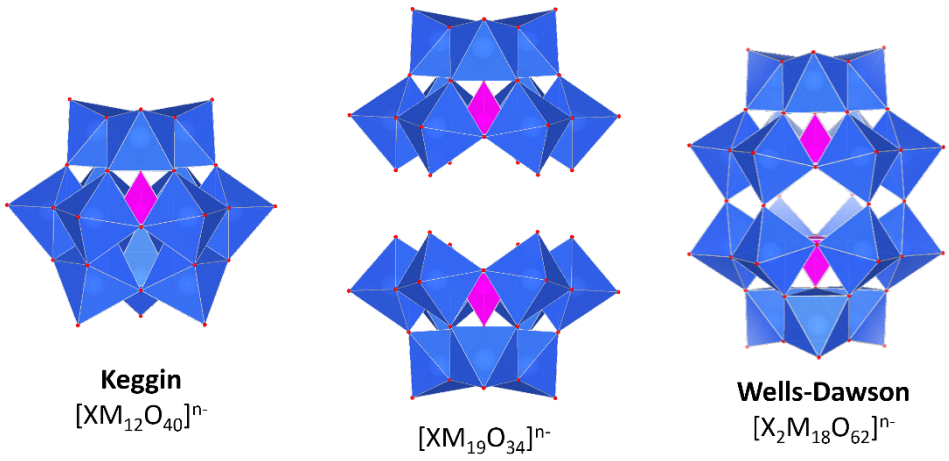



**Figure 7.** Polyhedral representation showing the relationship between the Keggin and Wells-Dawson structures.

In both the Keggin and the Wells-Dawson archetypes, the controlled removal of one or more addenda atoms, formally an M=O vertex, can be achieved through pH-controlled hydrolysis of the cluster. This process generally involves the treatment of a plenary POM (often termed parent POM) with a controlled quantity of base or *via* one-pot reactions of monomeric addenda atoms and heteroanions, under precise pH control.[43] As a result, a sub-class of structures known as *lacunary POMs* is formed, characterised by the presence of unfilled space or gaps, referred to as lacuna, within the POM structure.[44] Mono-, di- and tri-lacunary structures exhibit unique properties and reactivities compared to their parent analogues, including differences in charge, electronic properties,

and cluster shape. Furthermore, the vacant sites allow for the formation of mixed-metal POMs or the covalent grafting of organic or organometallic compounds directly onto the POM framework. This unique feature of lacunary POMs makes them highly valuable as synthetic building blocks in the design of novel POMs with tailored functionalities.[24]

The lacunary structures based on the Wells-Dawson and Keggin archetypes have been extensively studied.[34] For the Keggin POM, up to three addenda atoms can be selectively removed from the cluster framework through successive hydrolysis. This results in the formation of mono-, di- and trivacant species $[XM_{11}O_{39}]^{(n-4)}$,$[XM_{10}O_{36}]^{(n-4)}$ and $[XM_9O_{34}]^{(n-6)}$ respectively (where n represents the charge of the parent anion).[45,46] Similar to the plenary POMs, lacunary Keggin POMs exhibit structural isomerism, also determined by the specific positions from which the addenda atoms are removed (**Figure 8**).[47]

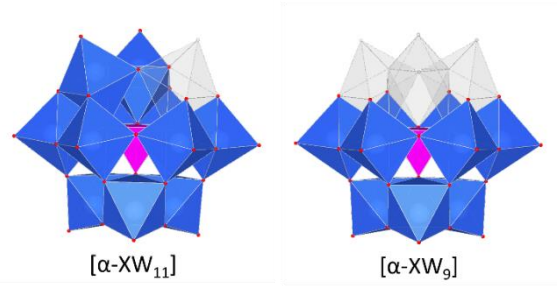



**Figure 8.** Polyhedral representation of two possible lacunary species of the Keggin cluster where missing octahedra are shaded in grey.

Relative to the Keggin POM, fewer lacunary structures are accessible for the Wells-Dawson cluster. Only the α-$\{X_2W_{18}\}$ structure can form stable lacunary species, with polyhedral removal occurring from either one of the two cap positions or from one of the two belt positions (**Figure 9**).[48] Beyond these mono-lacunary structures, the Wells-Dawson has also been reported to form tri-lacunary and hexa-lacunary structures, involving the removal of an $\{M_3O_{13}\}$ cap or six addenda atoms which form a 'face'-type unit $\{M_6O_{14}\}$.

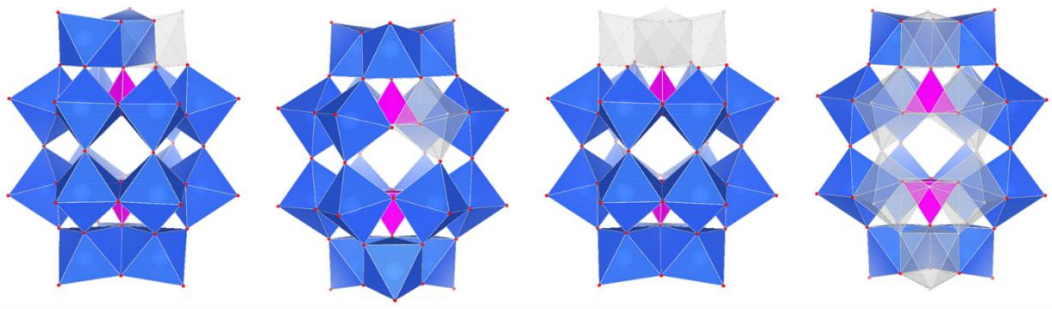



**Figure 9.** Polyhedral representation of the four possible lacunary species of the Wells-Dawson cluster where missing octahedra are shaded in grey.

The compositional diversity of the Keggin and Wells-Dawson archetypes is extensive, offering various addenda atoms (such as tungsten or molybdenum), in combination with a range of elements capable of acting as the central heteroatom. The selection of the addenda can also impact the stability of the POM. For instance, isolated lacunary species are often composed of tungsten, as the lacunary species of polyoxomolybdates and polyoxovanadates have been observed to be less stable and more reactive.[49] In the Keggin architecture, commonly reported *p*-block heteroatoms include $Si^{IV}$, $Ge^{IV}$, $P^{V}$ and $S^{VI}$, although structures templated by $B^{III}$, $Al^{III}$, $Ga^{III}$, $As^{V}$, and $Se^{VI}$ are also known.[19] The increased versatility and structural variation of the Keggin and Wells-Dawson archetypes contribute to their prominence in POM photochemistry.

## 1.3 Organofunctionalisation of POMs

### 1.3.1 General POM Functionalisation

As previously noted, POMs are widely recognised for their remarkable ability to self-assemble into a seemingly limitless variety of structures from simple metal-oxo building blocks. However, the field takes a new dimension when considering the interactions of these inorganic clusters with other species. The concept of hybrid polyoxometalates, which involves the combination of POMs with diverse inorganic and organic components, has gathered significant interest in recent years. This approach has proven effective in tailoring the intrinsic properties of POMs and the incorporation of specific functionalities into them.

POM functionalisation can be generally divided into three approaches: 1) the substitution of addenda atoms in lacunary POMs with transition metals, lanthanides, or main-group elements; 2) the non-covalent interactions of organic cationic molecules with the POM; 3) the covalent grafting of organic or organometallic species, which can occur either through addenda atom substitution in lacunary POMs or by attachment to terminal oxidants (**Figure 10**).[50,51]

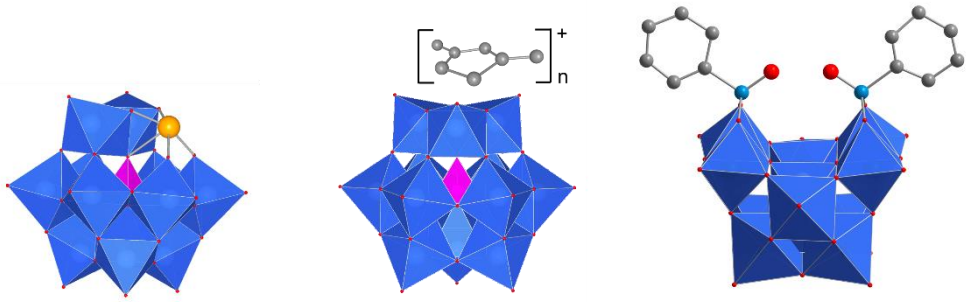



**Figure 10**. Polyhedral and ball and stick representations of different types of POM functionalisation.[52]

The last two approaches represent two distinct sub-classes of organic-inorganic hybrid POMs, characterised by the specific type of interaction formed between the components. In the first subclass, the interaction between the POM and

organic moiety relies on weak non-bonding interactions, such as electrostatic interactions, hydrogen bonding and Van der Waals forces. The most prevalent electrostatic hybrids are typically synthesised by salt metathesis and exchanging the counter-cation associated with the inorganic POM.[18,53] While these POMs offer simplicity in terms of synthesis, their stability is hindered by the weak interactions by which they are held together. Furthermore, control over the spatial relationship and prediction of charge transfer characteristics between the two components is limited.

In contrast, the second sub-class involves stronger interactions, such as covalent bonds, that directly link the organic moiety onto the POM framework.[54] Although this covalent organofunctionalisation strategy presents greater synthetic challenges, it can result in hybrids that exhibit a higher degree of stability and structural integrity. More importantly, the selection of organic and inorganic components, along with the strategic use of linking bridging group, allows precise modulation of the chemical properties of the POMs. This, in turn, facilitates the creation of functional materials with unique characteristics, making them highly versatile and applicable in various fields.

### 1.3.2 Covalent Organofunctionalisation Strategies

Several comprehensive reviews exploring the diverse array of covalent organofunctionalisation approaches for POMs have been reported, with contributions from researchers such as Dolbeq,[55] Streb,[5] Proust,[56,57] and Parac-Vogt.[43] These reviews highlight essential aspects of various organofunctionalisation strategies, with emphasis on the crucial role played by the type of POM addenda atom and bridging unit used in effectively anchoring the organic moieties onto the POM framework.

The organofunctionalisation of molybdate- and vanadate-based isopolyoxometalates, such as the Lindqvist hexamolybdate (with general formula $[M_6O_{19}]^{n-}$), is typically achieved through a diimide-catalysed

condensation reaction with primary amines (**Figure 11**).[58,59] This approach, applicable to organo-imido, -hydrazido, and -diazenido bridges, facilitates the substitution of one or more of the terminal oxo-groups of the POM, leading to the formation of molybdenum-nitrogen triple and double bonds. Another bridging group employed in POM organofunctionalisation includes tripodal alcohols (triols), used in the modification of the Anderson molybdate (general formula $[XMo_6O_{24}]^{n-}$), Lindqvist hexavanadate, and vanadate-capped mixed-addenda Wells-Dawson polyoxometalates (such as $[P_2W_{15}V_3O_{62}]^{9-}$). The triols act as bridging moieties in a tridentate arrangement, binding to a POM face featuring a trigonal arrangement of bridging oxygen atoms. This hybridisation process takes place *via* esterification of the hydroxy or alkoxo groups with the bridging oxo-ligands of the POM addenda atoms. Similarly, the related diolamide linkage has also found application in the organofunctionalisation of the vanadate-capped tungsten Wells-Dawson anion.

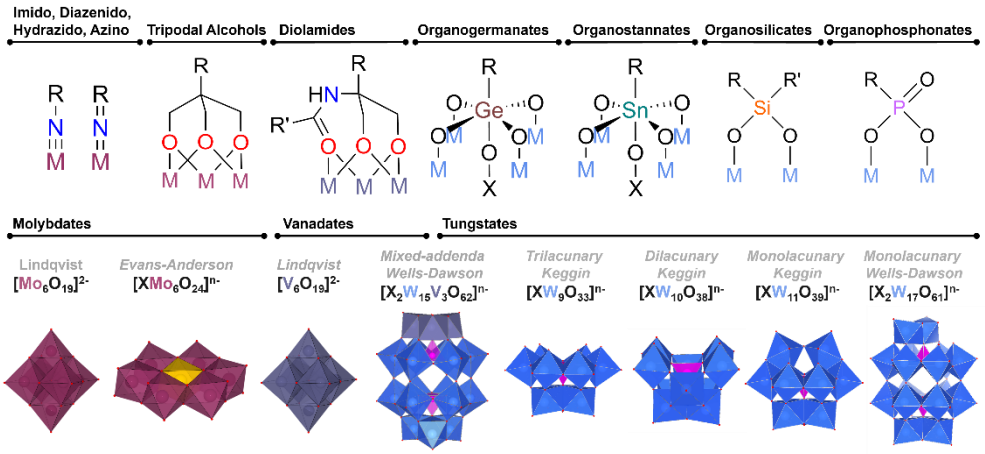



**Figure 11.** Covalent organofunctionalisation routes for a variety of archetypal and lacunary structures**.** Figure adapted from reference [59].

Compared to the polyoxomolybdate and polyoxovanadate anions, the higher stability and lower reactivity of polyoxotungstates presents challenges for direct covalent organofunctionalisation. As a result, researchers have focused on lacunary polyoxotungstates, involving the removal of one or more metal polyhedra units $[W_xO_{2x}]$ from a plenary POM, creating exposed and more

accessible unshared oxygen atoms. The oxygen sites exhibit increased nucleophilicity, offering suitable points for the covalent attachment of organic groups. Through condensation-type synthetic approaches organic groups, usually as their oxyacid or chloro-derivative, can be selectively introduced onto these exposed oxygen atoms, facilitating the functionalisation of polyoxotungstates.

Amongst the various organogroups used in the functionalisation of polyoxotungstates, the organosilicates are one of the most prominent, used to incorporate silicon centres into lacunary Keggin and Wells-Dawson clusters.[60] The functionalisation process relies on the hydrolysis of Si–Cl or Si–OR bonds present in trichlorosilanes and trialkoxysilanes. As a result, two organosilyl groups are integrated within a mono-lacunary site, with each silicon centre linked together *via* a siloxane bridge (-Si-O-Si-).

Beyond organosilyl derivates, organophosphonate and organoarsenate hybrids have been reported, with the latter receiving comparatively less extensive exploration.[61] Two organophosphonate groups can be introduced to a vacant lacunary site *via* the use of phosphonic dichloride ($RPOCl_2$) or phosphonic acid ($RPO(OH)_2$).[37] The arsonate analogue is synthesised in a similar manner using arsonic acids ($RAsO(OH)_2$). Recent interest has driven the accelerated exploration of organophosphonate and organoarsenate hybrids, attributed to the electronic conjugation found between the organic moiety and the POM core.

### 1.3.3 Electronic Nature of POMs

One of the most extensively studied characteristics of POMs is their electronic nature and remarkable reversible redox properties. [62] Given the anionic nature and the presence of numerous oxygen atoms capable of donating electrons to electron acceptors, POMs can be described as Lewis bases. In addition to this, the unoccupied orbitals of metal addenda atoms within POMs, render these centres susceptible to reduction. According to molecular orbital theory, POM complexes constructed from octahedral metal-oxo building blocks, each featuring only one terminal M=O bond, have one vacant non-bonding $t_{2g}$ orbital. This orbital can accommodate one or two electrons through reduction. Given the abundance of these metal-oxo building blocks within POMs, these compounds can therefore undergo multiple accessible reductions of their metal centres. Furthermore, the reduced POMs typically retain the general structure of their parent molecule, resulting in clusters which exhibit reversible electron loading and unloading properties. Examples of such structures include the Keggin and Wells-Dawson archetypes.

Throughout the literature, reduced POMs have been recognised with a characteristic intense blue colouration.[63,64] These electron-rich POMs are commonly referred to as 'heteropoly blues'. The colour arises as a result of d-d electron transitions and intervalence charge transfers (IVCT).[63] Driving into the underlying mechanisms, IVCT involves the rapid thermally assisted electron transfer process which occurs between metal centres within the core structure of the POM. This transfer mechanism, typically occurring between 650 and 1100 nm, results in pronounced absorptions in the low-energy visible and infrared regions of the compounds. Although they are not photochemically active, IVCT bands can be used as a method to monitor the population of various reduced states of POMs in solution.

The variable characteristics and electrochemical responses of POMs, specifically the capacity to accept electrons, are influenced by several factors. The first factor involves the size and charge (otherwise termed charge density) of the POM. Pioneered by Pope *et al*., in the early 1960s, the relationship between the size and charge of various Keggin anions $[XW_{12}O_{40}]^{n-}$ (where *n* denotes the molecular charge) on the reduction potentials was assessed.[65] The group observed that the capacity of the POMs to accept electrons was dependant on the ratio q/m, where 'q' signified the overall negative charge and 'm' referred to the number of metal ions in the structure. Consequently, larger POMs with a low negative charge were found to be easily reduced, while smaller, highly charged POMs exhibited a reduced affinity for accepting electrons.[62]

The overall negative charge 'q' can be influenced by the size, nature, and charge of the central heteroatom found within the POM.[66] Applied to Keggin anions, reduction potentials of first and second redox processes have been shown to decrease linearly with a decrease in the valence of the heteroatom.[67] This relationship is attributed to the changes in surface charge density of the clusters with the different heteroatoms.[68] To this effect, for POMs of the same charge, the smaller the size of the heteroatom, the harder it is for the POM to accept electrons.[69] Notably, even though the variation of the heteroatom affects the first redox potentials, the number of peaks for each POM tended to remain the same. This indicated that POMs cannot be altered to receive more electrons by changing the heteroatom elements, as demonstrated in the Keggin series where X = P, As and Si.[70]

The second factor that can influence the oxidising power of POMs is the type of addenda atom used when constructing the anionic species. When compared to Keggin polyoxotungstates, the lesser energy of the lowest d-metal orbitals in polyoxomolybdates were found to increase the reducibility of the clusters.[71] This highlighted the direct relationship between the energy of the lowest unoccupied molecular orbital (LUMO), which accepts the electron, and the

electronic properties of the POM. Furthermore, when applied to mixed addenda atom POM species, the substitution of a single metal addenda atom with a more electronegative $d^0$ metal ion causes the LUMO energy of the POM to decrease.[72] This in turn, causes the cluster to become more readily reduced, with the additional electron going into the orbital of the more electronegative ion. The trend of electronegativity of the metal ions is as follows: $XW^{6+} < XMo^{6+} < XV^{6+}$.

In recent years, the development of organofunctionalised POMs has introduced another parameter influencing the electronic properties of the POM systems. The redox properties of various organofunctionalised hybrid POMs have been shown to vary greatly due to type of organogroup anchored onto the POM. In 2013, Proust *et al*., reported the development of various hybrid POMs covalently grafted to organosilyl and organotin functionality.[73] The group found that POM derivatives exhibiting an organosilyl group, were easier to reduce than organotin hybrids, attributed to the one-charge difference between the resulting hybrids.

Another example of the influence of organofunctionalisation on the electronic properties of POMs was demonstrated by Boujtita *et al*., in the design of three organic-inorganic Wells-Dawson POMs, bearing either an organophosphonate or organosilyl group (**Figure 12**).[74] The electrochemical investigation of the organophosphonate phosphotungstate hybrid $[P_2W_{17}O_{61}(POC_6H_5)_2]^{6-}$ revealed four reversible reduction processes. Relative to the plenary POM, the first and second reduction potentials of the hybrid were positively shifted, indicating a strong electron-withdrawing effect of the phosphonate group on the negatively charged POM. In contrast, the organosilyl functionalised POMs ($[P_2W_{17}O_{61}(Si_2OPh_2)]^{6-}$ and ($[P_2W_{17}O_{61}(Si_2O^tBu_2)]^{6-}$) were found to have the inverse effect, with a negative shift in the first reduction process when compared to the plenary POM.

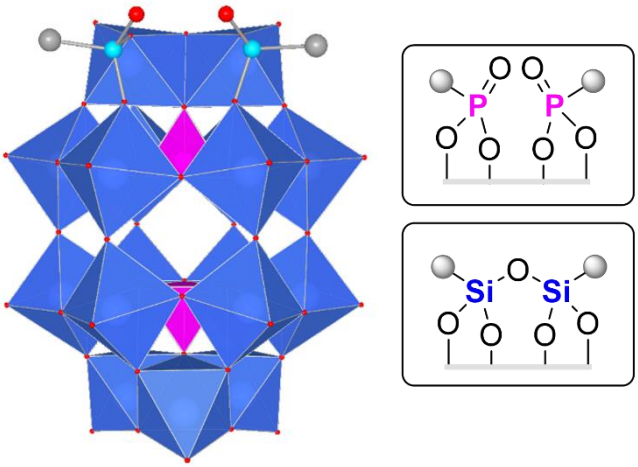



**Figure 12.** Schematic representation of functionalised phosphotungstate Wells-Dawson POMs - $[P_2W_{17}O_{61}(POC_6H_5)_2]^{6-}$ and $[P_2W_{17}O_{61}(Si_2OR_2]^{6-}$.[74]

Expansion of this study involved work published by Fujimoto and Cameron *et al.,* through the synthesis and electronic characterisation of various *para*-substituted organophosphonate Wells-Dawson POMs (**Figure 13**).[75] Three phenylphosphorus moieties with differing electronic natures (namely 4-carboxyphenyl-, 4-methoxyphenyl-, and phenylpropionates) were covalently grafted to the lacunary Wells-Dawson phosphotungstate. Computational studies revealed that the POM systems bearing a more electron-donating substituent on the ring exhibited a more negative first redox potential. This in turn, resulted in the POM systems being more difficult to reduce.

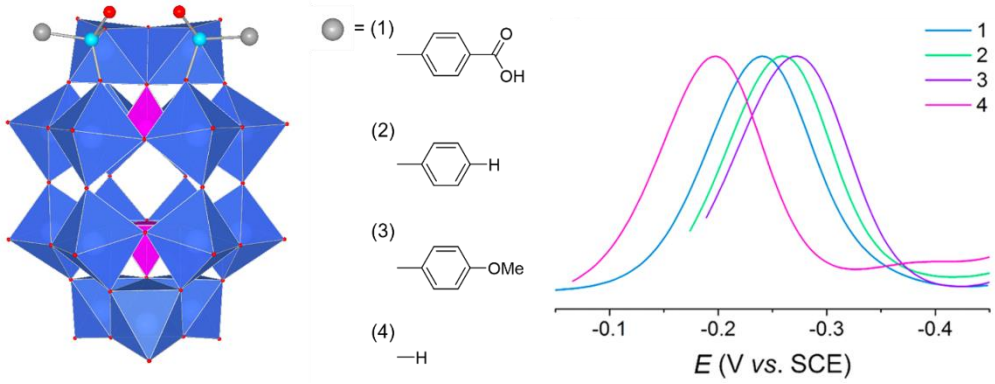



**Figure 13.** Structural representation of organophosphonate hybrid POMs bearing different R-groups and the differential pulse voltammograms highlighting the first reduction wave of each species (current plotted on an arbitrary scale to aid comparison). Adapted from reference [76].

These factors highlight how careful design, including selection of the addenda atoms, heteroanions, and nature of the organic moiety attached, can play a major role in influencing the electronic properties of the resultant POM systems. Exploiting this to its full potential and utilising this strategy to design POMs with specific electronic properties, can lead to POM materials with properties tailored for a specific application.

## 1.4 Application of POMs in Catalysis

In the last decade, one of the key objectives in the pursuit of environmental and economic sustainability in chemical production is the development of novel catalysts. These catalysts, play a pivotal role in minimising waste generation and reducing energy consumption.[77] Ideally, catalysts should be stable, easy to synthesise from inexpensive precursors and can transform starting substrates into products without additional additives, all under mild, energy-efficient reaction conditions.

The use of POM clusters as catalysts remains widely acknowledged, representing the forefront of POM applications.[78–80] While traditional photoredox catalysts, like transition-metal complexes or organic chromophores, offer advantages such as established synthetic methods and broad substrate scope, POMs over unique benefits. These include well-defined structures, acid-base properties, and a high degree of redox flexibility, enabling them to engage in a large array of chemical reactions. As mentioned previously, POMs can undergo multielectron redox processes without significant structural degradation, rendering them durable and efficient as catalysts. Moreover, the modular nature of hybrid POMs proves advantageous, allowing fine-tuning of their catalytic properties to meet specific reaction requirements, optimising performance across diverse chemical contexts. Furthermore, when compared with organic- or organometallic-based homogeneous catalysts, POMs are thermally and oxidatively stable.[31,81] Additional noteworthy characteristics, such as cation-controlled solubility in aqueous and organic solvents, high Bronsted-acidity and multiple protonation sites, high redox-activity and oxygen transfer capability, high stability under harsh conditions, and lastly, high photoactivity in the UV and near-visible region, further solidify POMs as excellent catalytic materials.

### 1.4.1 Introduction to POM Photocatalysis

Following the elucidation of heteropoly blues and reduced POMs, the early 1980s witnessed a surge in investigations into the photochemical properties of POMs and their role in catalysis.[82–84] Early studies focussed on plenary and lacunary POMs, with a particular emphasis on the Keggin, Wells-Dawson and Decatungstate archetypes.[85–89] These archetypes were shown to be efficient photocatalysts in the oxidation of organic substrates, such as alkanes, alcohols, sulphides, and alkenes, using UV-light. Driving away from the classical POMs, the aforementioned development of novel POMs systems with various functionalities has expanded the scope of POM photocatalysed applications to transformations such as $H_2$ evolution,[90] water oxidation ($O_2$ evolution),[91–94] $CO_2$ reduction,[81,95] and the degradation of organic pollutant and dyes.[96–98] The primary objectives of these reports have centred around (1) investigating the impact of modification on the properties of POMs, (2) achieving visible-light activation through structural modifications, and (3) expanding the applications of POMs in photocatalysis. However, reports entailing these objectives, when applied to organic photocatalysis, has been limited to the use of decatungstate.

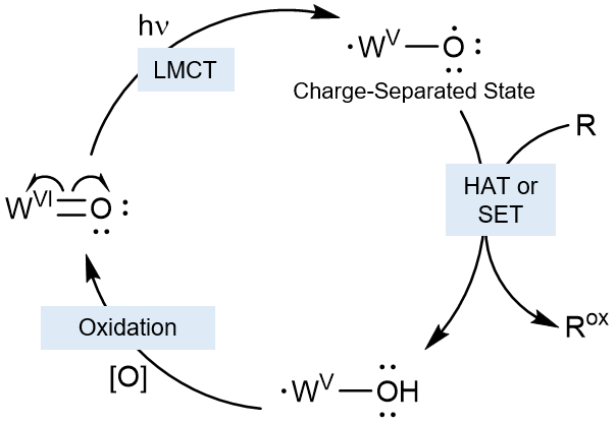
To address this, a compressive approach surveying the various design elements of different POMs and the types of photochemical mechanisms they employ is required. Such an analysis not only provides valuable insights into the intricate relationships between structural modifications and ensuing photochemical behaviour, but also enhances our understanding of the versatility of POMs as photocatalysts in different areas of chemistry. As a result, the next section will look at the different photochemical mechanisms of POMs, highlighting the influence of varying POM designs on the frontier orbital energies.

### 1.4.2 Photochemical Properties of POMs

The inherent photochemistry of classical POM clusters, such as the Keggin, Wells-Dawson, and decatungstate archetypes, is dictated by their capability to undergo intermolecular oxygen-to-metal charge transfers, otherwise known as

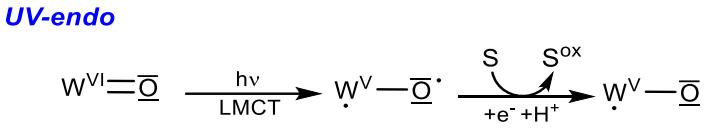
ligand-to-metal charge transfer (LMCT). From a molecular orbital perspective, this charge transfer interaction typically involves an electron movement and promotion from a doubly occupied 2p bonding orbital of a terminal oxygen $O^{2-}$ ion (the highest occupied molecular orbital or HOMO) to an empty antibonding d-orbital on the metal (LUMO). Like semiconductors, this light-initiated electron transfer essentially represents the HOMO-LUMO energy gap of the compound, resulting in a strong characteristic absorption in the UV to near visible region of the spectrum.[99]

When applied to organic photocatalysis, irradiation, excitation of the LMCT band and electron transfer results in a localised $d^1$ electron on the metal centre and a highly reactive oxo-centred radical cation with a short-lived triplet state (**Scheme 1**). This charged-separated state is then quenched by either hydrogen atom transfer (HAT) or single electron transfer (SET) mechanisms, dependent on the type of substrate '*R*' and POM present.[100] This leads to the trapping of a $d^1$ electron in the POM core. Subsequent closing of the catalytic cycle with re-oxidation of the POM back to the $d^0$ ground state can then be achieved with the use of an oxidant or sacrificial electron acceptor, closing the POM catalytic cycle.[94]



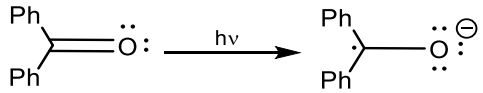

**Scheme 1.** Charge–separation mechanism of polyoxotungstates under photochemical irradiation, where R is the substrate undergoing a HAT mechanism.

As the photo-induced charge separation is centred entirely on the terminal W=O groups of the POM core, this mechanism type can be termed '*UV-endo*' where UV-light initiates the LMCT, which is localised on the terminal W=O groups of the POM core (*endo* = internal; from inside).[50] This method relies on the intrinsic photochemistry of the POM, devoid of additional functionality and often requiring energy-intensive UV-light for activation (**Scheme 2**).




**Scheme 2.** *UV-endo* charge separation mechanism, in which the photo-induced charge separation is centred entirely on the POM, where S is the substrate being oxidised typically *via* hydrogen-atom abstraction. This results in trapping of an electron on the POM core. Subsequent oxidation of the POM core can be used to regenerate the $d^o$ ground state.

Interesting, parallels can be drawn between the photocatalytic SET processes exhibited by POMs and organic photoredox catalysts, exemplified by diaryl ketones such as benzophenone. Analogous to POMs exposure of UV-light to benzophenone induces the formation of a highly reactive triplet state capable of undergoing SET reactions, including the initiation of polymerisation processes (**Scheme 3**).[101]

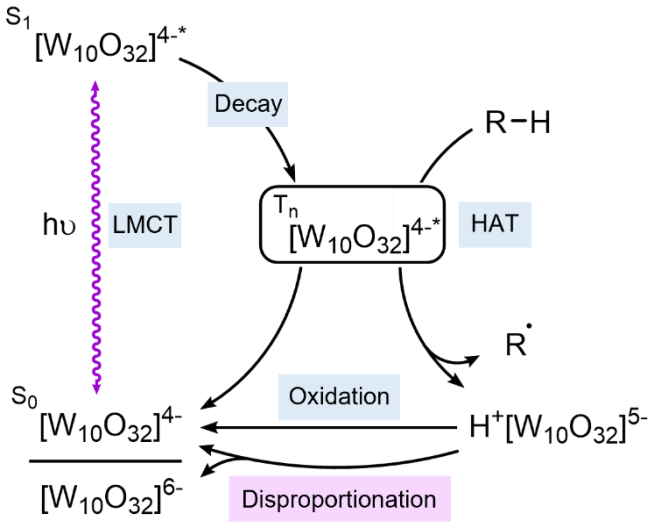



**Scheme 3.** UV-light activation of benzophenone resulting in a highly reactive triplet state.

### 1.4.3 Decatungstate Photocatalysis

*Tetra-n*-butyl ammonium decatungstate, or **TBADT**, has received considerable attention in the field of organic photocatalysis.[102–106] The heightened interest can be attributed to the POM's high photochemical activity, robust nature, and its ready availability from inexpensive precursors.

Insight into the mechanistic activation process of organic substrates by **TBADT** has been thoroughly explored through the combination of computational and experimental studies. Similar to the general photoactivation mechanism of POMs discussed in the previous section, UV light irradiation of $[W_{10}O_{32}]^{4-}$ ($\lambda_{max}$ = 324 nm, ε = 14100 $M^{-1}$ $cm^{-1}$) initiates an intramolecular O-to-W LMCT process, leading to the formation of a highly reactive oxo-species denoted as $[W_{10}O_{32}]^{4-*}$ (**Scheme 4** - LMCT).[107] Notably, this POM displays an extended excited state lifetime for $[W_{10}O_{32}]^{4-*}$, distinguishing it from other POMs.[18,108] In contrast to the UV-endo mechanism in POM photocatalysis, this oxo-species then undergoes rapid decay, forming the actual reactive state, assumed to have a triplet multiplicity (**Scheme 4** - decay). Subsequently, this state can participate in HAT or SET mechanisms, facilitating functional group transformations. Furthermore, **TBADT** exhibits a unique propensity for spontaneous disproportion over an extended timeframe (**Scheme 4** - disproportionation).[109,110] This property, not observed in other POM photocatalysts, may contribute to the increased utility of **TBADT** in various photocatalytic reaction types.




**Scheme 4.** Excitation and reactivity of the decatungstate anion $[W_{10}O_{32}]^{4-}$.

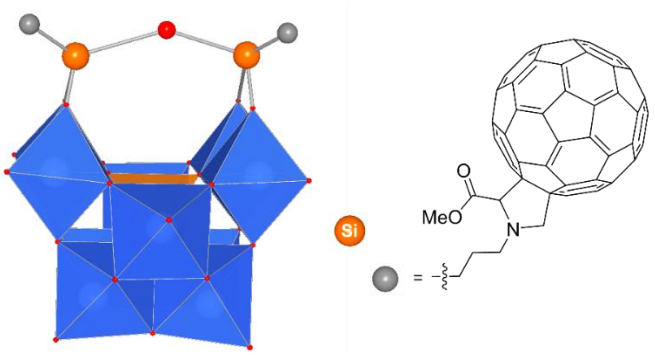
Despite **TBADT** showcasing the potential of POMs as excellent photocatalysts, with the direct photoactivation of the W=O centres, limitations arise in **TBADT**-catalysed photochemical reactions. Firstly, owing to the large gap between the oxo-based HOMO and the metal-based LUMO in **TBADT** (typically >3.5 eV), the activation of the POM requires high-energy and intensive UV-light irradiation. In addition to this, the highly powerful oxidising nature of TBADT, combined with site-selectivity dependence on polar and steric effects, can result in minimal control over its reactivity. Lastly, regarding structural modifications, only a limited number of reports have explored decatungstate functionalisation,109 emphasising that the chemistry catalysed by **TBADT** is inherently restricted by its innate properties. As a result, there is a need for the development of new POM-based photocatalysts that expand beyond the scope of **TBADT**, accessing different chemical reactivities.

## 1.5 Functionalised POM Photocatalysis

### 1.5.1 Photosensitiser–Hybridisation in POM Photocatalysis

Moving away from **TBADT** and towards POMs with additional functionality, one synthetic design that alters the photochemical mechanism type at which the POM is activated by, involves the covalent attachment of photoactive chromophores or photosensitisers onto the POM cluster. Such examples of photoactive species include organometallic complexes, organic dyes and $C_{60}$ fullerene.[111–113] The attachment of these species results in the photosensitisation of the POM clusters towards visible-light activity. Photochemical applications of these POMs have been shown in $H_2$ evolution, water oxidation, and $CO_2$ reduction.[90,114–116] Unfortunately, when applied to functional group transformations, only a limited number of POMs combined with photosensitisers have been reported.

In 2004, Bonchio *et al*., reported the synthesis of a di-vacant Keggin-type lacunary POM $[\gamma\text{–}SiW_{10}O_{36}]^{8-}$, hybridised with a photoactive fulleropyrrolidine (**Figure 14** - a).[117] Bound to the POM through RSi–O–W bonds, the fullerene moieties serve as the photosensitisers, activated by photoirradiation ($\lambda > 375$ nm), resulting in a functionalised POM that could facilitate the oxidation of phenol in water. Under visible-light irradiation, the fullerene sensitiser 'L' (**Figure 14** – b) undergoes photoexcitation, leading to the transfer of electron density from the HOMO based on the photosensitiser to the POM-based LUMO. The electron transfer process results in the formation of a short-lived charged separated state, exhibiting a hole localised on the photosensitiser and electron on the now-reduced POM. Following this, quenching of the charge separated state can then occur using a sacrificial oxidant 'S', preventing charge recombination, and trapping an electron on the POM core. This mechanism type can be termed '*vis-exo' (*where *exo* = external; from outside).[50]




*vis-exo*

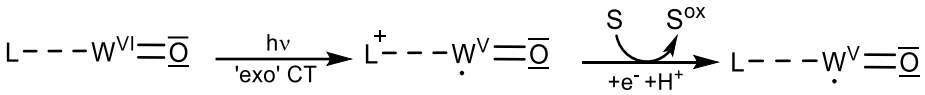



**Figure 14.** a) Fullerene-substituted silicotungstate hybrid POM. b) *vis*-exo charge separation mechanism, where the photo-induced charge separation occurs between an oxidised photosensitiser and a reduced POM.

### 1.5.2 Organofunctionalised POM Photocatalysis

The low optical transitions found in POM systems featuring Mo, or more usually V addenda atoms, allows the cluster to be activated with visible-light. In contrast, W-based POMs have typically been shown to be inactive (requiring UV-light irradiation) or rely on the aforementioned *vis-exo* sensitisation approach for visible-light activation. In recent years, a different approach used to fine-tune the photoactivity of POMs has emerged. In the previous chapter, structural modification of various organogroups was shown to influence the electronic properties of the resultant organic-inorganic hybrid POMs. Given that the reduction potential of the redox process can be directly related to the LUMO of the system, relationships between structural modifications and the energies of the frontier orbitals can be formed. An example of such a relationship was demonstrated in the organofunctionalisation of lacunary phosphotungstate $[P_2W_{17}O_{61}]^{10-}$ with 4-carboxyphenylphosphonic acid.[76] Attachment of the organogroup resulted in a positive shift in the first redox potential of the POM, relative to the parent anion. The positive shift indicated a change in the electronic properties of the hybrid and a lowering of the LUMO energy level.

Computational and experimental data of the hybrid revealed an alteration in the electron density distribution within the HOMO and LUMO energy states of the hybrid POM when compared to the plenary phosphotungstate. Specifically, it was observed that in the parent POM, the electron density predominately resided in the belt region of the POM core. However, in the hybrid structure, the electron density was strongly delocalised between the organogroup π* orbitals and the tungstate oxide POM. This observed change in the HOMO and LUMO energy levels indicated the combined inductive and resonance effects of the organic moiety on the stability of the frontier orbital energy levels. In this context, destabilisation of the HOMO energy level and concurrent stabilisation of the LUMO energy level led to a significant reduction of the HOMO-LUMO gap and enhanced photoactivity of the POM, relative to the unsubstituted parent. Similar HOMO-LUMO energy modulation trends were observed for the other organofunctionalised hybrid POMs synthesised, with more electron-donating substituents on the organogroup destabilising the LUMO of the POM, resulting in more negative redox potentials (**Figure 15**).[75]

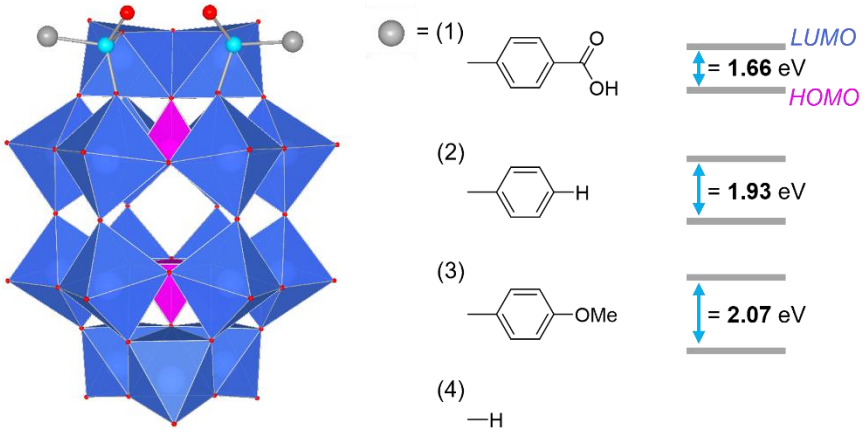
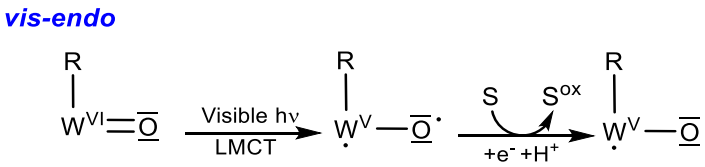



**Figure 15.** Organophosphonate hybrid POMs bearing different R-groups and the respective HOMO-LUMO energy gaps. Figure adapted from reference.[76]

Regarding the photochemical characteristics of the hybrids, modulation of HOMO-LUMO energy levels serves to alter the required light wavelength for activation. In the case of visible-light activation, the organofunctionalisation approach relies on the extension of the 'tail' of the O → M LMCT absorption band of the hybrid POM into the high energy region of the visible spectrum, while still maintaining an absorption maximum located in the UV range. This organofunctionalised strategy can therefore be seen as a method to synthesise POM catalysts that exhibit visible-light responsiveness. In this context, visible-light irradiation results in a POM-based LMCT, facilitating the formation of the same highly reactive charge-separated state formed in the UV-endo mechanism. Given that visible-light irradiation is used, the charge-separation mechanism for this approach can be described as '*vis-endo'* (**Scheme 5**).




**Scheme 5.** *vis*-endo charge-separation mechanism, where POM hybridisation with moiety 'R' allows visible light activation of the POM LMCT band.[50]

The photochemical application of the organophosphonate hybrid POMs was demonstrated in the degradation of indigo dye. In this time-dependant decolourisation study, Xenon light was used to irradiate the POMs and dye (in a POM/indigo ratio of 1:5), dissolved in DMF. The degradation was monitored by absorption spectroscopy. The lacunary POM $[P_2W_{17}O_{61}]^{10-}$ showed minimal activity relative to the 'blank' control reaction, whereas the plenary POM $[P_2W_{18}O_{62}]^{5-}$ showed moderate/slow decomposition of the dye substrate. In comparison, the hybrid had the best performance with a faster rate of dye degradation. Repeating the reaction with a wavelength of above 420 nm, only the hybrid showed any photo-oxidation of the indigo dye, whilst the plenary performed similarly to the blank. Both studies indicated that only the hybrid was capable of effectively operating under true visible-light irradiation.

POM functionalisation has been shown to access various POM clusters with unique features, facilitating diverse photocatalytic processes. These examples highlight the relationships between structural modification, electronic properties involving HOMO-LUMO energy gap modulation, and the photochemical reactivity of the POM hybrids (**Figure 16**). However, except for **TBADT**, current POM photocatalysts depend on the incorporation of platinum-group metals, photosensitisers or organic chromophores for visible light activation. Furthermore, despite the development of the *vis*-endo strategy, with POM clusters directly activated with visible-light irradiation, their photocatalytic application has only been demonstrated in dye degradation. Advancing in this area involves conducting an in-depth study into the design, synthesis, and characterisation of organic-inorganic POMs, in relation to their photochemical properties.

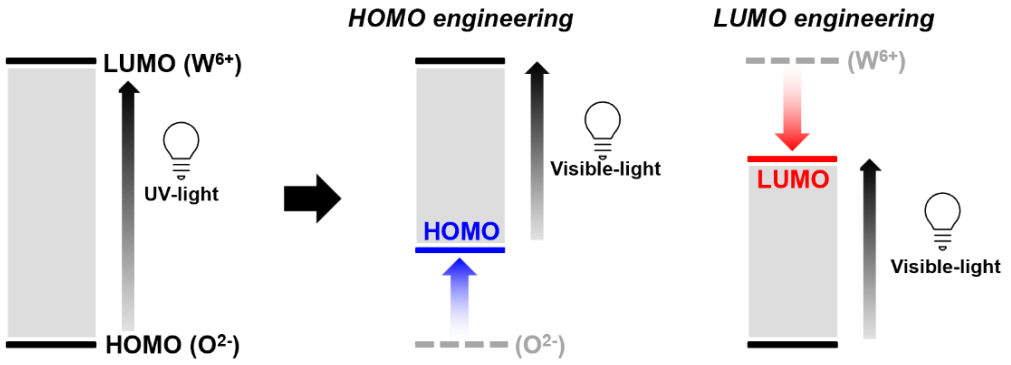



**Figure 16.** Development of visible-light responsive POM photocatalysts *via* HOMO and LUMO modulation using structural modifications. Figure adapted from reference [118].

# 2 General Aims and Objectives

The organofunctionalisation of POMs has shown promise in the development of various clusters with tuneable electrochemical and photochemical properties. However, their application to organic photocatalysis is limited. The work presented in this thesis aims to advance the scope of organic-inorganic hybrid POMs beyond the current state-of-the-art, and to gain a greater understanding between the impact of structural variation on the photochemical properties of the POMs.

**Chapter 3 – Organofunctionalisation of Phosphotungstate Hybrid POMs**

This work involves the synthesis of various organic-inorganic phosphotungstate hybrid Wells-Dawson POMs and the study of their electro- and photochemical properties through voltametric and spectroscopic analysis. Influence of structural variation, including Keggin exploration, on the estimated frontier orbital energies of the POMs will be discussed.

**Chapter 4 – Organofunctionalisation of Borotungstate Hybrid POMs**

The work presented in this chapter involves the synthesis and structural determination of novel borotungstate Keggin hybrids, with exploration into the distinctive characteristics of this family of POMs.

**Chapter 5 – Photocatalytic Investigation of POMs**

Initial proof of concept studies surrounding organic-inorganic hybrid POM photocatalysis will be discussed in this chapter, with focus on single electron transfer reactivity of novel borotungstate hybrid POMs.

# 3 Organofunctionalisation of Phosphotungstate Hybrid POMs

## 3.1 Introduction

Much like semiconductor photocatalysts, the energy gap between the frontier orbitals significantly influences the optical properties, and therefore the photocatalytic properties of the POMs. Previous work has highlighted the impact of structural changes (such as the archetype, addenda atom, heteroanion, and organogroup functionalisation) on the redox properties of the POMs, which in turn, alters the energies of the frontier orbitals of the resultant systems. Given the structural diversity of POMs, a wide range of energy levels and inherent optical characteristics can be observed. To this end, the measurement of energy levels in POMs is an invaluable tool in developing a comprehensive understanding between structural variation and the properties of the POMs as photocatalysts.

In the development of novel photocatalysts, it is essential that the energy of the HOMO level is more negative than the energy of the organic substrate, in order for electron transfer to occur from the organic substrate to the excited POM (**Figure 17** – step a). Simultaneously, the energy of the LUMO level needs to be more positive to the energy level of the oxidant, to oxidise the reduced POM back to its ground state (**Figure 17** – step b).[4] By strategically aligning the energy levels of the POMs with the redox species involved (for example the substate and oxidant), catalytic efficiency and quantum yield can be optimised, thereby advancing POM photocatalysts for various organic photochemical reactions.

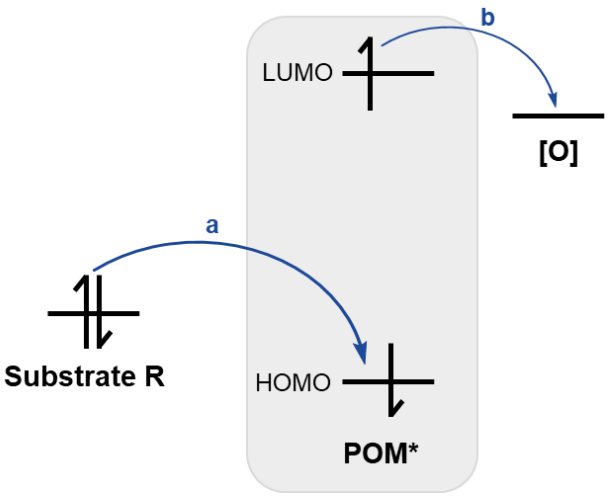



**Figure 17.** Schematic representation of a SET POM photocatalytic cycle from a molecular orbital theory perspective with a) representing the reduction of the POM with accepting an electron from the substrate to the POM HOMO, followed by b) oxidation of the reduced POM and removal of an electron from the LUMO of the POM to the oxidant.

### 3.2 POM Frontier Orbital Calculations

One method to estimate the frontier orbital energy levels of POMs involves the use of Density Functional Theory (DFT). While DFT is a widely utilised method, the large size, high negative charge, and presence of transition metal ions in POMs poses challenges leading to computational limitations, reducing the output of high-level computation studies on POMs. For this reason, various other approaches have been proposed for estimating the HOMO-LUMO energy levels.

In 2016, Sworakowski *et al*., described an indirect method for calculating the energy levels of small-molecule organic semiconductors.[119,120] In their work, the group explored the application of cyclic voltammetry (CV) to estimate the LUMO energy level and UV-vis absorption spectroscopy to indirectly predict the HOMO energy level. Frontier orbital estimation through the use of CV and spectroscopic analysis is relatively simple to measure and calculate, however, obtaining reliable energy values requires proper calibration, considering

factors such as ionisation energy, electron affinity, and solvation effects. Through comparisons in the experimental data between indirect and direct methods (including UV photoelectron spectroscopy and inverse photoelectron spectroscopy), the group calculated calibration parameters, which served to minimise the errors when employing indirect methods for determining the energy levels.

When applied to estimating the frontier orbital energy levels of POMs, this indirect method offers a rapid and accessible means of comparing the relative energy levels of POMs.[53,121,122] The next section will go into more detail regarding the energy level estimation methods, including the formulas and correlation coefficients determined by this research group.

### 3.2.1 LUMO Energy Level Calculations

In the indirect estimation of the LUMO through electrochemical voltammetry, the determination of the potential for the first reduction process can be approached in two ways. The first method entails calculating the '$E_{mid}$' of the first redox process, representing the midpoint between the first reduction peak and its corresponding oxidation peak. This approach is exemplified in **Figure 18** (top), where the $E_{mid}$ of the first redox process is calculated to be –1.27 V vs $Fc^+|Fc$. The second method involves determining the 'onset reduction' of the first reduction process. Here, the equations of two linear segments of the potential curve (at the start and during the first reduction process) are assessed. The potential at which these two lines intersect, determined through simultaneous equations, is defined as the onset reduction potential. An example of this is shown in **Figure 18** (bottom) where the value of x in both equations is calculated to be -1.19 V vs $Fc^+|Fc$.

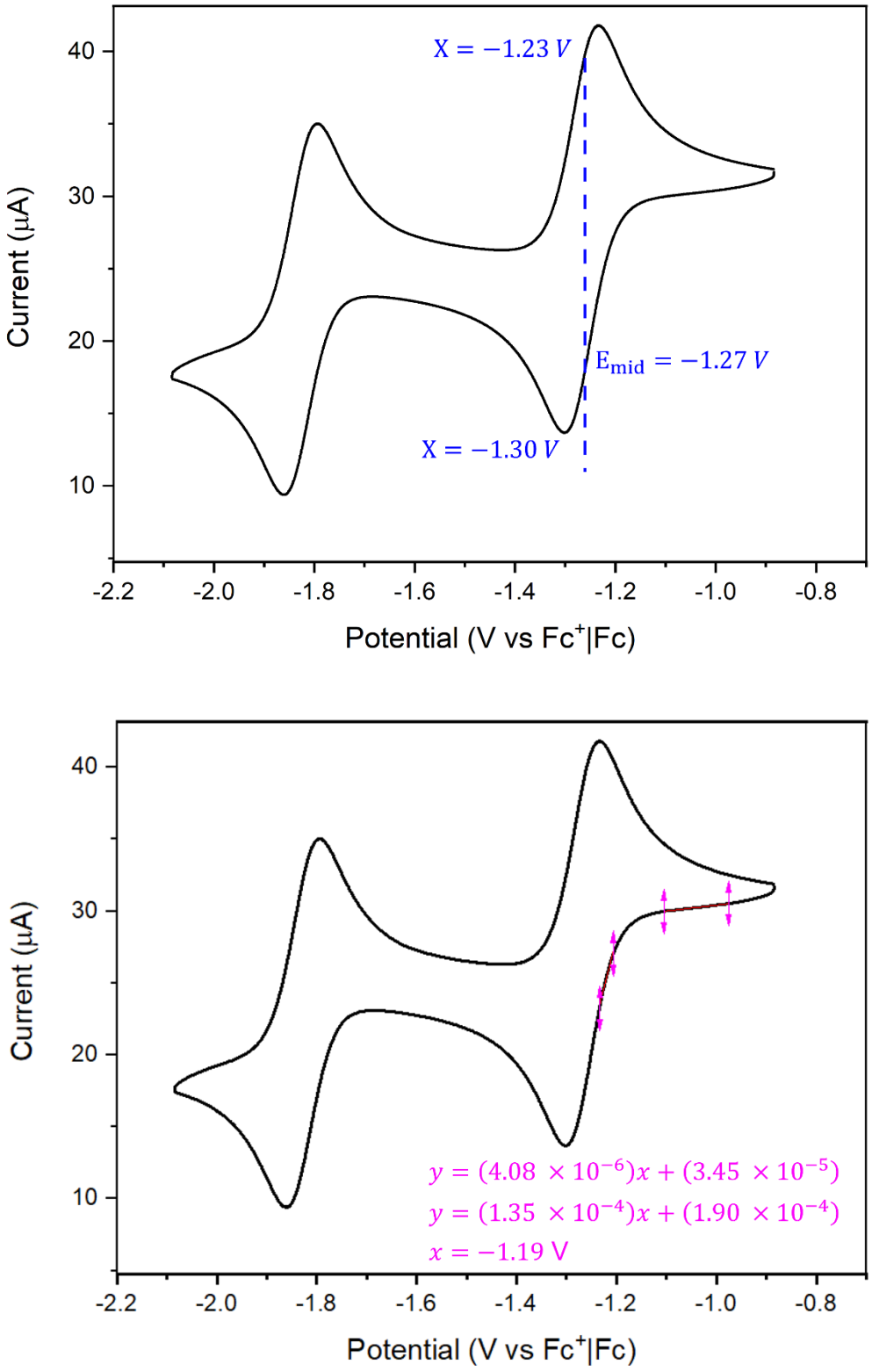



**Figure 18.** Top) Reduction potential calculated using the $E_{mid}$ of the first redox process. Bottom) Reduction potential calculated using the onset reduction of the first reduction peak.

When choosing between methods, the onset reduction potential is favourable. The use of $E_{mid}$ potential depends on the electrochemical reversibility of the first redox process, which further depends on the redox species analysed and the experimental conditions used. In contrast, the onset reduction potential, regardless of whether the redox processes are electrochemically reversible or irreversible, can be determined. Within this thesis, $E_{mid}$ of the CV data (referred to as the standard potential) will be discussed for relative comparisons, however, for LUMO calculations and estimations, the onset potential will be used.

Following the determination of the reduction potential, it becomes possible to estimate the relative LUMO energy level of the redox active species using **Equation 1**, proposed by Sworakowski and coworkers. In this equation, '*A*' represents the electron affinity, '*e*' represents the unit charge, parameters '$\alpha$' and '$\beta$' are the correlation coefficients, and the energies are expressed in eV. The commonly employed electrochemical reference, ferrocene, is used in these systems to calculate the energy levels of both the HOMO and LUMO. Thus, the ferrocene value of –4.83 eV, with respect to vacuum level, is factored into the equation. Additionally, the value of $\alpha$ corresponds to the solvent correction factor experimentally determined by the Thompson group in 2009.[123]

$$A = -E^{LUMO} = (\alpha^{-} \times (e\pi_{red}) + \beta^{-}) \quad (1)$$

### 3.2.2 HOMO Energy Level Calculations

In the indirect estimation of the HOMO energy level, the energy gap ($\Delta^{\mathrm{E}}$, otherwise known as the absorption edge) of the redox species is determined using UV-Vis absorption spectroscopy. Similar to calculating the onset reduction from the cyclic voltammetry, the optical gap is calculated at the onset of the lowest energy absorbance. Sworakowski *et al*., empirically determined that the HOMO-LUMO energy gap ($\Delta\mathrm{E}$) calculated using direct

methods was consistently 37% larger than the energy gap determined using indirect methods.[119,120] As a result, **Equation 2** was introduced for determining the HOMO-LUMO energy gap.

$$\Delta \mathrm{E} = 1.37 \times \Delta^{AE} \quad (2)$$

From this energy gap calculation and estimation, the HOMO energy level can be estimated from **Equation 3** involving using calculating the difference between the LUMO energy level and the HOMO-LUMO energy gap.

$$E^{HOMO} = E^{LUMO} - \Delta \mathrm{E} \quad (3)$$

While these calculations provide indirect estimations of the frontier orbital energy levels, the advantage lies in conducting both voltametric and spectroscopic data in the same system for all compounds analysed. This approach allows for accurate comparisons to be made between the different POM clusters, indicating the influence of structural variation on the frontier orbitals of the resulting POM systems.

### 3.3 Advancing Phosphotungstate Organic-Inorganic Hybrid POMs

As outlined in **Section 1.5.2**, the synthesis and electronic characterisation of organophosphonate and organosilyl phosphotungstate hybrid POMs, namely ($^{n}Bu_4N)_6[P_2W_{17}O_{61}(POC_6H_5)_2]$ {**PPhP$_2$W$_{17}$**} and ($^{n}Bu_4N)_6[P_2W_{17}O_{61}(Si_2O(C_6H_5)_2)]$ {**SiPhP$_2$W$_{17}$**}, have been previously documented.[74] This research highlights the significance of structural variations, specifically the choice of the bridging group, in influencing the electronic properties of the functionalised POMs. These modifications induce alterations in the frontier orbital energies, thereby impacting the photochemical properties of the resulting POMs.[76]

To broaden our understanding in this area, a study on the influence of substituting the phosphonate bridging atom with another element in the same group on the electronic properties of the POMs, is necessary. An example would involve employing an organoarsonate group, introducing a smaller difference in the bridging atom as compared to the literature-known organophosphorus and organosilyl hybrids, with P and Si in different groups.

In addition to this, current reports on the effect of various *para*-substitution on the electronic properties of organic-inorganic hybrid POMs focuses solely on organophosphonate hybrid POMs.[75,76] Expansion of this work could involve the synthesis of various organoarsonate hybrid POMs bearing different *para*-substituted functionality.

Within our group, preliminary studies on the organoarsonate phosphotungstate Well-Dawson POMs, denoted as $(Et_4N)_6[P_2W_{17}O_{61}(AsOR)_2]$ (where R = Ph, $C_6H_4NO_2$, and $C_6H_4NH_2$) have been initiated, establishing the synthesis and structural characterisation of this novel POM family. Despite this initial work, there were challenges in exploring the electronic properties of the POMs. For instance, the POMs exhibited insolubility in various organic solvents, such as acetonitrile, and a tendency to undergo rapid reduction over time, making fundamental electronic studies and application to organic photocatalysis challenging. To address this, one potential modification involves altering the type of cation associated with the POM clusters. Past studies have shown that the type, and more significantly, the size of the cations, can profoundly affect the physical properties of the resultant POMs, including solubility, hydrolytic and electronic stability.[124]

### 3.4 Aims and Objectives

While POM organofunctionalisation has been demonstrated to alter the frontier orbital energies of the resulting systems, current state-of-the-art research has only begun to delve into the intricate relationships between the specific structural changes in POMs and their electronic properties. Moreover, only a limited number of publications on the orbital engineering and modification of the HOMO-LUMO energy levels in POMs for photocatalytic applications have been reported.[50,125] As a result, it becomes necessary to gain a comprehensive understanding of both the orbital energy influence, determined by the structure of the POM, on the photochemical properties of these compounds. In this work, we set out to do the following:

1) To synthesise various organoarsonate phosphotungstate POMs exhibiting structural diversity expanding the current work previously conducted in the research group.
2) To characterise the electronic properties of various phosphotungstate POMs through cyclic voltammetry and UV-Vis spectroscopy.
3) To estimate the POM frontier orbital energies of structurally diverse POMs, to establish relationships between structural modifications and frontier orbital energies.

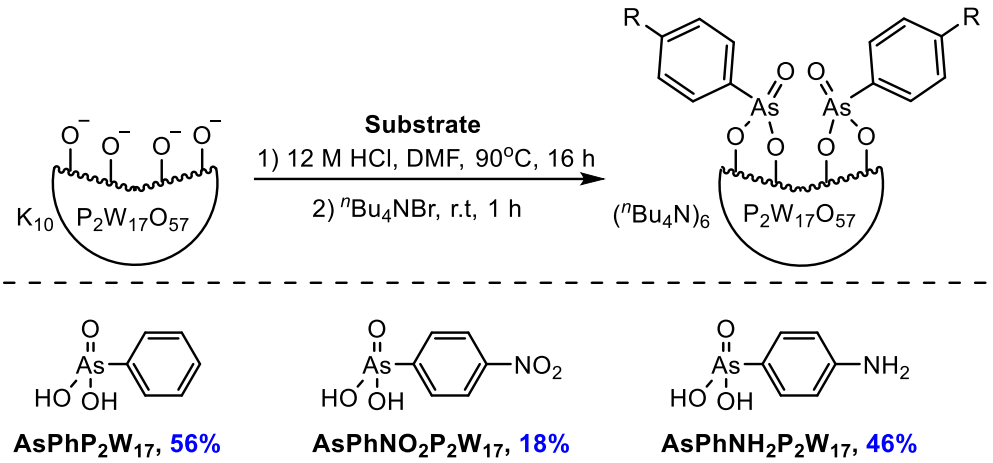
Once established, application of these structures can then be explored in various reactivity types including visible-light initiated SET and HAT transformations, with structural modulations used to tune the properties of the POMs as photocatalysts.

## 3.5 Results and Discussion

### 3.5.1 Design and Synthesis

The organophosphonate and organosilyl phosphotungstate Wells-Dawson POMs {**PPhP$_2$W$_{17}$**} and {**SiPhP$_2$W$_{17}$**} were synthesised from the potassium lacunary POM $K_{10}[P_2W_{17}O_{61}]$, using literature reported procedures.[126–128] Replication of these transformations, with covalent attachment of the organogroups to the mono-lacunary site, were successful in affording the desired POMs as their $^n$Bu$_4$N salts. For modification of the bridging group, the synthesis of the novel organoarsonate hybrid POM as it's $^n$Bu$_4$N salt - $(^n Bu_4N)_6[P_2W_{17}O_{61}(AsOC_6H_5)_2]$ {**AsPhP$_2$W$_{17}$**} was attempted.

Initial work in the synthesis of {**AsPhP$_2$W$_{17}$**} commenced with modification of the one-pot synthetic approach previously developed in our group, involving variation of the associated cations. In the synthesis of {**AsPhP$_2$W$_{17}$**} acid-catalysed condensation of phenylarsonic acid and lacunary POM $K_{10}[P_2W_{17}O_{61}]$ was conducted in DMF and the reaction mixture was heated to 90°C (**Scheme 6**). In this reaction, replacement of Et$_4$NBr with $^n$Bu$_4$NBr in the ion exchange of the POM proved successful in obtaining {**AsPhP$_2$W$_{17}$**} as the $^n$Bu$_4$N salt, in a moderate yield of 56%. Upon synthesis, a distinctive difference in colour between the Et$_4$N hybrid and the $^n$Bu$_4$N hybrid was observed. While hybrid $(Et_4N)_6[P_2W_{17}O_{61}(AsOC_6H_5)_2]$ appeared as a blue powder, {**AsPhP$_2$W$_{17}$**} in its $^n$Bu$_4$N form, presented as an off-white powder. As mentioned in **Section 1.3.3**, this is indicative of the 'heteropoly blues' and reduction of the Et$_4$N hybrid POM. This, in turn, indicates one of two things, that either the POM, as its $^n$Bu$_4$N form, is more difficult to reduce under atmospheric conditions, or it is easier for the POM to re-oxidise back in air.




**Scheme 6.** Top) Synthetic route to {**AsPhRP$_2$W$_{17}$**} hybrid POMs. Bottom) Organic substrates used in the hybridisation. Yield for POM synthesis is highlighted in blue.

Adaptation of the procedure to involve *p*-nitarsone and *p*-arsanilic acid as the starting substates, resulted in the synthesis of two additional organoarsonate hybrid POMs bearing different *para*-substituents, with opposing electronic behaviour. These were $(^n\text{Bu}_4\text{N})_6[\text{P}_2\text{W}_{17}\text{O}_{61}(\text{AsOC}_6\text{H}_4\text{NO}_2)_2]$ {**AsPhNO$_2$P$_2$W$_{17}$**}, featuring a nitro-substituent on the aromatic ring of the organogroup, and $(^n\text{Bu}_4\text{N})_6[\text{P}_2\text{W}_{17}\text{O}_{61}(\text{AsOC}_6\text{H}_4\text{NH}_2)_2$ {**AsPhNH$_2$P$_2$W$_{17}$**}, incorporating an amino-substituent. The introduction of the electron-withdrawing nitro-substituent led to a significant reduction in yield from 56% to 18%, while attachment of the electron-donating amino-substituent caused a marginal decrease of the yield to 46% (**Scheme 6**). By increasing the alkyl length of the cations from $\text{Et}_4\text{N}$ to $^n\text{Bu}_4\text{N}$, a decrease in yield was observed for the synthesis of these organoarsonate hybrids, with POMs $(\text{Et}_4\text{N})_6[\text{P}_2\text{W}_{17}\text{O}_{61}(\text{AsOC}_6\text{H}_5)_2]$, $(\text{Et}_4\text{N})_6[\text{P}_2\text{W}_{17}\text{O}_{61}(\text{AsOC}_6\text{H}_4\text{NO}_2)_2]$, and $(\text{Et}_4\text{N})_6[\text{P}_2\text{W}_{17}\text{O}_{61}(\text{AsOC}_6\text{H}_4\text{NH}_2)_2]$ obtained with yields of 70%, 51%, and 78%, respectively. This observed decrease in yield for the $^n\text{Bu}_4\text{N}$ POMs could be due to the increased steric hinderance of the longer alkyl groups, under the reaction conditions.

For the unsubstituted {**AsPhP$_2$W$_{17}$**} hybrid, $^1$H NMR spectroscopy revealed three distinctive peaks, aromatic in character, and in the range of 7.6 - 8.1 ppm (**Figure 19**). These peaks corresponded to the aromatic protons in the organoarsonate groups. Using $^1$H NMR spectroscopy, the estimation of the number of cations associated to the POM cluster was achieved by comparing the relative integrations of the aromatic protons with the aliphatic proton peaks corresponding to the $^n$Bu$_4$N counterions (in the range 0 - 3.50 ppm). Analysis of this data revealed the association of six cations with each cluster, supporting the general formula of these POMs as ($^n$Bu$_4$N)$_6$[P$_2$W$_{17}$O$_{61}$(AsOC$_6$H$_5$)$_2$]. This observation was found to be consistent across the phenyl arsonate analogues, with all hybrids demonstrating an association with six cations.

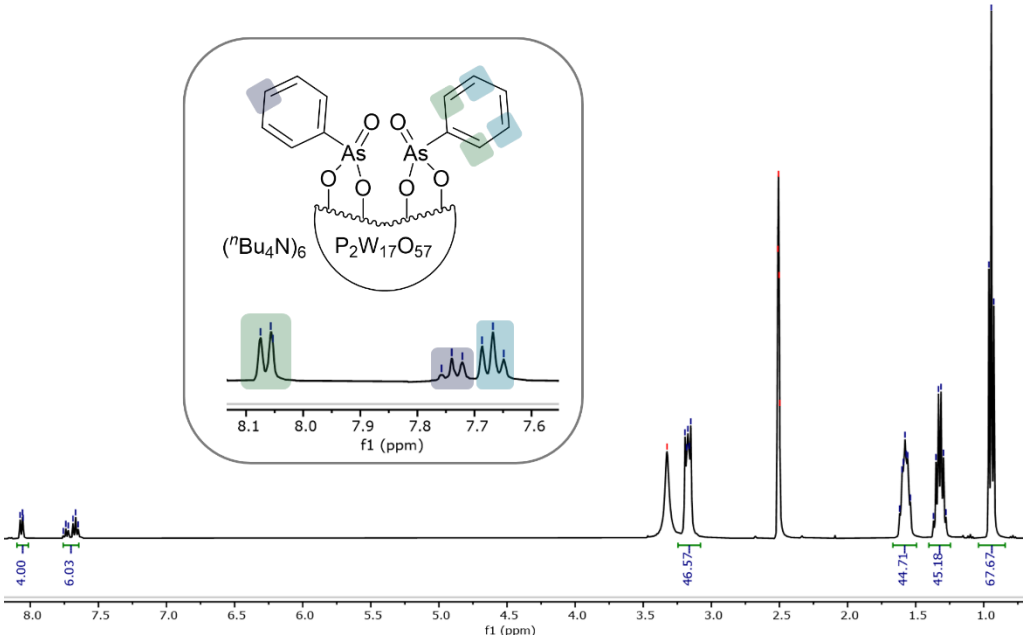



**Figure 19.** $^1$H NMR (400 MHz, DMSO–$d_6$) spectroscopy of ($^n$Bu$_4$N)$_6$[P$_2$W$_{17}$O$_{61}$(AsOC$_6$H$_5$)$_2$] – {**AsPhP$_2$W$_{17}$**}.

In the relative comparison of the aromatic protons of {**AsPhP$_2$W$_{17}$**}, {**AsPhNH$_2$P$_2$W$_{17}$**}, and {**AsPhNH$_2$P$_2$W$_{17}$**}, a downfield shift was observed for the aromatic protons adjacent to the nitro-substituent, while an upfield shift was observed for the protons adjacent to the amino-substituent (**Figure 20**). This observation correlates well to the electronic effects of the different substituents, with protons adjacent to electron-withdrawing substituents, exhibiting a higher ppm.

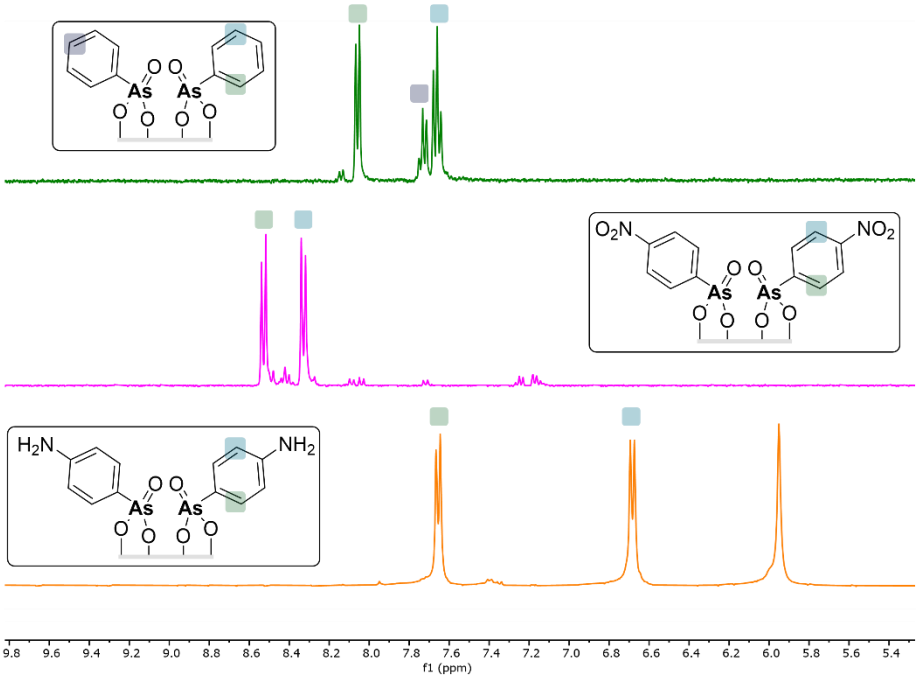



**Figure 20.** Stacked $^{1}$H NMR (400 MHz, DMSO–*d*$_6$) spectroscopy of organoarsonate hybrids in the region 5.5 – 10.2 ppm.

In the $^{31}$P NMR spectrum of lacunary precursor $K_{10}[P_2W_{17}O_{61}]$, two distinctive peaks can be observed at –7.23 ppm and –14.24 ppm in DMSO-*d*$_6$, corresponding to the two non-equivalent templating phosphate anions. This desymmetrisation occurs as a result of the localised negative oxo-anions at the lacuna, resulting in a more de-shielded environment for the phosphate residing closest to the lacunary site. Assignment of the two peaks has been reported previously by Thouvenot,[129] with the phosphate anion located nearest to the lacuna (labelled $P_1$) occurring more downfield, and the second phosphonate (termed $P_2$) residing more upfield.

For {**AsPhP$_2$W$_{17}$**}, these two peaks were found to be at -11.33 ppm and -13.27 ppm (**Figure 21** - green). The downfield shift (~4 ppm) of $P_1$ is attributed to the removal of the negative charge through organofunctionalisation, while the slight upfield shift (~1 ppm) of the second phosphonate (termed $P_2$) can be explained by the redistribution of anionic charge in the cluster upon hybridisation. Comparing to the $Et_4N$ analogue, the phosphonate peaks of $(Et_4N)_6[P_2W_{17}O_{61}(AsOC_6H_5)_2]$ occurred in the same region, reported to be –11.34 ppm and –13.26 ppm.

Relative to {**AsPhP$_2$W$_{17}$**}, the position of $P_1$ found in the hybrids {**AsPhNO$_2$P$_2$W$_{17}$**} (**Figure 21** - pink) and {**AsPhNH$_2$P$_2$W$_{17}$**} (**Figure 21** - orange), remained in the same location (-11.3 ppm), while the position of $P_2$ was found to be dependent on the electronics of the aromatic ring, despite residing further away from the hybridisation site. In {**AsPhNO$_2$P$_2$W$_{17}$**}, the introduction of an electron-withdrawing nitro-group led to a de-shielding effect of $P_2$, shifting its peak downfield from -13.27 ppm to -13.15 ppm. Conversely, in {**AsPhNH$_2$P$_2$W$_{17}$**}, the addition of an electron-donating amino-group resulted in an upfield shift of $P_2$ to -13.42 ppm. This interesting observation suggests that functionalisation induces changes in electron density and charge distribution not only locally but also across the entire complex, highlighting how even subtle structural modifications can alter the chemical properties of the resultant POM.

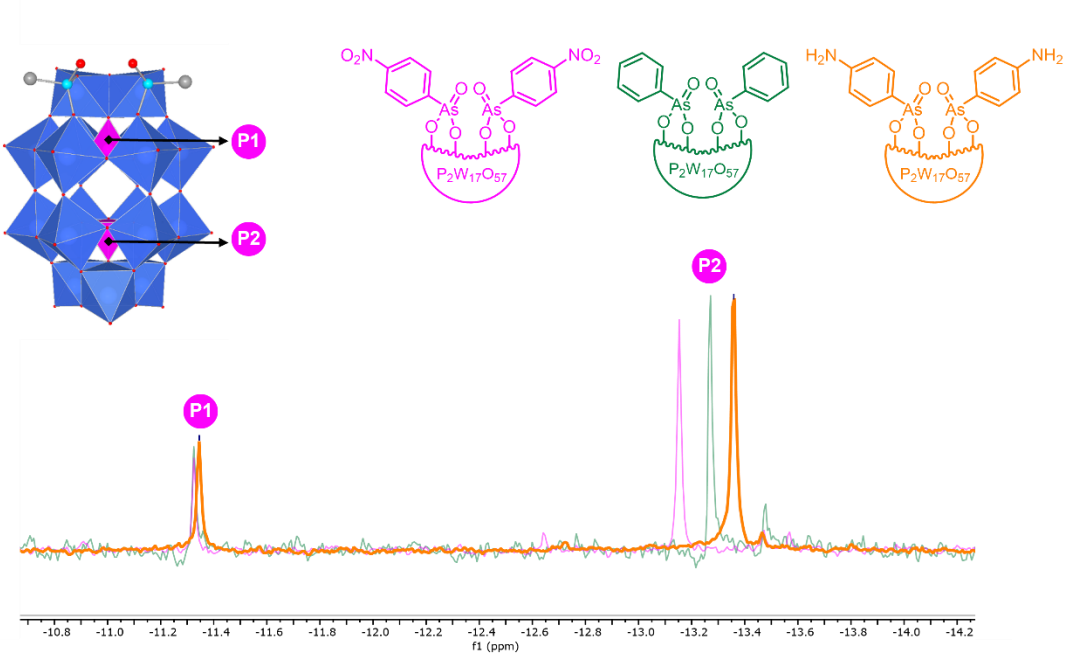



**Figure 21.** Superimposed $^{31}$P NMR (162 MHz, DMSO–$d_6$) of organoarsonate hybrids in the region -14.2 ppm and -10.8 ppm.

### 3.5.2 Electronic Characterisation and Investigation

With confirmation of POM functionalisation, the impact of the organogroups on the electronic properties of the POMs was investigated. In this work, plenary ($^n$Bu$_4$N)$_5$[P$_2$W$_{18}$O$_{62}$] {**P$_2$W$_{18}$**} and hybrids {**PPhP$_2$W$_{17}$**}, {**AsPhP$_2$W$_{17}$**}, and {**SiPhP$_2$W$_{17}$**} were evaluated using cyclic voltammetry (CV). Measurements were performed in anhydrous MeCN with $^n$Bu$_4$PF$_6$ (0.1 M) as the supporting electrolyte, under inert conditions. The voltammetry of {**P$_2$W$_{18}$**} showed four reversible redox processes, with the standard potential of the first reduction process ($W^{VI}/W^{V}$) occurring at –0.86 V vs $Ag^+|Ag$ (**Figure 22**). Incorporation of the organosilyl moiety to form {**SiPhP$_2$W$_{17}$**}, resulted in a negative shift in the first peak potential by 40 mV ($E_{mid}$ = −0.90 V vs $Ag^+|Ag$) relative to {**P$_2$W$_{18}$**}. The behaviour of {**SiPhP$_2$W$_{17}$**} relative to the parent POM corresponds well with previous reports demonstrating an observed cathodic shift due to the electron-donating effect of the siloxane group. In contrast, functionalisation with an organophosphonate group in {**PPhP$_2$W$_{17}$**} resulted in a large positive shift in first peak potential, with a difference of 380 mV ($E_{mid}$ = −0.48 V vs $Ag^+|Ag$). The opposite effect of the electron-withdrawing organophosphonate

group has also been demonstrated previously.[74] This work highlights the influence of electron-donating and -withdrawing bridging groups on shifting the potential of the first redox process.

For organoarsonate hybrid {**AsPhP$_2$W$_{17}$**}, a similar behaviour to the {**PPhP$_2$W$_{17}$**} hybrid was observed, with a positive shift in the standard potential of the first redox process observed, attributed to the electron-withdrawing phenyl arsonate moiety and the removal of electron density from the POM cluster. This resulted in a 300 mV shift and a standard potential of −0.54 V vs $Ag^+|Ag$. The 60 mV difference between {**PPhP$_2$W$_{17}$**} and {**AsPhP$_2$W$_{17}$**} is likely due to the shorter P=O, P–O and P–C bonds in {**PPhP$_2$W$_{17}$**}, resulting in better frontier orbital overlap of the phosphonic and the oxo-groups of the POM and the carbon of the phenyl ring. As a result, a slightly stronger electron-withdrawing effect occurs, causing the POM core in {**PPhP$_2$W$_{17}$**} to be more susceptible to gaining an electron. This in turn, causes the reduction potentials of {**PPhP$_2$W$_{17}$**} to be more positive than that of {**AsPhP$_2$W$_{17}$**}.

Beyond the first redox process, the organoarsonate hybrid {**AsPhP$_2$W$_{17}$**} showed a similar voltametric profile to the organophosphorus analogue {**PPhP$_2$W$_{17}$**}. The first four processes of the arsonate POM were found to be chemically reversible, residing within 100 mV of the corresponding processes found in the organophosphorus POM. In all cases, the peak-to-peak separation of the processes become slightly larger, the more negative the potentials, but remained in the range of 60 – 150 mV.

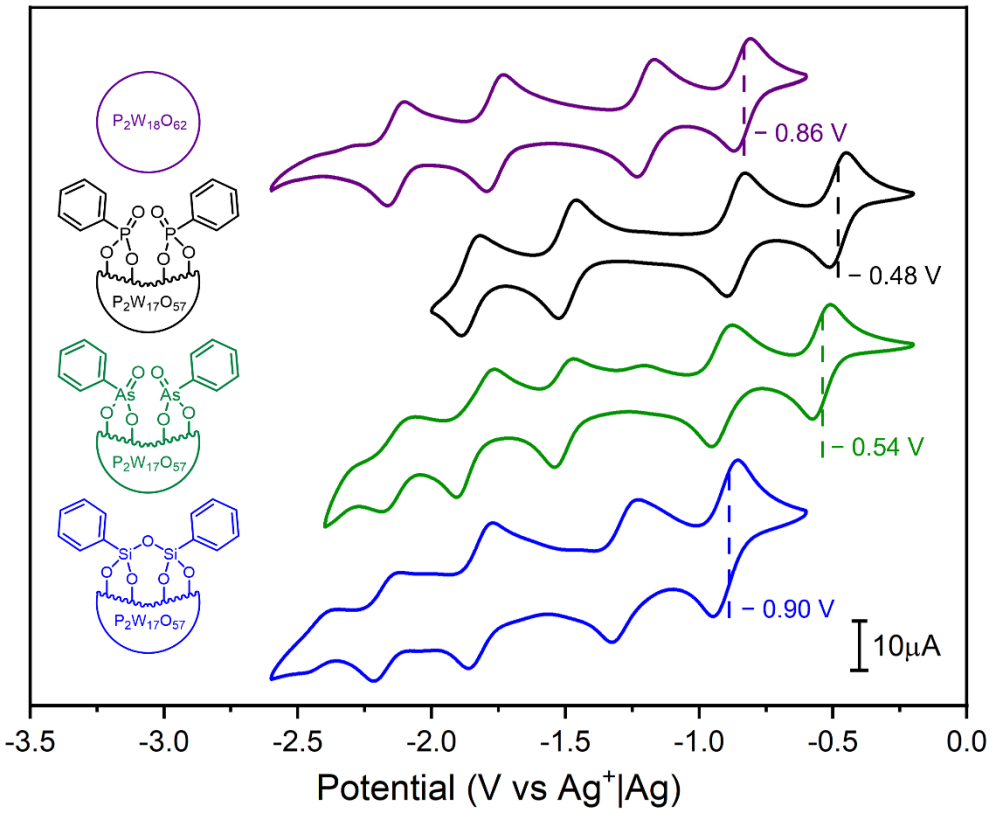



**Figure 22.** A stacked CV of 1mM of compounds {**$P_2W_{18}$**}, {**$PPhP_2W_{17}$**}, {**$AsPhP_2W_{17}$**}, and {**$SiPhP_2W_{11}$**} in anhydrous MeCN with 0.1 M $^{n}Bu_4NPF_6$ supporting electrolyte. All CVs were recorded at 100 $mVs^{-1}$ using a glassy carbon working electrode (d = 3 mm and $A$ = 0.071 $cm^2$), Pt wire counter electrode and a $AgNO_3$|Ag non-aqueous reference electrode. The standard potentials are highlighted for the first redox processes.

The degree of redox tuneability of the organoarsonate hybrids was then investigated by comparing the voltammetry of the unsubstituted organoarsonate hybrid {**$AsPhP_2W_{17}$**} with {**$AsPhNH_2P_2W_{17}$**} (bearing *p*-substituted electron-donating amino groups) and {**$AsPhNO_2P_2W_{17}$**} (bearing *p*-substituted electron-withdrawing nitro groups). Relative to {**$AsPhP_2W_{17}$**}, a 40 mV negative shift in potential was observed for amino derivative {**$AsPhNH_2P_2W_{17}$**} ($E_{mid}$ = -0.58 V vs $Ag^+$|Ag), whilst a positive shift in potential of 100 mV was shown for {**$AsPhNO_2PW_{17}$**} ($E_{mid}$ = −0.48 V vs $Ag^+$|Ag - **Figure 23**). With this data, it is evident that the electronics of the aryl ring, alters the

electronic potential of the POM, whereby the redox potentials become more positively shifted as the electron deficiency of the ring system is increased.

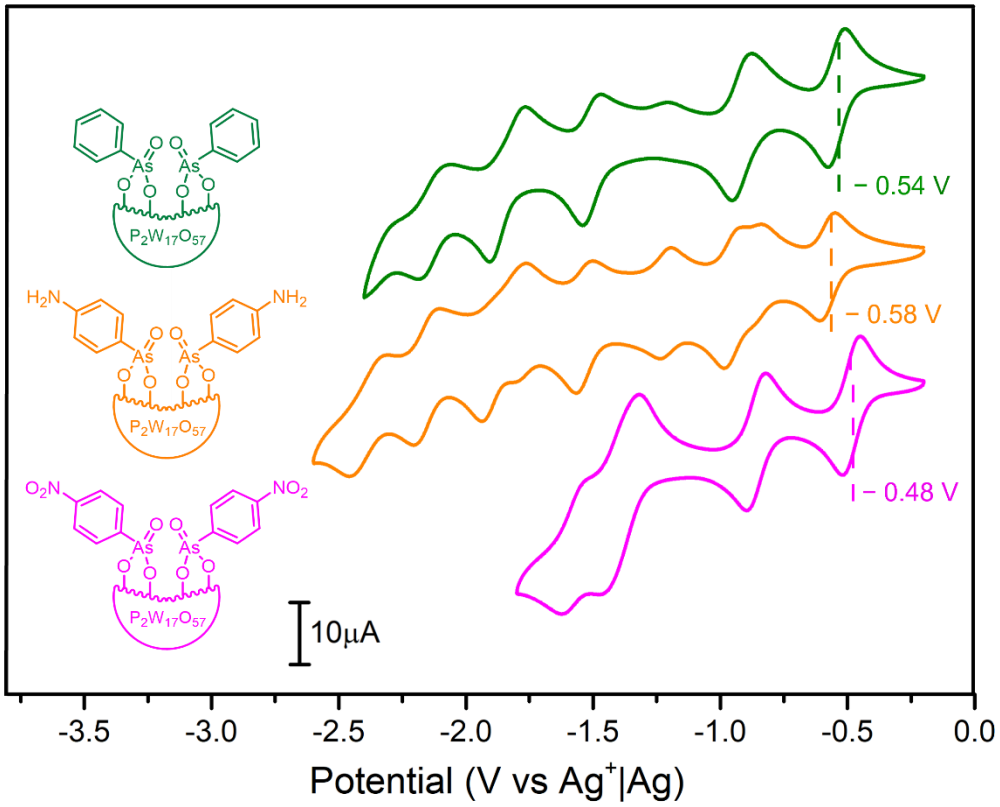



**Figure 23.** A stacked CV of 1mM of POMs {**AsPhP$_2$W$_{17}$**}, {**AsPhNH$_2$P$_2$W$_{17}$**} and {**AsPhNO$_2$P$_2$W$_{17}$**}. The standard potentials are highlighted for the first redox processes.

Beyond the first redox process, different redox behaviours were displayed for the substituted organoarsonate hybrids, relative to {**AsPhP$_2$W$_{17}$**}. Additional to the six redox processes observed in hybrid {**AsPhP$_2$W$_{17}$**}, amino derivate {**AsPhNH$_2$P$_2$W$_{17}$**} displayed two further redox processes with standard potentials occurring at –0.84 V and –1.22 V vs Ag$^+$|Ag. These additional reductions could be ascribed to the higher hydrophilicity of the amine groups, thus higher quantity of water in the sample, resulting in the occurrence of proton-coupled redox processes. This corroborates with the increased amount of water detected in the $^1$H NMR spectrum of the amino derivative relative to the other organoarsonate hybrids. For the nitro derivative {**AsPhNO$_2$P$_2$W$_{17}$**}, a

new multielectron reduction –1.39 V vs $Ag^{+}|Ag$ was observed in the CV data. This type of irreversible signal has been reported previously in the reduction of *p*-substituted nitroarenes.[130] No further processes were observed at more negative potentials due to the onset of solvent degradation.

To probe the photochemical nature of the hybrids, UV-Vis spectroscopy was employed (**Figure 24**). For all hybrid POMs, only minimal differences in the absorption edge were observed, with the exception of amino derivative {**$AsPhNH_2P_2W_{17}$**} which exhibited extended tailing into the visible region. For {**$PPhP_2W_{17}$**}, {**$SiPhP_2W_{17}$**} and {**$AsPhP_2W_{17}$**}, an absorption profile similar to the plenary {**$P_2W_{18}$**} POM was observed. This suggests that the POM core and not the organogroups are solely responsible for these absorption edges. For the amino and nitro arsonate derivatives, both hybrids displayed a discrete peak in the UV region, at 258 nm, where ε = 91,654 and at 259 nm, where ε = 64,582, respectively. These enhanced absorbances are most likely attributed to the absorption of the *N*-substituted aromatic rings. Generally, *p*-substitution of the aromatic organoarsonate group has a much less profound effect on the absorption properties, when compared to the redox characteristics of the POM species.

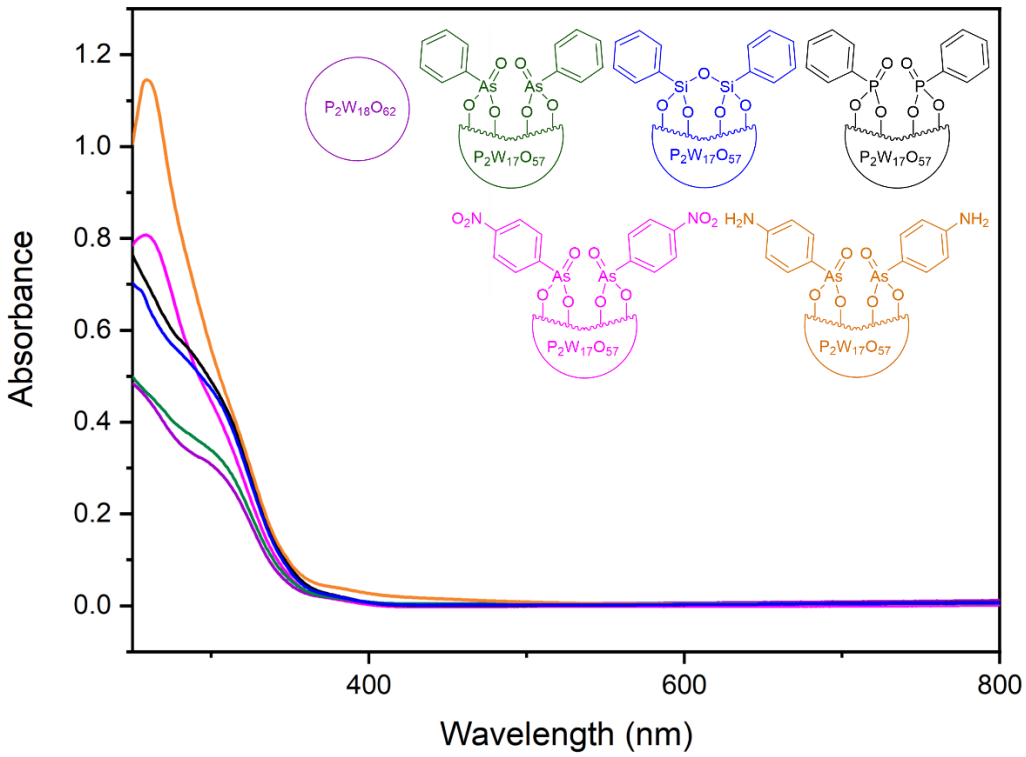



**Figure 24.** UV–vis absorption spectrum of phosphotungstate POMs in MeCN at 12.5 µM.

### 3.5.3 POM HOMO–LUMO Determination

The indirectly determined HOMO and LUMO energy levels of various POMs, along with the HOMO-LUMO energy gap, were determined using the equations described by Sworakowski *et al.,* utilising CV and UV-vis absorption data (specific values provided in Appendix).

In this study, the POMs were categorised into three different series (**Figure 25**):

(1) The first involved the study of plenary POMs and the effect of various archetypes, addenda atoms, and central templating anions, on the HOMO and LUMO energy levels. This selection includes **TBADT**, Wells-Dawson {**$P_2W_{18}$**}, and Keggins ($^n$Bu$_4$N)$_3$[PW$_{12}$O$_{40}$] {**$PW_{12}$**}, ($^n$Bu$_4$N)$_3$[PMo$_{12}$O$_4$] {**$PMo_{12}$**}, and ($^n$Bu$_4$N)$_4$[SiW$_{12}$O$_{40}$] {**$SiW_{12}$**}.

(2) The second series focuses on POM organofunctionalisation and the effect of various bridging atoms on the orbital energies, with the analysis of plenary {**$P_2W_{18}$**} and hybrids {**$PPhP_2W_{17}$**}, {**$AsPhP_2W_{17}$**}, and {**$SiPhP_2W_{17}$**} all bearing identical aromatic components.

(3) Lastly, the effect of aromatic substitution across identically bridged hybrids was evaluated with the study of POMs {**$AsPhP_2W_{17}$**}, {**$AsPhNO_2P_2W_{17}$**}, and {**$AsPhNH_2P_2W_{17}$**}, with focus on the impact of the electronics of the ring on the orbital energy levels.

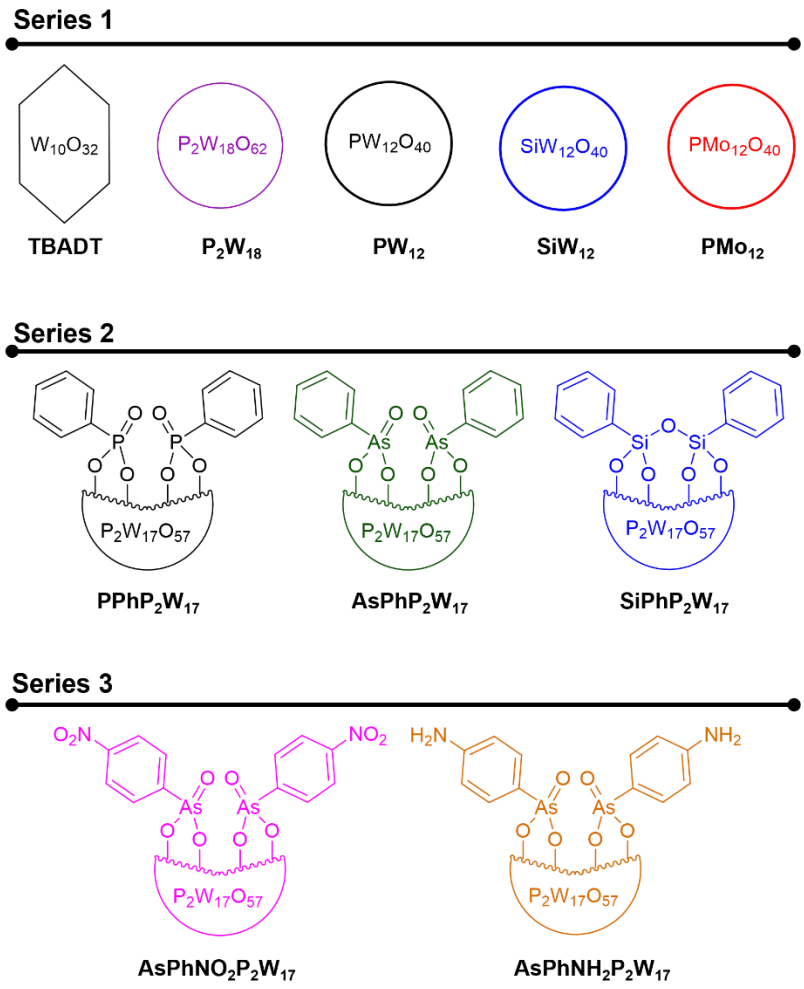



**Figure 25.** Selected polyoxometalates, categorised in to three series, analysed in the study of the impact of structural variations on the estimated frontier orbital energies.

In the HOMO-LUMO energy calculations of the first series, **TBADT** exhibited a HOMO level at –7.71 eV, a LUMO at –3.84 eV, and a corresponding energy gap of 4.30 eV. When compared to {$\mathbf{P_2W_{18}}$}, a similar energy gap of 4.21 eV was shown for the phosphonate POM, indicating the requirement of UV-light irradiation for POM activation in photochemical reactions. Notably, **TBADT** has been shown to be activated with visible-light, suggesting tailoring of its UV-vis absorption edge into the visible-light region, when compared to the plenary {$\mathbf{P_2W_{18}}$} POM. For the orbital energy levels of {$\mathbf{P_2W_{18}}$}, both the HOMO and LUMO levels were found to exhibit a lower energy than **TBADT**, displayed at –8.00 eV and –3.79 eV respectively.

Variation of the archetype from the Wells-Dawson {$\mathbf{P_2W_{18}}$} to the plenary Keggin {$\mathbf{PW_{12}}$} resulted in the decrease in energy for both the HOMO (from –8.00 eV to –8.78 eV) and LUMO (from –3.79 eV to –4.10 eV), accompanied by an increase in energy gap (from 4.21 eV to 4.67 eV - **Figure 26**). Replacement of the tungsten addenda atoms in {$\mathbf{PW_{12}}$} for molybdenum in {$\mathbf{PMo_{12}}$} led to a smaller energy gap of 4.80 eV, with destabilisation of the HOMO at (from 8.41 eV to -8.32 eV), and stabilisation of the LUMO (from –4.23 eV to –4.16 eV). This decrease in the energy gap as a result of addenda atom substitution is consistent with literature precedence demonstrating the enhanced visible-light activity of molybdenum-substituted POMs relative to the analogous fully tungstate POMs.[131] Replacement of the phosphonate heteroatom in {$\mathbf{PW_{12}}$} with a central silicate in {$\mathbf{SiW_{12}}$}, resulted in destabilisation of both the HOMO (from –8.41 eV to –7.89 eV) and LUMO energy levels (from –4.23 eV to –3.75 eV), with a marginal increase in the energy gap, from 4.67 eV to 4.73 eV. The observed influence of heteroanion substitution on the HOMO and LUMO energy levels is consistent with previously reported literature for Keggin POMs,[132] supporting the reliability of this indirect method to estimate frontier orbital energies.

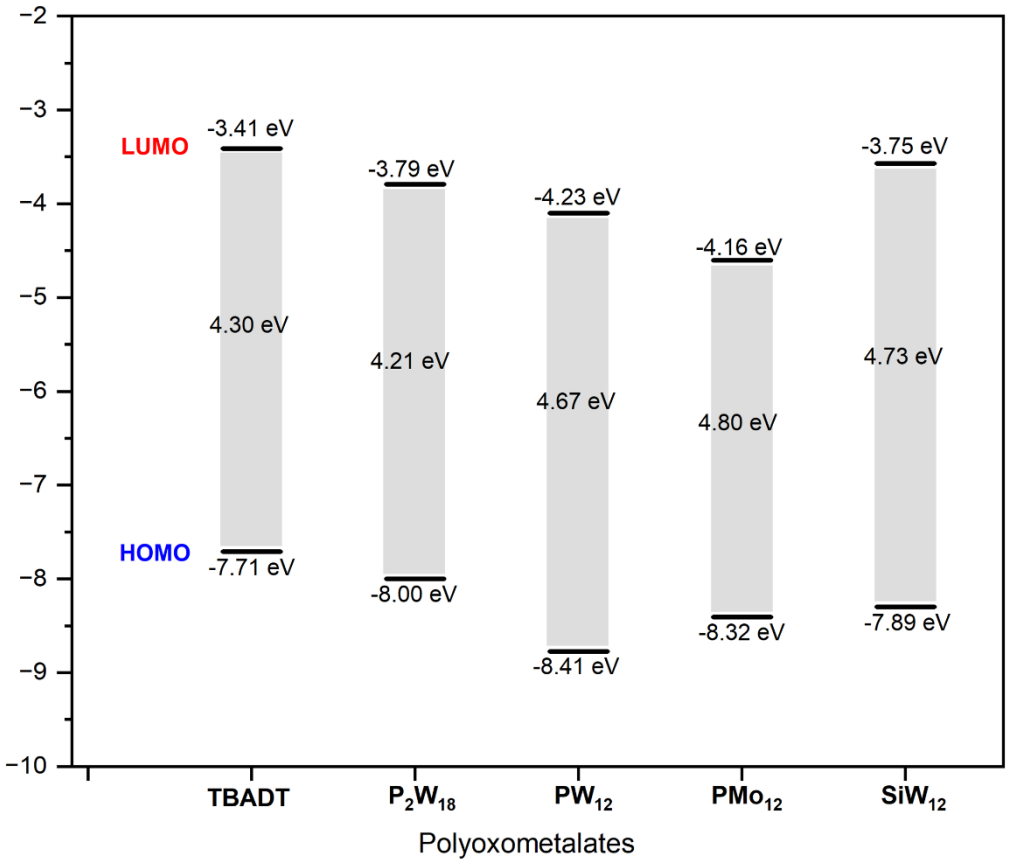



**Figure 26.** Schematic representation of the estimated HOMO-LUMO levels derived from CV and UV-Vis absorption spectroscopy for Series 1.

In the investigation of the influence of organofunctionalisation on the HOMO-LUMO energy levels of the POMs, the next series of POMs analysed included plenary {**$P_2W_{18}$**}, and hybrids {**$PPhP_2W_{17}$**}, {**$AsPhP_2W_{17}$**}, and {**$SiPhP_2W_{17}$**} (**Figure 27**). In all cases, hybridisation led to the stabilisation of both the HOMO and LUMO energy levels, as shown by a decrease in energy for both orbitals. Relative to {**$PW_{18}$**}, the energy levels in hybrid {**$PPhP_2W_{17}$**} were found to exhibit the most significant energy decrease (~0.45 eV) which resulted in a HOMO energy level at –8.41 eV and a LUMO at –4.23 eV. Furthermore, the organophosphonate functionalisation narrowed the energy gap from 4.21 eV to 4.18 eV. This reduction in the HOMO-LUMO energy gap suggests a shift in absorption edge of {**$PPhP_2W_{17}$**} towards the visible-light end of the spectrum, relative to the plenary POM. Observing this small shift *via* UV-vis absorption data directly can be challenging, with the main absorbance peaks originating from the POM core. As a result, both LUMO energy estimations, combined with the UV-Vis absorption data are required to assess the photoactivity of the POMs.

The orbital energies in the organoarsonate hybrid {**$AsPhP_2W_{17}$**} displayed a similar trend to {**$PPhP_2W_{17}$**} with the HOMO shifting from –8.00 eV to –8.32 eV relative to {**$P_2W_{18}$**}, and the LUMO going from –3.79 eV to –4.16 eV. Additionally, a narrowed energy gap of 4.16 eV was observed. For hybrid {**$SiPhP_2W_{17}$**}, organosilyl functionalisation led to minute changes to the frontier orbital energies compared to {**$P_2W_{18}$**}, with only a 0.04 eV difference between the LUMO levels (from –3.79 eV to –3.75 eV) and a 0.11 eV difference between the HOMO levels (from –8.00 eV to –7.89 eV). Furthermore, a very similar energy gap of 4.29 eV was observed. For this series, hybridisation was shown to have variable effects on the orbital energies, with dependence on the type of specific bridging atom used in the organofunctionalisation. In the comparison between the different bridging group atoms, replacement of the phosphonate for the arsonate had minimal impact on the orbital energy levels shown by a slight destabilisation for {**$AsPhP_2W_{17}$**} (~0.08 eV), and a small difference in the energy gap (~0.02 eV).

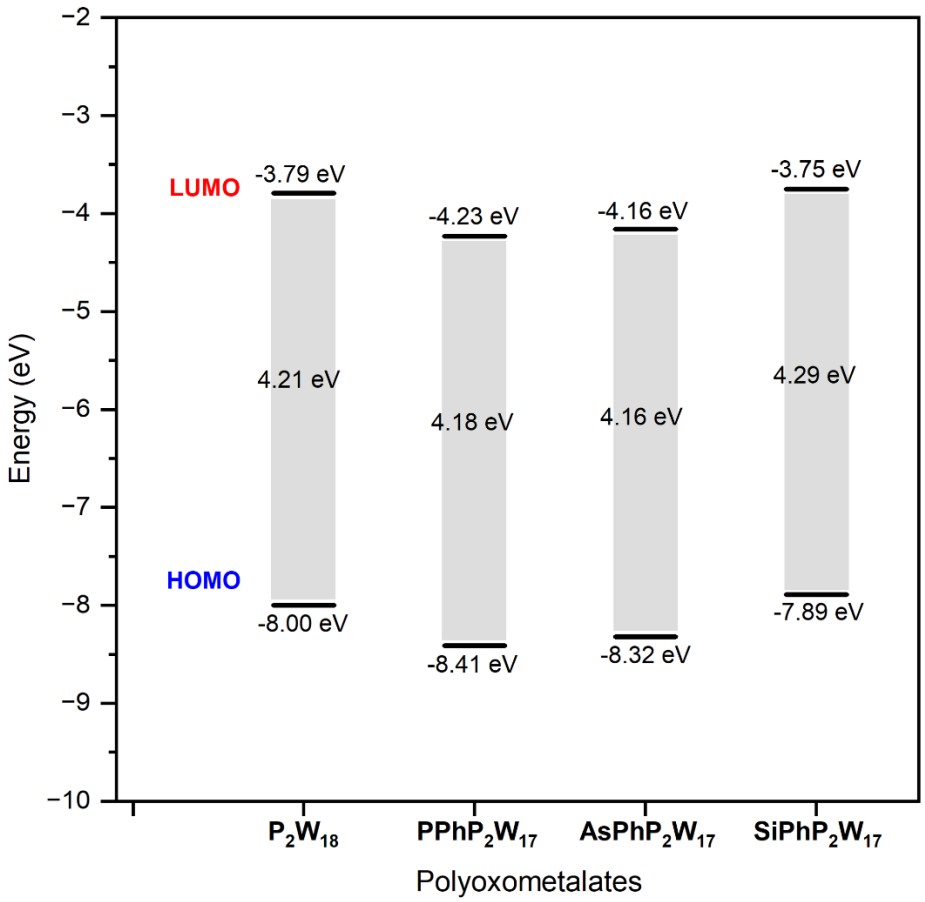



**Figure 27.** Schematic representation of the estimated HOMO-LUMO levels derived from CV and UV-Vis absorption spectroscopy for Series 2.

In the case of the substituted organoarsonate hybrids {**AsPhNO$_2$P$_2$W$_{17}$**} and {**AsPhNH$_2$P$_2$W$_{17}$**}**,** variations in the electron density of the aromatic ring were shown to induce a subtle shift in frontier orbital energies. The electron-withdrawing nitro analogue {**AsPhNO$_2$P$_2$W$_{17}$**} exhibited more negative HOMO and LUMO energy levels when compared to {**AsPhP$_2$W$_{17}$**}**.** In contrast, the electron-donating amino analogue {**AsPhNH$_2$P$_2$W$_{17}$**} displayed more positive HOMO and LUMO energy levels (**Figure 28**). Additionally, a constant energy gap of ~4.15 eV was observed. From this series, it becomes apparent that the choice of bridging atom has a larger influence on the orbital energies compared to organogroup substitution. While the impact of organogroup substitution has less significant, the subtle changes resulting from *para*-substitution, can be strategically exploited for fine-tuning frontier orbital energies in specific applications.

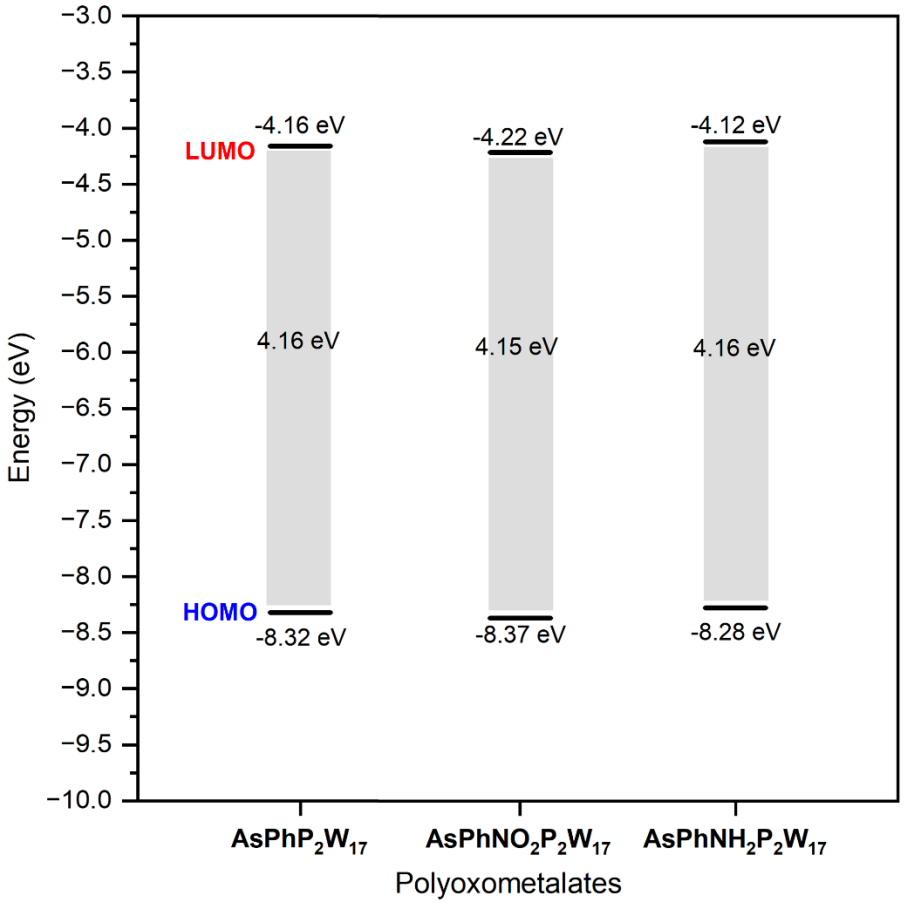



**Figure 28.** Schematic representation of the estimated HOMO-LUMO levels derived from CV and UV-Vis absorption spectroscopy for Series 3.

### 3.5.4 POM Frontier Orbital Estimations Relative to Oxygen

In the application of POMs in photocatalysis, closing of the catalytic cycle, oxidation of the reduced POM requires the use of an oxidant. This process involves removal of an electron from the POM's singly occupied molecular orbital (SOMO) to the oxidant. Theoretically, increasing the energy of the SOMO (or relative POM LUMO) could enhance the efficiency of this electron transfer process, facilitating the recycling of the POM catalyst. Previous literature has demonstrated oxygen to be excellent in closing the POM photocatalytic cycle. To this end, the LUMO energy level of oxygen was measured and compared. Under the same CV conditions as the POMs, the LUMO level of oxygen was estimated to occur at –3.39 eV. Interestingly, the estimated LUMO levels for all POMs were found to be lower in energy than the LUMO of oxygen.

Among the POMs, **TBADT** exhibited a LUMO level most similar to that of oxygen, with only a small difference of 0.02 eV. Additionally, owing to **TBADT**'s unique propensity to disproportionate, the secondary reduced state (corresponding to the LUMO+1), has been demonstrated to be accessible in photochemical reactions.[107] From the CV data, the LUMO+1 was estimated to be –2.76 eV. The accessibility of this secondary reduced state accelerates electron donation from **TBADT** to the oxidant, thereby further enhancing the catalytic efficiency of the POM.

## 3.6 Conclusions

From this data, it can be concluded that structural variations of the POM's core, including addenda atom substitution and central templating anion replacement can be used to influence the electronic characterises, and hence the frontier orbital energies, of the resultant POMs. Furthermore, organofunctionalisation of the POMs with various organic moieties shows a clear and predictable influence on the orbital energies of the hybrid POMs, based on the electron-withdrawing and -donating effects of the substituents and nature of the bridging atom. Relative to altering the optical and absorption properties of the POMs, variation of the components comprising the POM's core shows a greater influence on modification of the HOMO-LUMO energy gap, relative to functionalisation and changing the organogroup attached onto the POM. As a result, these structural changes could be exploited to tune the orbital energies of the POMs, and hence their photocatalytic properties.

# 4 Organofunctionalisation of Borotungstate Hybrid POMs

## 4.1 Introduction

The synthesis of phosphotungstate and silicotungstate Keggin systems share several similarities. Firstly, acid-mediated condensation of tungstates with silicate or phosphate can directly lead to the POM Keggin structures, with general formulas represented as α-$[PW_{12}O_{40}]^{3-}$ and α-$[SiW_{12}O_{40}]^{4-}$.[133] Secondly, pH-controlled hydrolysis results in the formation of the mono-, and tri-vacant derivatives, with examples including α-$[PW_{11}O_{39}]^{7-}$, α-$[PW_9O_{34}]^{9-}$, α-$[SiW_{11}O_{39}]^{8-}$, and α-$[SiW_9O_{34}]^{10-}$.[134] The key difference between the two lies in the charge of the central templating anion, with $P^V$ in place of $Si^{IV}$ resulting in a cluster with a higher overall anionic charge. Varying the charge of the POM alters the structures interconversion kinetics. For example, β-isomers ($\beta_1 \rightarrow \beta_2 \rightarrow \beta_3 \rightarrow \alpha$) for the monovacant phosphotungstate POM derivatives have been observed,[135,136] however isolation of these intermediates is challenging in contrast to the isomers of silicotungstates which are readily accessible.[137]

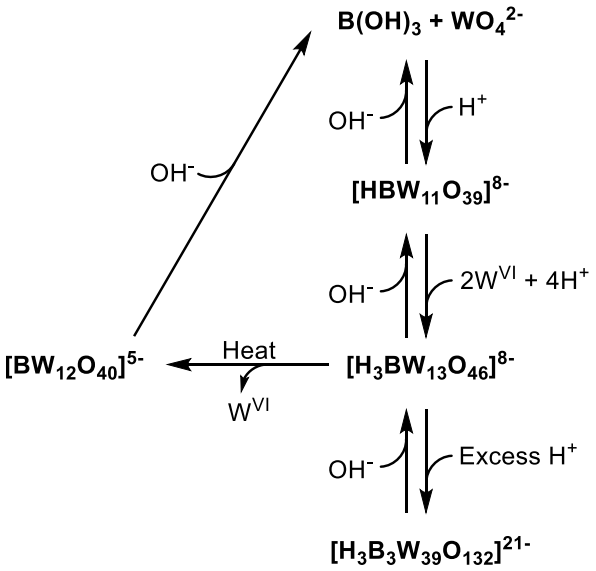
Comparatively, borotungstate Keggin-type derivatives have received little attention. While the general form $[BW_{12}O_{40}]^{5-}$, and α-lacunary is readily accessible by the use of boric acid $H_3BO_3$ ($B^{III}$), they remain largely underexplored.[138] Relative to other non-metal central atoms, $B^{III}$ has the lowest charge, coordination number, and smallest atomic size. Additionally, as an electron-deficient atom, boron can adopt different coordination motifs. As a result of these characteristics, borotungstate POMs have been shown to exhibit distinctive characteristics and properties not observed in other tungstate systems.

### 4.1.1 Plenary and Lacunary Borotungstate POMs

In 1982, Rocchiccioli-Deltcheff *et al.,* reported the first synthesis of α-$K_5[BW_{12}O_{40}]$, marking the beginning in the exploration of borotungstate POMs.[133] Despite this report, the subsequent years witnessed a noticeable gap in the documentation of the use of boron as the central templating anion,

especially when compared to phosphorus- and silicon-centred analogues. In 1997, a noteworthy development emerged as Tézé, Hervé and colleagues reported the synthesis of the lacunary borotungstate of general formula $[HBW_{11}O_{39}]^{8-}$.[138]

Unlike $SI^{IV}$ and $P^{V}$ centred clusters, synthesis of the lacunary borotungstate POM was not observed when the plenary POM α-$K_5[BW_{12}O_{40}]$ was exposed to basic conditions (pH 7-10).[139] In contrast, POM decomposition resulted in borate and tungstate ions found in solution. Alternatively, direct lacunary POM synthesis was achieved through the combination of tungstate and boric acid, under acidic conditions (pH 6-7). Furthermore, formation of the plenary α-$[BW_{12}O_{40}]^{5-}$ Keggin ion was not observed when $[HBW_{11}O_{39}]$ was exposed to acidic conditions, instead monomeric, dimeric, or trimeric species were formed.[140–143] These unconventional anionic species included α-$[H_3BW_{13}O_{46}]^{8-}$ (stable at pH 1–5) and α-$[H_6B_3W_{39}O_{184}]^{15-}$ (stable at pH 0). Increasing the temperature of intermediate α-$[H_3BW_{13}O_{46}]^{8-}$ led to the formation of the plenary POM.[138] The reaction routes for the varying cluster intermediates are shown in **Scheme 7**.




**Scheme 7.** Routes of formation of the borotungstate heteropolyanions.[138]

Previous literature in borotungstate POMs have indicated that the plenary $[BW_{12}O_{40}]^{5-}$ exhibits a highly symmetric tetrahedral $\{BO_4\}$ unit located at the centre of the POM.[142] This symmetric environment results in a sharp singlet peak in the $^{11}B$ NMR spectrum.[142] Formation of the lacunary POM through the removal of a polyhedra results in the lacunary which also exhibits the $BO_4$ central unit. However, due to the high negative charge resulting from the lower oxidation state of the boron atom, reports have indicated that the central borate anion in lacunary POMs is protonated. This protonation results in an unsymmetrical $BO_4$ unit, with the presence of a B-O-H bond. Due to the quadrupolar effect, a broad singlet peak in the $^{11}B$ NMR spectrum for the lacunary POM is observed.[142] Attempts to deprotonate the hydrated borate under basic conditions proton was shown to not be possible without causing POM degradation.[138] The protonation of the internal oxo-ligand adjacent to the heteroanion is a feature not observed for phosphotungstate and silicotungstate POMs and is unique to this family of POMs.

Comprising of the smallest group III heteroatom, borotungstate Keggin POMs exhibit more negative reduction potentials when compared to other group III containing Keggin POMs. In a comparative analysis involving Keggins of equivalent charge - $[BW_{12}O_{40}]^{5-}$, $[AlW_{12}O_{40}]^{5-}$, and $[GaW_{12}O_{40}]^{5-}$, atom size was shown to impact the electronic properties.[144] The small size of boron was shown to increase the HOMO of $[BW_{12}O_{40}]^{5-}$ by around 0.35 eV, relative to the other clusters of the same charge. This observation offers insight into the relationship between charge density on the frontier orbital energies of the POMs. Furthermore, the increased charge density of borotungstate POMs could explain as to why the $BO_4$ unit, despite sharing an equivalent formal charge, demonstrates greater instability than $AlO_4$ or $GaO_4$.

### 4.1.2 Organofunctionalised Borotungstate Hybrid POMs

In the year 2000, Liu and co-workers reported the synthesis of an organophosphorus borotungstate polyoxometalate (**Figure 29**).[145] In this work, α-$K_7NaHBW_{11}O_{39}\cdot 13H_2O$ was reacted with cyclohexyl phosphonyl chloride in acetonitrile to give the functionalised POM with the reported formula $(^nBu_4N)_4H[BW_{11}O_{39}(POC_6H_{11})_2]$ {**PCyBW$_{11}$**}. While the structural assignments confirmed POM functionalisation, the structure of the central $BO_4$ unit was not identified and no electronic characterisation was made. Only three other instances of organophosphorus-functionalised borotungstate POMs have been synthesised since (**Figure 29**). In 2005, the same group reported the aromatic phosphonate and thiophosphonate functionalisation of the same lacunary POM, yielding the hybrids $(^nBu_4N)_4H[BW_{11}O_{39}(POC_6H_5)_2]$ {**PPhBW$_{11}$**} and $(^nBu_4N)_4H[BW_{11}O_{39}(PSPh)_2]$ in a 45% and 67% yield, respetively.[146] A similar preparation to the aforementioned aliphatic analogue {**PCyBW$_{11}$**} was used, with the phosphonyl chloride reagent replaced by phenyl phosphonic dichloride. The same characterisation techniques were applied, with similar limitations.

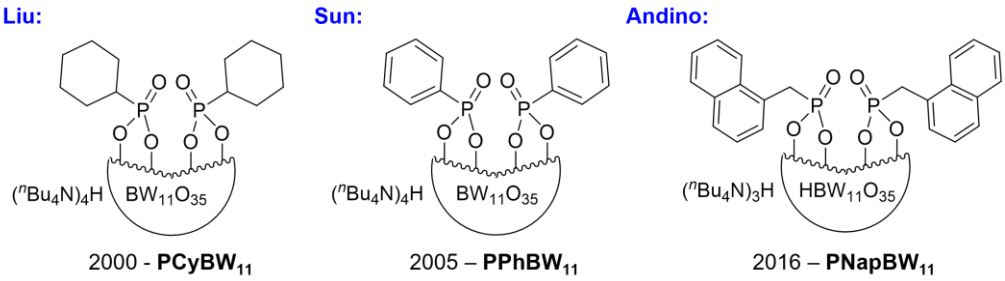



**Figure 29.** Previously reported organophosphorus borotungstate hybrid polyoxometalates.

It was not until 2016, when structural confirmation of an organophosphorus borotungstate hybrid Keggin cluster was achieved using X-ray crystallography.[147] Their synthesis differed to earlier reports by the use of phosphonic acid precursors over phosphoryl chlorides. This required conducting the reaction under an inert atmosphere to prevent hydrolysis of the

phosphoryl reagent. Crystallographic data revealed the presence of a monolacunary α-Keggin-type anion with two 1-naphylmethylphosphonate moieties in the vacant position of the POM.

Furthermore, the work by Andino presented a more in-depth study into the structural elucidation of the borotungstate POM, with spectroscopic analysis (including NMR and IR spectroscopy), providing supporting evidence for the previously reported protonation of the central oxo-ligand adjacent to the borate, and formation of the B-O-H peak. With this data, the formula for the synthesised hybrid was reported to be $(^{n}Bu_4N)_3H[HBW_{11}O_{39}(POC_{11}H_9)_2]$, with three $^{n}Bu_4N$ cations and protonation of the central borate anion. This formula differs from the previous reports by Sun *et al*., with the POMs reported to follow the general formula trend of $[POC_6H_5]_2X^{n+}W_{11}O_{39}]^{(8-n)}$ (where X = $P^{5+}$, $Si^{4+}$, $B^{3+}$), combined with no discussion surrounding central oxo-protonation.

Progressing in this field relies on achieving clarity in structural elucidation which entails exploring the general formula and individual components of borotungstate POMs. Additionally, investigation into the B-O-H protonation and understanding its influence on the overall properties of the POMs is crucial. Finally, synthesising other borotungstate hybrid POMs is important to broaden our understanding of this relatively underexplored family of POMs.

## 4.2 Aims and Objectives

The design, synthesis, and characterisation of organofunctionalised borotungstate POMs is underexplored compared to its silicotungstate and phosphotungstate analogues. The synthesis and assembly of the borotungstate plenary and lacunary POMs have highlighted distinctive characteristics unique to this family, attributed to the charge density of the central borate heteroanion, leading to several reports exploring their electro- and photochemical properties in applications such as energy storage,[148–150] photoreduction,[151] photochemical sensing,[152–154] and small molecule oxidations.[155–157]

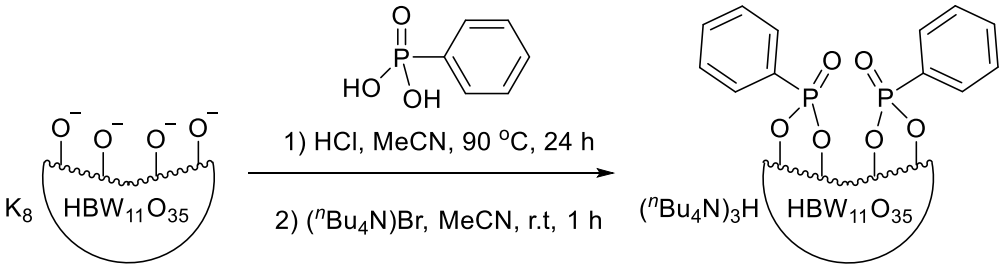
However, organic-inorganic hybrid borotungstates are hugely understated, with only four instances being synthesised and limited exploration into the electronic properties of these clusters. Furthermore, only organophosphonate hybridisation has been explored with the borotungstate POM core, with no work surrounding other bridging groups. Advancing this field involves a broader exploration into the scope of hybrid borotungstate POMs, delving into their structural and electronic properties and influence from the central borate anion. As a result, we set out to do the following:

1) To synthesise and structural determine various hybrid borotungstate POMs bearing different organogroup functionality.
2) To characterise the electronic properties of the borotungstate hybrids.
3) To investigate into the central borate protonation within these hybrid POMs.

## 4.3 Results and Discussion

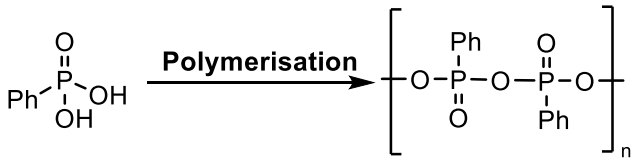
### 4.3.1 Design, Synthesis & Structural Elucidation

The synthesis of the organophosphorus borotungstate hybrid $K_3H[HBW_{11}O_{39}(POC_6H_5)_2]$ {**K•PPhBW$_{11}$**} was first attempted following the acid-catalysed condensation procedure as reported for the Wells-Dawson {**PPhP$_2$W$_{17}$**} POM (**Scheme 8**). Specifically, lacunary POM $K_8[HBW_{11}O_{39}]$ and phenylphosphonic acid were combined in a 1:2.5 ratio in MeCN, followed by the addition of a catalytic amount of 12M HCl. The reaction mixture was then refluxed and stirred for 24 h.



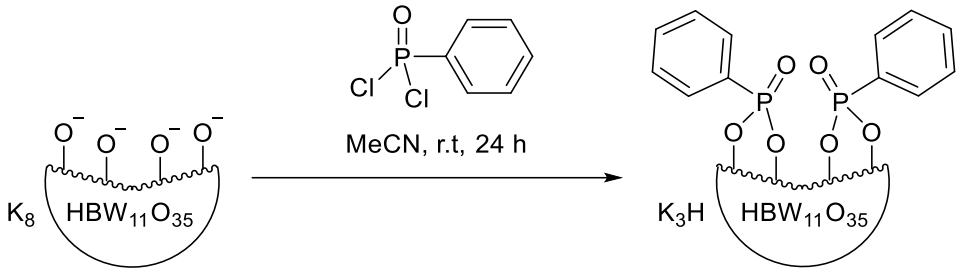

**Scheme 8.** Synthesis of the organophosphorus borotungstate hybrid POM under acid-catalysed condensation reaction conditions.

Unlike the Wells-Dawson equivalent, the isolated material presented with unidentified impurities, aromatic in character, as indicated by $^1$H NMR spectroscopy. Efforts to further purify the target POM with trituration or cation exchange to the $^n$Bu$_4$N salt, to exploit alternative solubilities, failed. The impurity was theorised to originate from the oligomerisation of starting material phenylphosphonic acid, resulting in the formation of a polymeric species (**Scheme 9**).[158]




**Scheme 9.** Proposed oligomer by-product of the hybridisation reaction.[158]

As a result, the synthetic method was altered by the use of phenylphosphonic dichloride, to avoid the side-product formation. The dropwise addition of phenylphosphonic dichloride was added to the lacunary POM $K_8[HBW_{11}O_{39}]$ in MeCN, under inert conditions (**Scheme 10**). The suspension was then stirred at room temperature for 24 h. Unfortunately, the presence of the polymeric species was also detected in this preparation. This could occur through the hydrolysis of the dichloride reagent to the acid, resulting in the same polymerisation route.[159] Efforts to reduce the rate of polymerisation including conducting the reaction in the absence of light and variation of reaction parameters, including dilution and rate of addition of the dichloride reagent, were unsuccessful. $^1$H NMR spectroscopic analysis following these alterations showed additional peaks in the range of 4-5 ppm. As the peak in this region was expected to correspond to the B-O-H peak, the presence of multiple peaks could suggest the formation of isomers or decomposition of the POM.




**Scheme 10.** Attempted synthesis of the potassium phenyl phosphorus borotungstate hybrid POM under acid-catalysed condensation reaction conditions.

Fortunately, successful isolation of {**K•PPhBW$_{11}$**} as the potassium salt was achieved *via* crystal growth using vapour diffusion techniques. Diffusion of an antisolvent (methyl *tert*-butyl ether) into a saturated solution of the POM in MeCN, afforded crystals suitable for POM characterisation. The $^{1}$H NMR spectrum saw three distinctive peaks, in the aromatic region (7.50 – 8.20 ppm), integrating in a 4:2:4 ratio (**Figure 30**). This corresponded well to the three aromatic proton environments of the proposed organogroups tethered to the POM, supporting the proposed structure of {**K•PPhBW$_{11}$**}. Furthermore, a distinctive singlet peak at 4.53 ppm, with an integral suggesting a singular proton, was also identified. This signal shares similarities to that reported for {**PNapBW$_{11}$**}, which was assigned to the B-O-H peak of the hybrid organophosphonate.

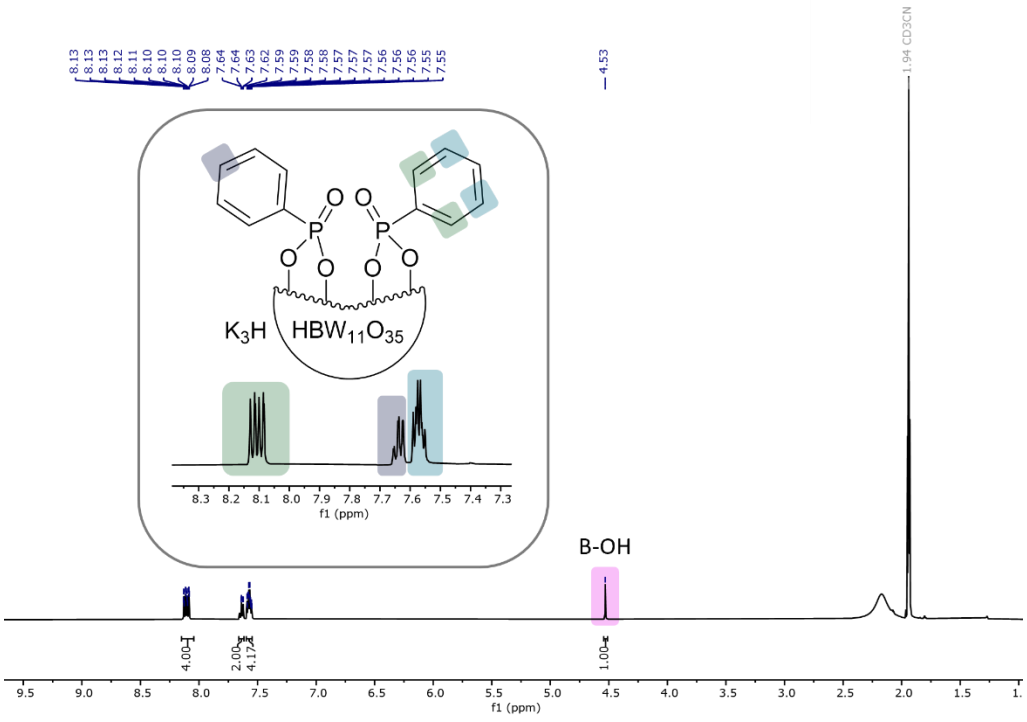



Figure 30. $^{1}$H NMR (400 MHz, $CD_3CN$) spectrum of {**K•PPhBW$_{11}$**}.

The $^{31}$P NMR experiment for {**K•PPhBW$_{11}$**} displayed a single peak at 20.39 ppm, indicating a single phosphorus environment, and attributed to the phosphonate bound to the lacunary site of the POM (**Figure 31**). No additional peaks were observed, indicating the absence of any unreacted phosphonic acid. Relative to the unhybridized lacunary POM $[HBW_{11}O_{39}]^{8-}$, a marginal shift of the singular broad peak for hybrid {**K•PPhBW$_{11}$**} was observed at 1.93 ppm in the $^{11}$B NMR spectroscopic data, compared to 2.21 ppm of the lacunary species. Furthermore, no sharp peak was observed, indicating the absence of any unreacted {**K•BW$_{12}$**}.

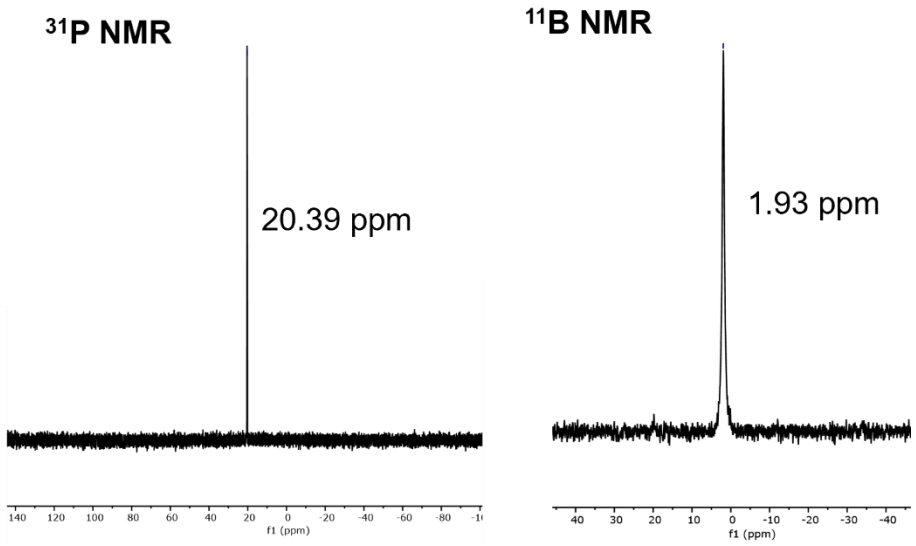



**Figure 31.** $^{31}$P NMR (162 MHz, $CD_3CN$) and $^{11}$B NMR (128 MHz, $CD_3CN$) of {**K•PPhBW$_{11}$**}**.**

Analysis by mass spectrometry for {**K•PPhBW$_{11}$**} showed multiple populated regions between 1450 and 1500 ppm (**Figure 32**). Various peaks corresponding to different cationic combinations are assigned in **Table 1**.

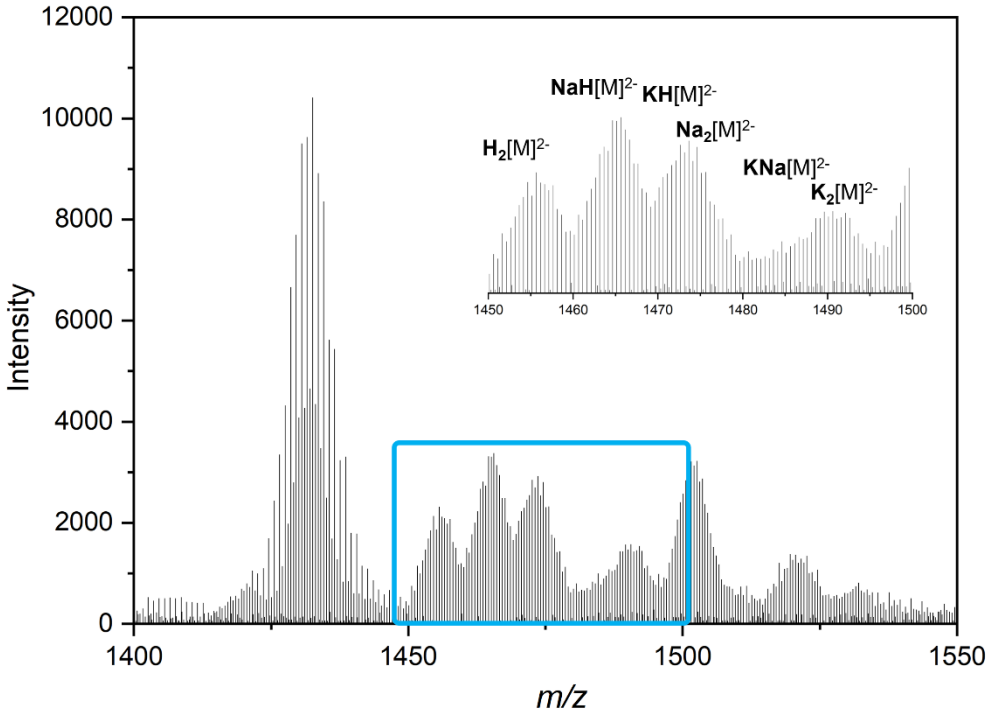


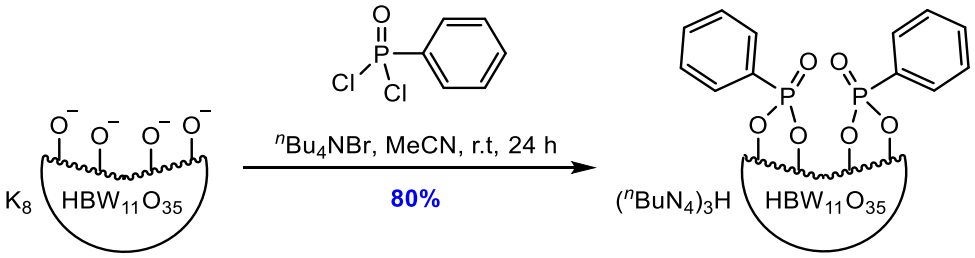

**Figure 32.** Negative mode ESI-MS spectrum of compound {**K•PPhBW$_{11}$**} in the *m/z* range 1300–1600, where M = [$HBW_{11}O_{39}(POC_6H_5)_2$].

**Table 1.** Mass spectra (ESI) assignments of {**K•PPhBW$_{11}$**}

| Assignment | *z* | *m/z* (calc.) | *m/z* (obs.) |
|---|---|---|---|
| **H$_2$**[$HBW_{11}O_{39}(POC_6H_5)_2$] | 2– | 1453.66 | 1453.66 |
| **NaH**[$HBW_{11}O_{39}(POC_6H_5)_2$] | 2– | 1464.65 | 1464.65 |
| **KH**[$HBW_{11}O_{39}(POC_6H_5)_2$] | 2– | 1472.63 | 1472.64 |
| **Na$_2$**[$HBW_{11}O_{39}(POC_6H_5)_2$] | 2– | 1475.64 | 1475.65 |
| **KNa**[$HBW_{11}O_{39}(POC_6H_5)_2$] | 2– | 1483.62 | 1483.62 |
| **K$_2$**[$HBW_{11}O_{39}(POC_6H_5)_2$] | 2– | 1492.11 | 1492.13 |

Overall, the NMR and mass spectrometry data corresponded well to the proposed structure of the organophosphonate borotungstate Keggin POM. Despite gaining insight into the structure of this POM, purification by crystallisation failed to yield the POM in significant quantities. As a result, the synthetic method was revisited.

Modification of the previous preparation involved direct synthesis of the organophosphorus POM as its $^{n}Bu_4N$ form, with the addition of $^{n}Bu_4NBr$ as a reagent in the reaction (**Scheme 11**). This modification was proposed to determine whether the formation of the lacunary POM as its $^{n}Bu_4N$ salt, prior to the addition of the phosphonate reagent, would reduce the formation of the impurities during the hybridisation step. In this context, the addition of phenylphosphorus dichloride into the reaction mixture containing lacunary $K_8[HBW_{11}O_{39}]$ and $^{n}Bu_4NBr$ in MeCN, was successful in the formation of target hybrid $(^{n}Bu_4N)_3H[HBW_{11}O_{39}(POC_6H_5)_2]$ {**PPhBW$_{11}$**}. Alternative purification techniques, including washings with EtOH, proved effective in isolating the desired product as an off-white powder in a yield of 80%. Notably, modification of the procedure and isolation of the POM as its $^{n}Bu_4N$ form seemed to have prevented the formation of the polymeric species, with no broad aromatic peaks detected in the $^{1}H$ NMR spectrum.




**Scheme 11.** Synthesis of {**PPhBW$_{11}$**} hybrid POM.

Structural elucidation was confirmed using $^{1}H$, $^{31}P$, and $^{11}B$ NMR spectroscopy. In comparison to the potassium form, the $^{1}H$ NMR spectrum of {**PPhBW$_{11}$**} displayed additional peaks corresponding to the aliphatic protons in the $^{n}Bu_4N$ cations. With reference to the cationic ratio, three $^{n}Bu_4N$ cations and were shown to be associated with the POM cluster. This observation aligns well with the previously reported {**PNapBW$_{11}$**}, which also demonstrated an association with three $^{n}Bu_4N$ cations.

From this data, two questions emerge: 1) Why do the borotungstate hybrid POMs deviate from the expected general formula of $[POC_6H_5]_2X^{n+}W_{11}O_{39}]^{(8-n)}$ (where X = $P^{5+}$, $Si^{4+}$, $B^{3+}$)? and 2) what accounts for the specific association with only three $^{n}Bu_4N$ cations and not four? Regarding the first question, one theory explaining the observed 4- anionic charge instead of the anticipated 5- involves the unique property of borotungstate POMs to undergo oxo-protonation. This phenomenon could alter the charge distribution, resulting in a cluster with reduced overall anionic charge and subsequently leading to an association of only four cations. For the second question, a potential explanation for the association of only three cations could be due to a hydrogen bonding interaction occurring between the oxo groups in the P=O bonds and a proton (**Figure 33**). This proton would reside between the two organogroups, aligning well with previously reports of phosphonates crystallised with a proton.

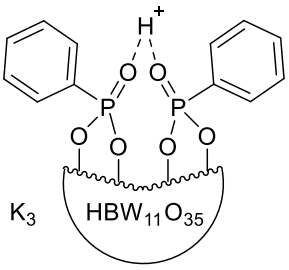
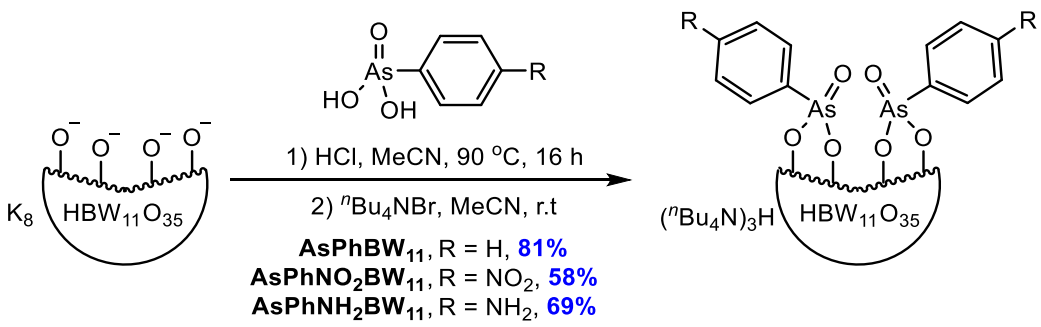



**Figure 33.** Proposed hydrogen bonding found in the organophosphorus and organoarsonate hybrid POMs.

Building upon the successful synthesis of the phosphonate borotungstate hybrid POM {**PPhBW$_{11}$**}, the question naturally arose as to whether other bridging groups would be compatible with the lacunary borotungstate cluster. As prior research has primarily focused on organophosphorus functionalisation, conducting this study would broaden the scope and enhance the diversity of borotungstate hybrid POMs. With this objective in mind, the synthesis of an organoarsonate borotungstate Keggin hybrid derivative ($^n$Bu$_4$N)$_3$H[HBW$_{11}$O$_{39}$(AsOC$_6$H$_5$)$_2$] {**AsPhBW$_{11}$**} was pursued.

Following an adapted acid-catalysed condensation method used for the synthesis of the organoarsonate Wells-Dawson POM {**AsPhP$_2$W$_{17}$**}, lacunary POM K$_8$[HBW$_{11}$O$_{39}$] and phenylarsonic acid in MeCN was stirred at reflux, overnight. Upon reaction completion, the reaction mixture was cooled, followed by centrifugation to remove the insoluble white powder, found to be unreacted lacunary POM (**Scheme 12**). Subsequent ion exchange with $^n$Bu$_4$NBr in MeCN, centrifugation, and trituration in Et$_2$O, gave the organoarsonate borotungstate hybrid in an excellent yield of 81%. Encouraged by this yield, two *p*-substituted phenylarsonate borotungstate POMs were synthesised following a similar synthesis, with the replacement of the phenyl arsonic acid with *p*-nitarsone and *p*-arsanilic acid. Hybrid POMs ($^n$Bu$_4$N)$_3$H[HBW$_{11}$O$_{39}$(AsOC$_6$H$_4$NO$_2$)$_2$] {**AsPhNO$_2$BW$_{11}$**} and ($^n$Bu$_4$N)$_3$H[HBW$_{11}$O$_{39}$(AsOC$_6$H$_4$NH$_2$)$_2$] {**AsPhNH$_2$BW$_{11}$**} were successfully synthesised in good to moderate yields of 58% and 69%, respectively.




**Scheme 12.** Synthesis organoarsonate borotungstate hybrid POM.

The $^{1}$H NMR spectrum of the unsubstituted phenyl arsonate hybrid {**AsPhBW$_{11}$**} resembled that of the phenyl phosphonate hybrid {**PPhBW$_{11}$**}. Aromatic protons positioned in the similar range of 7.70–8.30 ppm, accompanied by the distinctive B-O-H peak located at 4.93 ppm indicated the successful hybridisation of the organoarsonate groups (**Figure 34**). Similar spectroscopic evidence was also observed for the two substituted organoarsonate hybrid analogues, with minimal effect on the position of the B-O-H peaks in the $^{1}$H NMR spectra of {**AsPhNO$_2$BW$_{11}$**} (located at 4.90 ppm) and {**AsPhNH$_2$BW$_{11}$**} (at 4.91 ppm) relative to {**AsPhBW$_{11}$**} were observed (**Figure 35**). In determining the number of cations associated with the cluster, three $^{n}$Bu$_4$N cations were found to accompany these POMs.

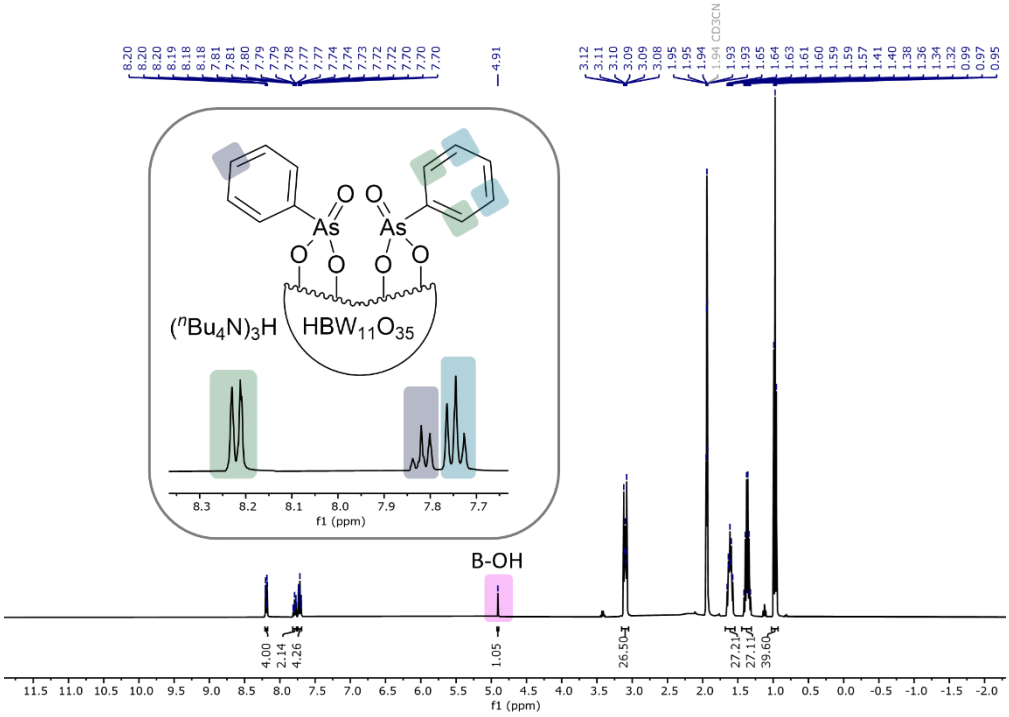



**Figure 34.** $^{1}$H NMR (400 MHz, $CD_3CN$) spectroscopy of {**AsPhBW$_{11}$**}.

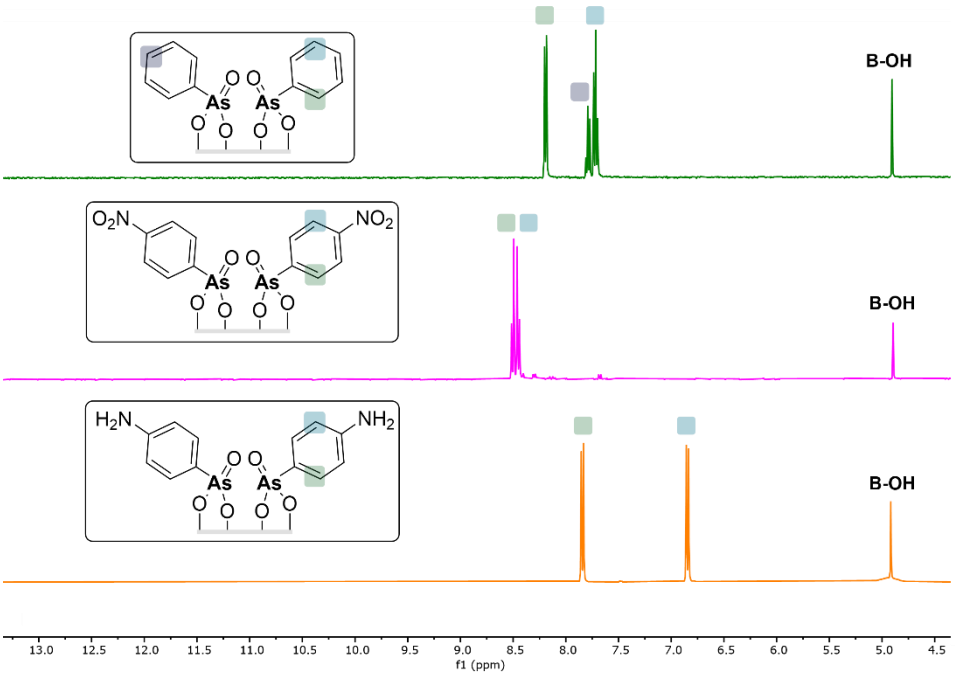
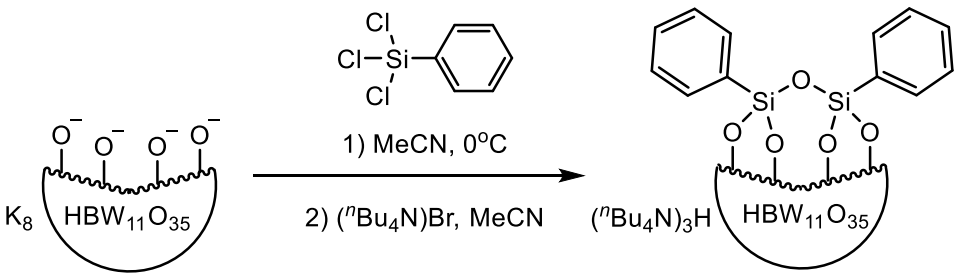



**Figure 35.** Stacked $^{1}$H NMR (400 MHz, $CD_3CN$) of organoarsonate hybrids in the region 4.50-13.00 ppm.

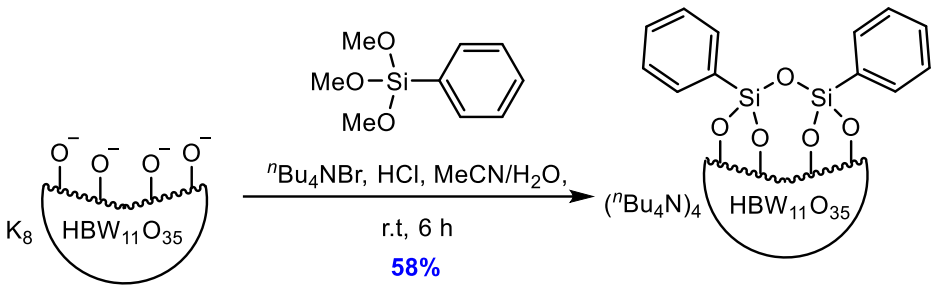
With literature precedence and Chapter 2 highlighting the influence of electron-accepting and -donating properties of various bridging groups on the electronic characteristics of the hybrid POMs, it becomes important to explore whether a comparable trend would be observed for the borotungstate Keggin family. For this, the organosilyl borotungstate POM hybrid POM $(^{n}Bu_4N)_4[HBW_{11}O_{39}(Si_2OPh_2]$ {**SiPhBW$_{11}$**} was targeted as the last POM in this series. Exploration into the synthesis of the POM began with the dropwise addition of tricholoro(phenyl)silane into a mixture of the potassium lacunary $K_8[HBW_{11}O_{39}]$ in MeCN at 0°C (**Scheme 13**).[10,160]




**Scheme 13.** Attempted synthesis of the siloxane hybrid POM {**SiPhBW$_{11}$**}.

The resulting crude material contained an aromatic impurity, as indicated by a broad multiplet in the $^{1}$H NMR spectrum. Furthermore, POM decomposition was observed following the addition of EtOH, shown by the appearance of {**BW$_{12}$**} peaks in the $^{11}$B NMR spectrum. Cation exchange followed by hybridisation resulted in the appearance of additional resonances attributed to B-O-H by-products. Alternatively, ion exchange post-hybridisation did not remove the impurity. Notably, dissolution of the crude POM in MeCN resulted in the distinctive heteropoly-blue colour, indicative of facile POM reduction in the solvent.

It was proposed that the chlorosilanes were reacting with residual water forming oligomeric silanol impurities, similarly to the phosphoryl reaction. To reduce this, an alternative silating agent was used, trimethoxysilane, that has shown success in previous hybridisations.[161] Trimethoxyphenylsilane was added dropwise to a solution of $K_8[HBW_{11}O_{39}]$ dissolved in a MeCN/water solvent ratio of 2:1 (**Scheme 14**). The reaction was stirred at room temperature, under acidic conditions. Upon reaction completion, ion exchange to the $^{n}Bu_4N$ salt afforded the desired hybrid POM {**SiPhBW$_{11}$**} as a white solid and a yield of 58%.




**Scheme 14.** Synthesis of organosilyl borotungstate hybrid POM {**SiPhBW$_{11}$**}.

From the $^{1}$H NMR spectroscopy, aromatic protons can be observed in the region 7.30–8.00 ppm, accompanied with the B-O-H peak located at 4.88 ppm (**Figure 36** - B). One noteworthy observation during the synthetic preparation of {**SiPhBW$_{11}$**} was the detection of two POM species when the amount of acid added was varied. The second species was found to have a similar spectroscopic profile to the desired hybrid, entailing two aromatic peaks and a B-O-H peak observed at 4.71 ppm (**Figure 36** - A). However, an additional peak at 5.91 ppm, with an integration of two, was observed. Addition of higher equivalents of acid or conducting the reaction over longer periods of time, resulted in conversion of this species into the desired POM hybrid. From this data, it can be postulated that the second species was an intermediate of the desired hybrid cluster, likely to be the silane reagent partially hybridised to the POM, with the proton peak attributed to the two Si-O-H protons.

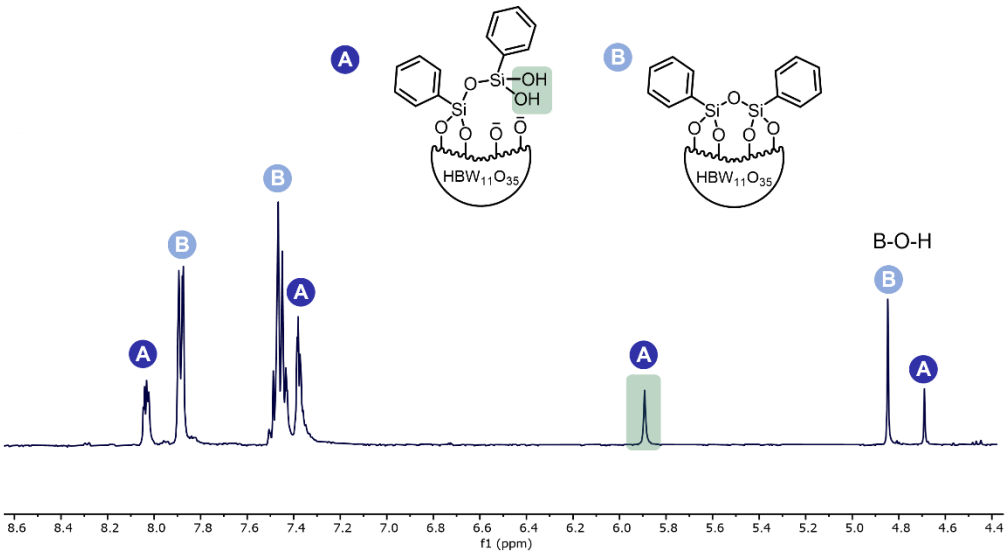



**Figure 36.** $^{1}$H NMR spectra highlighting the peaks corresponding to the intermediate and desired hybrid product {**SiPhBW$_{11}$**}. Additional proton peak shown in the intermediate is highlighted.

$^{1}$H NMR spectroscopy revealed the association of four $^{n}Bu_4N$ cations with each POM cluster, differing from both the organophosphorus and organoarsonate borotungstate hybrids (**Figure 37**). The observation of four $^{n}Bu_4N$ cations aligns well with the theory of hydrogen bonding of a proton in {**PPhBW$_{11}$**} and {**AsPhBW$_{11}$**}. This interaction, observed in these cases, would not be present in the silyl derivative. Furthermore, conformation of hybridisation was also achieved through $^{11}$B NMR spectroscopy, displaying a broad singlet at 2.18 ppm, along with IR and elemental analysis.

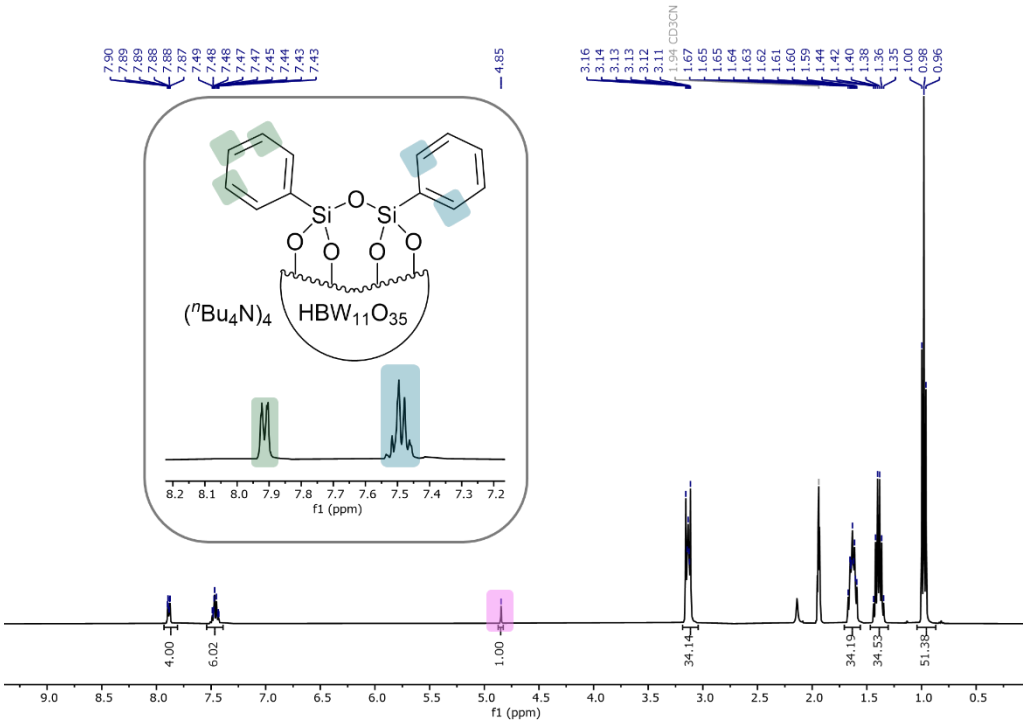



**Figure 37.** $^{1}$H NMR (400 MHz, $CD_3CN$) of {**SiPhBW$_{11}$**} in $CD_3CN$.

Having obtained {**PPhBW$_{11}$**}, {**AsPhBW$_{11}$**}, and {**SiPhBW$_{11}$**}, a comparative analysis of their $^{1}$H NMR spectra revealed a shift in the B-O-H peak, influenced by the different bridging atom involved. In {**PPhBW$_{11}$**}, the B-O-H peak was situated at 4.52 ppm, while in {**AsPhBW$_{11}$**}, this peak was displayed at 4.93 ppm (**Figure 38**). For {**SiPhBW$_{11}$**}, the B-O-H peak occurred at 4.88 ppm. The observed shift in position of this peak suggests that structural variation, associated with organogroup hybridisation, can influence the electron density distribution of the POM. This in turn, may contribute to the difference electrochemical and redox properties exhibited by the POMs.

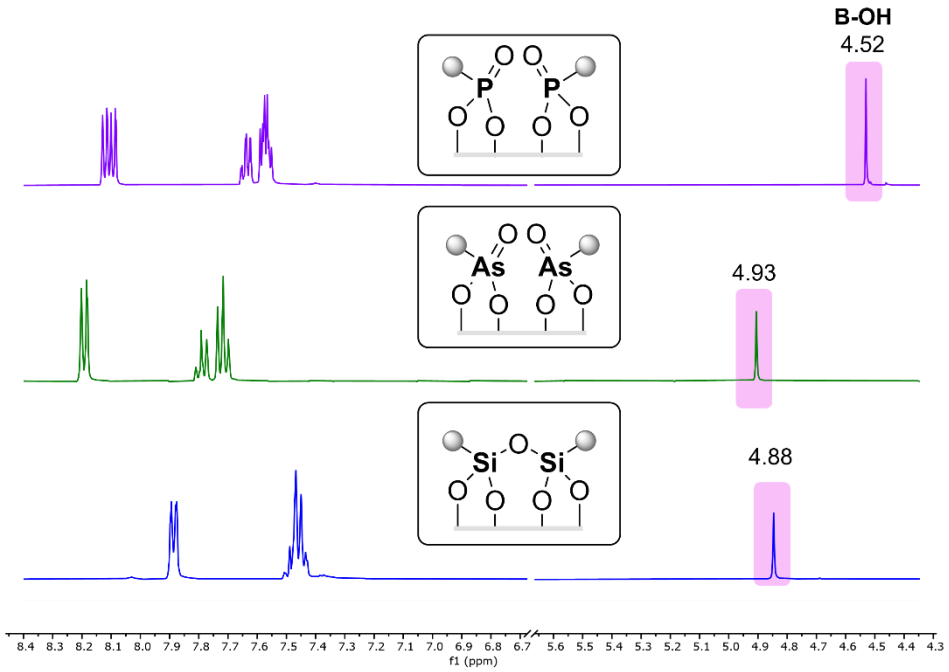



**Figure 38.** Stacked $^{1}$H NMR (400 MHz, $CD_3CN$) of borotungstate hybrids in the region 4.3 – 8.4 ppm.

In the infra-red (IR) spectroscopic data of the plenary {**BW$_{12}$**}, lacunary {**BW$_{11}$**}, and hybrids {**PPhBW$_{11}$**}, {**AsPhBW$_{11}$**}, and {**SiPhBW$_{11}$**}, the first notable peaks appeared in the range of 3000 cm$^{-1}$ and 2900 cm$^{-1}$ (**Figure 39**). These peaks were attributed to the symmetric and asymmetric C–H stretching modes occurring from the aliphatic counter–cations present in all POMs, along with the aromatic organic groups in the hybrid POMs. Additionally, peaks at *ca*. 1483

and 1382 $cm^{-1}$, were observed, corresponding to the C–H bends of the same organic groups in all POMs. The W=O stretches of the terminal oxo–groups appeared at ~950 $cm^{-1}$ and W–O–W bends of the bridging oxygens resulted in broad bands observed in the region of 800 to 700 $cm^{-1}$. In all POMs, a small peak at ~1000 $cm^{-1}$ was displayed, ascribed to the asymmetric B–O vibrations from the central borate anion.[162] For organophosphonate hybrid {**PPhBW$_{11}$**}, presence of a peak at 1135 $cm^{-1}$ is characteristic of a P=O stretch. For the organosilyl hybrid {**SiPhBW$_1$**}$_1$, a diagnostic peak at 1128 $cm^{-1}$ was observed, corresponding to the Si–O–Si bending mode.

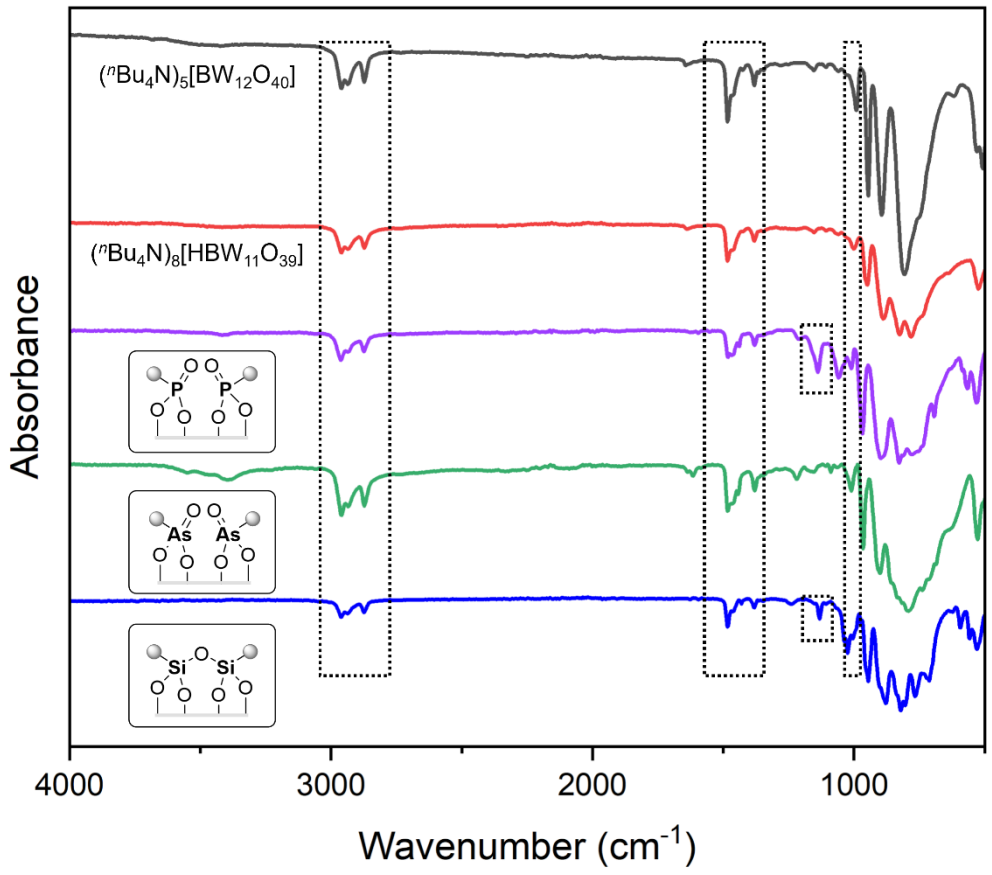



**Figure 39.** Stacked IR (ATR) spectra of plenary {**BW$_{12}$**}, lacunary {**BW$_{11}$**} and hybrid borotungstate POMs ({**PPhBW$_{11}$**}, {**AsPhBW$_{11}$**}, and {**SiPhBW$_{11}$**}) as their $^n$Bu$_4$N salts.

### 4.3.2 X-ray Crystallography

Single crystal growth of organoarsonate hybrid {**K•AsPhBW$_{11}$**} was achieved through the vapour diffusion method, where diffusion of the antisolvent *tert*-butyl methyl ether (TBME) into a saturated solution of the POM dissolved in nitromethane. {**K•AsPhBW$_{11}$**} crystallised as a monoclinic system with the space group of $P2_1/n$ (**Figure 40**). The structure was found to be compositionally disordered, where the hybrid had co-crystallised with a minor component of the unmodified plenary Keggin {**BW$_{12}$**}. Both species overlapped within the crystal structure. The only unique atom modelled for the {**BW$_{12}$**} component was a tungsten atom $W_{12}$, modelled with an isotropic displacement parameter; the lighter boron and oxygen atoms associated with this minor disorder component were not visible in the electron density map.

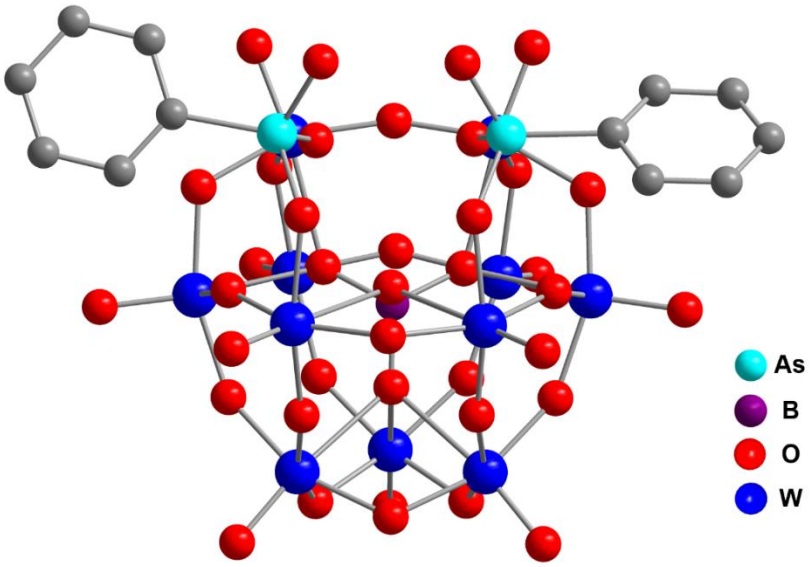



**Figure 40.** Ball and stick representation of the crystal structure of {**K•AsPhBW$_{11}$**} with solvent and hydrogens omitted for clarity. Rint = 0.068.

The hybrid structure was shown to agree with the assignment of two phenylarsonate moieties occupying the lacunary site of the POM in a 2:1 ratio. The central borate ion exhibited a tetrahedral $BO_4$ environment, connected to four oxo-ligands. For three of those oxo-ligands, association of three octahedral

polyhedra [$WO_6$] units were observed. This is depicted in **Figure 41** (a, b, and c), where the oxo-ligands of focus are circled in red and the three octahedral polyhedra associated are shaded in grey. In contrast for the last oxo-ligand bound to the borate ion, only two polyhedra units can be seen associated (**Figure 41** – d). This particular lacuna-facing oxo-ligand (labelled as O1C – circled pink in Figure) causes the central borate unit to be de-symmetrised. Therefore, it can be postulated that protonation of the oxo-ligand occurs at this site.

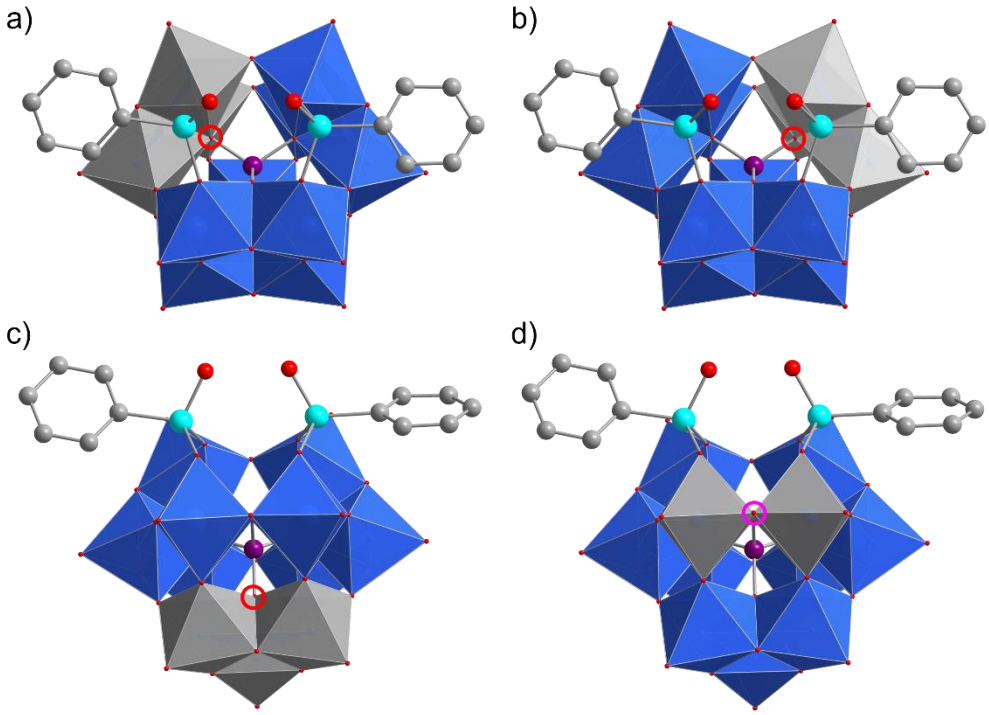



**Figure 41.** Polyhedra representation of the crystal structure of {**K•AsPhBW$_{11}$**} shown in different orientations highlighting the four different oxo-ligands adjacent to the borate ion (circled in red, with O1C circled in pink), and their associated octahedral [$WO_6$] polyhedra units (shown in grey).

Relative to a single proton, tungsten atoms are extremely electron rich. As a result, modelling, and identification of the B-O-H proton in borotungstate POMs through X-ray crystallography is a significant challenge. For this to be successful, a crystal with high quality would be required for the analysis. Fortunately, investigation of the crystal structure of {**K•AsPhBW$_{11}$**} revealed the presence of residual electron density positioned by O1C, with a bond distance restrained to 0.95 Å. The presence and placement of a hydrogen atom H1C located on the oxygen atom O1C was found to be supported by both spectroscopic analysis of the compound in solution and examination of electron density maps. An exert of the electron density with focus on the borate anion can be observed in **Figure 42**. Furthermore, a hydrogen omit map calculated for all of the data revealed an electron density peak of 0.49 Å$^{-3}$ in the refined location of the hydrogen atom H1C. This is the first instance of SCXRD used to support the previously reported internal proton, successfully achieved due to the high quality of the crystal paired with synchrotron data collection.

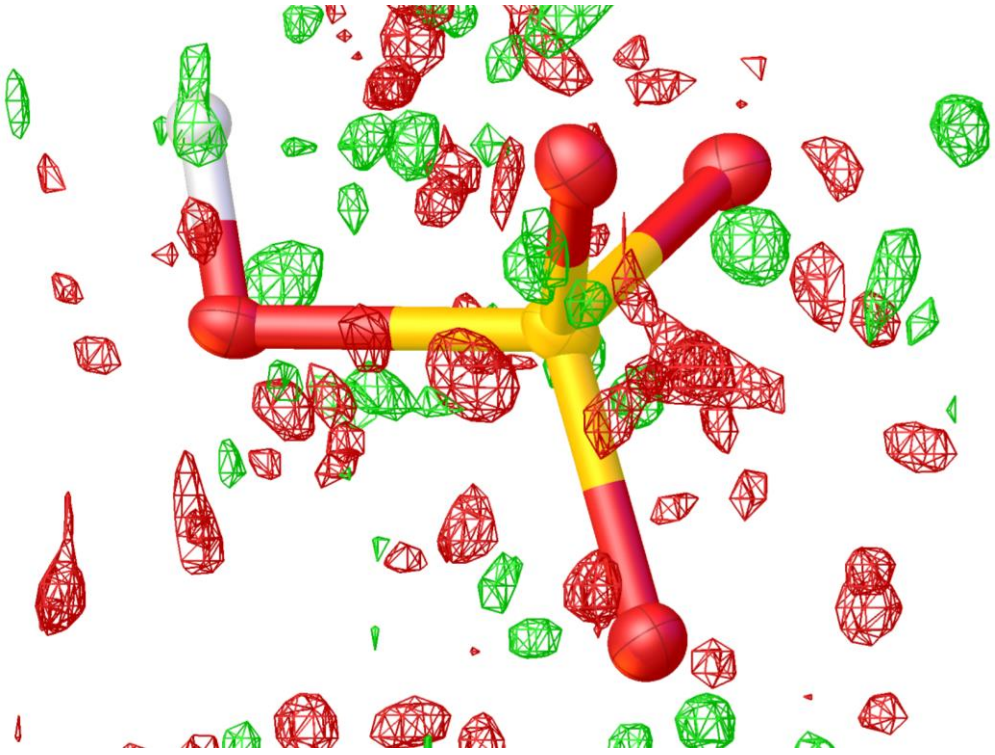


**Figure 42.** Electron density map exert highlighting the borate ion in {**K•AsPhBW$_{11}$**}**.** The remainder of the structure is omitted for clarity.

Similarly, single crystal growth of hybrid {**K•PPhBW$_{11}$**} was also achieved using the same vapour diffusion solvent system employed for hybrid {**K•AsPhBW$_{11}$**}, with nitromethane and TBME. {**K•PPhBW$_{11}$**} crystallised as a monoclinic system with the space group of $P2_1$. The structural arrangement corroborates well with the analysis of the arsonate analogue, with two phenylphosphonate moieties at the lacuna site and presence of a central $BO_4$ heteroanion. Notably, a common feature shared between the organoarsonate and organophosphonate borotungstate hybrids is the occurrence of three potassium cations, associated with the terminal oxo-ligands of the POMs. In both instances, the expected O-K bond distance of 2.7 Å was observed, with three potassium cations unambiguously identified (**Figure 43**). This observation aligns well with the previously discussed data indicating the consistent identification of the cation system surrounding both the organophosphonate and organoarsonate borotungstate POMs.

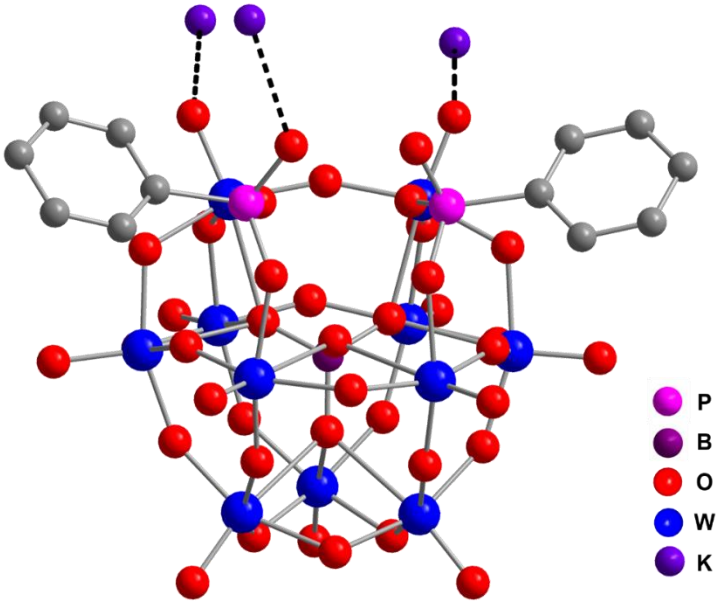



**Figure 43.** Ball and stick representation of the crystal structure of {**K•PPhBW$_{11}$**} with hydrogens and solvent omitted for clarity. Dashed bonds representing the coordination between the terminal oxo-ligands and the three potassium cations.

Whilst attempts to obtain the crystallographic data for the nitro-substituent {**AsPhNO$_2$BW$_{11}$**} was unsuccessful, the X-ray crystal structure of the amino-substituted {**AsPhNH$_2$BW$_{11}$**} was successfully achieved through the slow evaporation of a saturated solution of the POM in $MeCD_3$ over a period of 12 months. Hybrid {**AsPhNH$_2$BW$_{11}$**} crystallised as a triclinic system with a space group of $P_1$. Within the α-Keggin POM, two *para*-substituted anilines were positioned in the lacuna site. Additionally, three $^n$Bu$_4$N cations associated with each POM cluster were identified, supporting the cation composition of ($^n$Bu-$_4$N)$_3$H for the organoarsonate borotungstate POMs.

Interestingly, the crystallisation of the amino-POM resulted in a different packing arrangement than the unsubstituted borotungstate {**K•AsPhBW$_{11}$**}. Arranged in pairs of POM clusters per unit cell, bond distances of approximately 2.1 Å were observed between the terminal oxo-group O=W of one POM, and the amino-substituent of another. Given the presence of the amino-groups with their hydrogen-donating nature and the terminal oxo-ligands, demonstrating a hydrogen-accepting propensity, the interaction observed is strongly indicative of hydrogen bonding. In addition to this, the same interaction was also observed between the bridging oxo-ligands O-W(W) of one POM and amino-substituents of another, resulting in bond-distances of around 2.3 Å. A ball and stick representation of the crystal structure of two {**K•AsPhBW$_{11}$**} is depicted in **Figure 44**.

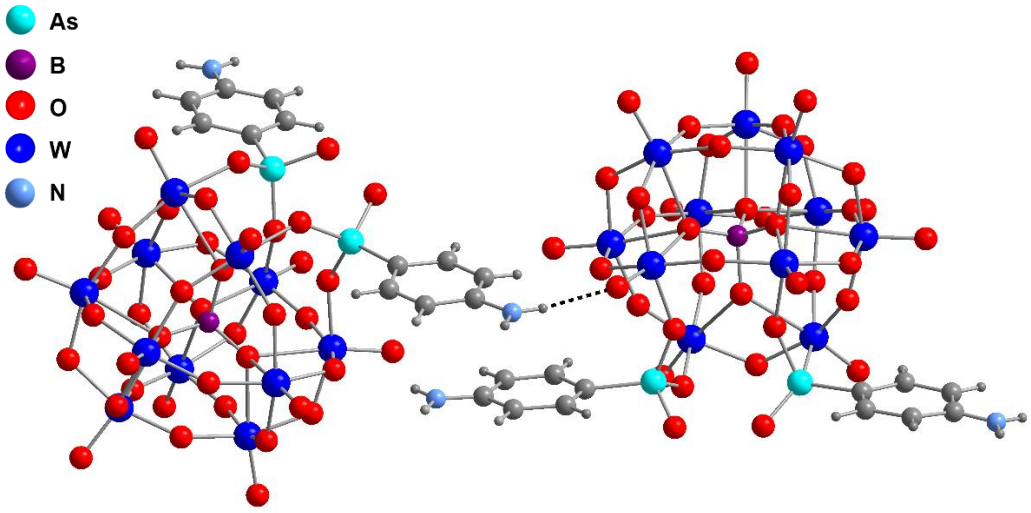



**Figure 44.** Ball and stick representation of the crystal structure of {**K•PPhBW$_{11}$**} with solvent omitted for clarity. Dashed bond representing hydrogen bonding.

Due to the hydrogen bonding interactions, the amino-POMs crystallised as a controlled polymeric complex (**Figure 45**). Unfortunately, the quality of the data is moderate to low resulting in lower precision in the certainty of bond distances, and ambiguity in electron density at the B-O-H and select cation-solvent regions. Consequently, a single methyl unit on one of the cations and internal hydrogen were not identified. Fortunately, the atom identities, connectivity and geometries can still be confidently inferred, suggesting a fascinating hydrogen bonded polymeric structure that warrants further investigation.

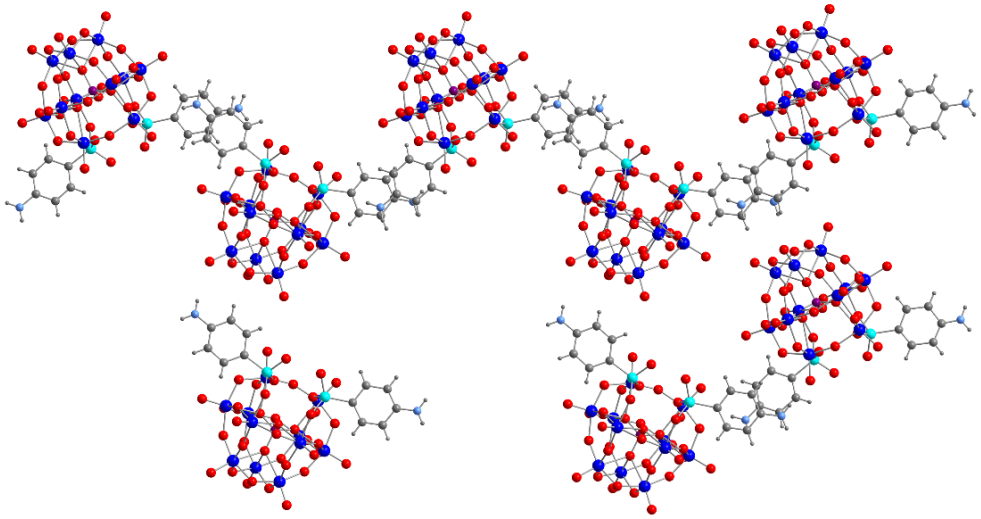


**Figure 45.** Crystal structure of {**AsPhNH$_2$BW$_{11}$**} as a polymeric complex, with solvent omitted for clarity.

### 4.3.3 Hydrolytic Stability

Given the novelty of the borotungstate structures, it becomes important to assess the hydrolytic effects of these POMs as this may limit the stability and versatility of the POMs as catalysts in photochemical reactions. Previous research has demonstrated that organophosphorus Keggin POMs, represented by the general formula $[POC_6H_5]_2X^{n+}W_{11}O_{39}^{(8-n)-}$ where X = $P^{5+}$ or $Si^{4+}$, are hydrolytically unstable.[128]

For the phosphotungstate hybrid, Hill *et al*., demonstrated that dissolution of the POM in wet DMSO resulted in partial hydrolytic cleavage of the attached phosphonic acid group with formation of an intermediate cluster that could be isolated (**Figure 46** - a).[128] In contrast, the silicotungstate Keggin was found to undergo complete hydrolytic cleavage of the phosphoryl group from the POM cluster under similar conditions. This resulted in the formation of $[PhPO_3]^{2-}$ and the lacunary precursor $[SiW_{11}O_{39}]^{8-}$, with no observation of any partially hydrolysed species (**Figure 46** - b).

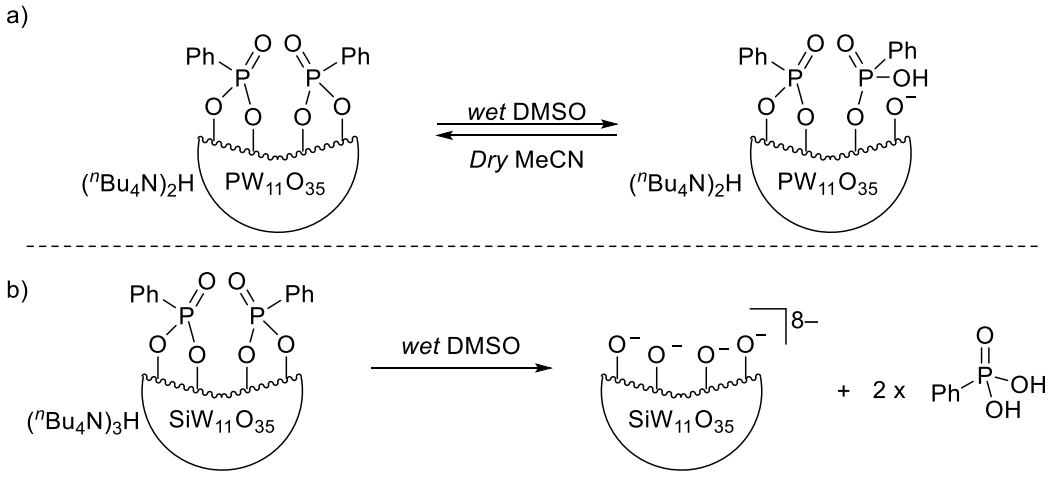



**Figure 46.** Hydrolysis pathways of organophosphorus hybridised Keggin POMs. Figure adapted from reference [128].

Building upon the insights gained from this study into the hydrolytic stability of Keggin POMs, similar experiments were conducted with the three borotungstate hybrids.[53] The POMs were dissolved in DMSO-$d_6$/$D_2O$ (9:1) and monitored by $^1H$ NMR spectroscopy over time. Organoarsonate hybrid {**AsPhBW$_{11}$**} was found to be readily hydrolysed with the addition of $D_2O$, as observed by the immediate disappearance of the B-O-H peak in the $^1H$ NMR spectrum (**Figure 47** - a) and a shift in the peaks corresponding to the aromatic protons. Furthermore, presence of a sharp peak in the $^{11}B$ NMR spectrum was also observed, corresponding to the appearance of {**BW$_{12}$**}.

Organophosphonate hybrid {**PPhBW$_{11}$**} showed a slower rate of hydrolysis on addition of $D_2O$, with the appearance of new peaks in the aromatic region of the $^1H$ NMR spectrum (between 7.4-8 ppm) (**Figure 47** – b). In addition to this, a behaviour similar to Hill's report for {**PPhSiW$_{11}$**} silicotungstate POM was shown, with no evidence of partial hydrolysis of the phosphonate groups observed for either {**AsPhBW$_{11}$**} or {**PPhBW$_{11}$**}).

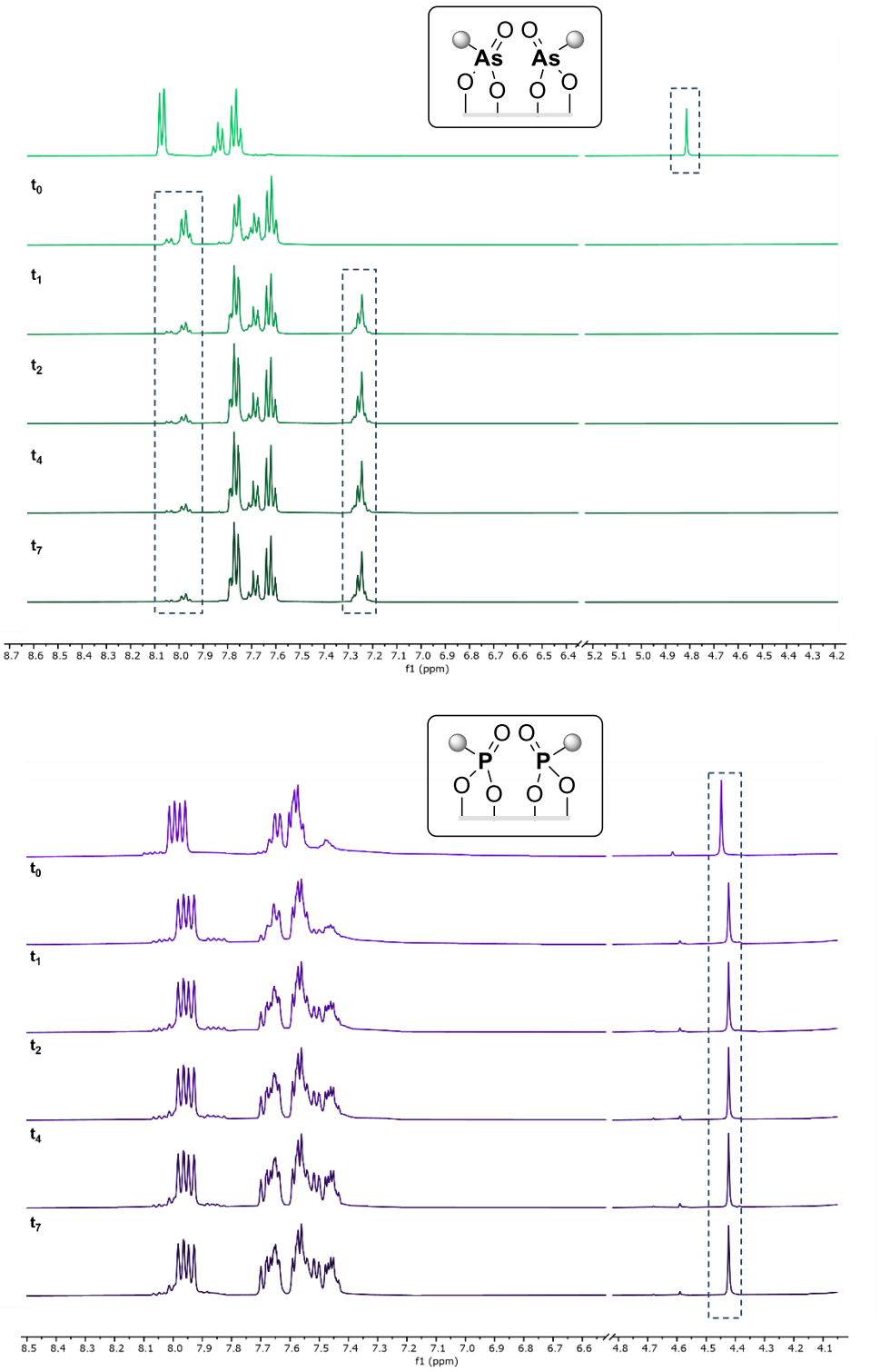



**Figure 47.** Solution of {**AsPhBW$_{11}$**} (top) and {**PPhBW$_{11}$**} (bottom) in DMSO-$d_6$ (0.70 mL) with $D_2O$ (10%, v/v = 70 µL) monitored by $^1$H NMR (400 MHz) over $t_{days}$. Spectra window restrained to highlight areas of interest. When not being analysed, the sample was kept in the dark.

In contrast to the organoarsonate and organophosphonate analogues, the organosilyl POM {**SiPhBW$_{11}$**} was found to have great hydrolytic stability over a month with no apparent change in the aromatic region of the $^{1}$H NMR spectrum and consistent $^{11}$B NMR spectroscopic data (**Figure 48**). Notably, over the period of a week, the slow disappearance of the B-O-H peak was observed in the $^{1}$H NMR spectrum. From this data, it can be postulated that proton-deuterium exchange (B–OH/D) may have occurred suggesting a potential interaction between the $D_2O$ and borotungstate POM. Further analysis and investigation is required to elucidate the mechanism behind this observed behaviour and its impact on the stability of the hybrid POM.

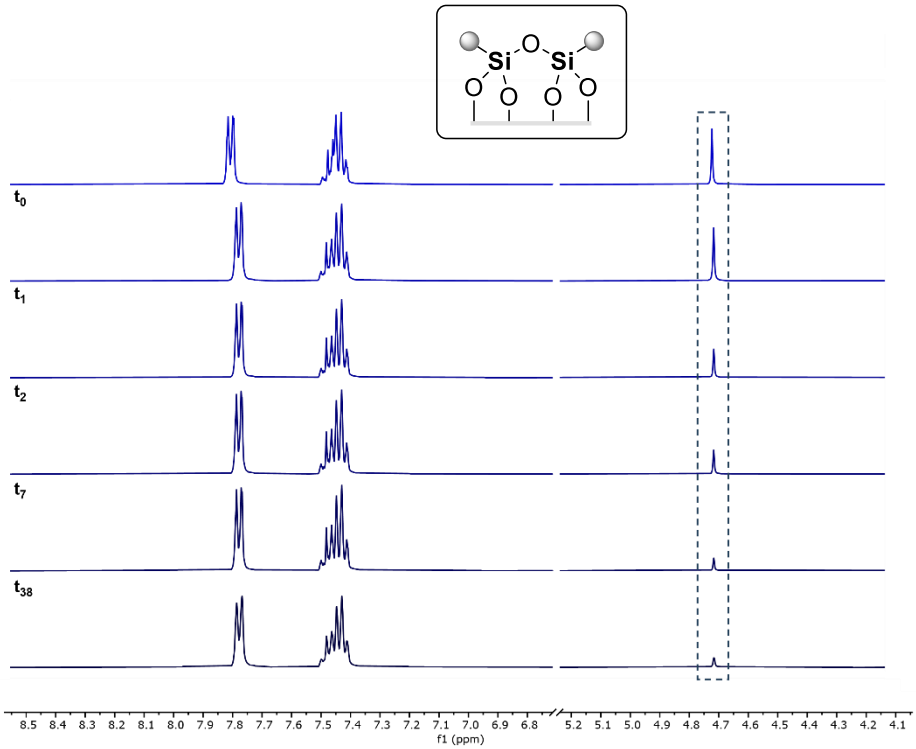



**Figure 48.** Solution of {**SiPhBW$_{11}$**} in DMSO-d$_6$ (0.75 mL) with $D_2O$ (10%, v/v = 75 µL) monitored by $^{1}$H NMR (400 MHz) over $t_{days}$. Spectra window restrained to highlight areas of interest. When not being analysed, the sample was kept in the dark.

In summary, five organic-inorganic borotungstate hybrid POMs were successfully synthesised and characterised through spectroscopic analysis. Crystallographic data of the organoarsonate borotungstate hybrid {**K•AsPhBW$_{11}$**}$_1$ revealed evidence supporting the protonation of the central borate anion found in the lacunary POMs, while crystallisation of {**K•PPhBW$_{11}$**} confirmed the cationic ratio of the POM clusters to exhibit three potassium (or $^n$Bu$_4$N) cations and a proton. Hybrid {**AsPhNH$_2$BW$_{11}$**} was shown to crystallise as a polymeric complex, formed through hydrogen bonding occurring between the oxo-ligands of one POM and the amino-substituent of another. Hydrolytic studies of the POM demonstrated the excellent hydrolytic stability of hybrid {**PPhBW$_{11}$**}, while hybrid {**AsPhBW$_{11}$**} was shown to undergo facile hydrolysis in the presence of water. For hybrid {**SiPhBW$_{11}$**}, $^1$H NMR spectroscopy revealed the slow disappearance of the B-O-H peak, over a period of 30 days.

### 4.4 Electronic Characterisation and Investigation

With a series of borotungstates in hand, the electronic properties were evaluated with two primary objectives. Firstly, to comprehend the impact of organogroup functionalisation on the electronic properties of these borotungstate POMs. Secondly, to investigate whether the trends observed in for the organofunctionalised Wells-Dawson POMs are replicated in this novel family of POMs. In this work, the cyclic voltammetry of plenary {**$BW_{12}$**} and hybrids, as their $^{n}Bu_4N$ salts, were analysed. The CVs were conducted in DMF (0.1 M, $^{n}Bu_4NPF_6$), with a glassy carbon working electrode, platinum counter electrode, and a $Ag^{+}|Ag$ reference electrode.

In all cases, quasi-reversible redox couples corresponding to one-electron $W^{VI}/W^{V}$ processes, were observed, with the standard potential of the {**$BW_{12}$**} process occurring at –1.80 V (**Figure 49**). Relative to the plenary Keggin, all hybrid POMs showed a positive shift in standard potential for the first redox event, with a shift ranging from 0.3 V to 1 V. As established previously, the hybrids exhibit an anionic charge of 4-, while the {**$BW_{12}$**} cluster carries an anionic charge of 5-. This difference in anionic charge contributes to the increased reducibility of the plenary POM, resulting in more negative potentials when compared to the hybrid POMs. Among the POMs, the organophosphonate hybrid {**$PPhBW_{11}$**} displayed the most positive first redox process ($E_{mid}$ = −0.80 V vs $Ag^{+}|Ag$), followed by the organoarsonate hybrid {**$AsPhBW_{11}$**} ($E_{mid}$ = −0.88 V vs $Ag^{+}|Ag$), and the organosilyl functionalised hybrid {**$SiPhBW_{11}$**} ($E_{mid}$ = –1.42 V vs $Ag^{+}|Ag$) (**Table 2**). This observed trend in reducibility can be ascribed to the electron-withdrawing nature of the phosphonate and arsonate groups compared to the silyl group (for further details please see **Section 3.5.2**).[74] Furthermore, in a similar manner to the Wells-Dawson POMs {**$PPhP_2W_{17}$**} and {**$AsPhP_2W_{17}$**}, the 80mV difference between the phosphonate {**$PPhBW_{11}$**} and arsonate {**$AsPhBW_{11}$**}, is likely due to the slightly stronger electron-withdrawing effect of the organophosphonate group relative to the organoarsonate group.

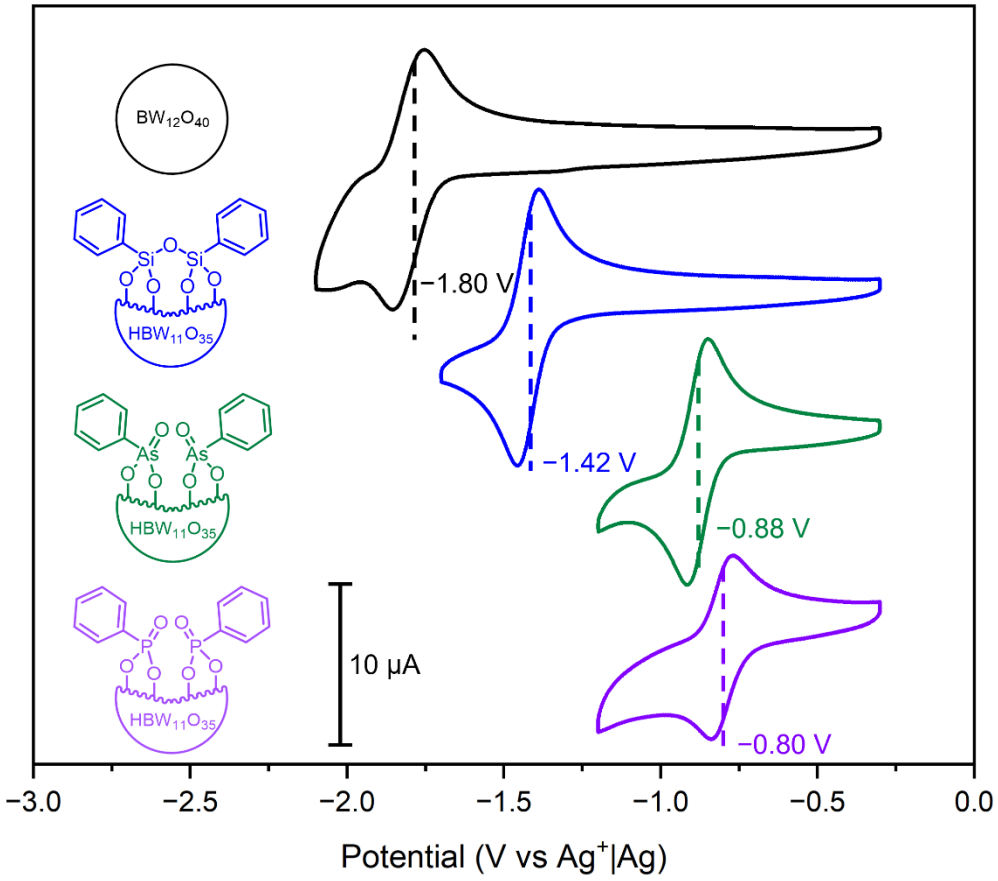



**Figure 49.** A stacked CV of 1mM of compounds {**$BW_{11}$**}, {**$SiPhBW_{11}$**}, {**$AsPhBW_{11}$**}, and {**$PPhBW_{11}$**} in anhydrous DMF with 0.1 M $^{n}Bu_4NPF_6$ supporting electrolyte. All CVs were recorded at 100 $mVs^{-1}$ using a glassy carbon working electrode (d = 3 mm and *A* = 0.071 $cm^2$), Pt wire counter electrode and a $AgNO_3|Ag$ non-aqueous reference electrode. The standard potentials are highlighted for the first redox process.

**Table 2.** Electrochemical parameters, $E_{mid}$ and $\Delta E_p$ for the first redox couple for each POM (1 mM) obtained from CVs at 0.1 $Vs^{-1}$.

| POM | Standard Potential ($E_{mid}$, V) | $\Delta E_p$ (mV) |
|---|---|---|
| **$BW_{12}$** | –1.80 | 109 |
| **$PPhBW_{11}$** | –0.80 | 67 |
| **$AsPhBW_{11}$** | –0.88 | 66 |
| **$SiPhBW_{11}$** | –1.42 | 68 |
| **$PPhSiW_{11}$** | –0.75 | 64 |

Beyond the first redox process, the CV of the phosphonate hybrid {**PPhBW$_{11}$**} displayed three reversible redox processes, and potentially a fourth tailoring beyond the solvent window (**Figure 50**). The broadening observed may be due to the working electrode gaining a capacitive charge, through double-layer capacitance, masking the faradaic charge from the POM.

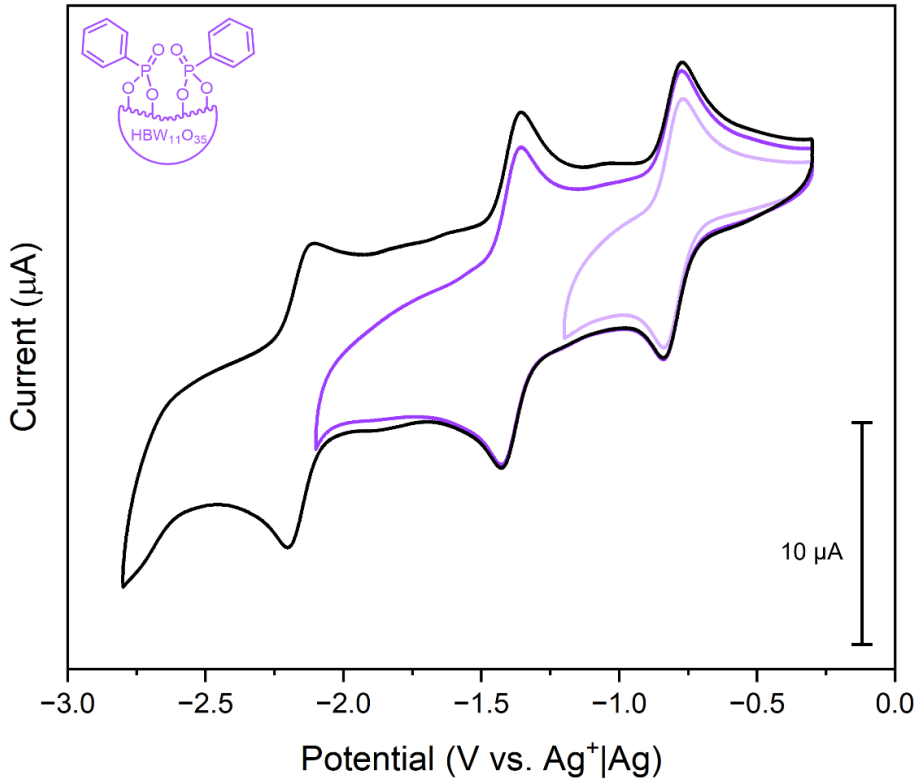



**Figure 50.** A stacked CV of 1mM of compound {**PPhBW$_{11}$**} in anhydrous DMF, measured at different potential windows.

Furthermore, relative to {**PPhBW$_{11}$**}, hybrids {**AsPhBW$_{11}$**} and {**SiPhBW$_{11}$**} exhibit a different electronic profile, with subsequent reductions (for example $W^{V}/W^{IV}$) resulting in irreversible processes observed at a lower potential (**Figure 51**). The difference in redox stability could be attributed to the more effective electron-withdrawing nature of the organophosphonate group, causing the {**PPhBW$_{11}$**} hybrid to be more stable when gaining electrons in the subsequent reductions. This observed redox stability of {**PPhBW$_{11}$**} relative to the other analogous may be advantageous when applying these systems as photocatalysts in organic synthesis.

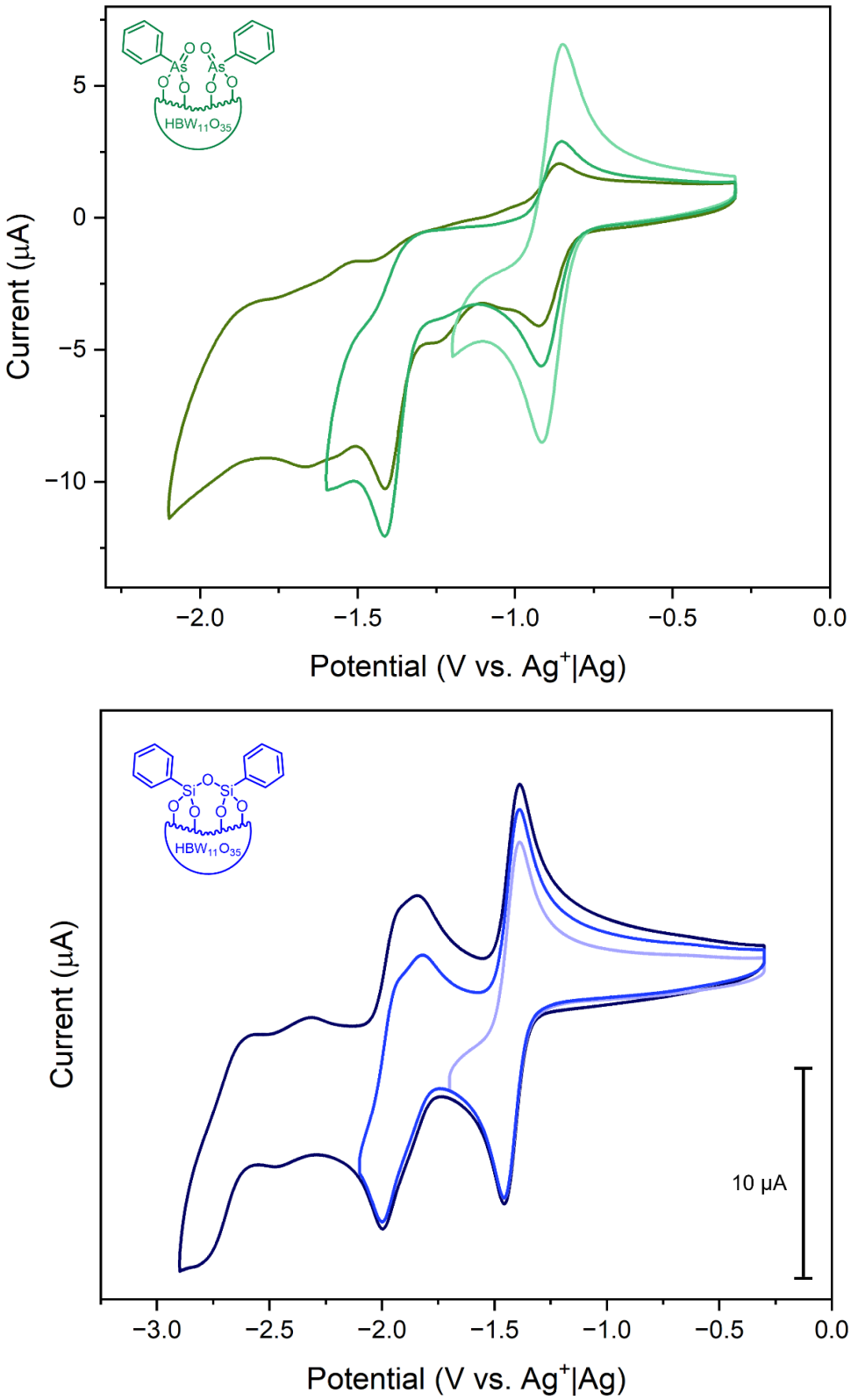



**Figure 51.** A stacked CV of 1mM of compounds {**AsPhBW$_{11}$**} and {**SiPhBW$_{11}$**} in anhydrous DMF with 0.1 M $^{n}Bu_4NPF_6$ supporting electrolyte, measured at different potential windows.

As an extension of this study, the previously reported organofunctionalised silicotungstate $(^{n}Bu_4N)_3H[SiW_{11}O_{39}(POC_6H_5)_2]$ {**PPhSiW$_{11}$**} was also synthesised and electrochemically analysed (**Figure 52**). Given that the borotungstate hybrid POMs were found to have an anionic charge of 4–, the silicotungstate hybrid could be considered as an isoionic, topologically equivalent analogue of the organophosphorus borotungstate hybrid {**PPhBW$_{11}$**}, with the central templating anion being the sole point of differentiation. As the silicotungstate hybrid is a well-documented and a recognised hybrid, it serves as a dual purpose in this study. Firstly, it acts as a benchmark against which the borotungstate POM can be assessed. Secondly, it allows for a comparison, specifically investigating the subtle change of heteroatom and its impact on the electro- and photochemical properties of the POMs.

The CV data of isoionic analogue {**PPhSiW$_{11}$**} showed a very similar electronic profile to that of borotungstate {**PPhBW$_{11}$**}, revealing four redox processes within the range of 0 V to –3.5 V vs $Ag^+|Ag$ (**Figure 52**). Bearing the same bridging atom and organogroup, the electronic profile of {**PPhSiW$_{11}$**} supports the hypothesis that functionalisation with an electron-withdrawing phosphonate group enhances the stability of the POMs during subsequent reductions at lower potentials. Moreover, the redox processes found in {**PPhSiW$_{11}$**} displayed a positive shift of ~60 mV when compared to the borotungstate POM. This could be attributed to the smaller size and increased charge density of the borate anion in {**PPhBW$_{11}$**}, relative to the silicate anion found in {**PPhSiW$_{11}$**}.

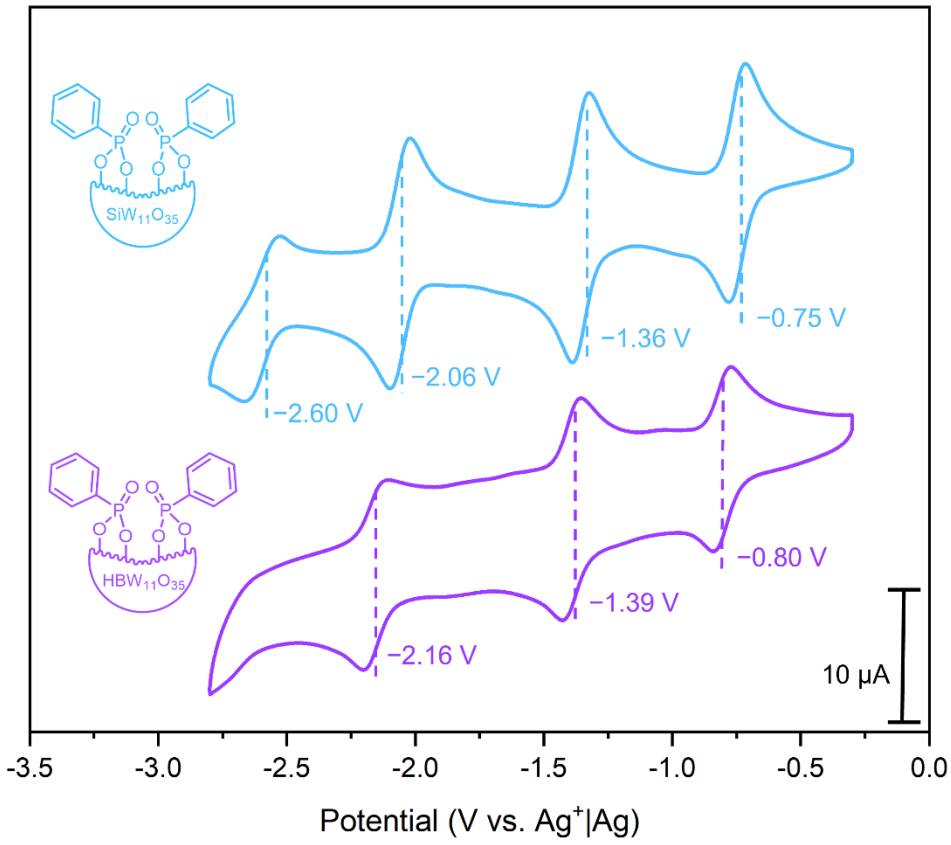



**Figure 52.** A stacked CV of 1mM of {**PPhBW$_{11}$**} and {**PPhSiW$_{11}$**} in anhydrous DMF with 0.1 M $^{n}Bu_4NPF_6$ supporting electrolyte.

In the electronic characterisation of the three phenyl arsonate borotungstate Keggin POMs, namely {**AsPhBW$_{11}$**}, {**AsPhNO$_2$BW$_{11}$**}, and {**AsPhNH$_2$BW$_{11}$**}, a trend similar to the Wells-Dawson analogues (**AsPhP$_2$W$_{17}$**}, {**AsPhNO$_2$P$_2$W$_{17}$**}, and {**AsPhNH$_2$P$_2$W$_{17}$**}) was observed in the CV data. **Figure 53** shows the first redox processes for the hybrids with standard potentials highlighted. Presence of the electron–donating amino group in {**AsPhNH$_2$BW$_{11}$**} resulted in a negative shift in potential by 90 mV ($E_{mid}$ = –0.97 V vs Ag$^+$|Ag) relative to unsubstituted {**AsPhBW$_{11}$**}. In contrast, presence of the electron-withdrawing nitro group in {**AsPhNO$_2$BW$_{11}$**}, resulted in a positive shift in potential of the first redox process by 70 mV ($E_{mid}$ = –0.81 V vs Ag$^+$|Ag), relative to {**AsPhBW$_{11}$**}.

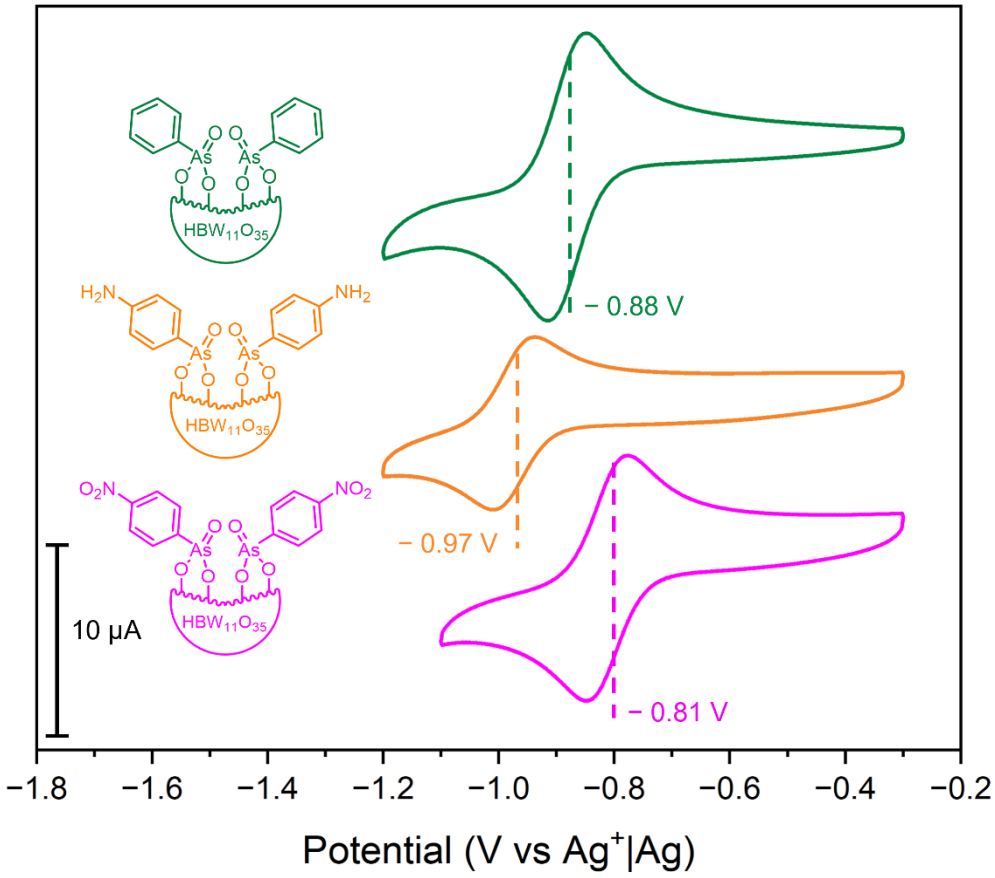



**Figure 53.** A stacked CV of 1mM of compounds {**AsPhBW$_{11}$**}, {**AsPhNH$_2$BW$_{11}$**}, {**AsPhNO$_2$BW$_{11}$**} in anhydrous DMF with 0.1 M $^n$Bu$_4$NPF$_6$ supporting electrolyte.

In summary, the voltametric analytical study has illustrated that organofunctionalisation of the lacunary borotungstate POM leads to a notable

shift in redox potentials of the hybrids compared to the plenary {**$BW_{12}$**}. In a similar manner to the Wells-Dawson phosphotungstate POMs, the extent of the shift is dependent on the type of bridging atom used, with the organophosphonate displaying the most positive shift. Furthermore, the electron-withdrawing nature of the substituents on the aromatic rings of the organogroups influences this shift. Moreover, the work has demonstrated the stabilising effect of the organophosphonate group on the redox properties of the POMs, particularly at lower potentials. This observed effect could prove advantageous when employing these POM systems as catalysts in photochemical reactions.

Transitioning from the electrochemical nature to the photochemical properties of the POMs, UV-Vis spectroscopy emerges as a crucial analytical technique in understanding the impact of organofunctionalisation on the absorption priorities of the hybrid POMs. In the absorption spectra, all hybrids exhibit a LMCT absorption band in the UV-region between 250 and 275 nm (**Figure 54**). The extinction coefficients for the POMs were calculated and are shown in **Table 3**. Compared to the plenary borotungstate {**$BW_{12}$**}, hybrids {**$PPhBW_{11}$**}, {**$AsPhBW_{11}$**} and {**$SiPhBW_{11}$**} demonstrate heightened absorbance in the UV-region, with the organosilyl derivative showing particularly enhanced absorption. Additionally, all hybrids exhibit a bathochromic shift (red shift) relative to {**$BW_{12}$**}, resulting in a peak height occurring at higher wavelengths of light and the absorption edge of the POMs extending into the deeper UV-A region/visible region of the spectrum. This is exemplified by POM {**$PPhBW_{11}$**} displaying heightened absorbance in the region of 370 nm.

When comparing {**$PPhBW_{11}$**} to {**$PPhSiW_{11}$**}, a similar absorption profile was observed, featuring a LMCT process in the same region. Absorbance for {**$PPhSiW_{11}$**} was found to be lower than that of the borotungstate analogue in the UV-region, and the peak was shown to reside at a higher wavelength of light (from 261 nm in {**$PPhBW_{11}$**} to 264 nm in {**$PPhSiW_{11}$**}). Furthermore, a similar absorption profile is observed of the POM at 370 nm.

While the shift of the absorption edge towards the visible-light region is subtle, the hybrid POMs, particularly the {**PPhBW$_{11}$**}, has the potential to be activated by higher wavelengths of light which is a promising feature when considering these species as photocatalyst.

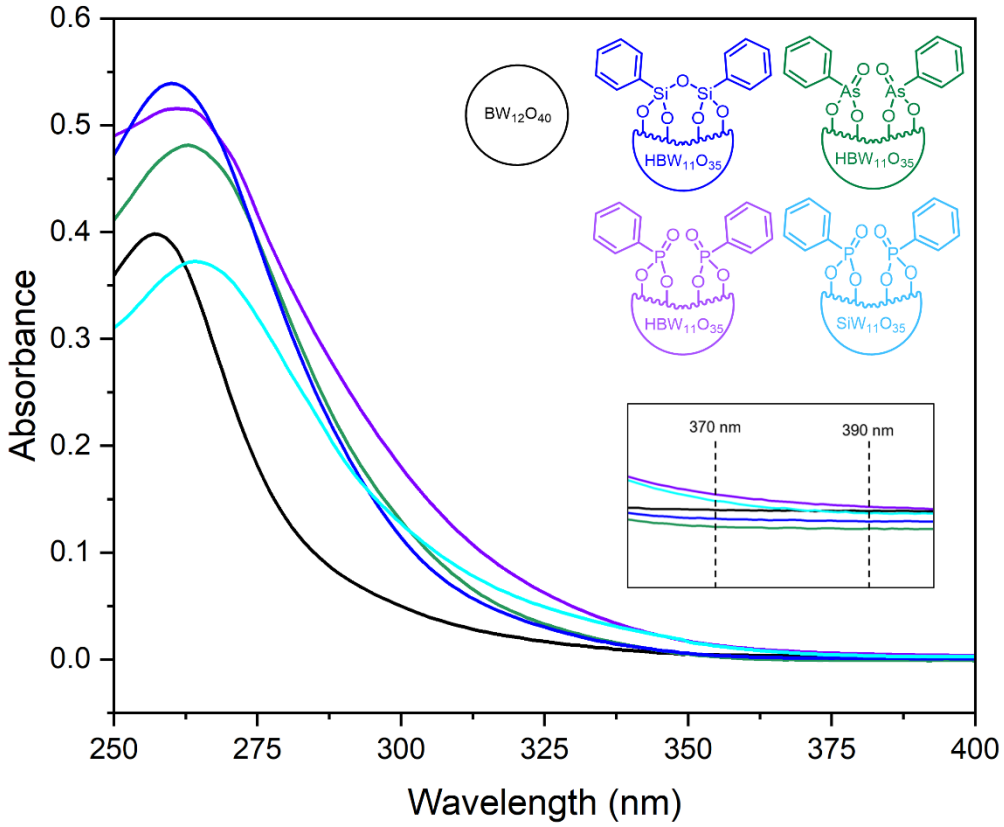



**Figure 54.** UV-vis absorption spectra of borotungstates in MeCN at 12.5 µM.

**Table 3.** Extinction coefficient determined from the UV-vis absorption spectra of the borotungstate POMs at 12.5 µM.

| Entry | POM | $\lambda_{max}$ (nm) | ε ($cm^{-1}mol^{-1}dm^3$) |
|---|---|---|---|
| 1 | **$BW_{12}$** | 257 | 31867 |
| 2 | **$AsPhBW_{11}$** | 263 | 38503 |
| 3 | **$PPhBW_{11}$** | 261 | 41241 |
| 4 | **$SiPhBW_{11}$** | 260 | 43137 |
| 5 | **$PPhSiW_{11}$** | 264 | 29798 |

## 4.5 Conclusions

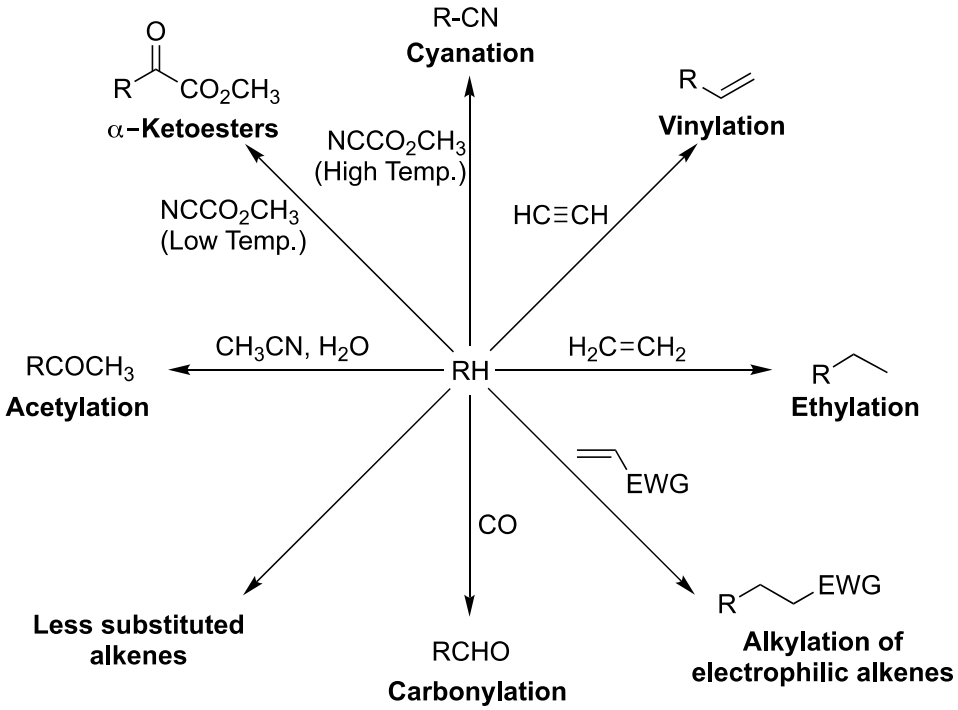
A family of organic-inorganic borotungstate hybrid POMs were successfully derived from the lacunary borotungstate Keggin. The synthesis of borotungstate POMs bearing organoarsonate and organosilyl groups extends the literature precedence beyond the organophosphonate group. Structural characterisation of the hybrids indicated protonation of the central borate anion, evidenced by NMR spectroscopy and X-ray crystallography, resulting to a unique general formula differing from analogous phosphotungstate and silicotungstate hybrid POMs.

Introduction of organic functional groups to the POM resulted in a positive shift in redox potentials, with organophosphorus {**PPhBW$_{11}$**}, bearing the most electron-withdrawing bridging atom, exhibiting the most significant shift. Additionally, organophosphonate functionalisation was shown to stabilise the subsequent reductions of the POM at lower potentials, compared to the other organofunctionalised hybrids. UV-Vis absorption data demonstrated the hybrids to have an increased absorbance in the UV-region, relative to the plenary {**BW$_{12}$**}, with {**SiPhBW$_{11}$**} showing the most enhanced absorption. Furthermore, a bathochromic shift was observed for the hybrid POMs relative to {**BW$_{12}$**}, with the absorption edge of {**PPhBW$_{11}$**} extending towards the shorter wavelength visible region of the spectrum. This data highlights how structural modifications of borotungstate POMs provide significant tunability to the electronic and photochemical properties of these systems, offering potential in the application of photocatalysis.

# 5 Photocatalytic Investigation of POMs

## 5.1 TBADT Photocatalysis

**TBADT**, renowned for its ability to harness near-visible light energy and facilitate intricate chemical reactions under mild conditions, has garnered significant interest as a photocatalyst in modern organic chemistry.[100,107] Its catalytic repertoire spans an array of organic transformations, including C-H functionalisation, C-C bond formation, and oxidative coupling reactions (**Scheme 15**).



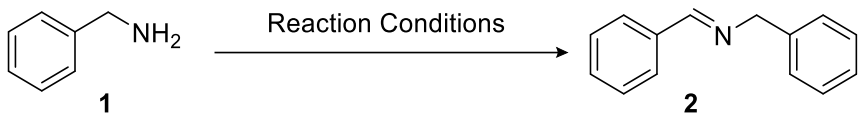

**Scheme 15.** Functionalisation of unactivated C-H bonds in alkanes photocatalysed by **TBADT** under anaerobic conditions, where EWG = electron-withdrawing group.[105,125,163]

While the prevalence of **TBADT** has demonstrated the potential of POMs as excellent photocatalysts, particularly in HAT processes, the progress of **TBADT** photocatalysis in SET catalysis remains somewhat restrained. These limitations include the necessity for precise control over redox potentials, efficient electron transfer pathways, and compatibility with diverse substrates. As mentioned previously, one promising avenue for achieving precise control and modulation of redox potentials involves the development of functionalised POM photocatalysts.

### 5.2 Photocatalytic Oxidative Coupling of Amines

In recent years, researchers have employed diverse strategies to functionalise POMs, significantly broadening their utility as photocatalysts. This expansion introduces a new dimension to their applicability, particularly in the field of organic photocatalysis. Functionalised POMs, with their tailored properties and reactivity, have emerged as promising candidates for SET-driven transformations. Among these, the photocatalytic oxidative coupling of amines stands out as an intriguing area of exploration.

An example of this is found in the work published by Suzuki and co-workers, with the synthesis of a $Ce^{3+}$-containing γ-Keggin-type polyoxometalate - $(^{n}Bu_4N)_6[\{Ce(H_2O)\}_2\{Ce(CH_3CN)\}_2(\mu_4\text{-}O)(\gamma\text{-}SiW_{10}O_{36})_2]$ – termed **CePOM**.[164] DFT calculations of the silicotungstate POM revealed a new $Ce^{3+}$-based HOMO, resulting in a smaller HOMO-LUMO energy gap, enabling POM activation with visible-light (λ = 400 nm). Upon irradiation, the POM was shown to be successful at catalysing an aerobic oxidative coupling reaction of amines into imines, achieving yields of up to 96%.[164] The model reaction is shown in **Scheme 16** where benzylamine **1** is used the starting substrate and reaction is conducted in MeCN under air, for 24 h.




**Suzuki** A) **CePOM**, 400 nm, $O_2$, MeCN, r.t, 24 h, **96%**

**Chen** B) **Mo/T/W POM**, Xe light, air, MeCN, r.t, 24 h, **96%**

**He** C) **ZnW-DPNDI-PYI**, 10 W White LED lamp, air, MeCN, r.t, 16 h, **99%**

**Scheme 16.** POM-catalysed oxidative coupling of benzylamine with reaction conditions reported by Suzuki, Chen, He, and co-workers.

Similarly, Chen *et al*., demonstrated that the coupling reaction could also be accomplished using a giant phosphorus-centred mixed-addenda POM composed of Mo, Ta, and W.[165] POM activation was achieved using a Xenon light source, resulting in the synthesis of the desired imines in up to 97%. However, the use of filter to restrict irradiation to visible-light irradiation led to a substantial decrease in yield.

Expanding beyond silicate and phosphonate-centred POMs, the same year witnessed the synthesis of a POM-incorporated metal-organic framework, featuring the borotungstate plenary POM $[BW_{12}O_{40}]^{5-}$. Comprising of three different components (namely N,N'-bis(4-pyridylmethyl)naphthalene diimide (abbreviated to DPNDI), the plenary POM, and pyrrolidine-2-yl-imidazole (abbreviated to PYI), this supramolecular system relied on the photosensitising properties of the DPNDI, and the oxidising nature of the reduced POM to form singlet oxygen. As a result, this **ZnW-DPNDI-PYI** system was shown to be activated by visible-light irradiation, using a 10 W white LED lamp, facilitating the amine coupling reaction in yields of up to 99%.

For the mechanism of the oxidative coupling reaction of benzylamine, two pathways have been proposed in literature (**Figure 55**). In both cases, irradiation leads to the POM in its excited state. SET between the starting substrate benzylamine **1** and the POM results in the formation of amino radical

cation (ARC) species **3** and reduced POM. Closing of the POM catalytic cycle occurs by reduction of oxygen and formation of the superoxide radical anion. The radical anion then reacts further by abstracting a hydrogen from the activated benzylic position to form imine intermediate $RCH{=}NH_2^+$ **4**. Following this, the two pathways separate. In pathway A, transamination of the imine intermediate with a secondary benzylamine substrate **1** results in intermediate **5**. Subsequent removal of ammonia leads to the desired imine **2**. In pathway B, hydrolysis of imine **4** results in the formation of aldehyde **6**. Following this, attack of a secondary amine and condensation affords the desired imine **2**.

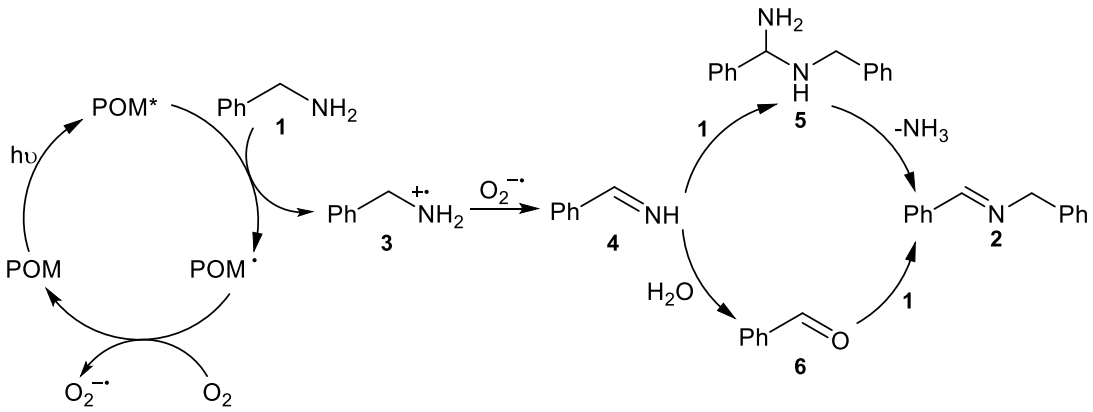



**Figure 55.** Proposed mechanism of the photocatalytic oxidative coupling of benzyl amine.[166]

The transformation of amines into imines has been demonstrated to be a robust reaction as exemplified by these functionalised POM catalysing the reaction with excellent yields, despite the differences in POM archetype and structure.[167–169] Furthermore, the use of atmospheric oxygen, as a clean and sustainable oxidant, is an additional benefit to this transformation. As a result, this reaction type serves as an effective benchmark for evaluating the impact of POM organofunctionalisation on their performance as SET photocatalysts.

## 5.3 Aims and Objectives

POMs have emerged as excellent oxidation catalysts in a wide range of organic transformations.[4] While **TBADT** has proved effective in organic photocatalysis, there exists a clear need to advance the field by developing new functionalised POM photocatalysts. These new catalysts should not only build on the inherent strengths of TBADT but address its limitations, particularly in terms of selectivity and substrate scope.

The concept of organofunctionalisation has been pivotal in this pursuit, introducing the possibility of modulating the electronic properties of POMs through careful synthesis and organogroup design. Despite these advancements, the application of these organic-inorganic hybrid POMs as photocatalysts has thus far been limited to the degradation of indigo dye. This highlights the need for a comprehensive exploration of the photochemical properties of these hybrid POMs in the area of organic photocatalysis. To this end, we set out to do the following:

1) To investigate the influence of hybridisation on the photocatalytic performance of the POMs in organic photocatalysis.

2) To examine and explore the interactions of POMs in a SET photochemical reaction.

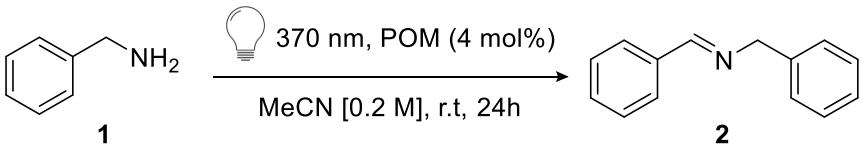
## 5.4 Results and Discussion

### 5.4.1 Phosphotungstate Photocatalysis

A series of POMs as their $^{n}Bu_4N$ salts were investigated as catalysts for the oxidative dimerization of benzyl amine. In this preparation, the POM (4 mol%) and benzylamine in MeCN, were irradiated at 370 nm for 24 h. NMR yield of the target imine product was determined by $^{1}H$ NMR spectroscopy, using 1,3-benzodioxozole as the internal standard.

Conducting the reaction in air, without the presence of a POM photocatalyst, resulted in no detection of the desired imine product (**Table 4** – entry 1). Similarly, conducting the reaction in an oxygen environment, without the presence of a POM photocatalysts, resulted in trace amounts of the desired imine product (2% NMR yield, **Table 4** – entry 2 ). Lastly, removal of light and conducting the reaction in the dark, saw no formation of the desired imine product (**Table 4** – entry 3). In all cases, starting material was observed after the reactions, suggesting a lack of reactivity.

**Table 4.** Control reactions for the photooxidative dimerization of benzyl amine.



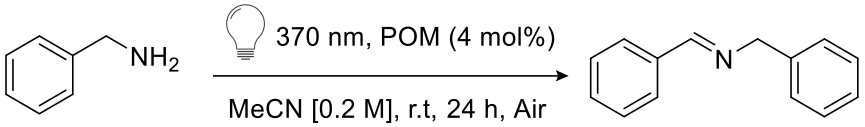

| Entry | Condition Variation | Environment | NMR Yield (%) |
|---|---|---|---|
| 1 | No POM | Air | 0 |
| 2 | No POM | Oxygen | 2 |
| 3 | Dark | Air | 0[a] |

Reaction conditions: Benzyl amine (0.2 mmol) and POM (4 mol%) in acetonitrile (1 mL) were irradiated at 370 nm for 24 h under described atmosphere. Determined by $^{1}H$ NMR analysis using 1,3-benzodioxole as an internal standard. [a]$SiPhBW_{11}$ used as the POM catalyst.

In the presence of TBADT, only trace amounts of the desired imine were observed (5%, **Table 5** – entry 1). Other indistinguishable products were also present in the $^{1}$H NMR spectrum of the reaction. This reaction outcome could be attributed to the strongly oxidising nature of **TBADT** when irradiated with energy-intensive UV-light, resulting in the decomposition of the starting material or products formed in the reaction.

For Wells-Dawson {**$P_2W_{18}$**}, a slight increase in NMR yield was observed at 13%, relative to **TBADT** (**Table 5** – entry 2). Hybrids {**$PPhP_2W_{17}$**} and {**$AsPhP_2W_{17}$**}, were shown to behave similarly to the plenary POM {**$P_2W_{18}$**}, with both hybrids achieving a yield of 16% (**Table 5** – entry 3 and 4). As a result, hybridisation in this case, had very little influence on the catalytic efficiency of the POMs.

**Table 5.** Preliminary results of plenary and hybrid POMs in the photooxidative dimerization reaction.




**1** **2**

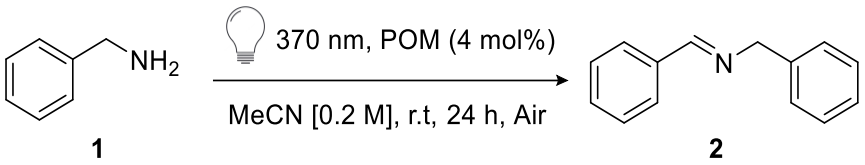
| Entry | POM | NMR Yield (%) |
|---|---|---|
| 1 | TBADT | 5 |
| 2 | **$P_2W_{18}$** | 13 |
| 3 | **$PPhP_2W_{17}$** | 16 |
| 4 | **$AsPhP_2W_{17}$** | 16 |

Reaction conditions: Benzyl amine (0.2 mmol) and POM (4 mol%) in acetonitrile (1 mL) were irradiated at 370 nm for 24 h under described atmosphere. Determined by $^{1}$H NMR analysis using 1,3-benzodioxole as an internal standard.

Expansion of this work involved exploration into various Keggin clusters. Starting with phosphotungstate plenary {**$PW_{12}$**}, only trace amounts of the desired imine product was observed with an NMR yield of 4% , (**Table 6** – entry 1). Hybridisation of the cluster with an organosilyl moiety in {**$SiPhP_2W_{17}$**}, increased the NMR yield to 17% (**Table 6** – entry 2). Replacement of the central

templating anion in {$PW_{12}$} with a siloxane in {$SiW_{12}$} saw a large increase in NMR yield from 4% to 25% (**Table 6** – entry 3), while hybridisation of the silicotungstate with the organophosphonate saw very little difference in yield (27%, **Table 6** - entry 4).

**Table 6.** Preliminary results of plenary and hybrid POMs in the photooxidative dimerization reaction.




**1** **2**

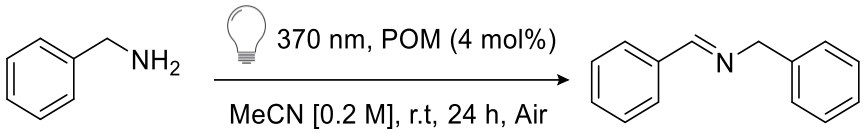
| Entry | POM | NMR Yield (%) |
|---|---|---|
| 1 | **$PW_{12}$** | 4 |
| 2 | **$SiPhPW_{11}$** | 17 |
| 3 | **$SiW_{12}$** | 25 |
| 4 | **$PPhSiW_{11}$** | 27 |

Reaction conditions: Benzyl amine (0.2 mmol) and POM (4 mol%) in acetonitrile (1 mL) were irradiated at 370 nm for 24 h under described atmosphere. Determined by $^{1}H$ NMR analysis using 1,3-benzodioxole as an internal standard.

### 5.4.2 Borotungstate Photocatalysis

With focus directed towards the borotungstate POMs, plenary {**$BW_{12}$**} obtained the desired imine with an NMR yield of 10%, while lacunary {**$BW_{11}$**}, achieved the synthesis in a 20% yield (**Table 7** – entries 1,2). Under the same reaction conditions, hybrids {**$PPhBW_{11}$**}, {**$AsPhBW_{11}$**}, and {**$SiPhBW_{11}$**} were found to facilitate the reaction more efficiently than {**$BW_{12}$**}, with yields ranging from 32% to 37% (**Table 7** – entries 3-5). This indicates that the hybridisation of borotungstate {**$BW_{11}$**} has a beneficial impact on the photocatalytic performance of the POMs in this reaction type, relative to plenary {**$BW_{12}$**}.

**Table 7.** Borotungstate-photocatalysed oxidative dimerization of benzyl amine.




**1** **2**

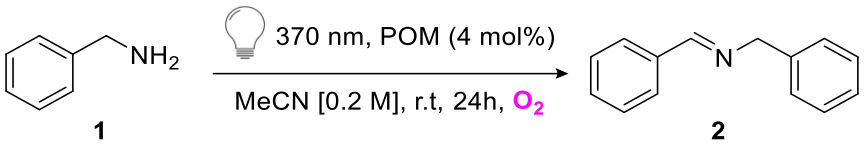
| Entry | POM | NMR Yield (%) |
|---|---|---|
| 1 | No POM | 0 |
| 2 | **$BW_{12}$** | 10 |
| 3 | **$BW_{11}$** | 20 |
| 4 | **$PPhBW_{11}$** | 36 |
| 5 | **$AsPhBW_{11}$** | 32 |
| 6 | **$SiPhBW_{11}$** | 37 |

Reaction conditions: Benzyl amine (0.2 mmol) and POM (4 mol%) in acetonitrile (1 mL) were irradiated at 370 nm for 24 h under described atmosphere. Determined by $^{1}$H NMR analysis using 1,3-benzodioxole as an internal standard.

With previous literature indicating the use of atmospheric oxygen to help facilitate closing of the POM photocatalytic cycle, natural progression of this study involved conducting the reaction under an atmosphere of oxygen (**Table 8**).[18,170] In this preparation, oxygen enrichment was achieved by sparging the reaction mixtures with oxygen for 1 min. This additional step resulted in a 5% increase in yield of the desired imine observed for both the plenary {**$BW_{12}$**} (with an NMR yield of 15%) and lacunary {**$BW_{11}$**} (with a yield of 25%). Among

the hybrid POMs, {**PPhBW$_{11}$**} and {**SiPhBW$_{11}$**} were shown to have the largest increase in yield, with {**PPhBW$_{11}$**} achieving the yield of 55% (with a 28% increase) and {**SiPhBW$_{11}$**} obtaining the imine in a 51% yield (displaying a 14% increase). In contrast, hybrid {**AsPhBW$_{11}$**} saw a marginal decrease in NMR yield by 7%, with a yield of 25%.

**Table 8.** Borotungstate POM photocatalysis under an oxygen environment.



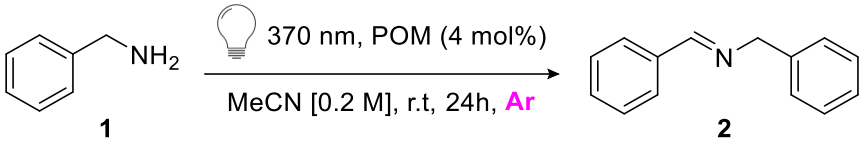

**1** **2**

| Entry | POM | NMR Yield (%) |
|---|---|---|
| 1 | **BW$_{12}$** | 15 |
| 2 | **BW$_{11}$** | 25 |
| **3** | **PPhBW$_{11}$** | **55** |
| 4 | **AsPhBW$_{11}$** | 25 |
| 5 | **SiPhBW$_{11}$** | 51 |
| 6 | **SiPhBW$_{11}$** | 51[a] |
| 7 | **PPhSiW$_{11}$** | 40 |

Reaction conditions: Benzyl amine (0.2 mmol) and POM (4 mol%) in acetonitrile (1 mL) were irradiated at 370 nm for 24 h under described atmosphere. Determined by $^{1}$H NMR analysis using 1,3-benzodioxole as an internal standard. [a]Anhydrous solvent was used.

By extension, replication of the reactions in an anaerobic environment, thus the removal of atmospheric oxygen, resulted in a diminished performance of the borotungstate POMs, with a significant effect on {**PPhBW$_{11}$**} displaying a decrease of ~30% (**Table 9**). One notable observation was the emergence of the heteropoly-blue colour in the reaction mixtures after 24 h. This colourisation serves as evidence for the POMs existing in their reduced form. This in turn, indicates that catalyst regeneration - and concurrent formation of superoxide - is hindered in the absence of oxygen, thereby preventing the synthesis of imines from taking place.

**Table 9.** Borotungstate POM photocatalysis under an argon environment.




**1** **2**

| Entry | POM | NMR Yield (%) |
|---|---|---|
| 1 | **BW$_{12}$** | 9 |
| 2 | **BW$_{11}$** | 7 |
| 3 | **PPhBW$_{11}$** | 8 |
| 4 | **AsPhBW$_{11}$** | 10 |
| 5 | **SiPhBW$_{11}$** | 13 |
| 6 | **PPhSiW$_{11}$** | 9 |

Reaction conditions: Benzyl amine (0.2 mmol) and POM (4 mol%) in acetonitrile (1 mL) were irradiated at 370 nm for 24 h under described atmosphere. Determined by $^{1}$H NMR analysis using 1,3-benzodioxole as an internal standard.

Summary of the influence of the reaction environment on the photocatalytic performance of the borotungstate POMs is shown in **Figure 56**, where a comparative bar chart displays the collected data. This work highlights the importance of oxygen, required to oxidise the reduced POM, and close the POM photocatalytic cycle.

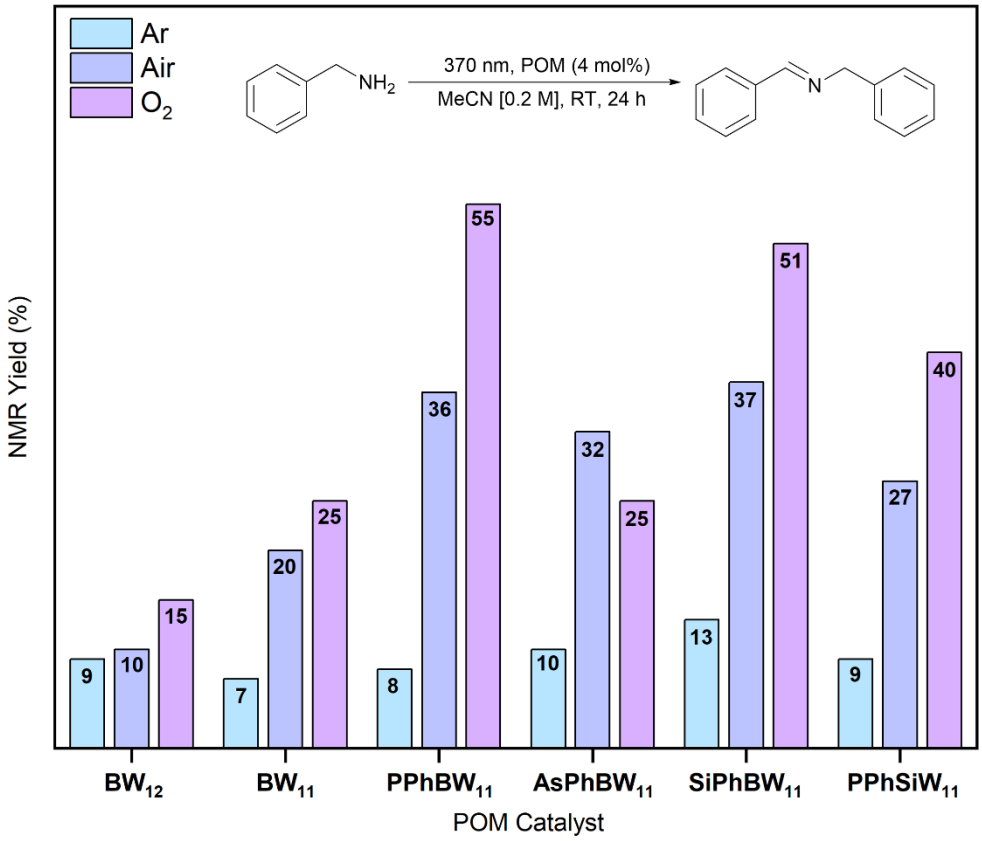



**Figure 56.** Bar graph displaying NMR yield in different reaction environments.

Building on the photocatalytic study, it is important to also evaluate the isoionic analogue {**PPhSIW$_{11}$**}. As shown previously, the silicotungstate POM exhibits a similar electronic behaviour to {**PPhBW$_{11}$**}, as observed by cyclic voltammetry, and a similar level of absorbance at 370 nm, as displayed in the UV-Vis spectroscopy. As a result, analysis of the silicotungstate isoionic POM would indicate how variation of the central heteroanion influences the photocatalytic properties of the POM in this SET transformation.

For isoionic analogue {**PPhSiW$_{11}$**}, a similar trend to organophosphonate hybrid {**PPhBW$_{11}$**} was observed, with an increase of yield from 27% to 40% achieved with an oxygen-enriched environment (**Table 8** – entry 7). In the comparison of the POMs, the {**PPhBW$_{11}$**} was shown to outperform the silicotungstate analogue. The cyclic voltammetry of {**PPhBW$_{11}$**} revealed redox processes occurring at more negative potentials when compared to {**PPhSiW$_{11}$**}, suggesting that the borotungstate would be more difficult to reduce. As a

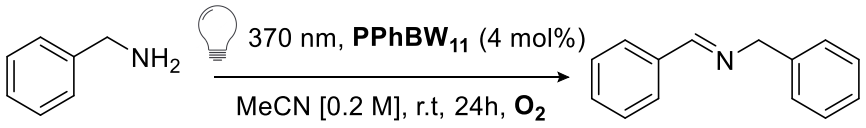
result, the difference in performance must be due to other factors influencing the reaction outcome. Examples of such factors include the effective closing of the POM photocatalytic cycle through oxidation of the reduced POM, and secondly, the presence of any potential interactions or pre-association occurring between the POM and the amine substrate. Investigations into the interactions of the borotungstate POM in the photocatalytic reaction will be discussed later on in this chapter.

Optimisation of the model reaction conditions for the oxidative coupling reaction of benzylamine are outlined in **Table 11**. Hybrid {**PPhBW$_{11}$**} was selected as the lead candidate in this study owing to its enhanced electronic stability compared to the other hybrids, as observed by cyclic voltammetry, and increased performance in oxygen as shown in the previous study (**Figure 56**). In this model reaction, hybrid {**PPhBW$_{11}$**} (4 mol% catalyst loading) and the amine were dissolved in MeCN [0.2 M]. The reaction mixture was irradiated (370 nm) for 24 h in an oxygen-enriched environment, resulting in the desired imine product with a yield of 55%. The evaluated parameters in this conditions-based screen included catalyst loading, solvent, concentration, and light source. NMR yields were calculated using 1,3-benzodixole, and the percentage deviation from the model reaction was determined.

A catalyst loading of 2 mol% for hybrid {**PPhBW$_{11}$**} was identified as optimum, with a smaller loading (0.5 mol%, **Table 10** – entry 2) leading to a decrease in yield (38%, -33% deviation from model). Conversely, a higher loading (6 mol%, **Table 10** – entry 3) did not significantly improve the reaction yield (55%, 2% deviation from model). Therefore, a 2 mol% catalyst loading was chosen for subsequent analysis. Changing the concentration from 0.2 M to 0.05 M or 0.4 M (**Table 10** – entries 3-5) had minimal impact on the reaction outcome, while increasing the concentration to 0.8 M (**Table 10** – entry 6) saw a decrease in NMR yield to 49% (a –52% deviation from the model). Replacement of the solvent from MeCN to pivalonitrile or acetone (**Table 10** – entries 8, 9) proved unfavourable, particularly in the case of acetone where no imine product was

detected. While using DMF as a solvent did not alter the reaction yield (**Table 10** – entry 7), MeCN was deemed preferable due to the facile removal of the solvent after reaction completion. The use of a higher wavelength of light (390 nm, **Table 10** – entry 10) proved ineffective, as expected from the absorption spectrum of {**PPhBW$_{11}$**}, resulting in the minimal production of imine product, obtained in poor yield (4%, –90% deviation from model). The tabulated data was transformed into a radar graph,[171,172] as displayed in **Figure 57**.

**Table 10.** Results of the condition–based sensitivity screening.




**1** **2**

| Entry | Light Source (nm) | Catalyst Loading (mol %) | Solvent | Conc. (M) | NMR Yield (%) | Deviation from Model (%) |
|---|---|---|---|---|---|---|
| 1 | **370** | **4** | **MeCN** | **0.2** | **55** | **Model** |
| 2 | 370 | 0.5 | MeCN | 0.2 | 38 | –33 |
| 3 | 370 | 6 | MeCN | 0.2 | 55 | 2 |
| 4 | 370 | 2 | MeCN | 0.05 | 56 | 2 |
| **5** | **370** | **2** | **MeCN** | **0.4** | **57** | **4** |
| 6 | 370 | 2 | MeCN | 0.8 | 49 | –52 |
| 7 | 370 | 2 | DMF | 0.2 | 49 | –52 |
| 8 | 370 | **2** | Acetone | 0.2 | 0 | –100 |
| 9 | 370 | 2 | Pivalonitrile | 0.2 | 42 | –59 |
| 10 | 390 | 2 | MeCN | 0.4 | 4 | –90 |

Reaction conditions: Benzyl amine (0.2 mmol) and POM in the described solvent were irradiated at under the described reaction conditions. Determined by $^{1}$H NMR analysis using 1,3-benzodioxole as an internal standard.

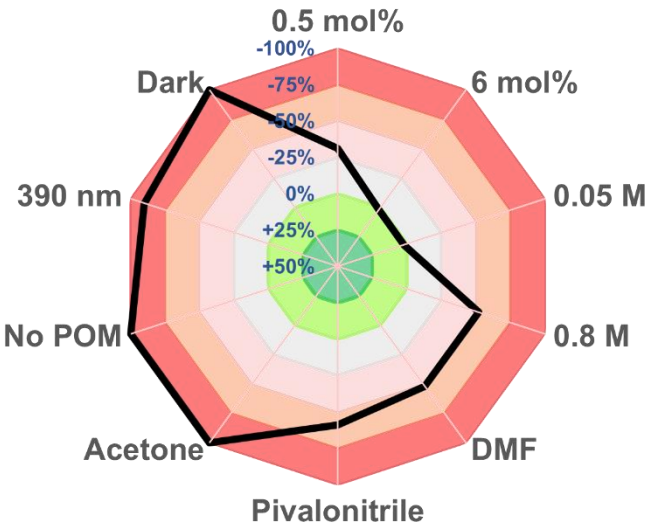
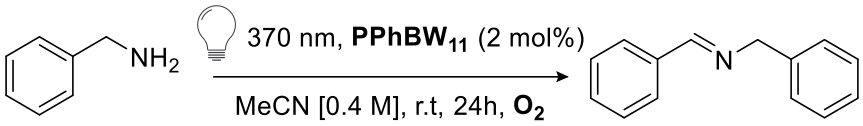



**Figure 57.** Radar graph displaying the data collected in **Table 10**.[171]

Monitoring the reaction over a period of 90 h initially showed an increase in yield, reaching its optimum between 24-48 h, with a yield ranging from 55-67% (**Table 11**). However, beyond this timeframe, the yield began to decrease, accompanied by an increase in aldehyde side product.

**Table 11**. Time-study of the photocatalytic dimerization reaction using **PPhBW$_{11}$**.




**1** **2**

| Entry | Time (h) | NMR Yield (%) |
|---|---|---|
| 1 | 0 | 0 |
| 2 | 6 | 18 |
| 3 | 18 | 54 |
| 4 | 48 | 67 |
| 5 | 54 | 53 |
| 6 | 72 | 13 |
| 7 | 90 | 9 |

Reaction conditions: Benzyl amine (0.2 mmol) and PPhBW$_{11}$ (2 mol%) in acetonitrile (1 mL) were irradiated at 370 nm for the described time frame. Determined by $^{1}$H NMR analysis using 1,3-benzodioxole as an internal standard.

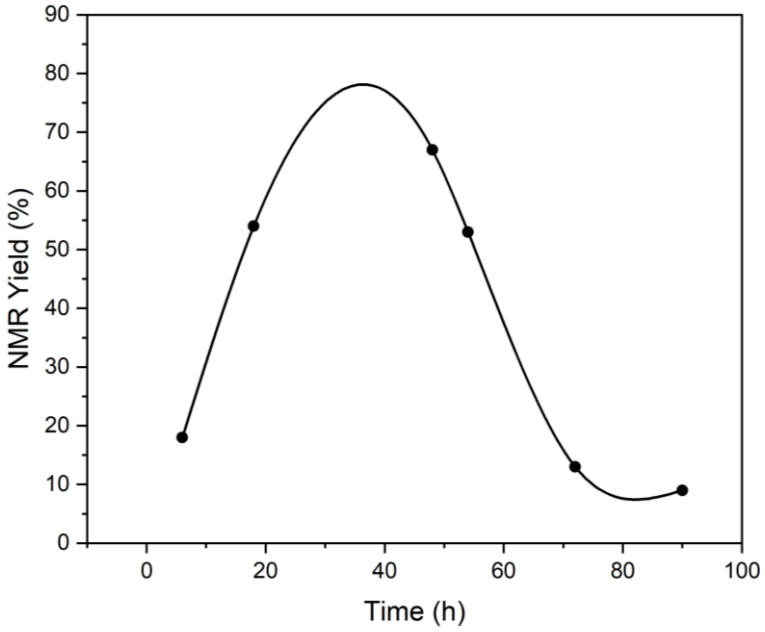



**Figure 58.** Graph displaying NMR yield over time. The trendline is fitted to a 4$^{th}$ order polynomial.

Following the optimisation process, the refined reaction conditions were determined. This involved UV-light irradiation (370 nm) of benzyl amine, with a 2 mol% catalyst loading of {**PPhBW$_{11}$**}, dissolved in MeCN [0.4 M]. After 24 h of irradiation in an oxygen-enriched environment, the desired imine was obtained with a yield of 57% (**Table 10** – entry 5).

### 5.4.3 Substrate Scope

With optimised conditions in hand, the scope of the borotungstate photocatalytic oxidative dimerization reaction of various amines was explored (**Figure 59**). In the presence of the POM, the model substrate benzylamine **1** yielded the desired imine at 57%, accompanied by a 41% yield of unreacted starting material. Cyclohexylmethylamine **17** gave the corresponding imine in an 8% yield indicating the importance of an activated methylene unit for acceptable yields. Thus, a series of para-, meta-, and ortho- substituted benzyl amines bearing alkyl, methoxy, phenyl, as well as halogen-containing groups were evaluated. These substrates gave the desired imines in moderate yields with little variance (44 - 62%)), irrespective of substituent effects. Given the use

of an energetic UV-A light source with an atmosphere of oxygen, catalyst- free reactions were also conducted to assess radical-initiated autoxidation reaction pathways for each substrate. Generally, without the POM catalyst, oxidative dimerization of primary benzylic amines was insignificant (yields <10%), highlighting the efficacy of {**PPhBW$_{11}$**} as a catalyst in this reaction. However, anisole-, biphenyl-, and thiophene-bearing amines (**7**, **15**, **16** respectively) yielded secondary aldimines in low to moderate yields (34 – 40%).

Overall, the versatility of the photooxidative coupling reaction under the optimised conditions with the use of {**PPhBW$_{11}$**} was demonstrated with various primary amines. In the majority of cases, the presence of the POM proved crucial for achieving moderate yields, with its absence resulting in diminished yields. In contrast, secondary amines proved challenging with the self-promotion of substrates activated by UV-light.

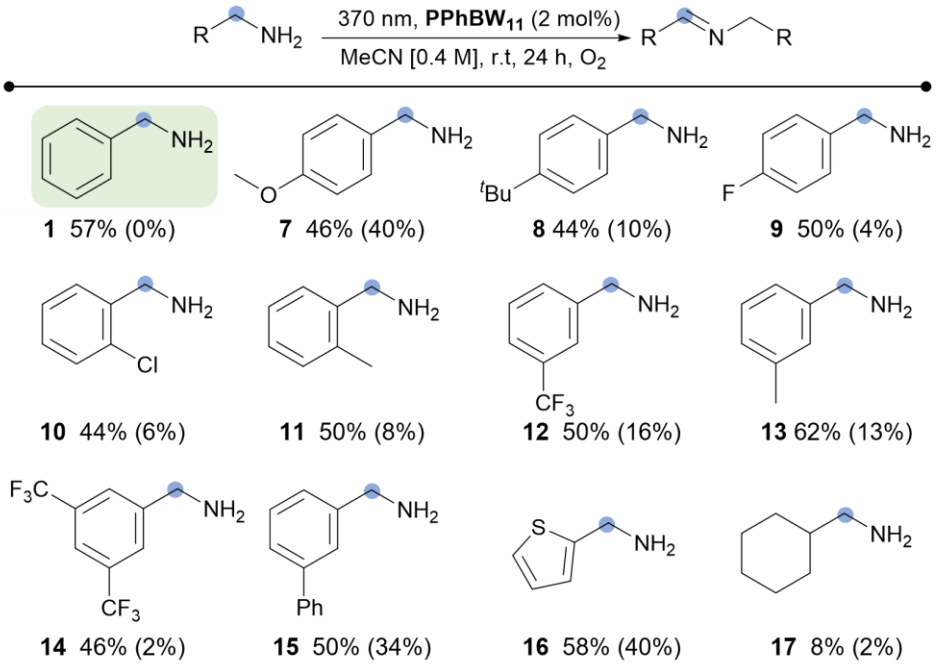


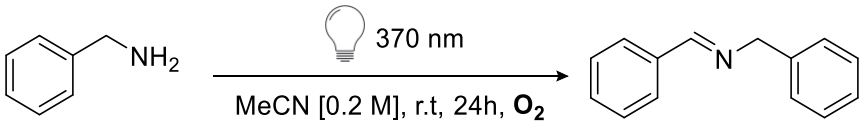

**Figure 59.** Reaction conditions: Amine (0.2 mmol) and POM in MeCN were irradiated at under the described reaction conditions. Determined by $^{1}$H NMR analysis using 1,3-benzodioxole as an internal standard.

### 5.4.4 POM-Substrate Interactions

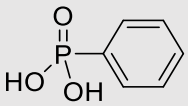
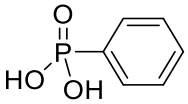
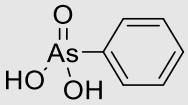
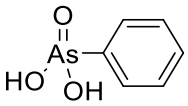
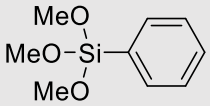
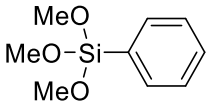
In investigating these hybrid POMs as photocatalysts, one crucial question emerges: is organogroup hybridisation necessary for the reaction to proceed or can the addition of the individual components still facilitate the process? With the hydrolysis studies demonstrating the potential degradation of the POM, separating the POM core from its organogroup, it becomes important to investigate the active catalyst component in the reaction. To explore this, reactions were conducted with the organic substrates (phenylphosphonic acid, phenylarsonic acid and trimethoxyphenylsilane) both with and without the presence of the lacunary {**$BW_{11}$**} (**Table 12**). The reactions were irradiated at 370 nm, at room temperature, for 24h.

Conducting the reaction with only {**$BW_{11}$**} yielded 18% (**Table 12** – entry 1). When using the respective substrates (termed Component 1 in **Table 12**), in the absence of the POM (referred to as Component 2) only trace amounts of the desired imine were produced, with yields ranging from 2-4% (**Table 12** – entries 2,4,6). In the reactions containing the phosphonic acid and silane reagents, the presence of {**$BW_{11}$**} resulted in an increased yield of 27% and 29% respectively (**Table 12** – entries 3,5). In contrast, no notable difference was observed in the reactions of {**$BW_{11}$**}, with and without the addition of phenyl arsonic acid, with the imine obtained in the yield of 18% (**Table 12** – entry 5). This data highlights the necessity of the POM in the reaction for the reaction to proceed. Secondly, when comparing this data of the separate components to the hybrid POMs, the difference in yield demonstrates that combining both components through hybridisation is required to increase reaction efficiency.

**Table 12**. Control reactions involving hybrid POM components




**1** **2**

| Entry | Component 1 (5 mol%) | Component 2 (2 mol%) | NMR Yield (%) |
|---|---|---|---|
| 1 | | **BW$_{11}$** | 18 |
| 2 |  | | 2 |
| 3 |  | **BW$_{11}$** | 27 |
| 4 |  | | 4 |
| 5 |  | **BW$_{11}$** | 18 |
| 6 |  | | 2 |
| 7 |  | **BW$_{11}$** | 29 |

Standard reaction conditions: Benzyl amine (0.2 mmol), organic substrates (5 mol%, component 1) and {**BW$_{11}$**} (2 mol%, component 2) were dissolved in MeCN and irradiated at 370 nm, for 24h. Yields determined by $^{1}$H NMR analysis using 1,3-benzodioxole as an internal standard.

Beyond the interactions between the organogroup and POM cluster, two components that need to be considered include the benzyl amine and the organogroup functionalised onto the POM core. One potential interaction involves the formation of electron donor-acceptor (EDA) complexes (**Figure 60**).[173] This interaction involves the association of an electron acceptor substrate and an electron-rich donor molecule resulting in the formation of a new molecular aggregation, known as an electron donor-acceptor complex.

Previous work on these systems have shown that separately, the two components may not absorb visible-light themselves, but the resulting EDA complex does. Referring back to the POM photochemical system, this would involve association of the electron-donating amino group of the benzylamine and the electron-accepting phosphonate located on the POM.

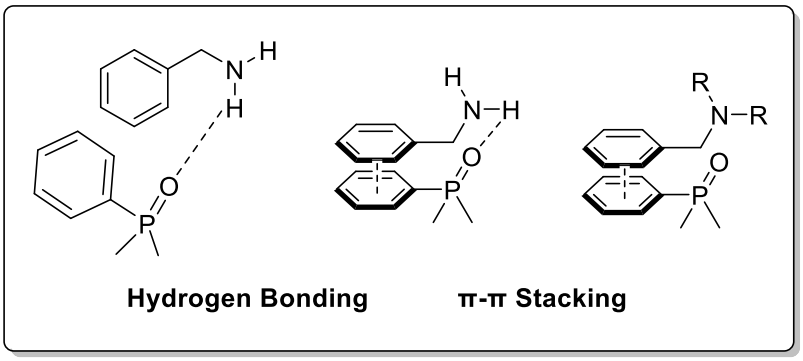



**Figure 60.** Graphical representation of potential interactions occurring between the organophosphorus group located on the POM and the benzyl amine substrate.

To this end, an NMR titration study was conducted to evaluate any interactions between the organophosphonate borotungstate POM and benzyl amine. In this study, combination of the POM and amine in various ratios were dissolved in deuterated MeCN and analysed through $^{1}H$ NMR spectroscopy. The $CH_2$ peak in benzyl amine and B-O-H peak in the borotungstate hybrids were monitored in the different experiments. Starting with plenary {**$BW_{12}$**}, addition of varying equivalents of benzyl amine (from 1 to 10 equiv.) saw no change to the amine with the proton peak corresponding to $CH_2$ remaining around 3.78 ppm (**Figure 61**).

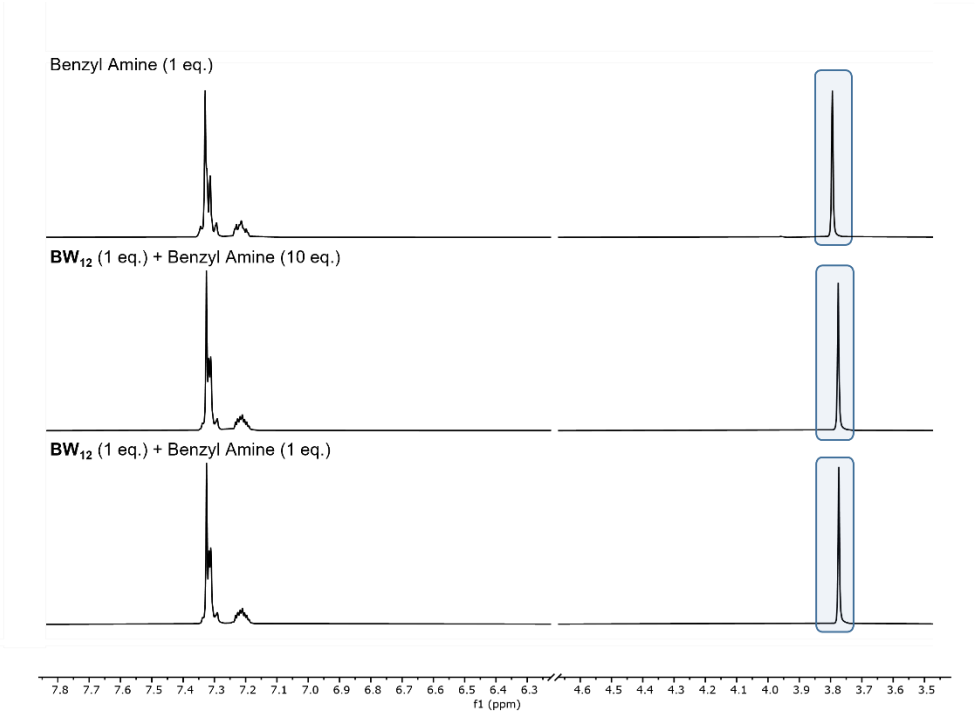



**Figure 61.** Stacked $^{1}H$ NMR (400 MHz, $CD_3CN$) of varying ratios of $BW_{12}$ and benzyl amine. The $CH_2$ proton peak in benzyl amine is highlighted by a blue square. Spectra window restrained to highlight areas of interest.

For organophosphorus borotungstate hybrid {**PPhBW$_{11}$**}, decreasing the ratio between the POM and benzyl amine from 1:10 to 1:1 saw a notable shift in peak position for the $CH_2$ in benzyl amine, combined with broadening of the peak (**Figure 62** - a). In addition to this, increasing the amount of amine saw the shift of the aromatic proton peaks associated to the organophosphonate groups functionalised onto the POM cluster, combined with shifting of the B-O-H peak. In the comparison between the organophosphonate {**PPhBW$_{11}$**} and hybrid {**AsPhBW$_{11}$**}, a similar trend was observed involving the shift in peak corresponding to the $CH_2$ protons in benzyl amine. In contrast, for hybrid {**SiPhBW$_{11}$**}, no change in the $CH_2$ proton peak is observed, with the peak remaining in the same region (**Figure 62** - b).

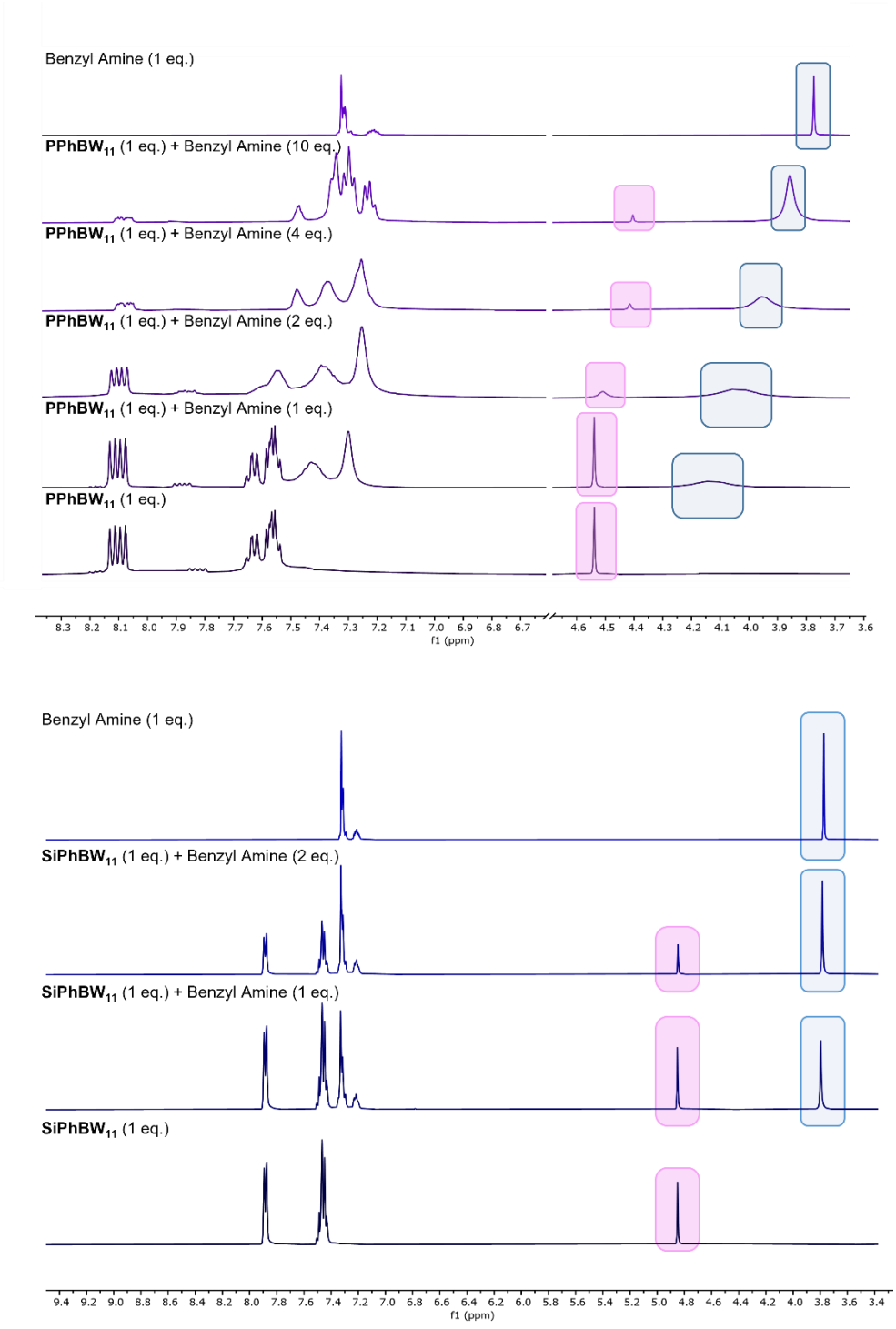
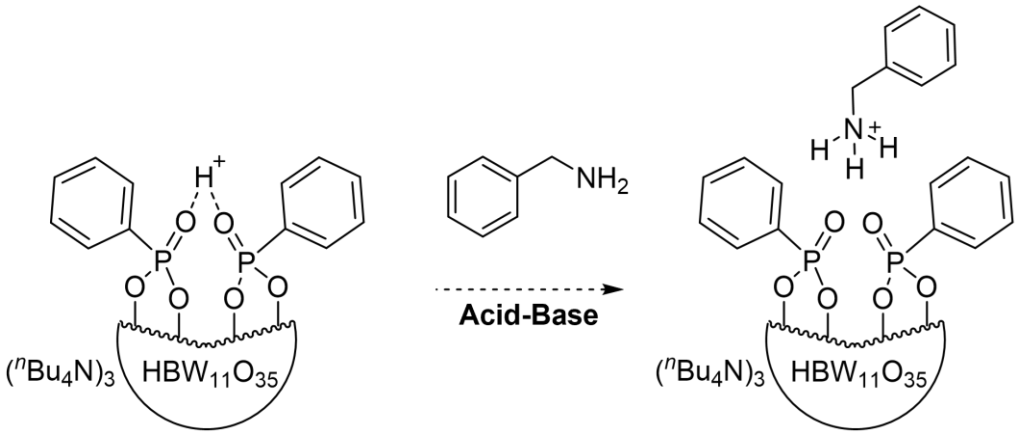



**Figure 62.** Stacked $^{1}H$ NMR (400 MHz, $CD_3CN$) of varying ratios of the borotungstate hybrids (top - {**PPhBW$_{11}$**}, bottom - {**SiPhBW$_{11}$**}) and benzyl amine. The $CH_2$ proton peak in benzyl amine is highlighted by a blue box and the B-O-H peak in the POM is highlighted by a pink box. Spectra window restrained to highlight areas of interest.

From this data, it can be postulated that the additional proton situated between the organogroups in {**PPhBW$_{11}$**} and {**AsPhBW$_{11}$**}, has the potential to protonate the benzyl amine, *via* an acid-base reaction, resulting in the formation of an ammonium cation in solution (**Scheme 17**). This would corroborate with the shifting of the $CH_2$ peak found in benzyl amine, which in turn, could alter the electronics of the aromatic groups situated on the POM core in {**PPhBW$_{11}$**} and {**AsPhBW$_{11}$**}. Furthermore, given that {**SiPhBW$_{11}$**}, does not exhibit this acidic proton, this could explain as to why this trend is not observed in this POM.

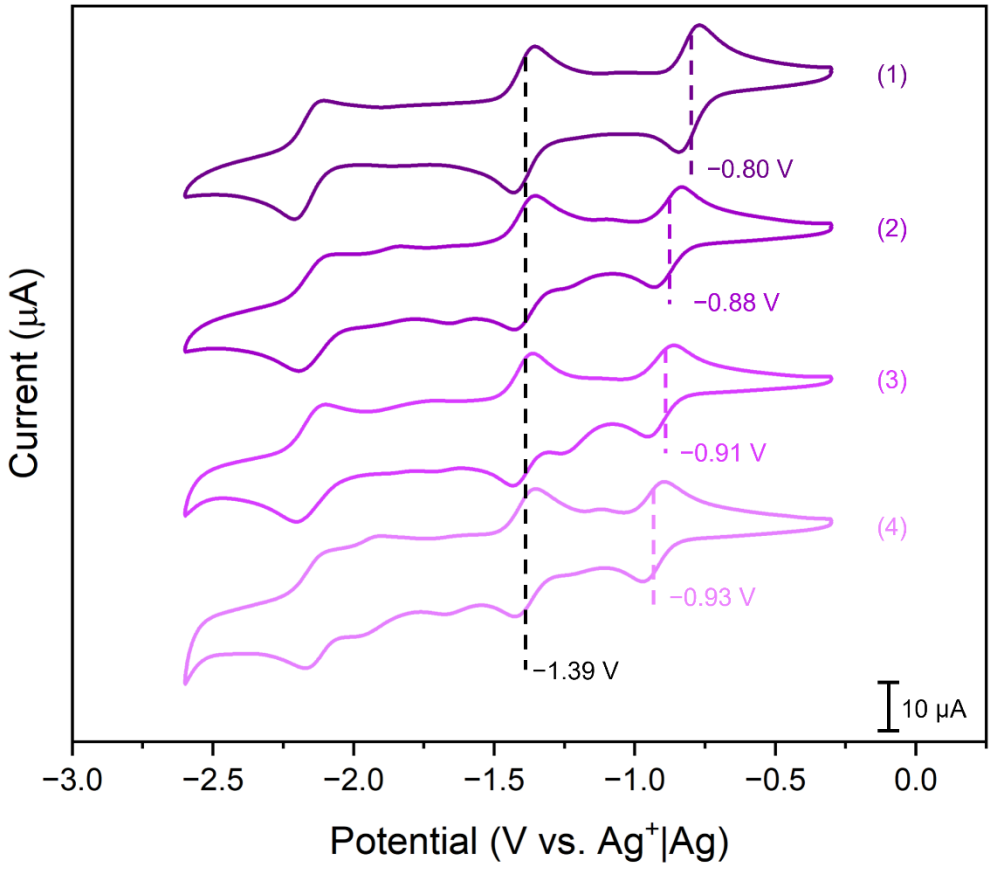



**Scheme 17.** Schematic representation of the proposed acid-base reaction occurring between the proton situated in the POM cation sphere and benzyl amine substrate.

With the prospect of protonation of the benzyl amine and formation of the ammonium cation, this would lead to ion exchange of the proton and thus, a change in the cation sphere surrounding the POM. As previously mentioned, the associated cations have an impact on the electrochemical properties of the POMs. In this context, the electronic characteristics of {**PPhBW$_{11}$**} were analysed using cyclic voltammetry with the subsequent addition of benzyl amine into the system (**Figure 63**).

Upon the addition of the amine into the system, a notable negative shift in redox potential was observed for the first redox process. The magnitude of the shift increased proportionally with the quantity of amine added. Interestingly,

the shift of the first redox process had very little influence on the position of the second redox process, with the standard potential for this process was found to remain constant at the same potential of –1.39 V (vs $Ag^+|Ag$). Given the change in the potential of the first redox process, this implies a change occurring to the LUMO of the system. Although further investigation is required to identify the specific type of interaction, it is evident that an interaction is taking place between the amine and POM.




| Experiment | $PPhBW_{11}$ (Equiv.) | Benzyl Amine (Equiv.) |
|---|---|---|
| 1 | 1 | - |
| 2 | 1 | 5 |
| 3 | 1 | 9 |
| 4 | 1 | 86 |

**Figure 63.** CV of 1mM of {**$PPhBW_{11}$**} in anhydrous DMF with 0.1 M $^nBu_4NPF_6$ supporting electrolyte. The standard potentials for the first and second redox processes are highlighted and labelled.

## 5.5 Conclusion

The borotungstate hybrids were evaluated as catalysts for the photooxidation of amines. Oxygen enrichment was found to further facilitate the catalytic process in most cases, with hybrid {**PPhBW$_{11}$**} determined to be the most effective. Comparatively, the organophosphorus borotungstate hybrids surpassed the performance of the literature-known isoionic silicotungstate hybrid {**PPhSiW$_{11}$**}, highlighting the untapped potential of borotungstate hybrid POMs in this area. Overall, *p*-block organofunctionalisation was found to enhance the activation of these novel borotungstate POMs as photocatalysts for the oxidative dimerization of amines, when compared to the plenary Keggin POM.

# 6 Summary

The work presented in this thesis demonstrates that structural variations in POMs can influence the electronic characteristics, and thus the frontier orbital energies of the resultant POMs systems. Organofunctionalisation with diverse organic moieties shows a clear and predictable influence on the orbital energies of the hybrid POMs, dictated by the electron-withdrawing and -donating effects of the substituents, nature of the bridging atom, and type of heteroanion located within the POM core.

In the pursuit of exploring novel organic-inorganic hybrid POMs, a family of borotungstate POMs, bearing organoarsonate and organosilyl groups, were successfully synthesised. This work expanded the literature precedence beyond the organophosphonate group. Structural characterisation confirmed protonation of the central borate anion, evidenced by NMR spectroscopy and X-ray crystallography, resulting to a unique general formula distinct from analogous phosphotungstate and silicotungstate hybrid POMs. The introduction of organic functional groups led to positive shifts in redox potentials, with {**PPhBW$_{11}$**}, featuring the most electron-withdrawing bridging atom, exhibiting the most significant shift. Additionally, organophosphonate functionalisation was shown to stabilise the subsequent reductions of the POM at lower potentials, compared to the other organofunctionalised hybrids.

Subsequently, the borotungstate hybrid POMs were evaluated as catalysts for the photooxidation of amines. Oxygen enrichment further facilitated the catalytic process in most cases, with hybrid {**PPhBW$_{11}$**} emerging as the most effective catalyst. Comparatively, the organophosphorus borotungstate hybrid surpassed the performance of the literature-known isoionic silicotungstate hybrid {**PPhSiW$_{11}$**}, highlighting the untapped potential of borotungstate POMs in this area. Overall, *p*-block organofunctionalisation enhanced the activation of these borotungstate POMs as photocatalysts for the oxidative dimerization of amines, when compared to the plenary Keggin POM.

# 7 Perspectives

Organic-Inorganic hybrid POMs have shown to exhibit structural diversity with tuneable electro- and photochemical properties distinguishing them from their plenary analogues. The exploration into their structural features and role as photocatalysts has highlighted the need for a deeper investigation into potential interactions between the various catalyst components and organic substrates in photochemical reactions. While these novel hybrids may not enhance the innate photochemical properties and application of **TBADT** as photocatalysts, they present an opportunity for tailored functionalities. This potential is realised through the careful design of specific photocatalysts that exhibit targeted photochemical properties, offering a promising avenue for specialised applications.

# 8 Future Work

## 8.1 POM-Substrate Interactions Study A

The combination of organic reagents and lacunary borotungstate POM as separate species resulted in imine formation, albeit in very low yields (Section **0**). One possible hypothesis suggests that interactions may occur between the reagents and the lacunary POM, or an *in situ* condensation reaction might take place, leading to the formation of an active species capable of catalysing the reaction. The condensation could be possible with the phenyl phosphonic acid (for example) acting as both the acid source and the organic reagent.

Future work on this would involve irradiation of the lacunary POM and organic reagent (in a 1:2 ratio) in the same reaction conditions used in the photocatalytic coupling (**Figure 64**). This includes both components in MeCN irradiated at room temperature for 24 h. Upon reaction completion, isolation of the POM from the reaction mixture could be achieved through solvent evaporation and precipitation of the POM through trituration.

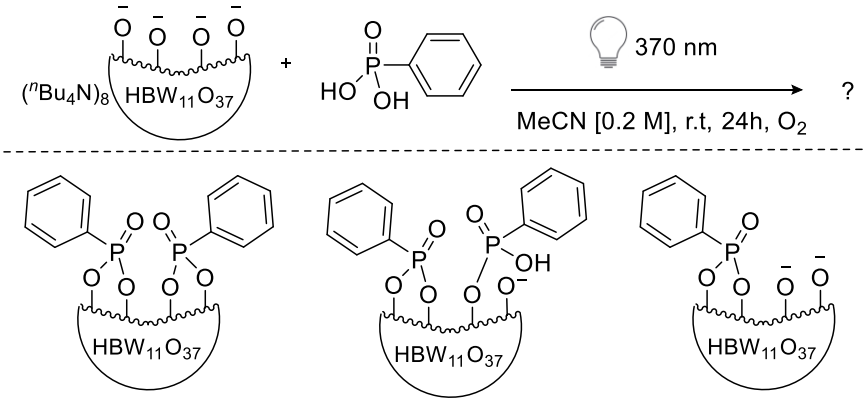
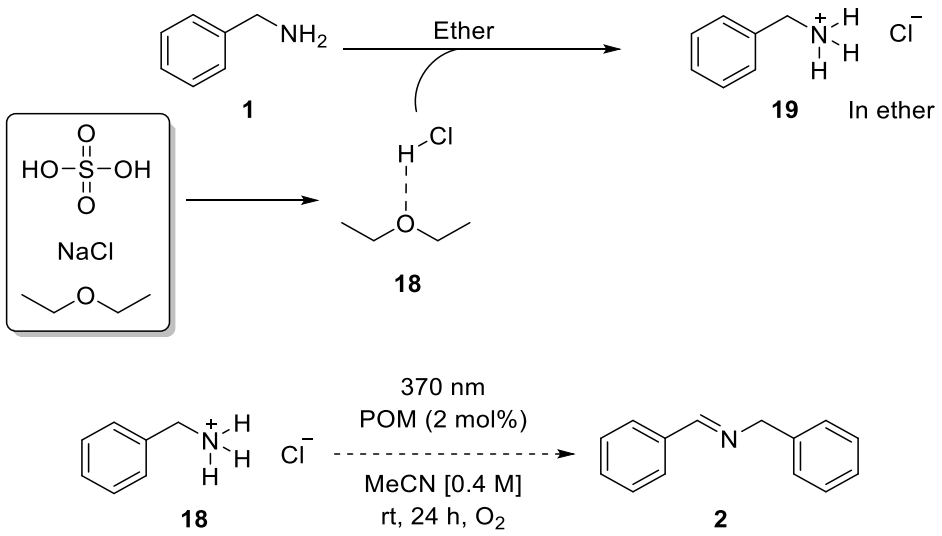



**Figure 64.** Proposed *in situ* POM generation of {**PPhBW$_{11}$**} through UV-light irradiation.

## 8.2 POM-Substrate Interactions Study B

With evidence supporting ammonium cation synthesis in the NMR titration study, it raised the query as to whether the ammonium cation was the reactive substrate in the photocatalytic reaction instead of the benzylamine, or whether it becomes a side product of the reaction, preventing some of the benzyl amine substrate from participating in the imine formation. Future work would involve the synthesis of the ammonium cation though previously reported methodology and subjecting the cation into the reaction conditions as the substrate (**Scheme 18**). The $^{1}$H NMR spectrum of the reaction would indicate whether the reaction could proceed using the cation starting substrate or whether a small amount of the benzylamine is acidified in the reaction, with the remaining benzylamine proceeding with imine formation.




**Scheme 18.** Ammonium cation synthesis and optimised photochemical reaction systems in testing the reactive substrate in the reaction.

### 8.3 {AsPhNH$_2$BW$_{11}$} Crystallisation

Crystallographic data of {**AsPhNH$_2$BW$_{11}$**} revealed crystallisation of the POM as a controlled polymeric complex (**Figure 65**). Given the low quality of the crystal, future work would involve attempts to isolate a crystal of high quality and investigation into the hydrogen bonding interaction of the POM.

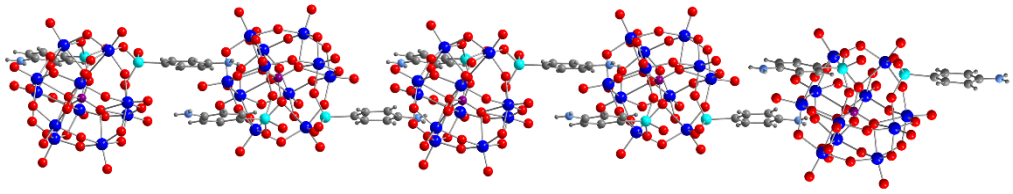


**Figure 65**. Crystal structure of {**AsPhNH$_2$BW$_{11}$**} as a polymeric complex**.** Solvent omitted for clarity.

In addition to this, the amino-substituent offers oppotunity for post-functionalisation of the POM. An example of this could involve amide coupling and covalent POM-peptide hybrid synthesis, as observed in work published in a recent review by the Mitchell group.[174]

# 9 Experimental

**Reactions.** All stirred reactions were fitted with a polytetrafluoroethylene (PTFE) coated magnetic stirring bar and magnetically stirred using a hot plate magnetic stirrer unless otherwise stated.

**Reagents and Solvents**. All commercially available reagents were used as received unless otherwise stated. All molarity (M) and normality (N) solutions are aqueous unless stated otherwise. The following compounds were synthesised from other members of the research group and analysed as received: $(^{n}Bu_4N)_3[PW_{12}O_{40}]$ {**$PW_{12}$**},[133] $(^{n}Bu_4N)_3[PMo_{12}O_4]$ {**$PMo_{12}$**},[133] and $(^{n}Bu_4N)_4[SiW_{12}O_{40}]$ {**$SiW_{12}$**},[133] $(^{n}Bu_4N)_3H[SiW_{11}O_{39}(POC_6H_5)_2]$ {**$PPhSiW_{11}$**}.[128]

**NMR Spectra.** $^{1}H$, $^{13}C$, $^{11}B$, $^{19}F$, and $^{31}P$ Nuclear Magnetic Resonance (NMR) spectra were acquired on a Bruker AV(III)400 HD or a Bruker AV(III)500 HD fitted with a 5 mm BBFO and 5 mm prodigy BBO probes, respectively. Processing of all NMR data was conducted with Bruker TopSpin or Mestrelab Research Mnova software suites. All signals $\delta$ are reported in parts per million (ppm). Where appropriate, chemical shifts in $^{1}H$ and $^{13}C$ spectra were referenced to the residual (partially) non-deuterated solvent according to Fulmer *et al*.,[175] $^{11}B$, $^{19}F$, and $^{31}P$ NMR spectra were referenced through the solvent lock ($^{2}H$) signal according to the IUPAC–recommended secondary referencing method following Bruker protocols.[176]

Data are reported as follows where appropriate: chemical shift, multiplicity, coupling constant, integration, and assignment. Multiplicity is abbreviated as follows: s (singlet), d (doublet), t (triplet), sext (sextet), dt (doublet of triplets), tt (triplet of triplets), and td (triplet of doublets). Broad signals are labelled with the prefix “br” (*e.g.,* br s = broad singlet). Complex signals of high order or due to signal overlap, that also display no apparent multiplicity, are reported with m (multiplet). Coupling constants *J* are reported in hertz (Hz).

**Mass Spectra.** Electrospray ionisation mass spectrometry (ESI–MS) was performed on a Bruker MicroTOF spectrometer. Samples were prepared for analysis by dissolving ca. 1 mg of the solid compound in 1 mL of HPLC grade acetonitrile. 50 µL of this stock solution was then introduced to the spectrometer through an auto–sampler by mixing into a stream of 30:70 $H_2O$: MeOH. All data was subsequently analysed using the Bruker DataAnalysis software suite. Modified instrument parameters were used for the detection of high molecular weight polyoxometalate anions while operating in negative mode.

**IR Spectra.** Attenuated Total Reflection Fourier–transform Infra–red spectroscopy (ATR–FTIR) was recorded on a Bruker Tensor 27 FTIR spectrometer equipped with a Pike GladiATR module with a diamond crystal.

**Cyclic Voltammetry.** Cyclic voltammetry (CV) was performed on a CHI600E workstation for solution state measurements. A standard three electrode set-up was employed with a glassy carbon (GC) working electrode (d = 3 mm), Pt wire counter electrode, and a $Ag^+|Ag$ reference electrode. CV was carried out on 1 mM of analyte in deoxygenated anhydrous DMF or MeCN (5 mL) with 0.1 M $^nBu_4NPF_6$ supporting electrolyte, scan rate 100 $mVs^{-1}$. Redox potentials are referenced to the $Ag^+|Ag$ or $Fc^+|Fc$ couple. The GC working electrode was polished using aqueous alumina slurries of decreasing particle size (1, 0.3, and 0.05 µm) and rinsed thoroughly with deionised water (18.2 MΩ cm, MilliQ). The Pt wire auxiliary electrode was cleaned in a butane flame prior to use. CHI or Autolab potentiostats were used for recording CVs. Internal resistance compensation was applied to electrochemical analysis of the POMs.

**UV/Vis.** All samples were measured in solution phase and performed on a Cary 5000 UV-Vis NIR Spectrometer using a quartz cuvette and samples dissolved in MeCN.

**Elemental Analysis.** CHN microanalysis was carried out using an Exeter Analytical CE–440 Elemental Analyser.

**X-ray Crystallography.** X-ray diffraction measurements were performed in Experiments Hutch 1 (EH1) of Beamline I19, at Diamond Light Source.[177] The data were collected at a wavelength of 0.6889 Å on a Fluid Film Devices 3-circle fixed-chi diffractometer using a Dectris Pilatus 2M detector. The crystal was mounted on a MiTeGen MicroMountTM using a perfluoropolyether oil and cooled for data collection by a Cryostream nitrogen-gas stream.[178] For {**K•AsPhBW$_{11}$**} and {**AsPhNH$_2$BW$_{11}$**}: The collected frames were integrated using XIA26 software[179] and the data were corrected for absorption effects using AIMLESS,[180] an empirical method. For {**K•PPhBW$_{11}$**}: Cell parameters were refined from the observed positions of all strong reflections and absorption corrections were applied using a Gaussian numerical method with beam profile correction (CrysAlisPro).[181] Structures were solved within Olex2[182] by dual space iterative methods (SHELXT)[183] and all non-hydrogen atoms refined by full-matrix least-squares on all unique F2 values with anisotropic displacement parameters (SHELXL).[183] Hydrogen atoms were refined with constrained riding geometries and thermal parameters linked to Uiso of their parent atoms. Structures were checked with checkCIF.[184] Refinement of crystallographic data conducted by Dr. Kieran D. Jones and Dr. Stephen Argent.

**Photoreactor and Light Source.** The EvoluChem PhotoRedOx Box™ (US Patent #10,906,022) and a 43W PR-160L-370nm Kessil LED light was used in all photochemical reactions. Only the front four vial slots were employed for reaction reproducibility. Reactions were stirred at 800 rpm. An in-built fan was used to maintain the air temperature inside the box at no more than 8°C above room temperature.

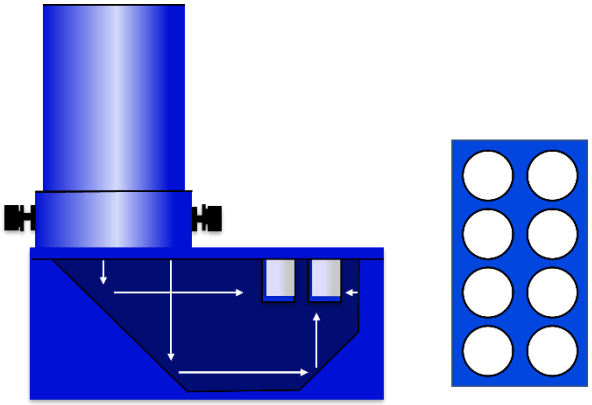
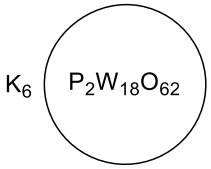


**Figure 66.** Left) Diagram representation of the EvoluChem PhotoRedOx Box. Right) Aerial viewpoint of the vial slot positions.

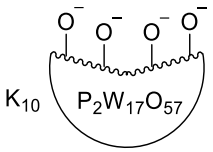
**$K_6[P_2W_{18}O_{62}]$**




The potassium plenary phosphotungstate Wells-Dawson was prepared using a modified procedure as described in literature.[185] $Na_2WO_4 \bullet 2H_2O$ (100 g, 0.30 mmol, 1.0 eq.) was dissolved in deionised water (117 mL) with vigorous stirring. After the $Na_2WO_4 \bullet 2H_2O$ had completely dissolved (ca. 5-10 minutes), resulting in a clear and colourless solution, HCl 4 M (84 mL, 0.33 mmol, 1.0 eq.) was added at a rate of 2 drops/second. A milky, white precipitate formed in solution during the addition of HCl. $H_3PO_4$ 4 M (84 mL, 0.33 mmol, 1.0 eq.) was added slowly to the reaction mixture. The solution was heated at reflux for 24 h. The resulting bright-yellow solution was allowed to cool to room temperature. Once cooled, the clear, yellow solution was stirred and KCl (50 g, 0.67 mmol, 2.0 eq.) was added to the solution, resulting in the formation of a yellow precipitate. The suspension was stirred for 10 min. The precipitate was then filtered from the solution and air dried. The crude product was dissolved a minimum amount of boiling water to produce a clear, yellow solution. This solution was allowed to cool to ambient temperature and then allowed to crystallise at 4°C for three days. The solid was filtered to give the title compound as yellow crystals (45.6 g, 0.009 mmol, 55%).

**$^{31}P\{^1H\}$ NMR** (162 MHz, $D_2O$) $\delta$ -13.00. **ATR-IR** (neat, $cm^{-1}$) 1085, 954, 906, 729. Analytical data consistent with those reported previously.[185] Lab book reference: NNT05.

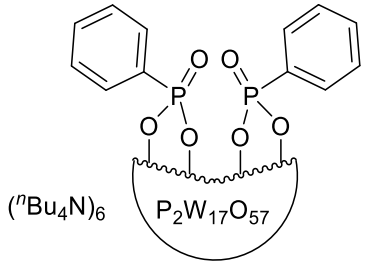
**$K_{10}[P_2W_{17}O_{61}]$**




$K_6[P_2W_{18}O_{62}]$ (20 g, 4.12 mmol, 1.0 eq.) was dissolved in deionised water (50 mL). $KHCO_3$ (5 g, 0.05 mmol, 0.02 eq.) was then added to the reaction mixture and stirred 24 h, forming a white precipitate. The precipitate was filtered and washed with deionised water (50 mL) and acetone (3 x 50 mL). The crude material was recrystallised from the minimum amount of hot water to give the title compound as a white solid (13.3 g, 2.92 mmol, 71%).

**$^{31}P$ {$^1H$} NMR** (162 MHz, $D_2O$) $\delta$ -7.21, -14.37. **ATR-IR** (neat, $cm^{-1}$): 3383, 2106, 1612, 1081, 1050, 101, 937, 908, 715. Analytical data consistent with those reported previously.[185] Lab book reference: NNT06.

**($^n$Bu$_4$N)$_6$[P$_2$W$_{17}$O$_{61}$(POC$_6$H$_5$)$_2$] / {PPhP$_2$W$_{17}$}**

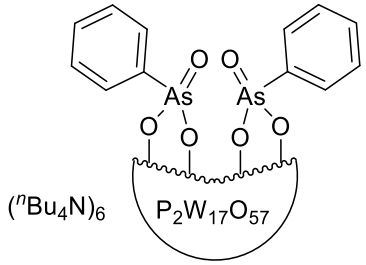



The organophosphorus phosphotungstate Wells-Dawson {**PPhP$_2$W$_{17}$**} was prepared using a modified procedure as described in literature.[76] Phenylphosphonic acid (39.5 mg, 0.250 mmol, 2.3 eq.) was dissolved in DMF (15 mL) with stirring to give a colourless solution. To this was added K$_{10}$[P$_2$W$_{17}$O$_{61}$] (500 mg, 0.110 mmol, 1.0 eq.) followed by 12 M HCl (49 µL, 0.588 mmol, 5.3 eq.). The resulting mixture was heated at 90°C for 16 h. The mixture was cooled to room temperature and filtered. Dry $^n$Bu$_4$NBr (324 mg, 1 mmol, 9.1 eq.) was added to the filtrate and the mixture was stirred for 1 h. The solvent was then removed *in vacuo*. The remaining solid was dissolved in minimum amount of MeCN (2 mL) followed by centrifugation (8000 rpm, 5 min), to remove any remaining solid, and precipitation with Et$_2$O (45 mL). Centrifugation (8000 rpm, 5 min) and decantation of the supernatant gave an off-white solid which was dried under vacuum. Dissolution in minimum MeCN (2 mL) followed by centrifugation (8000 rpm, 5 min), decantation and a final trituration, centrifugation, decantation, and vacuum drying sequence with H$_2$O (40 mL) gave the title compound as an off-white powder (430 mg, 0.07 mmol, 65%).

**$^1$H NMR** (400 MHz, DMSO-*d$_6$*) *δ* 8.03 – 7.94 (m, 4H, ArC<u>H</u>), 7.67 – 7.30 (m, 6H, ArC<u>H</u>), 3.22 – 3.13 (m, 48H, C<u>H</u>$_2$), 1.64 – 1.52 (m, 48H, C<u>H</u>$_2$), 1.33 (sext., *J* = 7.4 Hz, 48H, C<u>H</u>$_2$), 0.95 (t, *J* = 7.3 Hz, 72H, C<u>H</u>$_3$). **$^{13}$C NMR** (126 MHz, DMSO-*d$_6$*) *δ* 131.2 (4 x Ar<u>C</u>H), 131.1 (2 x Ar<u>C</u>H), 130.8 (2 x Ar<u>C</u>H), 127.6 (4 x Ar<u>C</u>H), 57.5 (6 x <u>C</u>H$_2$), 23.1 (6 x <u>C</u>H$_2$), 19.2 (6 x <u>C</u>H$_2$), 13.5 (6 x <u>C</u>H$_3$). **$^{31}$P {$^1$H} NMR** (162 MHz, DMSO-*d$_6$*) *δ* 14.81, -11.33, -12.95. **ATR-IR** (neat, cm$^{-1}$): 2960, 1483, 1378, 1137, 1086, 952, 905, 741. **Elemental Analysis** (%) for [C$_{16}$H$_{36}$N]$_6$[P$_2$W$_{17}$O$_{61}$(POC$_6$H$_5$)$_2$]

(5866.12)**:** Calc: C, 22.11; H, 3.88; N 1.43. Found: C, 19.56; H, 3.44; N, 1.14. Lab book reference: NNT01.

**($^n$Bu$_4$N)$_6$[P$_2$W$_{17}$O$_{61}$(AsOC$_6$H$_5$)$_2$] / {AsPhP$_2$W$_{17}$}**

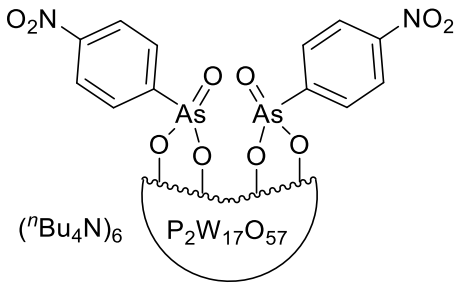



Phenylarsonic acid (50.5 mg, 0.250 mmol, 2.3 eq.) was dissolved in DMF (15 mL) with stirring to give a colourless solution. To this was added $K_{10}[P_2W_{17}O_{61}]$ (500 mg, 0.110 mmol, 1.0 eq.) followed by 12 M HCl (49 µL, 0.588 mmol, 5.3 eq.). The resulting mixture was heated at 90°C for 16 h after which it had become a cloudy off-white suspension. The mixture was cooled to room temperature and filtered. Dry $^n$Bu$_4$NBr (324 mg, 1 mmol, 9.1 eq.) was added to the filtrate and the mixture was stirred for 1 h. The solvent was then removed *in vacuo*. The remaining solid was dissolved in minimum amount of MeCN (2 mL) followed by centrifugation (8000 rpm, 5 min), to remove any remaining solid, and precipitation with $Et_2O$ (45 mL). Centrifugation (8000 rpm, 5 min) and decantation of the supernatant gave an off-white solid which was dried under vacuum. Dissolution in minimum MeCN (2mL) followed by centrifugation (8000 rpm, 5 min), decantation and a final trituration, centrifugation, decantation, and vacuum drying sequence with $Et_2O$ (40 mL) yielded the title compound as a pale-yellow powder (370 mg, 0.062 mmol, 56%).

**$^1$H NMR** (400 MHz, DMSO-*d*$_6$) *δ* 8.09 – 8.03 (m, 4H, ArC<u>H</u>), 7.78 – 7.61 (m, 6H, ArC<u>H</u>), 3.22 – 3.13 (m, 48H, C<u>H</u>$_2$), 1.64 – 1.52 (m, 48H, C<u>H</u>$_2$), 1.32 (sext., *J* = 7.3 Hz, 48H, C<u>H</u>$_2$), 0.94 (t, *J* = 7.3 Hz, 72H, C<u>H</u>$_3$). **$^{13}$C NMR** (126 MHz, DMSO-*d*$_6$) *δ* 133.0 (2 x Ar<u>C</u>H), 130.9 (4 x Ar<u>C</u>H), 130.5 (4 x Ar<u>C</u>H), 129.2 (2 x <u>C</u>), 57.5 (6 x <u>C</u>H$_2$)23.1 (6 x <u>C</u>H$_2$), 19.2 (6 x <u>C</u>H$_2$), 13.5 (6 x <u>C</u>H$_3$). **$^{31}$P {$^1$H} NMR** (162 MHz, DMSO-*d*$_6$) *δ* -11.33, -13.27. **ATR-IR** (neat, cm$^{-1}$): 2959, 1482, 1378, 1085, 952, 908, 785. **Elemental Analysis** (%) for $[C_{16}H_{36}N]_6[P_2W_{17}O_{61}$-

$(AsOC_6H_5)_2$] (5954.01)**:** Calc: C, 21.79; H, 3.83; N 1.41. Found: C, 19.38; H, 3.37; N, 1.14. Lab book reference: NNT02

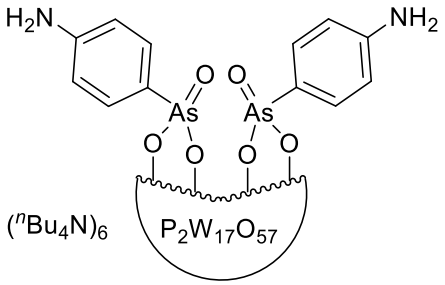
**($^{n}$Bu$_4$N)$_6$[P$_2$W$_{17}$O$_{61}$(AsOC$_6$H$_4$NO$_2$)$_2$] / {AsPhNO$_2$P$_2$W$_{17}$}**




*p*-Nitarsone (61.8 mg, 0.250 mmol, 2.3 eq.) was dissolved in DMF (15 mL) with stirring to give a colourless solution. To this was added $K_{10}[P_2W_{17}O_{61}]$ (500 mg, 0.110 mmol, 1.0 eq.) followed by 12 M HCl (49 µL, 0.588 mmol, 5.3 eq.). The resulting mixture was heated at 90˚C for 16 h. The mixture was cooled to room temperature and filtered. Dry $^{n}$Bu$_4$NBr (324 mg, 1 mmol, 9.1 eq.) was added to the filtrate and the mixture was stirred for 1 h. The solvent was then removed *in vacuo*. The remaining solid was dissolved in minimum amount of MeCN (2 mL) followed by centrifugation (8000 rpm, 5 min), to remove any remaining solid, and precipitation with $Et_2O$ (45 mL). Centrifugation (8000 rpm, 5 min) and decantation of the supernatant gave an off-white solid which was dried under vacuum. Dissolution in minimum MeCN (2mL) followed by centrifugation (8000 rpm, 5 min), decantation and a final trituration, centrifugation, decantation, and vacuum drying sequence with $Et_2O$ (40 mL) yielded the title compound as a pale-yellow powder (117 mg, 0.02 mmol, 18%).

**$^{1}$H NMR** (400 MHz, DMSO-*d*$_6$) *δ* 8.54 (d, *J* = 8.6 Hz, 4H, ArC<u>H</u>), 8.34 (d, *J* = 8.6 Hz, 4H, ArC<u>H</u>), 3.22 – 3.13 (m, 48H, C<u>H</u>$_2$), 1.64 – 1.52 (m, 48H, C<u>H</u>$_2$), 1.32 (sext., *J* = 7.3 Hz, 48H, C<u>H</u>$_2$), 0.94 (t, *J* = 7.3 Hz, 72H, C<u>H</u>$_3$). **$^{31}$P {$^{1}$H} NMR** (162 MHz, DMSO-*d*$_6$) *δ* -11.33, -13.15. **ATR-IR** (neat, cm$^{-1}$): 2961, 1602, 1525, 1482, 1378, 1347, 1085, 953, 916, 792. Lab book reference: NNT03.

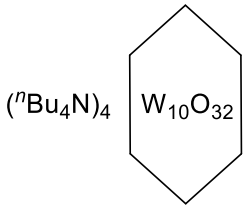
**($^n$Bu$_4$N)$_6$[P$_2$W$_{17}$O$_{57}$(AsOC$_6$H$_4$NH$_2$)$_2$)] / {AsPhNH$_2$P$_2$W$_{17}$}**




*p*-Arsanilic acid (54.3 mg, 0.250 mmol, 2.3 eq.) was dissolved in DMF (15 mL) with stirring to give a colourless solution. To this was added $K_{10}[P_2W_{17}O_{61}]$ (500 mg, 0.110 mmol, 1.0 eq.) followed by 12 M HCl (49 µL, 0.588 mmol, 5.3 eq.). The resulting mixture was heated at 90°C for 16 h after which it had become a cloudy off-white suspension. The mixture was cooled to room temperature and filtered. Dry $^n$Bu$_4$NBr (324 mg, 1 mmol, 9.1 eq.) was added to the filtrate and the mixture was stirred for 1 h. The solvent was then removed *in vacuo*. The remaining solid was dissolved in minimum amount of MeCN (2 mL) followed by centrifugation (8000 rpm, 5 min), to remove any remaining solid. The separated solution was then diluted with $Et_2O$ (45 mL) to form a red suspension. Centrifugation (8000 rpm, 5 min) and decantation of the supernatant gave a dark red solid which was dried under vacuum. Dissolution in minimum MeCN (2mL) followed by centrifugation (8000 rpm, 5 min), decantation and a final trituration, centrifugation, decantation, and vacuum drying sequence with $Et_2O$ (40 mL) yielded the title compound as a dark red powder (305 mg, 0.05 mmol, 46%).

**$^1$H NMR** (500 MHz, DMSO-$d_6$) $\delta$ 7.69 – 7.64 (m, 4H, ArC<u>H</u>), 6.72 – 6.68 (m, 4H, ArC<u>H</u>), 3.21 – 3.14 (m, 48H, C<u>H</u>$_2$), 1.57 (td, $J$ = 10.1 & 6.2 Hz, 48H, C<u>H</u>$_2$), 1.32 (sext., $J$ = 7.4 Hz, 48H, C<u>H</u>$_2$), 0.95 (t, $J$ = 7.3 Hz, 72H, C<u>H</u>$_3$). **$^{13}$C NMR** (126 MHz, $CD_3CN$) $\delta$ 153.4 (2 x Ar<u>C</u>H), 133.8 (4 x Ar<u>C</u>H), 132.8 (2 x <u>C</u>), 115.0 (4 x Ar<u>C</u>H), 59.3 (6 x <u>C</u>H$_2$), 24.4 (6 x <u>C</u>H$_2$), 20.4 (6 x <u>C</u>H$_2$), 13.9 (6 x <u>C</u>H$_3$). **$^{31}$P {$^1$H} NMR** (162 MHz, DMSO-$d_6$) $\delta$ -11.35, -13.42. **ATR-IR** (neat, cm$^{-1}$): 3355, 2959, 1594, 1482, 1378, 1085, 952, 910, 778. Lab book reference: NNT50.

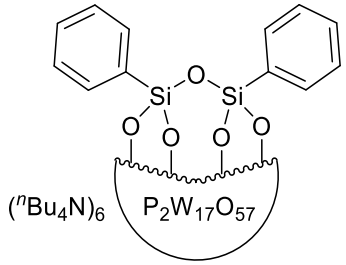
**($^n$Bu$_4$N)$_4$[W$_{10}$O$_{32}$] / TBADT**




The decatungstate POM (**TBADT**) was prepared using a modified procedure as described in literature.[109] Deionised water (100 mL) was heated to 90°C. To this was added $Na_2WO_4 \bullet 2H_2O$ (16 g, 48.5 mmol, 1.0 eq.). The reaction mixture was quickly acidified (10s) with hot concentrated hydrochloric acid (34 mL) at 90°C. The mixture was stirred for 1-2 min at 90°C. $^n$Bu$_4$NBr (6.4 g, 26.4 mmol, 1.8 eq.) was dissolved in cold deionised water (10 mL) and added to the reaction mixture. A white suspension was formed. Hot filtration using water, followed by washings using cold acetonitrile (50 mL), cold ethanol (50 mL), and cold ether (50 mL). The product was purified by recrystallisation (hot acetonitrile 1.5 g/1 mL) to afford the title compound as an off-white powder (4.7 g, 1.42 mmol, 29%).

**ATR-IR** (neat, cm$^{-1}$): 2961, 2872, 1482, 1379, 1152, 992, 954, 942, 885, 780. **Elemental Analysis** (%) for [C$_{16}$H$_{36}$N]$_4$[W$_{10}$O$_{32}$] (3320.24)**:** Calc. C, 23.15; H, 4.37; N 1.69, Found C, 23.14; H, 4.3; N, 1.51. Lab book reference: NNT04.

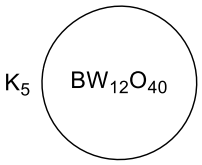
**($^n$Bu$_4$N)$_6$[P$_2$W$_{17}$O$_{61}$(SiC$_6$H$_5$)$_2$O)] / {SiPhP$_2$W$_{17}$}**




The organosilyl phosphotungstate Wells-Dawson {**SiPhP$_2$W$_{17}$**} was prepared using a modified procedure as described in literature.[74] K$_{10}$[P$_2$W$_{17}$O$_{61}$] (0.5 g, 0.085 mmol, 1.0 eq.) was dissolved in MeCN (30 mL). To this was added $^n$Bu$_4$NBr (0.210 g, 0.64 mmol, 7.5 eq.). Trichlorophenylsilane (70 µL, 0.43 mmol, 5.0 eq.) was added dropwise to the suspension at 0$^o$C and the suspension was left to warm up to rt for 24 h. The reaction was filtered *via* centrifugation at 8000 rpm for 3 minutes and solvent was removed *in vacuo.* The solid was redissolved in the minimum amount of MeCN and precipitated by the addition of a large excess of ether. The sample was sedimented by spinning at 8000 rpm in a centrifuge for 3 minutes, the supernatant discarded, and the solid was suspended in Et$_2$O using ultrasound. The solvent was removed *in vacuo* to give the title compound as a pale-yellow solid (128 mg, 0.02 mmol, 26%)

**$^1$H NMR** (400 MHz, DMSO) $\delta$ 7.76 – 7.73 (m, 4H, ArC<u>H</u>), 7.36 (d, *J* = 6.6 Hz, 6H, ArC<u>H</u>), 3.21 – 3.13 (m, 48H, C<u>H</u>$_2$), 1.56 (td, *J* = 9.9 & 5.9 Hz, 48H, C<u>H</u>$_2$), 1.32 (sext., *J* = 7.4 Hz, 48H, C<u>H</u>$_2$), 0.94 (t, *J* = 7.3 Hz, 72H, C<u>H</u>$_3$). **$^{13}$C NMR** (126 MHz, CD$_3$CN) $\delta$ 135.9 (2 x Ar<u>C</u>H), 134.6 (4 x Ar<u>C</u>H), 129.5 (2 x <u>C</u>), 127.7 (4 x Ar<u>C</u>H), 58.3 (6 x <u>C</u>H$_2$), 23.4 (6 x <u>C</u>H$_2$), 19.4 (6 x <u>C</u>H$_2$), 12.9 (6 x <u>C</u>H$_3$). **$^{31}$P NMR {$^1$H}** (162 MHz, DMSO-$d_6$) $\delta$ -10.80, -13.83. Analytical data consistent with those reported previously. Lab book reference: NNT108.

**$K_5[BW_{12}O_{40}]$ / {K•$BW_{12}$}**




The potassium plenary borotungstate Keggin {**K•$BW_{12}$**} was prepared using a modified procedure as described in literature.[138] $Na_2WO_4$•$2H_2O$ (100 g, 303 mmol, 1.0 eq.) and boric acid (5 g, 81 mmol, 0.27 eq.) were dissolved in boiling water (100 mL). A solution of 6 M HCl (60 mL) was added dropwise (with vigorous stirring in order to dissolve the local precipitate of tungstic acid) until the pH was 6. The solution was kept at reflux for 24 h then was allowed to cool to room temperature. The reaction mixture was gravity filtered and the filtrate was acidified with 6 M HCl (30 mL) until pH 2. The reaction mixture was allowed to boil for 30 min and allowed to cool to room temperature. Addition of KCl (20 g, 268 mmol, 3.3 eq.) resulted in a white precipitate. The cloudy suspension was stirred for 1 h at room temperature. The suspension was Buchner filtrated and the white solid was washed with ether. Recrystallization using hot $H_2O$ (30 mL) yielded the title compound as a white solid (8.6 g, 2.8 mmol, 11%).

**$^{11}$B NMR** (128 MHz, $D_2O$) $\delta$ 2.14 (s). **ATR-IR** (neat, $cm^{-1}$): 3419, 2114, 1614, 1000, 954, 616, 499, 424. Lab book reference: NNT96.

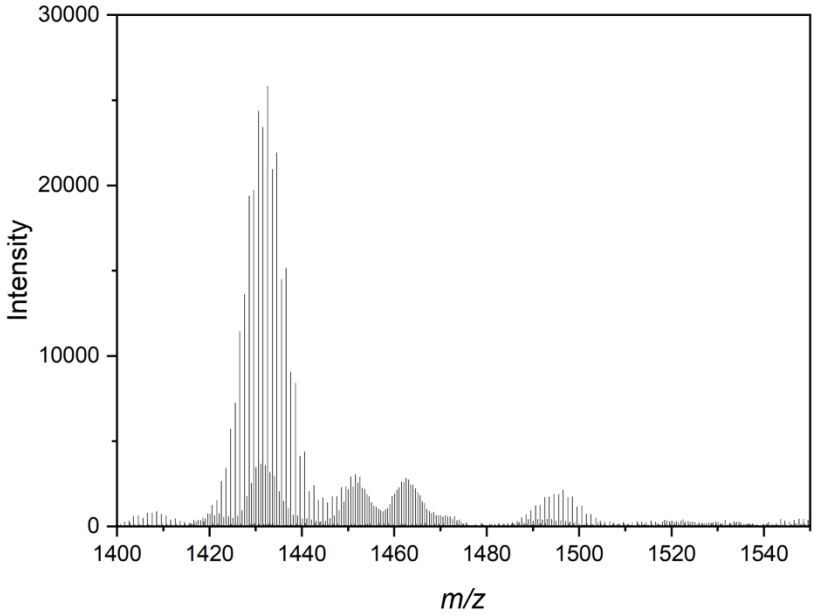
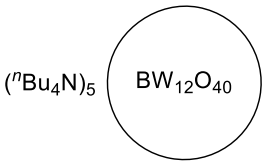



**Figure 67.** Negative mode ESI-MS spectrum of compound {**K•BW$_{12}$**} in the *m/z* range 1400-1550, in $H_2O$.

**Table 13.** Mass spectra (ESI) of {**K•BW$_{12}$**}.

| Assignment | *z* | *m/z* (calc.) | m/z (obs.) |
|---|---|---|---|
| $\{H_3[BW_{12}O_{40}]\}$ | 2- | 1429.62 | 1429.60 |
| $\{NaH_2[BW_{12}O_{40}]\}$ | 2- | 1440.61 | 1440.62 |
| $\{KH_2[BW_{12}O_{40}]\}$ | 2- | 1448.60 | 1448.59 |
| $\{Na_2H[BW_{12}O_{40}]\}$ | 2- | 1451.60 | 1451.60 |
| $\{KNaH[BW_{12}O_{40}]\}$ | 2- | 1459.59 | 1459.59 |
| $\{Na_3[BW_{12}O_{40}]\}$ | 2- | 1462.59 | 1462.60 |
| $\{K_2H[BW_{12}O_{40}]\}$ | 2- | 1467.58 | 1467.59 |
| $\{KNa_2[BW_{12}O_{40}]\}$ | 2- | 1470.58 | 1470.58 |

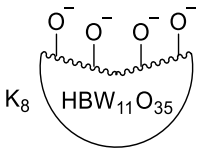
**($^n$Bu$_4$N)$_5$[BW$_{12}$O$_{40}$] / {BW$_{12}$}**




Borotungstate Keggin {**BW$_{12}$**} was prepared using a modified procedure as described in literature.[133] To a solution of $K_5[(HBW_{11}O_{39})(PO(C_6H_5))_2$ (2 g, 0.61 mmol, 1.0 eq.) in MeCN (20 mL) was added $^n$Bu$_4$NBr (1.2 g, 3.6 mmol, 6.0 eq.) in MeCN (12 mL). The reaction mixture was stirred for 1 h. The solid impurities were removed by centrifugation at 8000 rpm for 3 min. The solution concentrated *in vacuo.* The solid was redissolved in the minimum amount of MeCN, syringe filtered and precipitated by the addition of $Et_2O$. The sample was sedimented by spinning at 8000 rpm in a centrifuge for 3 min, the supernatant discarded, and the solid was suspended in of $Et_2O$ using ultrasound. This was repeated with acetone and ether. The solvent was removed *in vacuo* to give the title compound as a white solid (1.8 g, 0.44 mmol, 73%).

**$^1$H NMR** (400 MHz, $CD_3CN$) $\delta$ 3.21 – 3.13 (m, 40H, C$\underline{H}_2$), 1.66 (tt, $J$ = 8.2 & 6.1Hz, 40H, C$\underline{H}_2$), 1.42 (sext., $J$ = 7.4 Hz, 40H, C$\underline{H}_2$), 0.99 (t, $J$ = 7.3 Hz, 60H, C$\underline{H}_3$). **$^{11}$B NMR** (128 MHz, $CD_3CN$) $\delta$ 1.96 (s). **ATR-IR** (neat, cm$^{-1}$): 2960, 2873, 1644, 1484, 1381, 1152, 991, 946, 894, 807, 508, 424. Lab book reference: NNT104.

**$K_8[HBW_{11}O_{39}]$ / {K•$BW_{11}$}**




Borotungstate lacunary Keggin {**K•$BW_{11}$**} was prepared using a modified procedure as described in literature.[133] $Na_2WO_4$•$2H_2O$ (30 g, 91 mmol, 1.0 eq.) and boric acid (2 g, 32 mmol, 0.4 eq.) were dissolved in boiling water (50 mL). A solution of 6 M HCl (19 mL) was added dropwise until the pH was 6. The solution was kept at reflux for 1 h and after cooling to room temperature it was kept at 4°C for 24 h. The reaction mixture was gravity filtered and KCl (10 g, 134 mmol, 1.5 eq.) was added to the filtrate. The solid precipitate was isolated and recrystallised in hot $H_2O$ to give the title compound as a white powder (6.7 g, 2.26 mmol, 27%).

**$^{11}$B NMR** (128 MHz, $D_2O$) $\delta$ 2.70 (br s). **ATR-IR** (neat, $cm^{-1}$): 3382, 2119, 1926, 1622, 1230, 990, 952, 804, 709, 502, 472. Lab book reference: NNT97.

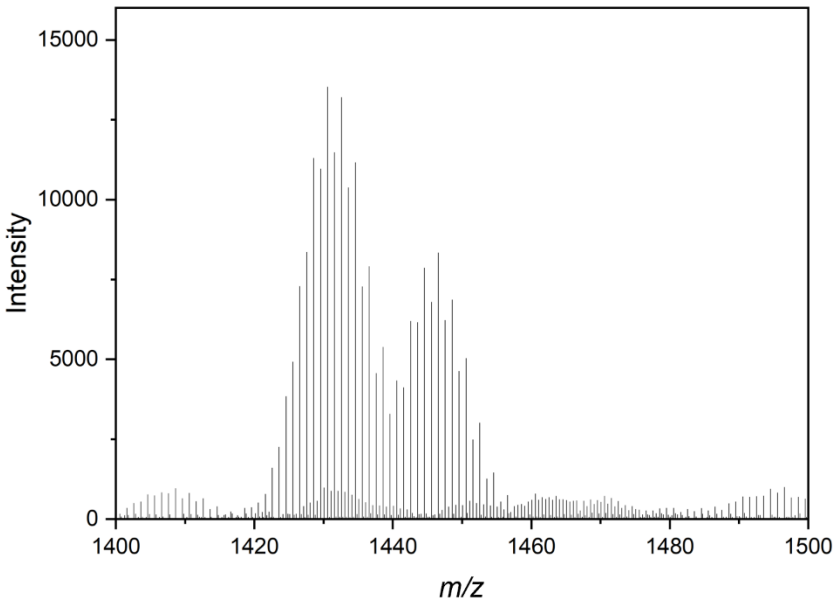
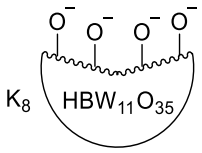



**Figure 68.** Negative mode ESI-MS spectrum of compound {**K•BW$_{11}$**} in the *m/z* range 1400-1500, in $H_2O$.

**Table 14.** Mass spectra (ESI) of {**K•BW$_{11}$**}.

| Assignment | *z* | *m/z* (calc.) | *m/z* (obs.) |
|---|---|---|---|
| $\{KH_4Na[HBW_{11}O_{39}]\}$ | 2- | 1361.63 | 1361.62 |
| $\{KNa_5[HBW_{11}O_{39}]\}$ | 2- | 1405.60 | 1405.61 |
| $\{KNa_5[HBW_{11}O_{39}]\}(H_2O)$ | 2- | 1416.60 | 1416.62 |
| $\{K_2Na_4[HBW_{11}O_{39}]\}(H_2O)$ | 2- | 1422.59 | 1422.59 |
| $\{K_4Na_2[HBW_{11}O_{39}]\}$ | 2- | 1430.56 | 1430.60 |
| $\{K_3Na_3[HBW_{11}O_{39}]\}(H_2O)$ | 2- | 1431.58 | 1431.61 |
| $\{K_5H[HBW_{11}O_{39}]\}(H_2O)$ | 2- | 1436.56 | 1436.61 |
| $\{K_2Na_4[HBW_{11}O_{39}]\}(EtOH)$ | 2- | 1436.60 | 1436.61 |
| $\{K_4Na_2[HBW_{11}O_{39}]\}(H_2O)$ | 2- | 1439.56 | 1439.59 |
| $\{K_5Na[HBW_{11}O_{39}]\}(H_2O)$ | 2- | 1447.55 | 1447.58 |

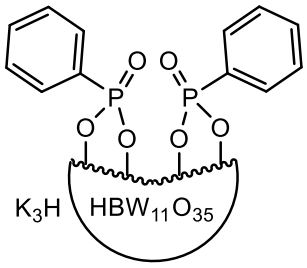
**($^{n}$Bu$_4$N)$_8$[HBW$_{11}$O$_{39}$] / {BW$_{11}$}**




Borotungstate Keggin **BW$_{11}$** was prepared using a modified procedure as described in literature.[186] To a solution of $K_8[HBW_{11}O_{39}]\bullet 13H_2O$ (250 mg, 0.078 mmol, 1.0 eq.) in MeCN (12 mL) was added $^{n}Bu_4NBr$ (226 mg, 0.7 mmol, 9 eq.) in MeCN (25 mL). The reaction mixture was stirred for 1h. The solid impurities were removed by centrifugation at 8000 rpm for 3 min. The solution concentrated *in vacuo.* The solid was redissolved in the minimum amount of MeCN, syringe filtered and precipitated by the addition of $Et_2O$. The sample was sedimented by spinning at 8000 rpm in a centrifuge for 3 min, the supernatant discarded, and the solid was suspended in of $Et_2O$ using ultrasound. This was repeated with acetone and ether. The solvent was removed *in vacuo* to give the title compound as a white powder (108 mg, 0.02 mmol, 30%).

**$^{1}$H NMR** (400 MHz, $CD_3CN$) $\delta$ 3.21 – 3.12 (m, 64H, C$\underline{H}_2$), 1.65 (tt, $J$ = 8.2 & 6.1 Hz, 64H, C$\underline{H}_2$), 1.41 (sext., $J$ = 7.3 Hz, 64H, C$\underline{H}_2$), 0.99 (t, $J$ = 7.3 Hz, 96H, C$\underline{H}_3$). **$^{11}$B NMR** (128 MHz, $CD_3CN$) $\delta$ 1.98 (br s). **ATR-IR** (neat, cm$^{-1}$): 2960, 2873, 1484, 1381, 1000, 949, 889, 852, 782, 524, 381, 330, 307. Lab book reference: NNT107

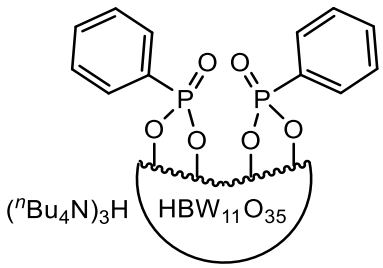
**$K_3H[HBW_{11}O_{39}(POC_6H_5)_2]$ / {K•PPhBW$_{11}$}**




To a stirring solution of phenylphosphonic acid (24 mg, 0.15 mmol, 2.0 eq.) in MeCN (3.9 mL), $K_8[HBW_{11}O_{39}]•13H_2O$ (250 mg, 0.078 mmol, 1.0 eq.) was added followed by dropwise addition of 4 M HCl (150 µL, 6.0 mmol, 40.0 eq.). The resulting mixture was heated at reflux for 16 h before cooling to room temperature and subjected to centrifugation (8000 rpm, 5 min) to remove any remaining precipitate. The solution was then diluted with $Et_2O$ (45 mL) to give an off-white suspension, centrifugation (8000 rpm, 5 min) and decantation gave a yellow precipitate which was dried under vacuum before dissolution in minimum MeCN (2 mL). Centrifugation (6000 rpm, 2 min), decantation and a final trituration ($Et_2O$, 40 mL), centrifugation, decantation, and vacuum drying sequence yielded a crude pale-yellow solid. Further purification was achieved via vapour diffusion crystallisation with *tert*-butyl methyl ether (antisolvent) and nitromethane to yield the title compound as a pale-yellow crystalline solid (130 mg, 0.043 mmol, 55%).

**$^1$H NMR** (500 MHz, $CD_3CN$) $\delta$ 8.14 – 8.08 (m, 4H, ArC<u>H</u>), 7.66 – 7.62 (m, 2H, ArC<u>H</u>), 7.59 – 7.55 (m, 4H, ArC<u>H</u>), 4.53 (s, 1H, BO<u>H</u>). **$^{13}$C NMR** (126 MHz, $CD_3CN$) $\delta$ 132.2 (d, $J^{C-P}$ = 3.2 Hz, 2 × Ar<u>C</u>), 132.9 (d, $J^{C-P}$ = 11.2 Hz, 4 × Ar<u>C</u>H), 129.2 (d, $J^{C-P}$ = 16.0 Hz, 4 × Ar<u>C</u>H), 129.1 (d, $J^{C-P}$ = 194.2 Hz, 2 × Ar<u>C</u>P). **$^{11}$B NMR** (128 MHz, $CD_3CN$) $\delta$ 1.93 (br s). **$^{31}$P NMR** (202 MHz, $CD_3CN$) $\delta$ 20.38 (tt, $J^{H-P}$ = 14.2, 4.5 Hz, 2 × Ph-<u>P</u>(O)). **ATR-IR** (neat, $cm^{-1}$): 3603, 1619, 1439, 1138, 1054, 971, 896, 826, 567. **Elemental Analysis** calc (%) for $K_3H[HBW_{11}O_{39}][P_2O_2(C_6H_5)_2]$ (3024.49): Calc: C, 4.77 ; H, 0.40; N, 0. Found: C, 4.36; H, 0.54; N, 0.63. Lab book reference: NNT109c.

**$(Bu_4N)_3H[HBW_{11}O_{39}(POC_6H_5)_2]$ / {PPhBW$_{11}$}**

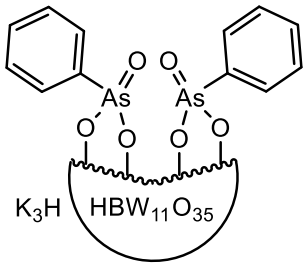



An oven-dried flask equipped with a stirrer bar was charged with $K_8[HBW_{11}O_{39}]\bullet 13H_2O$ (250 mg, 0.078 mmol, 1.0 eq.), $^n$Bu$_4$NBr (150 mg, 0.47 mmol, 6.0 eq.) and placed under an argon environment. Anhydrous MeCN (1 mL) was added followed by a dropwise addition of phenylphosphonic dichloride (44 µL, 0.31 mmol, 4.0 eq.) with stirring. The resulting mixture was stirred for 24 h at reflux. The reaction mixture was then cooled to room temperature and subjected to centrifugation (8000 rpm, 5 min) to remove the remaining solid. The separated solution was then diluted with EtOH (150 mL) to give a white suspension, centrifugation (8000 rpm, 5 min) and decantation gave a fine white precipitate which was dried under vacuum before dissolution in minimum MeCN (2 mL). Centrifugation (8000 rpm, 5 min), decantation and a final trituration, centrifugation, decantation, and vacuum drying sequence with $Et_2O$ (40 mL) gave the title compound as an off-white solid (228 mg, 0.063 mmol, 80%).

**$^1$H NMR** (400 MHz, $CD_3CN$) $\delta$ 8.15 – 8.05 (m, 4H, ArC<u>H</u>), 7.68 – 7.60 (m, 2H, ArC<u>H</u>), 7.60 – 7.52 (m, 4H, ArC<u>H</u>), 4.53 (s, 1H, BO<u>H</u>), 3.18 – 3.05 (m, 24H, C<u>H</u>$_2$), 1.62 (tt, $J$ = 8.3 & 6.1 Hz, 24H, C<u>H</u>$_2$), 1.38 (sext., $J$ = 7.4 Hz, 24H, C<u>H</u>$_2$), 0.98 (t, $J$ = 7.3 Hz, 36H, C<u>H</u>$_3$). **$^{13}$C NMR** (101 MHz, $CD_3CN$) $\delta$ 132.2 (2 x ArC<u>H</u>), 131.9 (d, $J$ = 11.0 Hz, 4 x ArC<u>H</u>), 129.1 (2 x <u>C</u>), 128.2 (d, $J$ = 16.0 Hz, 4 x ArC<u>H</u>), 58.4 (3 x C<u>H</u>$_2$), 23.4 (3 x C<u>H</u>$_2$), 19.4 (t, $J$ = 1.6 Hz, 3 x C<u>H</u>$_2$), 12.9 (3 x C<u>H</u>$_3$). **$^{11}$B NMR** (128 MHz, $CD_3CN$) $\delta$ 2.21 (br s). **$^{31}$P NMR** (162 MHz, $CD_3CN$) $\delta$ 20.33 (tt, $J_{HP}$ = 14.2 & 4.5 Hz, 2 x Ph<u>P</u>(O)). **ATR-IR** (neat, cm$^{-1}$): 2960, 2934, 2873, 1483, 1380, 1141, 1061, 1006, 958, 892, 825, 777, 647, 527. **Elemental Analysis** calc (%) for

$[C_{16}H_{36}N]_3H[HBW_{11}O_{39}][P_2O_2(C_6H_5)_2]$ (3634.58): Calc: C, 19.83; H, 3.33; N, 1.16. Found: C, 20.10; H, 3.40; N, 1.07. Lab book reference: NNT109cTBA

**$K_3H[HBW_{11}O_{39}(AsOC_6H_5)_2]$ / {K•AsPhBW$_{11}$}**




To a stirring mixture of $K_8[HBW_{11}O_{39}]•13H_2O$ (500 mg, 0.16 mmol, 1.0 eq.) and phenyl arsonic acid (63 mg, 0.30 mmol, 2.0 eq.) in MeCN (7.8 mL), 4 M HCl (150 µL, 6.0 mmol, 40.0 eq.) was added dropwise before heating at reflux for 16 h. The white mixture was then cooled to room temperature and subjected to centrifugation (8000 rpm, 5 min) to remove any remaining precipitate before trituration with $Et_2O$ (45 mL), centrifugation (8000 rpm, 5 min) and decantation to give a crude white powder. Dissolution in minimum MeCN (2 mL) followed by centrifugation (6000 rpm, 2 min), decantation and a final trituration ($Et_2O$, 40 mL), centrifugation, decantation, and vacuum drying sequence yielded the title compound as a white solid (290 mg, 0.093 mmol, 58%).

**$^1$H NMR** (400 MHz, $CD_3CN$) $\delta$ 8.21 – 8.18 (m, 4H, ArC<u>H</u>), 7.81 – 7.7 (m, 2H, ArC<u>H</u>), 7.74 – 7.70 (m, 4H, ArC<u>H</u>), 4.90 (s, 1H, BO<u>H</u>). **$^{13}$C NMR** (101 MHz, $CD_3CN$) $\delta$ 135.1 (2 × Ar<u>C</u>H), 132.4 (4 × Ar<u>C</u>H), 130.8 (4 × Ar<u>C</u>H), 130.1 (2 × Ar<u>C</u>). **$^{11}$B NMR** (128 MHz, $CD_3CN$) $\delta$ 2.13 (br s). **ATR-IR** (neat, $cm^{-1}$): 3505, 2255, 1612, 1441, 1404, 1368, 1218, 1085, 1015, 968, 898, 783, 524, 466. **Elemental Analysis** calc (%) for $K_3H[HBW_{11}O_{39}][As_2O_2(C_6H_5)_2]$ (3112.39): Calc: C, 4.63; H, 0.39; N, 0. Found: C, 5.83; H, 0.88; N, 0.51. Lab book reference: NNT110b.

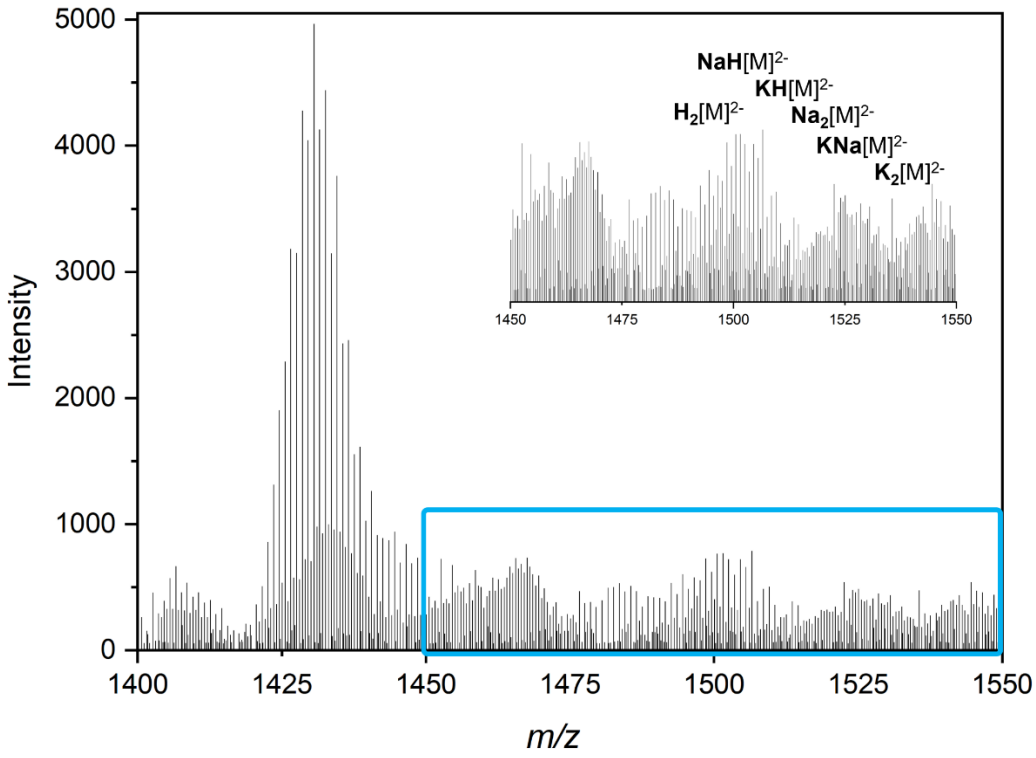
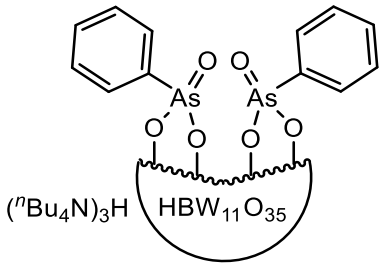



**Figure 69.** Negative mode ESI-MS spectrum of compound {**K•AsPhBW$_{11}$**} in the *m/z* range 1400-1550.

**Table 15.** Mass spectra (ESI) of {**K•AsPhBW$_{11}$**}.

| Assignment | *z* | *m/z* (calc.) | *m/z* (obs.) |
|---|---|---|---|
| {$H_2[HBW_{11}O_{39}(AsOC_6H_5)_2]$} | 2- | 1497.60 | 1497.58 |
| {$NaH[HBW_{11}O_{39}(AsOC_6H_5)_2]$} | 2- | 1508.59 | 1508.58 |
| {$KH[HBW_{11}O_{39}(AsOC_6H_5)_2]$} | 2- | 1516.58 | 1516.56 |
| {$Na_2[HBW_{11}O_{39}(AsOC_6H_5)_2]$} | 2- | 1519.59 | 1519.61 |
| {$KNa[HBW_{11}O_{39}(AsOC_6H_5)_2]$} | 2- | 1527.57 | 1527.58 |
| {$K_2[HBW_{11}O_{39}(AsOC_6H_5)_2]$} | 2- | 1536.06 | 1536.08 |

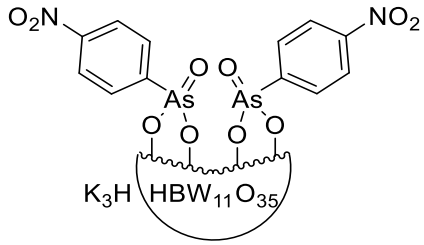
**($^n$Bu$_4$N)$_3$H[HBW$_{11}$O$_{39}$(AsOC$_6$H$_5$)$_2$] / {AsPhBW$_{11}$}**




A solution of $^n$Bu$_4$NBr (58 mg, 0.18 mmol, 6.0 eq.) in MeCN (2 mL) was added in one portion to a stirring solution of K$_3$H[HBW$_{11}$O$_{39}$(AsOPh)$_2$] (100 mg, 0.032 mmol, 1.0 eq.) in MeCN (5 mL) and the resulting mixture was stirred for 1 h at room temperature. Centrifugation (8000 rpm, 5 min) of the resulting suspension, decantation, and concentration *in vacuo* gave the crude alkyl ammonium salt as a white solid. The solid was redissolved in a minimum MeCN (~5 mL), aided by sonication, followed by centrifugation (8000 rpm, 5 min) and decantation to remove any remaining fine precipitate. Trituration with Et$_2$O (40 mL) resulted in a white suspension which was subjected to centrifugation (8000 rpm, 5 min), decantation, and vacuum drying of the resulting white powder. Dissolution in minimum MeCN (2 mL) followed by centrifugation (6000 rpm, 2 min), decantation and a final trituration (Et$_2$O, 40 mL), centrifugation, decantation, and vacuum drying sequence gave the title compound as a white solid (90.4 mg, 0.024 mmol, 75%).

**$^1$H NMR** (400 MHz, CD$_3$CN) $\delta$ 8.20 – 8.18 (m, 4H, ArC<u>H</u>), 7.81 – 7.77 (m, 2H, ArC<u>H</u>), 7.74 – 7.70 (m, 4H, ArC<u>H</u>), 4.91 (s, 1H, BO<u>H</u>), 3.12 – 3.08 (m, 24H, C<u>H</u>$_2$), 1.61 (ddd, *J* = 16.2, 9.0, 6.1 Hz, 24H C<u>H</u>$_2$), 1.37 (sext., *J* = 7.4 Hz, 24H, C<u>H</u>$_2$), 0.97 (t, *J* = 7.3 Hz, 36H, C<u>H</u>$_3$). **$^{13}$C NMR** (101 MHz, CD$_3$CN) $\delta$ 135.1 (2 × Ar<u>C</u>H), 132.4 (4 × Ar<u>C</u>H), 130.7 (4 × Ar<u>C</u>H), 130.1 (2 × Ar<u>C</u>), 59.3 (d, *J* = 2.9 Hz, 12 × <u>C</u>H$_2$), 24.3 (12 × <u>C</u>H$_2$), 20.3 (12 × <u>C</u>H$_2$), 13.8 (12 × <u>C</u>H$_3$). **$^{11}$B NMR** (128 MHz, CD$_3$CN) $\delta$ 2.13 (br s). **ATR-IR** (neat, cm$^{-1}$): 3549, 2960, 2873, 1615, 1483, 1380, 1219, 1089, 1010, 965, 900, 791, 738, 714, 687, 527, 429. **Elemental Analysis** calc (%) for [C$_{16}$H$_{36}$N]$_3$H[HBW$_{11}$O$_{39}$][AsOPh]$_2$[C$_4$H$_{10}$O] (3796.62): C, 20.25, H, 3.45, N, 1.11. Found: C, 20.18, H, 3.44, N, 0.81. Lab book reference: NNT110bTBA

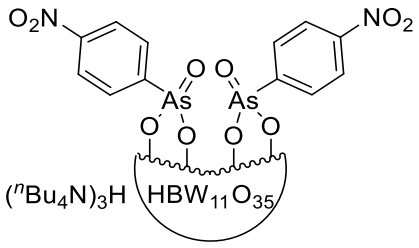
**$K_3H[HBW_{11}O_{39}(AsOC_6H_4NO_2)_2]$ / {K•AsPhNO$_2$BW$_{11}$}**




To a suspension of $K_8[HBW_{11}O_{39}]•13H_2O$ (250 mg, 0.078 mmol, 1.0 eq.) in MeCN (3.9 mL) stirred at room temperature, *p*-nitarsone (77 mg, 0.311 mmol, 4.1 eq.) was added. After 10 min, 4 M HCl (75 µL) was added dropwise, and the mixture was left for 24 h at reflux. The reaction mixture was allowed to cool to room temperature and the insoluble white solid was removed by centrifugation at 8000 rpm for 3 min. The solution concentrated *in vacuo.* The solid was redissolved in the minimum amount of MeCN, syringe filtered and precipitated by the addition of $Et_2O$. The sample was sedimented by spinning at 8000 rpm in a centrifuge for 3 min, the supernatant discarded, and the solid was suspended in of $Et_2O$ using ultrasound. This was repeated with acetone and ether. The solvent was removed *in vacuo* to give the title compound as a pale-orange powder (153.3 mg, 0.047 mmol, 60%).

**$^1$H NMR** (400 MHz, $CD_3CN$) $\delta$ 8.56 – 8.32 (m, 8H, ArC<u>H</u>), 4.89 (s, 1H, BO<u>H</u>). **$^{11}$B NMR** (128 MHz, $CD_3CN$) $\delta$ 2.20 (br s). **$^{13}$C NMR** (101 MHz, $CD_3CN$) $\delta$ 152.3 (2 x Ar<u>C</u>H), 136.5 (2 x <u>C</u>), 134.0 (4 x Ar<u>C</u>H), 125.5 (4 x Ar<u>C</u>H). Lab book reference: NNT111

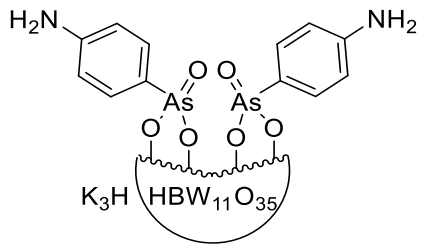
**($^n$Bu$_4$N)$_3$H[HBW$_{11}$O$_{39}$(AsOC$_6$H$_4$NO$_2$)] / {AsPhNO$_2$BW$_{11}$}**




To a solution of $K_3H[HBW_{11}O_{39}][AsOC_6H_4NO_2]_2$ (60 mg, 0.018 mmol, 1.0 eq.) in MeCN (5 mL) was added $^n$Bu$_4$NBr (58 mg, 0.18 mmol, 10.0 eq.) in MeCN (5 mL). The reaction mixture was stirred for 1h. The solid impurities were removed by centrifugation at 8000 rpm for 3 min. The solution concentrated *in vacuo.* The solid was redissolved in the minimum amount of MeCN, syringe filtered and precipitated by the addition of $Et_2O$. The sample was sedimented by spinning at 8000 rpm in a centrifuge for 3 min, the supernatant discarded, and the solid was suspended in of $Et_2O$ using ultrasound. This was repeated with acetone and ether. The solvent was removed *in vacuo* to give the title compound as a pale-yellow powder (38 mg, 0.01 mmol, 55%).

**$^1$H NMR** (400 MHz, $CD_3CN$) $\delta$ 8.57 – 8.45 (m, 8H, ArC<u>H</u>), 4.92 (s, 1H, BO<u>H</u>), 3.17 – 3.08 (m, 24H, C<u>H</u>$_2$), 1.64 (ddd, $J$ = 15.5 & 9.9 & 6.3 Hz, 24H, C<u>H</u>$_2$), 1.39 (sext., $J$ = 7.4 Hz, 24H, C<u>H</u>$_2$), 1.00 (t, $J$ = 7.3 Hz, 36H, C<u>H</u>$_3$). **$^{11}$B NMR** (128 MHz, $CD_3CN$) $\delta$ 2.11 (br s). **$^{13}$C NMR** (101 MHz, $CD_3CN$) $\delta$ 152.3 (2 x Ar<u>C</u>H), 136.5 (2 x <u>C</u>), 134.0 (4 x Ar<u>C</u>H), 125.5 (4 x Ar<u>C</u>H), 59.3 (3 x <u>C</u>H$_2$), 24.3 (3 x <u>C</u>H$_2$), 20.3 (3 x <u>C</u>H$_2$), 13.8 (3 x <u>C</u>H$_3$). **ATR-IR** (neat, cm$^{-1}$): 2961, 2873, 1602, 1526, 1463, 1348, 1285, 1219, 1152, 1013, 967, 906, 838, 795, 527, 426. **Elemental Analysis** calc (%) for $[C_{16}H_{36}N]_3H[HBW_{11}O_{39}(AsOC_6H_4NO_2)_2]$ (3812.47): Calc: C, 18.90; H, 3.12; N, 1.84. Found: C, 21.96; H, 3.48; N, 2.01. Lab book reference: NNT111TBA

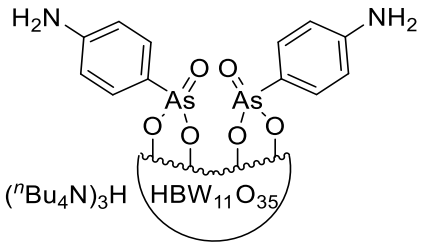
**$K_3H[HBW_{11}O_{39}(AsOC_6H_4NH_2)_2]$ / {K•AsPhNO$_2$BW$_{11}$}**




To a suspension of $K_8[HBW_{11}O_{39}]•13H_2O$ (500 mg, 0.156 mmol, 1.0 eq.) in MeCN (7.8 mL) stirred at room temperature, *p*-arsinilic (54 mg, 0.250 mmol, 2.3 eq.) was added. After 10 min, 4 M HCl (150 µL) was added dropwise, and the mixture was left for 24 h at reflux. The reaction mixture was allowed to cool to room temperature and the insoluble white solid was removed by centrifugation at 8000 rpm for 3 min. The solution concentrated *in vacuo.* The solid was redissolved in the minimum amount of MeCN, syringe filtered and precipitated by the addition of $Et_2O$. The sample was sedimented by spinning at 8000 rpm in a centrifuge for 3 min, the supernatant discarded, and the solid was suspended in of $Et_2O$ using ultrasound. This was repeated with acetone and ether. The solvent was removed *in vacuo* to give the title compound as a pale-red powder (300 mg, 0.093 mmol, 60%).

**$^1$H NMR** (400 MHz, $CD_3CN$) $\delta$ 8.03 – 7.59 (d, 4H, ArC<u>H</u>), 6.87 (d, $J$ = 8.7 Hz, 4H, ArC<u>H</u>), 4.95 (s, 1H, BO<u>H</u>). **$^{11}$B NMR** (128 MHz, $CD_3CN$) $\delta$ 2.13 (br s). Lab book reference: NNT114

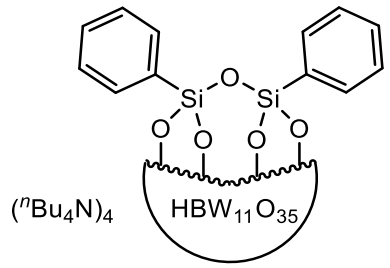
**($^n$Bu$_4$N)$_3$H[HBW$_{11}$O$_{39}$(AsOC$_6$H$_4$NH$_2$)$_2$] / {AsPhNH$_2$BW$_{11}$}**




To a solution of $K_3H[HBW_{11}O_{39}][AsOC_6H_4NH_2]_2$ (100 mg, 0.031 mmol, 1.0 eq.) in MeCN (2 mL) was added $^n$Bu$_4$NBr (60 mg, 0.186 mmol, 10.0 eq.) in MeCN (2 mL). The reaction mixture was stirred for 1h. The solid impurities were removed by centrifugation at 8000 rpm for 3 min. The solution concentrated *in vacuo.* The solid was redissolved in the minimum amount of MeCN, syringe filtered and precipitated by the addition of $Et_2O$. The sample was sedimented by spinning at 8000 rpm in a centrifuge for 3 min, the supernatant discarded, and the solid was suspended in of $Et_2O$ using ultrasound. This was repeated with acetone and ether. The solvent was removed *in vacuo* to give the title compound as a pale-red solid (89 mg, 0.02 mmol, 77%).

**$^1$H NMR** (400 MHz, $CD_3CN$) $\delta$ 7.83 (d, $J$ = 8.7 Hz, 4H, ArC<u>H</u>), 6.90 – 6.76 (m, 4H, ArC<u>H</u>), 4.93 (s, 1H, BO<u>H</u>), 3.16 – 3.07 (m, 24H, C<u>H</u>$_2$), 1.68 – 1.56 (m, 24H, C<u>H</u>$_2$), 1.37 (sext., $J$ = 7.4 Hz, 24H,C<u>H</u>$_2$), 0.97 (t, $J$ = 7.3 Hz, 36H,C<u>H</u>$_3$). **$^{13}$C NMR** (126 MHz, $CD_3CN$) $\delta$ 154.3(2 x Ar<u>C</u>H), 133.9 (4 x Ar<u>C</u>H), 115.3 (4 x Ar<u>C</u>H), 114.7 (2 x <u>C</u>), 59.37 (3 x <u>C</u>H$_2$), 24.3 (3 x <u>C</u>H$_2$), 20.3 (3 x <u>C</u>H$_2$), 13.7 (3 x <u>C</u>H$_3$). **$^{11}$B NMR** (128 MHz, $CD_3CN$) $\delta$ 2.12 (br s). **ATR-IR** (neat, cm$^{-1}$): 3366, 2963, 1624, 1592, 1503, 1463, 1223, 1186, 1084, 1013, 967, 909, 795, 653, 529, 512, 430. **Elemental Analysis** calc (%) for $[C_{16}H_{36}N]_3H[HBW_{11}O_{39}(AsOC_6H_4NH_2)_2]$ (3752.51): Calc: C, 19.20; H, 3.28; N, 1.87. Found: C, 19.67; H, 3.40; N, 1.61. Lab book reference: NNT114TBA

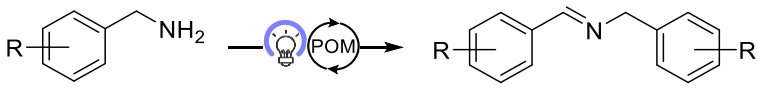
**($^n$Bu$_4$N)$_4$[HBW$_{11}$O$_{39}$(SiC$_6$H$_5$)$_2$O] / {SiPhBW$_{11}$}**




To a stirred solution of $K_8[HBW_{11}O_{39}]\bullet 13H_2O$ (250 mg, 0.078 mmol, 1.0 eq.) in MeCN:$H_2O$ (2:1, 7.5 mL), trimethoxyphenylsilane (44 µL, 0.23 mmol, 3.0 eq.) was added followed by the dropwise addition of 4M HCl (78 µL, 0.32 mmol, 4.0 eq.). The mixture was stirred at room temperature for 6 h before centrifugation (8000 rpm, 5 min) to remove the remaining solid. $^n$Bu$_4$NBr (154.7 mg, 0.48 mmol, 6.0 eq.) in water (3 mL) was added to the resultant solution in one portion to give a white suspension. The suspension was centrifuged (8000 rpm, 5 min) and the solvent decanted off. The remaining white solid was redissolved in a minimum MeCN (2 mL), aided by sonication, before centrifugation (6000 rpm, 2 min) and decantation to remove any remaining fine precipitate. Trituration with $Et_2O$ (40 mL) resulted in a white suspension which was subjected to centrifugation, decantation, and vacuum drying to give the title compound as a white solid (173.4 mg, 0.045 mmol, 58%).

**$^1$H NMR** (400 MHz, $CD_3CN$) δ 7.90 – 7.87 (m, 4H, ArC<u>H</u>), 7.49 – 7.43 (m, 6H, ArC<u>H</u>), 4.85 (s, 1H, BO<u>H</u>), 3.16 – 3.11 (m, 32H, C<u>H</u>$_2$), 1.67 – 1.59 (m, 32H, C<u>H</u>$_2$), 1.39 (sext., *J* = 7.4 Hz, 32H, C<u>H</u>$_2$), 0.98 (t, *J* = 7.3 Hz, 48H, C<u>H</u>$_3$). **$^{13}$C NMR** (101 MHz, $CD_3CN$) *δ* 134.6 (2 x Ar<u>C</u>H), 132.6 (2 x Ar<u>C</u>), 130.5 (4 x Ar<u>C</u>H), 128.0 (4 x Ar<u>C</u>H), 58.3 (t, *J* = 2.6 Hz, 16 × <u>C</u>H$_2$), 23.4 (16 × <u>C</u>H$_2$), 20.3 (16 × <u>C</u>H$_2$), 13.9 (16 × <u>C</u>H$_3$). **$^{11}$B NMR** (128 MHz, $CD_3CN$) *δ* 2.08 (br s). **ATR-IR** (neat, cm$^{-1}$): 2961, 2874,1483, 1381, 1239, 1132, 1038, 1005, 946, 878, 822, 767, 713, 594, 559, 530. **Elemental Analysis** calc (%) for $[C_{16}H_{36}N]_4[HBW_{11}O_{39}][Si_2O(Ph)_2]$ (3854.28): C, 23.68, H, 4.05, N, 1.45. Found: C, 23.23, H, 4.00, N, 1.23. Lab book reference: NNT113.

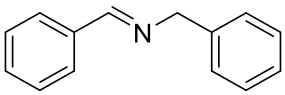
**Photocatalysis – Substrate Scope**




**Optimised reaction conditions (General procedure A)**: To an oven-dried microwave vial fitted with a magnetic stirrer, hybrid POM **2** (2 mol%) was added followed by MeCN[†] (0.5 mL) and amine (0.2 mmol). The vial was sealed with a septum-lined cap, sparged with oxygen for 1 min and then stirred while irradiated at 370 nm for 24 h. The resulting mixture was concentrated *in vacuo,* 1,3-benzodioxole:$CDCl_3$ stock solution (0.7 mL, 0.14 M) added, and the resulting suspension was subjected to centrifugation (6000 rpm, 2 min) to remove any fine precipitate. The resultant solution was analysed by NMR spectroscopy.

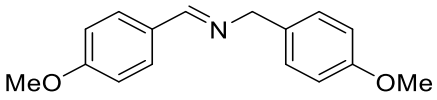
[†] Solvent undried and obtained from commercial vendors used without further purification.

***N*-Benzylidenebenzylamine (2)**



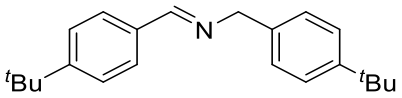
According to general procedure **A**, phenylmethanamine (22 µL, 0.2 mmol) and {**PPhBW$_{11}$**} (8.23 mg, 2 mol%) were found to produce the title compound (**2**, 57%) as determined by NMR yield. **$^1$H NMR** (400 MHz, $CDCl_3$) $\delta$ 8.41 (d, *J* = 1.5 Hz, 1H, C<u>H</u>), 7.85 – 7.76 (m, 2H, ArC<u>H</u>), 7.43 (dd, *J* = 5.2 & 1.9 Hz, 3H, ArC<u>H</u>), 7.36 (d, *J* = 4.4 Hz, 4H, ArC<u>H</u>), 7.29 (dd, *J* = 4.8 & 3.9 Hz, 1H, ArC<u>H</u>), 4.85 (d, *J* = 1.5 Hz, 2H, C<u>H$_2$</u>). **HRMS** (ESI) Calc. for $C_{14}H_{13}N^+$ $[M+H]^+$: 196.1121, found: 196.1116. The spectral data were in accordance with those reported in literature.[187]

***N*-(4-methoxybenzyl)-1-(4-methoxyphenyl)methanimine (7a)**



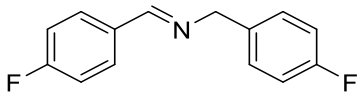

According to general procedure **A**, (4-methoxyphenyl)methanamine (26 µL, 0.2 mmol) and {**PPhBW$_{11}$**} (8.23 mg, 2 mol%) were found to produce the title compound (**7a,** 46%) as determined by NMR yield. **$^1$H NMR** (400 MHz, $CDCl_3$) $\delta$ 8.29 (d, *J* = 1.5 Hz, 1H, C<u>H</u>), 7.70 (d, *J* = 8.8 Hz, 2H, ArC<u>H</u>), 7.24 (d, *J* = 8.6 Hz, 2H, ArC<u>H</u>), 6.89 (dd, *J* = 17.3 & 8.6 Hz, 2H, ArC<u>H</u>), 4.71 (d, *J* = 1.3 Hz, 2H, C<u>H$_2$</u>), 3.82 (s, 3H, C<u>H$_3$</u>), 3.78 (s, 3H, C<u>H$_3$</u>). **HRMS** (ESI) Calc. for $C_{16}H_{17}NO_2^+$ $[M+H]^+$: 256.1332; found: 256.1334. The spectral data were in accordance with those reported in literature.[187]

***N*-(4-(tert-butyl)benzyl)-1-(4-(tert-butyl)phenyl)methanimine (8a)**



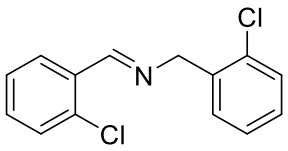

According to general procedure **A**, (4-(tert-butyl)phenyl)methanamine (35 µL, 0.2 mmol) and {**PPhBW$_{11}$**} (8.23 mg, 2 mol%) were found to produce the title compound (**8a**, 44%) as determined by NMR yield. **$^{1}$H NMR** (400 MHz, $CDCl_3$) $\delta$ 8.41 (s, 1H, C<u>H</u>), 7.76 (d, *J* = 8.4 Hz, 2H, ArC<u>H</u>), 7.57 – 7.43 (m, 2H, ArC<u>H</u>), 7.40 (d, *J* = 8.4 Hz, 2H, ArC<u>H</u>), 7.34 – 7.25 (m, 2H, ArC<u>H</u>), 4.83 (d, *J* = 1.3 Hz, 2H, C<u>H$_2$</u>), 1.37 (s, 9H, C<u>H$_3$</u>), 1.35 (s, 9H, C<u>H$_3$</u>). **HRMS** (ESI) Calc. for $C_{22}H_{29}N^+$ $[M+H]^+$: 308.2373, found: 308.2369. The spectral data were in accordance with those reported in literature.[188]

***N*-(4-fluorobenzyl)-1-(4-fluorophenyl)methanimine (9a)**



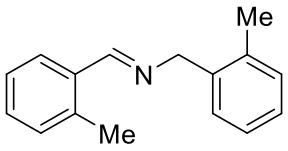

According to general procedure **A**, (4-fluorophenyl)methanamine (25 µL, 0.2 mmol) and {**PPhBW$_{11}$**} (8.23 mg, 2 mol%) were found to produce the title compound (**9a**, 50%) as determined by NMR yield. **$^{1}$H NMR** (400 MHz, $CDCl_3$) $\delta$ 8.34 (d, *J* = 1.5 Hz, 1H, C<u>H</u>), 7.82 – 7.73 (m, 2H, ArC<u>H</u>), 7.30 (dd, *J* = 8.3 & 5.7 Hz, 2H, ArC<u>H</u>), 7.10 (t, *J* = 8.6 Hz, 2H, ArC<u>H</u>), 7.06 – 7.00 (m, 2H, ArC<u>H</u>), 4.77 (s, 2H, C<u>H$_2$</u>). **$^{19}$F-NMR** (376 MHz, $CDCl_3$) $\delta$ -109.16, -115.94. **HRMS** (ESI) Calc. for $C_{14}H_{12}F_2N^+$ $[M+H]^+$: 232.0932; found: 232.0932. The spectral data were in accordance with those reported in literature.[189]

***N*-(2-chlorobenzyl)-1-(2-chlorophenyl)methanimine (10a)**



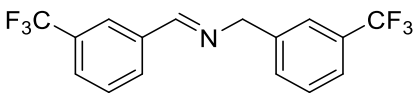

According to general procedure **A**, (2-chlorophenyl)methanamine (24 µL, 0.2 mmol) and {**PPhBW$_{11}$**} (8.23 mg, 2 mol%) were found to produce the title compound (**10a**, 44%) as determined by NMR yield. **$^1$H NMR** (400 MHz, $CDCl_3$) $\delta$ 8.88 (s, 1H, C<u>H</u>), 8.13 (dd, *J* = 7.7 & 1.8 Hz, 1H, ArC<u>H</u>), 7.40 (tdd, *J* = 11.2 & 7.3, 3.8 Hz, 5H, ArC<u>H</u>), 7.35 – 7.28 (m, 2H, ArC<u>H</u>), 4.95 (s, 2H, C<u>H</u>$_2$). **HRMS** (ESI) Calc. for $C_{14}H_{11}Cl_2N^+$ $[M+H]^+$: 254.0341; found: 264.0335. The spectral data were in accordance with those reported in literature.[187]

***N*-(2-methylbenzyl)-1-(o-tolyl)methanimine (11a)**



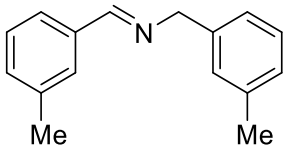

According to general procedure **A**, *N*-Methyl-1-(o-tolyl)methanamine (24 µL, 0.2 mmol) and {**PPhBW$_{11}$**} (8.23 mg, 2 mol%) were found to produce the title compound (**11a**, 50%) as determined by NMR yield. **$^1$H NMR** (400 MHz, $CDCl_3$) $\delta$ 8.68 (d, *J* = 1.6 Hz, 1H, C<u>H</u>), 7.35 – 7.13 (m, 8H, ArC<u>H</u>), 4.85 (d, *J* = 1.5 Hz, 2H, C<u>H</u>$_2$), 2.52 (s, 3H, C<u>H</u>$_3$), 2.41 (s, 3H, C<u>H</u>$_3$). **HRMS** (ESI) Calc. for $C_{16}H_{17}N^+$ $[M+H]^+$: 224.1434; found: 224.1437. The spectral data were in accordance with those reported in literature.[187]

***N*-(3-(trifluoromethyl)benzyl)-1-(3-(trifluoromethyl)phenyl)methanimine (12a)**



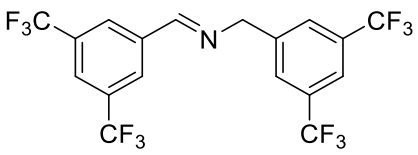

According to general procedure **A**, (3-(trifluoromethyl)phenyl)methanamine (35 µL, 0.2 mmol) and {**PPhBW$_{11}$**} (8.23 mg, 2 mol%) were found to produce the title compound (**12a**, 50%) as determined by NMR yield. **$^{1}$H NMR** (400 MHz, $CDCl_3$) *δ* 8.46 (d, *J* = 1.5 Hz, 1H, C<u>H</u>), 8.07 (s, 1H, ArC<u>H</u>), 7.98 (d, *J* = 7.7 Hz, 1H, ArC<u>H</u>), 7.72 (s, 1H, ArC<u>H</u>), 7.62 (s, 1H, ArC<u>H</u>), 7.56 (dd, *J* = 9.8 & 6.0 Hz, 3H, ArC<u>H</u>), 7.52 – 7.44 (m, 1H, ArC<u>H</u>), 4.89 (d, *J* = 1.4 Hz, 2H, C<u>H</u>$_2$). **$^{19}$F NMR** (376 MHz, $CDCl_3$) δ -62.56, -62.76. **HRMS** (ESI) Calc. for $C_{16}H_{11}F_6N^+$ $[M+H]^+$: 322.0868; found: 322.0865. The spectral data were in accordance with those reported in literature.[190]

***N*-(3-methylbenzyl)-1-(m-tolyl)methanimine (13a)**



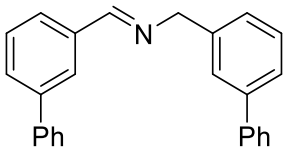

According to general procedure **A**, 3-methylbenzylamine (24 µL, 0.2 mmol) and {**PPhBW$_{11}$**} (8.23 mg, 2 mol%) were found to produce the title compound (**13a**, 62%) as determined by NMR yield. **$^{1}$H NMR** (400 MHz, $CDCl_3$) *δ* 8.39 (d, *J* = 1.4 Hz, 1H, C<u>H</u>), 7z.69 (s, 1H, ArC<u>H</u>), 7.58 (d, *J* = 7.5 Hz, 1H, ArC<u>H</u>), 7.34 (t, *J* = 7.6 Hz, 1H, ArC<u>H</u>), 7.31 – 7.24 (m, 2H, ArC<u>H</u>), 7.17 (d, *J* = 9.3 Hz, 2H, ArC<u>H</u>), 7.11 (d, *J* = 7.6 Hz, 1H, ArC<u>H</u>), 4.82 (s, 2H, C<u>H</u>$_2$), 2.42 (s, 3H, ArC<u>H</u>$_3$), 2.39 (s, 3H, ArC<u>H</u>$_3$). **HRMS** (ESI) Calc. for $C_{16}H_{17}N^+$ $[M+H]^+$: 224.1434; found 224.1433. The spectral data were in accordance with those reported in literature.[187]

***N*-(3,5-bis(trifluoromethyl)benzyl)-1-(3,5-bis(trifluoromethyl)phenyl)methanimine (14a)**



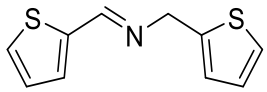

According to general procedure **A**, (3,5-bis(trifluoromethyl)phenyl) methanamine (35 µL, 0.2 mmol) and {**PPhBW$_{11}$**} (8.23 mg, 2 mol%) were found to produce the title compound (**14a**, 46%) as determined by NMR yield. **$^{1}$H NMR** (400 MHz, $CDCl_3$) $\delta$ 8.54 (d, *J* = 1.5 Hz, 1H, C<u>H</u>), 8.26 (d, *J* = 1.6 Hz, 2H, ArC<u>H</u>), 7.97 (s, 1H, ArC<u>H</u>), 7.83 (d, *J* = 4.2 Hz, 2H, ArC<u>H</u>), 7.74 (s, 1H, ArC<u>H</u>), 4.97 (s, 2H, C<u>H</u>$_2$). **$^{19}$F NMR** (376 MHz, $CDCl_3$) $\delta$ -62.88, -63.03. **HRMS** (ESI) Calc. for $C_{18}H_9F_{12}N^+$ $[M+H]^+$: 408.0616; found: 468.0615. The spectral data were in accordance with those reported in literature.[187]

**(*E*)-1-([1,1'-biphenyl]-3-yl)-N-([1,1'-biphenyl]-3-ylmethyl)methanimine (15a)**



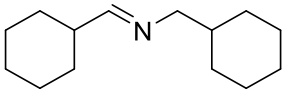

According to general procedure **A**, 3-phenylbenzylamine (37 µL, 0.2 mmol) and {**PPhBW$_{11}$**} (8.23 mg, 2 mol%) were found to produce the title compound (**15a**, 50%) as determined by NMR yield. **$^{1}$H NMR** (400 MHz, $CDCl_3$) $\delta$ 8.54 (d, *J* = 1.5 Hz, 1H, C<u>H</u>), 8.09 (t, *J* = 1.8 Hz, 1H, ArC<u>H</u>), 7.82 (dt, *J* = 7.7 & 1.4 Hz, 1H, ArC<u>H</u>), 7.77 – 7.32 (m, 16H), 4.96 (s, 2H, C<u>H</u>$_2$). **HRMS** (ESI) Calc. for $C_{26}H_{21}N^+$ $[M+H]^+$: 348.1714; found: 348.1752.

**1-(thiophen-2-yl)-*N*-(thiophen-2-ylmethyl)methanimine (16a)**



According to general procedure **A**, thiophen-2-ylmethanamine (23 µL, 0.2 mmol) and {**PPhBW$_{11}$**} (8.23 mg, 2 mol%) were found to the title compound (**16a**, 58%) as determined by NMR yield. **$^1$H NMR** (400 MHz, $CDCl_3$) $\delta$ 8.42 (s, 1H, C<u>H</u>), 7.42 (d, *J* = 5.0 Hz, 1H, ArC<u>H</u>), 7.33 (d, *J* = 3.6 Hz, 1H, ArC<u>H</u>), 7.28 – 7.22 (m, 1H, ArC<u>H</u>), 7.08 (dd, *J* = 5.1 & 3.5 Hz, 1H, ArC<u>H</u>), 7.02 – 6.94 (m, 2H), 4.95 (s, 2H, C<u>H$_2$</u>). **HRMS** (ESI) Calc. for $C_{10}H_9NS_2^+$ $[M+H]^+$: 208.0249; found: 208.0243. The spectral data were in accordance with those reported in literature.[187]

**1-cyclohexyl-*N*-(cyclohexylmethyl)methanimine (17a)**



According to general procedure **A**, cyclohexylmethanamine (26 µL, 0.2 mmol) and {**PPhBW$_{11}$**} (8.23 mg, 2 mol%) were found to produce the title compound (**17a**, 8%) as determined by NMR yield. **$^1$H NMR** (400 MHz, $CDCl_3$) $\delta$ 7.41 (d, *J* = 5.3 Hz, 1H, C<u>H</u>), 3.18 (dd, *J* = 6.5 & 1.2 Hz, 2H, C<u>H$_2$</u>), 2.26 – 2.11 (m, 1H, C<u>H$_2$</u>), 1.82 – 1.54 (m, 12H, C<u>H$_2$</u>), 1.28 – 1.06 (m, 9H, C<u>H$_2$</u>), 0.94 – 0.78 (m, 2H, C<u>H$_2$</u>). **HRMS** (ESI) Calc. for $C_{14}H_{25}N^+$ $[M+H]^+$: 208.2060; found: 208.2060. The spectral data were in accordance with those reported in literature.[191]

# 10 References


1 J. J. Berzelius, *Ann Phys*, 1826, **82**, 369.
2 M. Stuckart and K. Y. Monakhov, *Chem. Sci.*, 2019, **10**, 4364.
3 L. C. W. Baker and D. C. Glick, *Chem. Rev.*, 1998, **98**, 3.
4 S. S. Wang and G. Y. Yang, *Chem. Rev.*, 2015, **115**, 4893.
5 J.-H. Kruse, M. Langer, I. Romanenko, I. Trentin, D. Hernández-Castillo, L. González, F. H. Schacher, C. Streb, J.-H. Kruse, I. Romanenko, F. H. Schacher, M. Langer, I. Trentin, C. Streb, D. Hernández-Castillo and L. González, *Adv. Funct. Mater.*, 2022, **32**, 2208428.
6 J. W. Jordan, J. M. Cameron, G. A. Lowe, G. A. Rance, K. L. Y. Fung, L. R. Johnson, D. A. Walsh, A. N. Khlobystov, G. N. Newton, *Angew. Chem.* **2022**, *134*, e202115619.
7 Y. Ji, L. Huang, J. Hu, C. Streb and Y.-F. Song, *Energy Environ. Sci.*, 2015, **8**, 776.
8 S. Herrmann, C. Ritchie and C. Streb, *Dalton Trans.*, 2015, **44**, 7092.
9 Q. Li, L. Zhang, J. Dai, H. Tang, Q. Li, H. Xue and H. Pang, *Chem. Eng. J.*, 2018, **351**, 441.
10 C. L. Peake, A. J. Kibler, G. N. Newton and D. A. Walsh, *ACS Appl. Energy Mater.*, 2021, **4**, 8765.
11 S. Zhang, R. Liu, C. Streb and G. Zhang, *Polyoxometalates*, 2023, **2**, 9140037.
12 J. T. Rhule, C. L. Hill, D. A. Judd and R. F. Schinazi, *Chem. Rev.*, 1998, **98**, 327.
13 A. Bijelic, M. Aureliano and A. Rompel, *Angew. Chem.*, 2019, **58**, 2980.
14 F. F. Martins, Á. Sánchez-González, J. Lanuza, H. N. Miras, X. Lopez, N. A. Bandeira and A. Gil, *Chem. Eur. J.*, 2021, **27**, 8977.
15 D. E. Katsoulis, *Chem. Rev.*, 1998, **98**, 359.
16 M. T. Pope and A. Müller, *Angew. Chem.*, 1991, **30**, 34.
17 C. L. Hill and C. M. Prosser-McCartha, *Coord. Chem. Rev.*, 1995, **143**, 407.
18 J. J. Walsh, A. M. Bond, R. J. Forster and T. E. Keyes, *Coord. Chem. Rev.*, 2016, **306**, 217.
19 F. Steffler, G. F. De Lima and H. A. Duarte, *J. Mol. Struct.*, 2020, **1213**, 128159.
20 López, L. Vilà-Nadal, Aparicio-Anglès and J. M. Poblet, *Phys. Procedia.*, 2010, **8**, 94.
21 D. Yang, M. Babucci, W. H. Casey and B. C. Gates, *ACS Cent. Sci.*, 2020, **6**, 1523.
22 W. X. Lipscomb, *Inorg. Chem.*, 1965, **4**, 132.
23 Q. Chen and J. Zubieta, *Coord. Chem. Rev.*, 1992, **114**, 107.
24 D.-L. L. Long, R. Tsunashima and L. Cronin, *Angew. Chem.*, 2010, **49**, 1736.

25 H. N. Miras, J. Yan, D. L. Long and L. Cronin, *Chem. Soc. Rev.*, 2012, **41**, 7403.
26 A. Misra, K. Kozma, C. Streb and M. Nyman, *Angew. Chem. Int. Ed.* **2020**, *59*, 596.
27 D. Li, Z. Liu, J. Song, H. Li, B. Zhang, P. Yin, Z. N. Zheng, J. E. Roberts, M. Tsige, C. L. Hill and T. Liu, *Angew. Chem.*, 2017, **56**, 3294.
28 D. Gabb, C. P. Pradeep, T. Boyd, S. G. Mitchell, H. N. Miras, D. L. Long and L. Cronin, *Polyhedron*, 2013, **52**, 159.
29 K. Y. Monakhov, *Comments Inorg. Chem.*, 2022, **44**, 1.
30 Y. Gao, M. Choudhari, G. K. Such and C. Ritchie, *Chem. Sci.*, 2022,**13**, 2510.
31 K. Kamata and K. Sugahara, *Catalysts*, 2017, **7**, 345.
32 C. Falaise, S. Khlifi, P. Bauduin, P. Schmid, W. Shepard, A. A. Ivanov, M. N. Sokolov, M. A. Shestopalov, P. A. Abramov, S. Cordier, J. Marrot, M. Haouas and E. Cadot, *Angew. Chem.*, 2021, **60**, 14146.
33 Y. P. Jeannin, *Chem. Rev.*, 1998, **98**, 51.
34 X. López, J. J. Carbó, C. Bo and J. M. Poblet, *Chem. Soc. Rev.*, 2012, **41**, 7537.
35 L. E. Briand, G. T. Baronetti and H. J. Thomas, *Appl. Catal. A Gen.*, 2003, **256**, 37.
36 M. R. Horn, A. Singh, S. Alomari, S. Goberna-Ferrón, R. Benages-Vilau, N. Chodankar, N. Motta, K. Ostrikov, J. Macleod, P. Sonar, P. Gomez-Romero and D. Dubal, *Energy Environ. Sci.*, 2021, **14**, 1652.
37 J. F. Keggin, *Proc. R. Soc. A*, 1934, **144**, 75.
38 A. Tézé, E. Cadot, V. Béreau and G. Hervé, *Inorg. Chem.*, 2001, **40**, 2000.
39 I. A. Weinstock, J. J. Cowan, E. M. G. Barbuzzi, H. Zeng and C. L. Hill, *J. Am. Chem. Soc.*, 1999, **121**, 4608.
40 B. Dawson, *Acta. Crystallogr.*, 1953, **6**, 113.
41 E. Coronado and C. J. Gómez-García, *Chem. Rev.*, 1998, **98**, 273.
42 F. Q. Zhang, W. Guan, L. K. Yan, Y. T. Zhang, M. T. Xu, E. Hayfron-Benjamin and Z. M. Su, *Inorg. Chem.*, 2011, **50**, 4967.
43 A. V Anyushin, A. Kondinski and T. N. Parac-Vogt, *Chem. Soc. Rev.*, 2020, **49**, 382.
44 A. Patel, N. Narkhede, S. Singh and S. Pathan, *Catal. Rev. - Sci. Eng.*, 2016, **58**, 337.
45 J. Canny, A. Tézé, R. Thouvenot and G. Hervé, *Inorg. Chem.*, 1986, **25**, 2114.
46 W. A. Neiwert, J. J. Cowan, K. I. Hardcastle, C. L. Hill and I. A. Weinstock, *Inorg. Chem.*, 2002, **41**, 6950.
47 Q. Jia, J. Cao, Y. Duan and C. Hu, *Dalton Trans.,* 2015, **44**, 553.
48 M. Aureliano, *BioChem.,* 2022, **2**, 8.
49 A. Hashikawa, M. Fujimoto, Y. Hayashi and H. Miyasaka, *Chem. Comm.*, 2011, **47**, 12361.

50 J. M. Cameron, D. J. Wales and G. N. Newton, *Dalton Trans.*, 2018, **47**, 5120.

51 Y. Sunada, K. Yamaguchi and K. Suzuki, *Coord. Chem. Rev.*, 2022, **469**, 214673.

52 C. R. Mayer, P. Herson and R. Thouvenot, *Inorg. Chem.*, 1999, **38**, 6152.

53 A. J. Kibler, V. S. Souza, J. A. Fernandes, W. Lewis, S. P. Argent, J. Dupont and G. N. Newton, *Front. Chem.*, 2021, **8**, 612535.

54 J. Zhang, Y. Huang, G. Li and Y. Wei, *Coord Chem Rev*, 2019, **378**, 395.

55 A. Dolbecq, E. Dumas, C. R. Mayer and P. Mialane, *Chem. Rev.*, 2010, **110**, 6009.

56 A. Proust, B. Matt, R. Villanneau, G. Guillemot, P. Gouzerh and G. Izzet, *Chem. Soc. Rev.*, 2012, **41**, 7605.

57 P. Gouzerh and A. Proust, *Chem. Rev.*, 1998, **98**, 77.

58 J. M. Cameron, G. Guillemot, T. Galambos, S. S. Amin, E. Hampson, K. M. Haidaraly, G. N. Newton and G. Izzet, *Chem. Soc. Rev.*, 2022, **51**, 293.

59 A. J. Kibler and G. N. Newton, *Polyhedron*, 2018, **154**, 1.

60 B. Matt, S. Renaudineau, L. M. Chamoreau, C. Afonso, G. Izzet and A. Proust, *J. Org. Chem.*, 2011, **76**, 3107.

61 X. Yi, N. V. Izarova and P. Kögerler, *Inorg. Chem.*, 2017, **56**, 13822.

62 X. López, J. A. Fernández and J. M. Poblet, *Dalton Trans.*, 2006, **6**, 1162.

63 A. Müller, J. Meyer, E. Krickemeyer and E. Diemann, *Angew. Chem.*, 1996, **35**, 1206.

64 L. I. Kuznetsova, V. M. Berdnikov and K. I. Matveev, *React. Kinet. Catal. Lett.*, 1981, **17**, 401.

65 M. T. Pope, *Angew. Chem.*, 1984, **96**, 730.

66 V. A. Grigoriev, C. L. Hill and I. A. Weinstock, *J. Am. Chem. Soc.*, 2000, **122**, 3544

67 X. López, C. Bo and J. M. Poblet, *J. Am. Chem. Soc.*, 2002, **124**, 12574.

68 S. Himeno, M. Takamoto and T. Ueda, *J. Electroanal. Chem*, 2000, **485**, 49.

69 K. Nakajima, K. Eda and S. Himeno, *Inorg. Chem.*, 2010, **49**, 5212.

70 J. J. J. Chen and M. A. Barteau, *Ind. Eng. Chem. Res.*, 2016, **55**, 9857.

71 C. Bo and J. M. Poblet, *Isr. J. Chem.*, 2011, **51**, 228.

72 J. M. Poblet, X. López and C. Bo, *Chem. Soc. Rev.*, 2003, **32**, 297.

73 B. Matt, X. Xiang, A. L. Kaledin, N. Han, J. Moussa, H. Amouri, S. Alves, C. L. Hill, T. Lian, D. G. Musaev, G. Izzet and A. Proust, *Chem. Sci.*, 2013, **4**, 1737.

74 M. Boujtita, J. Boixel, E. Blart, C. R. Mayer and F. Odobel, *Polyhedron*, 2008, **27**, 688.

75 J. M. Cameron, S. Fujimoto, K. Kastner, R.-J. J. Wei, D. Robinson, V. Sans, G. N. Newton and H. H. Oshio, *Chem. Eur. J.*, 2017, **23**, 47.

76 S. Fujimoto, J. M. Cameron, R.-J. Wei, K. Kastner, D. Robinson, V. Sans, G. N. Newton and H. Oshio, *Inorg. Chem.*, 2017, **56**, 12169.

77 S. Omwoma, C. T. Gore, Y. Ji, C. Hu and Y. F. Song, *Coord. Chem. Rev.*, 2015, **286**, 17.

78 K. Xia, K. Yamaguchi and K. Suzuki, *Angew. Chem.*, 2023, **135**, e202214506.

79 Yao Zhang, Yanyan Li, Haoran Guo, Yunqiao Guo and Rui Song, *Mater. Chem. Front., 2024, **8**, 732.*

80 X. Chen, H. Wu, X. Shi and L. Wu, *Nanoscale*, 2023, **15**, 9242.

81 J. Gu, W. Chen, G.-G. Shan, G. Li, C. Sun, X.-L. Wang and Z. Su, *Mater. Today Energy,* 2021, **21**, 100760.

82 T. Yamase, *Chem. Rev.*, 1998, **98**, 307.

83 E. Papaconstantinou, *Chem. Soc. Rev*, 1989, **18**, 1.

84 D. C. Duncan, T. L. Netzel and C. L. Hill, *Inorg. Chem.*, 1995, **34**, 4640.

85 I. Tabushi, K. J. Morimitsu, I. Am ; Tabushi, A. Yazaki, I. Ibid ; Tabushi, N. Koga, Ibid, C. K. Chang, F. Ebina, N. Murugesan, S. M. Hecht, G. M. Ehrenfeld, R. B. Vanatta, C. C. Franklin, J. S. Valentine, R. B. Van Atta, A. Tai, F. Zonneville, C. M. Toume and G. F. Toume, *J. Am. Chem. Soc.*, 1986, **108**, 536.

86 C. L. Hill and D. A. Bouchard, *J. Am. Chem. Soc.*, 1985, **107**, 5148.

87 M. A. Fox, R. Cardona and E. Gaillard, *J. Am. Chem. Soc.*, 1987, **109**, 6347.

88 T. Yamase, R. Sasaki and T. Ikawa, *Dalton Trans.*, 1981, 628.

89 E. Papaconstantinou, *J. Chem. Soc. Chem. Commun.*, 1982, 12.

90 N. Li, J. Liu, B. X. Dong and Y. Q. Lan, *Angew. Chem.*, 2020, **59**, 20779.

91 D. Gao, I. Trentin, L. Schwiedrzik, L. González and C. Streb, *Molecules*, 2020, **25**, 157.

92 S. J. Folkman, J. Soriano-Lopez, J. R. Galán-Mascarós and R. G. Finke, *J. Am. Chem. Soc.*, 2018, **140**, 12040.

93 H. Lv, Y. V Geletii, C. Zhao, J. W. Vickers, G. Zhu, Z. Luo, J. Song, T. Lian, D. G. Musaev and C. L. Hill, *Chem. Soc. Rev.*, 2012, **41**, 7572.

94 C. Streb, *Dalton Trans*, 2012, **41**, 1651.

95 A. M. Khenkin, I. Efremenko, L. Weiner, J. M. L. Martin and R. Neumann, *Chem. Eur. J.*, 2010, **16**, 1356.

96 J. Lan, Y. Wang, B. Huang, Z. Xiao and P. Wu, *Nanoscale Adv.*, 2021, **3**, 4646.

97 P. Lei, C. Chen, J. Yang, W. Ma, J. Zhao and L. Zang, *Environ. Sci. Technol.*, 2005, **39**, 8466.

98 A. Dolbecq, P. Mialane, B. Keita and L. Nadjo, *J. Mater. Chem.*, 2012, **22**, 24509.

99 Y. Wu and L. Bi, *Catalysts,* 2021, **11**, 524.

100 L. Capaldo and D. Ravelli, *Eur. J. Org. Chem.,* **2017**, 2056.

101 T. Konry, A. Novoa, Y. Shemer-Avni, N. Hanuka, S. Cosnier, A. Lepellec and R. S. Marks, *Anal. Chem.*, 2005, **77**, 1771.

102 C. L. Hill, *J. Mol. Catal. A. Chem.*, 2007, **262**, 2.

103 I. Ryu, A. Tani, T. Fukuyama, D. Ravelli, S. Montanaro and M. Fagnoni, *Org. Lett.*, 2013, **15**, 2554.
104 D. Dondi, M. Fagnoni and A. Albini, *Chem. Eur. J.*, 2006, **12**, 4153.
105 M. D. Tzirakis, I. N. Lykakis and M. Orfanopoulos, *Chem. Soc. Rev.*, 2009, **38**, 2609.
106 T. Fukuyama, K. Yamada, T. Nishikawa, D. Ravelli, M. Fagnoni and I. Ryu, *Chem. Lett.*, 2017, **47**, 207.
107 V. De Waele, O. Poizat, M. Fagnoni, A. Bagno and D. Ravelli, *ACS Catal.*, 2016, **6**, 7174.
108 D. C. Duncan and M. A. Fox, *J. Phys. Chem. A,* 1998, 102, **24**, 4559.
109 I. B. Perry, T. F. Brewer, P. J. Sarver, D. M. Schultz, D. A. DiRocco and D. W. C. MacMillan, *Nature*, 2018, **560**, 70.
110 Z. Yuan and R. Britton, *Chem. Sci.***,** 2023,**14**, 12883.
111 B. Matt, C. Coudret, C. Viala, D. Jouvenot, F. Loiseau, G. Izzet and A. Proust, *Inorg. Chem.*, 2011, **50**, 7761.
112 S. Schönweiz, M. Heiland, M. Anjass, T. Jacob, S. Rau and C. Streb, *Chem. Eur. J.*, 2017, **23**, 15370.
113 A. Proust, B. Matt, R. Villanneau, G. Guillemot, P. Gouzerh and G. Izzet, *Chem. Soc. Rev.*, 2012, **41**, 7605.
114 J. Gao, S. Cao, Q. Tay, Y. Liu, L. Yu, K. Ye, P. C. S. Mun, Y. Li, G. Rakesh, S. C. J. Loo, Z. Chen, Y. Zhao, C. Xue and Q. Zhang, *Sci. Rep.,* 2013, **3**, 1.
115 S. Bhatt and S. Saha, *Prog. Solid St. Chem.*, 2023, **72**, 100430.
116 X. B. Han, Z. M. Zhang, T. Zhang, Y. G. Li, W. Lin, W. You, Z. M. Su and E. B. Wang, *J. Am. Chem. Soc.*, 2014, **136**, 5359.
117 M. Bonchio, M. Carraro, G. Scorrano and A. Bagno, *Adv. Synth. Catal.*, 2004, **346**, 648.
118 K. Suzuki, N. Mizuno and K. Yamaguchi, *J. Jpn. Petrol. Inst.*, 2020, **63**, 258.
119 J. Sworakowski, *Synth. Met.*, 2018, **235**, 125.
120 J. Sworakowski, J. Lipiński and K. Janus, *Org. Electron.*, 2016, **33**, 300.
121 F. Hasannezhad, L. Naji and M. Arvand, *Mater. Sci. Semicond. Process*, 2022, **139**, 106333.
122 H. M. Asif, N. Qu, Y. Zhou, L. Zhang, F. K. Shehzad, Z. Shi, Y. Long and S. U. Hassan, *Inorg. Chem. Front.*, 2017, **4**, 1900.
123 P. I. Djurovich, E. I. Mayo, S. R. Forrest and M. E. Thompson, *Org. Electron.*, 2009, **10**, 515.
124 B. Yang, Z. Fu, A. Su, J. She, M. Chen, S. Tang, W. Hu, C. Zhang and Y. Liu, *Appl. Catal. B*, 2019, **242**, 249.
125 K. Suzuki, N. Mizuno and K. Yamaguchi, *ACS Catal.*, 2018, **8**, 10809.
126 S. Amin, J. M. Cameron, J. A. Watts, D. A. Walsh, V. Sans and G. N. Newton, *Mol. Syst. Des. Eng.*, 2019, **4**, 995.
127 K. Kastner, A. J. Kibler, E. Karjalainen, J. A. Fernandes, V. Sans and G. N. Newton, *J. Mater. Chem. A Mater.*, 2017, **5**, 11577.
128 G. S. Kim, K. S. Hagen and C. L. Hill, *Inorg. Chem.*, 1992, **31**, 5316.

129 G. Lenoble, B. Hasenknopf and R. Thouvenot, *J. Am. Chem. Soc.*, 2006, **128**, 5735.
130 A. Kuhn, K. G. Von Eschwege and J. Conradie, *J. Phys. Org. Chem.*, 2012, **25**, 58.
131 S. S. Amin, J. M. Cameron, M. Winslow, E. S. Davies, S. P. Argent, D. Robinson and G. N. Newton, *Eur. J. Inorg. Chem.*, **2022**, e202200019.
132 P. Niemiec, R. Tokarz-Sobieraj and M. Witko, *Molecules,* 2021, **27**, 187.
133 C. Rocchiccioli-Deltcheff, M. Fournier, R. Franck and R. Thouvenot, *Inorg. Chem*., 1983, **22**, 2, 207.
134 A. Tézé and G. Hervé, *Inorg. Synth.*, 1990, **27**, 85.
135 T. Ueda, K. Kodani, H. Ota, M. Shiro, S. X. Guo, J. F. Boas and A. M. Bond, *Inorg. Chem.*, 2017, **56**, 3990.
136 S. Himeno, M. Takamoto and T. Ueda, *Bull. Chem. Soc. Jpn.*, 2005, **78**, 1463.
137 A. Tézé, E. Cadot, V. Béreau and G. Hervé, *Inorg. Chem.*, 2001, **40**, 2000.
138 A. Tézé, M. Michelon and G. Hervé, *Inorg. Chem.*, 1997, **36**, 505.
139 T. Yamase and R. Watanabe, *J. Chem. Soc. Dalton Trans.*, 1986, 1669.
140 N. Leclerc-Laronze, J. Marrot, R. Thouvenot and E. Cadot, *Angew. Chem.*, 2009, **48**, 4986.
141 N. Leclerc-Laronze, J. Marrot, G. Hervé, R. Thouvenot and E. Cadot, *Angew. Chem.*, 2007, **13**, 7234.
142 R. I. Maksimovskaya and G. M. Maksimov, *Inorg. Chem.*, 2011, **50**, 4725.
143 J. Jiang, J. Duan, J. Liu, L. Chen and J. Zhao, *Cryst. Growth Des.*, 2020, **20**, 362.
144 I. M. Mbomekallé, X. López, J. M. Poblet, F. Sécheresse, B. Keita and L. Nadjo, *Inorg. Chem.*, 2010, **49**, 7001.
145 Z. G. Sun, Q. Liu and J. F. Liu, *Polyhedron*, 2000, **19**, 125.
146 Z. G. Sun, L. Y. Cui, Z. M. Zhu, X. H. Yu and X. F. Zheng, *J. Coord. Chem.*, 2006, **58**, 1321.
147 N. Andino, B. Artetxe, S. Reinoso, P. Vitoria, L. S. Felices, J. I. Martínez, F. L. Arbeloa and J. M. Gutiérrez-Zorrilla, *Inorganics,* 2016, **4**, 14.
148 W. Zhang, L. Gong, N. Du, C. Wang, K. Yu, C. Wang and B. Zhou, *Inorg. Chem.*, 2021, **60**, 16357.
149 H. Gao and K. Lian, *J. Mater. Chem. A Mater.*, 2016, **4**, 9585.
150 Q. L. Liang, N. N. Du, L. G. Gong, C. X. Wang, C. M. Wang, K. Yu and B. Bin Zhou, *New J. Chem.*, 2021, **45**, 14444.
151 Z. Y. Du, Y. N. Xue, X. M. Liu, N. F. Li, J. L. Wang, H. Mei and Y. Xu, *J. Mater. Chem. A Mater.*, 2022, **10**, 3469.
152 K. K. Guo, X. Y. Jiang, M. Xu, F. Y. Li, S. M. Dong, Y. Zheng and L. Xu, *Chem. Comm.*, 2021, **57**, 11398.

153 Z. J. Song, L. Y. Wang, N. Kang, K. Yu, J. H. Lv and B. Bin Zhou, *J. Solid. State. Chem.*, 2023, **323**, 124038.
154 B. Khadro, I. Baroudi, A. M. Goncalves, B. Berini, B. Pegot, F. Nouar, T. N. Ha Le, F. Ribot, C. Gervais, F. Carn, E. Cadot, C. Mousty, C. Simonnet-Jégat and N. Steunou, *J. Mater. Chem. A Mater.*, 2014, **2**, 9208.
155 Y. Ma, H. Peng, J. Liu, Y. Wang, X. Hao, X. Feng, S. U. Khan, H. Tan and Y. Li, *Inorg. Chem.*, 2018, **57**, 4109.
156 W. J. Cui, S. M. Zhang, Y. Y. Ma, Y. Wang, R. X. Miao and Z. G. Han, *Inorg. Chem.*, 2022, **61**, 9421.
157 W. Zhao, Y. Zhang, B. Ma, Y. Ding and W. Qiu, *Catal. Commun.*, 2010, **11**, 527.
158 L. MacArie and G. Ilia, *Prog. Polym. Sci.*, 2010, **35**, 1078.
159 N. Harsági and G. Keglevich, *Molecules,* 2021, **26**, 2840.
160 D. Agustin, J. Dallery, C. Coelho, A. Proust and R. Thouvenot, *J. Organomet. Chem.*, 2007, **692**, 746.
161 C. R. Mayer, C. Roch-Marchal, H. Lavanant, R. Thouvenot, N. Sellier, J. C. Blais and F. Sécheresse, *Chem. Eur. J.*, 2004, **10**, 5517.
162 M. Daraie, M. Mirzaei, M. Bazargan, V. S. Amiri, B. A. Sanati and M. M. Heravi, *Sci. Rep.*, 2022, **12**, 12004.
163 B. S. Jaynes and C. L. Hill, *J. Am. Chem. Soc.*, 1993, **115**, 12212.
164 K. Suzuki, F. Tang, Y. Kikukawa, K. Yamaguchi and N. Mizuno, *Angew. Chem.*, 2014, **53**, 5356.
165 S. Li, G. Li, P. Ji, J. Zhang, S. Liu, J. Zhang and X. Chen, *ACS Appl. Mater. Interfaces.*, 2019, **11**, 43287.
166 B. He, S. Zhang, Y. Zhang, G. Li, B. Zhang, W. Ma, B. Rao, R. Song, L. Zhang, Y. Zhang and G. He, *J. Am. Chem. Soc.*, 2022, **144**, 4422.
167 W. Chen, H. Li, J. Song, Y. Zhao, P. Ma, J. Niu and J. Wang, *Inorg. Chem.*, 2022, **61**, 2076.
168 Y. Liu, J. Wang, K. Ji, S. Meng, Y. Luo, H. Li, P. Ma, J. Niu and J. Wang, *J. Catal.*, 2022, **416**, 149.
169 H. Li, W. Chen, Z. Yuan, Y. Jin, Y. Zhao, P. Ma, J. Niu and J. Wang, *Inorg. Chem.*, 2022, **61**, 9935.
170 R. Neumann, *Inorg. Chem.*, 2010, **49**, 3594.
171 L. Pitzer, F. Schäfers and F. Glorius, *Angew. Chem.*, 2019, **58**, 8572.
172 J. J. Douglas, *Nat. Chem.,* 2019, **11**, 683.
173 G. E. M. Crisenza, D. Mazzarella and P. Melchiorre, *J. Am. Chem. Soc.*, 2020, **142**, 5461.
174 H. Soria-Carrera, E. Atrián-Blasco, R. Martín-Rapún and S. G. Mitchell, *Chem. Sci.*, 2022, **14**, 10.
175 G. R. Fulmer, A. J. M. Miller, N. H. Sherden, H. E. Gottlieb, A. Nudelman, B. M. Stoltz, J. E. Bercaw and K. I. Goldberg, *Organometallics*, 2010, **29**, 2176.
176 R. K. Harris, E. D. Becker, S. M. De Cabral Menezes, P. Granger, R. E. Hoffman and K. W. Zilm, *Magn. Reson. Chem.*, 2008, **46**, 582.
177 D. R. Allan, H. Nowell, S. A. Barnett, M. R. Warren, A. Wilcox, J. Christensen, L. K. Saunders, A. Peach, M. T. Hooper, L. Zaja, S.

Patel, L. Cahill, R. Marshall, S. Trimnell, A. J. Foster, T. Bates, S. Lay, M. A. Williams, P. V. Hathaway, G. Winter, M. Gerstel and R. W. Wooley, *Crystals*, 2017, **7**, 336.
178 J. Cosier and A. M. Glazer, *J. Appl. Crystallogr.*, 1986, **19**, 105.
179 G. Winter, D. G. Waterman, J. M. Parkhurst, A. S. Brewster, R. J. Gildea, M. Gerstel, L. Fuentes-Montero, M. Vollmar, T. Michels-Clark, I. D. Young, N. K. Sauter and G. Evans, *Acta Crystallogr. D Struct. Biol.*, 2018, **74**, 85.
180 *Journal, 2018, CCP4 7.0.062 AIMLESS, version 060.067.062 027/005/018.*
181 *Rigaku Oxford Diffraction, 2018, CrysAlisPro Software system, version 1.171.40.45a, Rigaku Corporation, Oxford, UK.*
182 O. V Dolomanov, L. J. Bourhis, R. J. Gildea, J. A. K. Howard and H. Puschmann, *J. Appl. Crystallogr.*, 2009, **42**, 339.
183 *G. M. Sheldrick, Acta Crystallogr. A 2015, 71, 3.*
184 *"CheckCIF," can be found under http://checkcif.iucr.org*.
185 C. R. Graham and R. G. Finke, *Inorg. Chem.*, 2008, **47**, 3679.
186 Z. Yekke-Ghasemi, M. M. Heravi, M. Malmir, G. Jahani, M. B. Bisafar and M. Mirzaei, *Inorg. Chem. Commun.*, 2022, **140**, 109456.
187 Y. Goriya, H. Y. Kim and K. Oh, *Org. Lett.*, 2016, **18**, 5174.
188 J. Zhao, H. Sun, Y. Lu, J. Li, Z. Yu, H. Zhu, C. Ma, Q. Meng and X. Peng, *Green Chem.*, 2022, **24**, 8503.
189 P. Galletti, F. Funiciello, R. Soldati and D. Giacomini, *Adv. Synth. Cata.l*, 2015, **357**, 1840.
190 I. Kumar, R. Kumar, S. S. Gupta and U. Sharma, *J. Org. Chem.*, 2021, **86**, 6449.
191 P. Zhang, C. Yu, Y. Yin, J. Droste, S. Klabunde, M. R. Hansen and Y. Mai, *Chem. Eur. J.*, 2020, **26**, 16497.

# 11 Appendix

## 11.1 Additional Structural Analysis

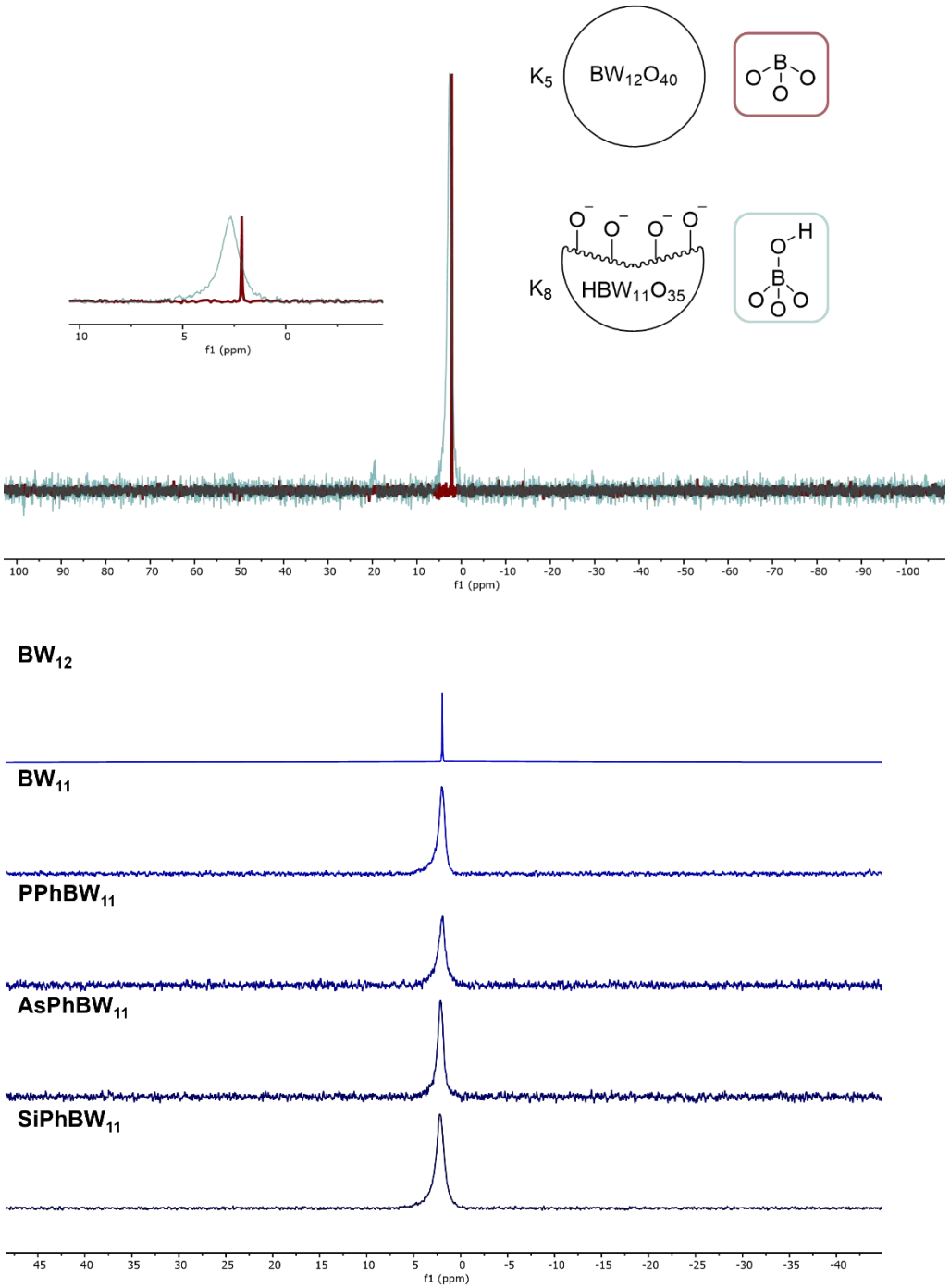



**Figure 70.** Top) $^{11}$B NMR (128 MHz, $D_2O$) of the potassium plenary and lacunary borotungstate POMs. Bottom) Stacked $^{11}$B NMR (128 MHz, $CD_3CN$) of the plenary, lacunary and hybrid borotungstate POMs as their $^{n}Bu_4N$ salts.

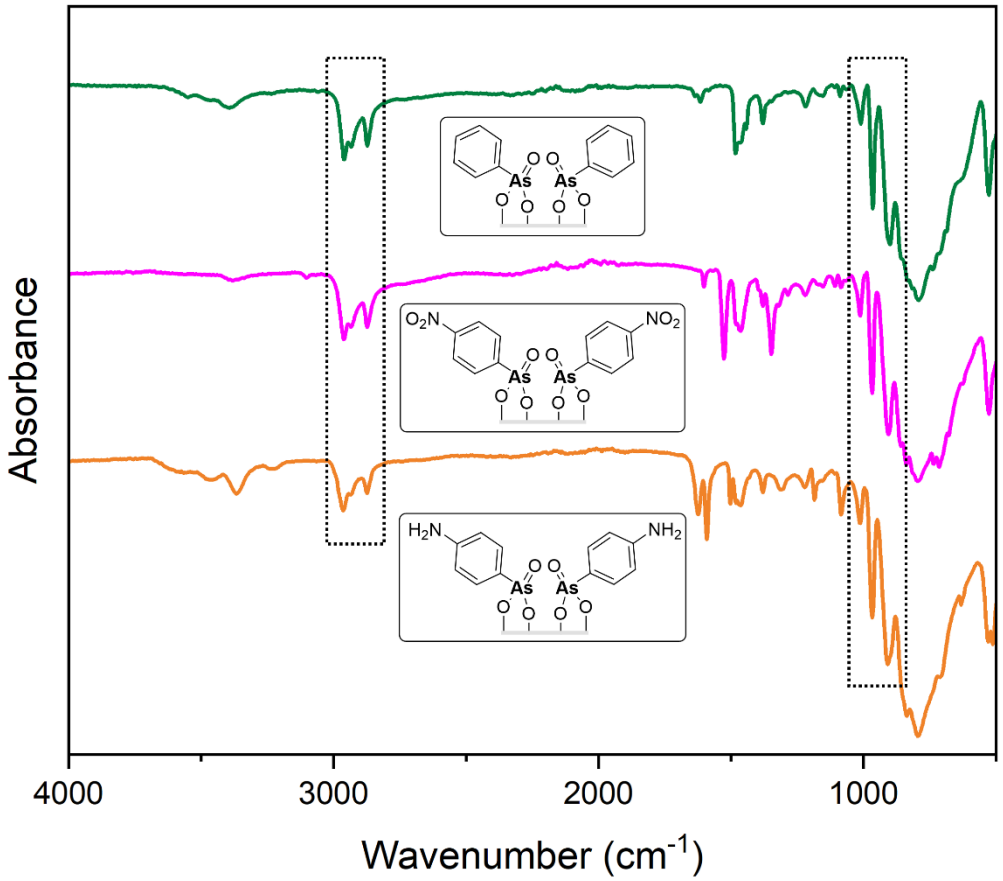



**Figure 71.** Stacked IR (ATR) spectra of organoarsonate borotungstate POMs ({**AsPhBW$_{11}$**}, {**AsPhNO$_2$BW$_{11}$**}, and {**AsPhNH$_2$BW$_{11}$**}) as their $^{n}$Bu$_4$N salts.

## 11.2 Additional CV and Spectroscopic Data

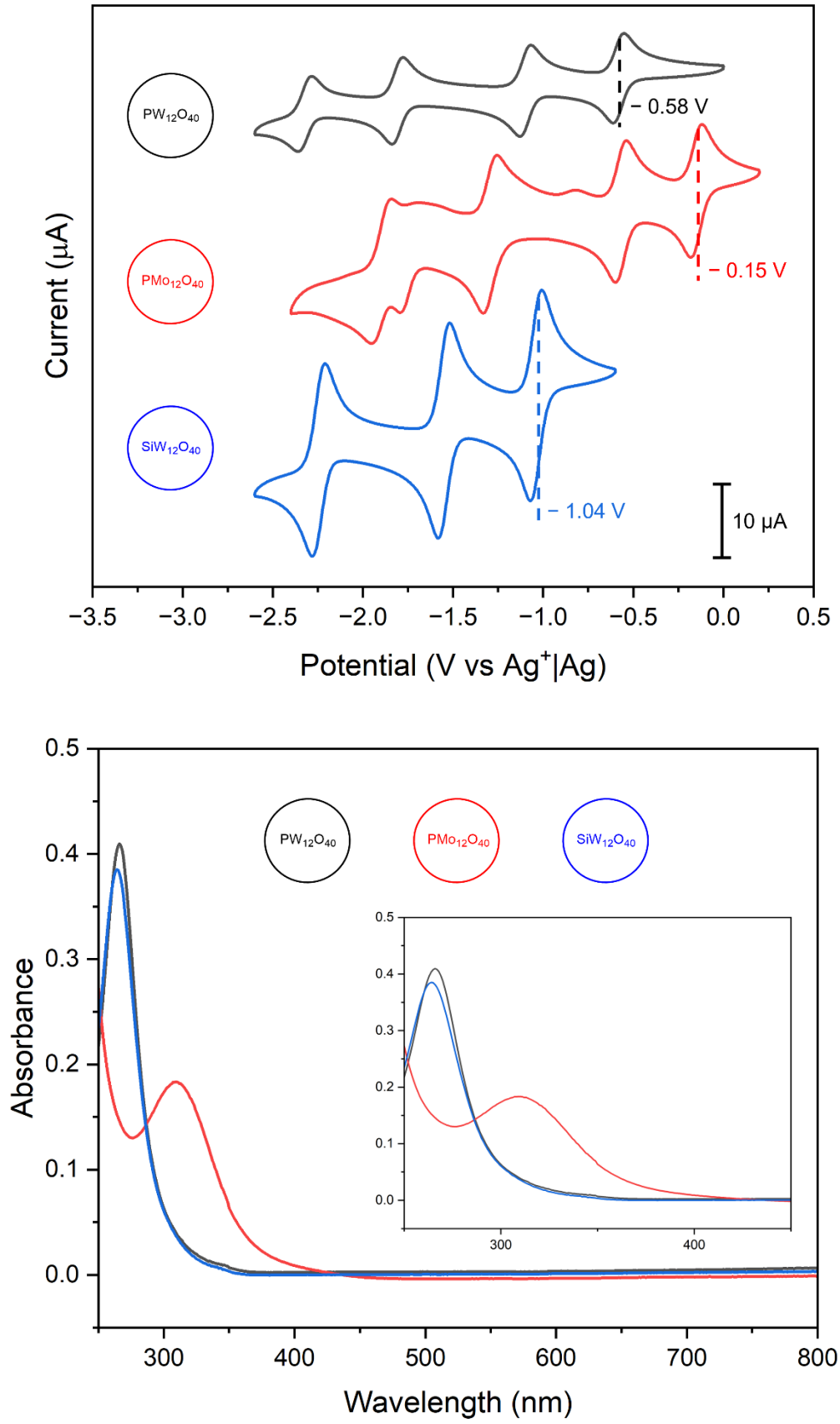



**Figure 72**. CV and UV-Vis data of plenary Keggin POMs conducted in MeCN.

### 11.3 Crystal Data and Structure Refinement for {K•AsPhBW$_{11}$}

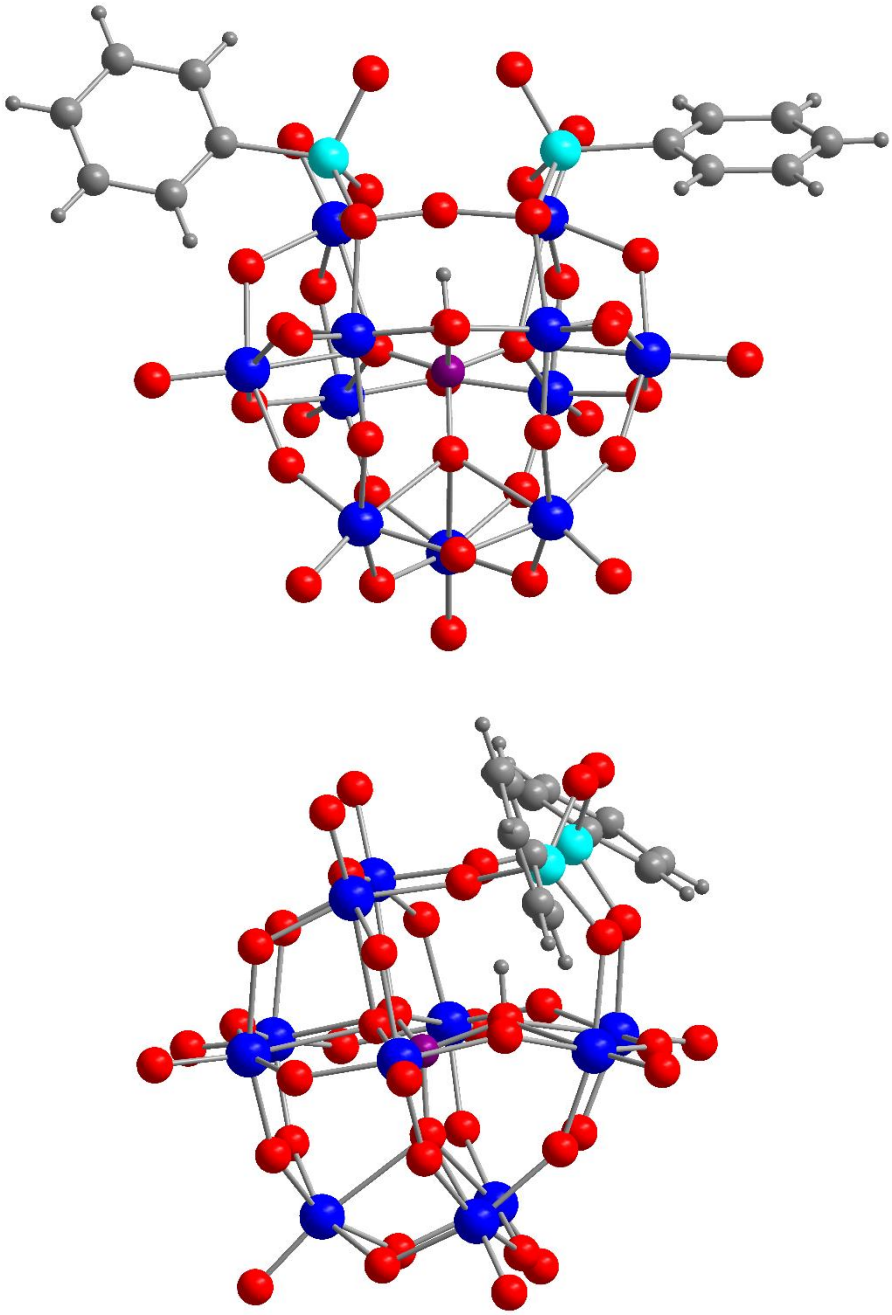


**Figure 73**. Crystal structure of {**K•AsPhBW$_{11}$**}. Solvent omitted for clarity.

**Table 16. Experimental details**

| **Crystal data – wkdjle_e1** | |
|---|---|
| Chemical formula | $0.99(C_{12}H_{11}As_2BO_{41}W_{11})\cdot 0.01(W_{12}O_{40}B)\cdot 3(K)\cdot 7(CH_3NO_2)\cdot H_2O$ |
| $M_r$ | 3555.46 |
| Crystal system, space group | Monoclinic, $P2_1/n$ |
| Temperature (K) | 100 |
| $a$, $b$, $c$ (Å) | 12.186, 23.1617 (1), 23.1375 (1) |
| b (°) | 97.73 |
| $V$ (Å$^3$) | 6471.15 (4) |
| $Z$ | 4 |
| Radiation type | Synchrotron, l = 0.6889 Å |
| m (mm$^{-1}$) | 19.00 |
| Crystal size (mm) | 0.13 × 0.05 × 0.03 |

| **Data collection** | |
|---|---|
| Diffractometer | Fluid Film Devices |
| Absorption correction | Empirical (using intensity measurements)<br>*CCP4* 8.0.003: AIMLESS, version 0.7.9 : 10/06/22 Scaling & analysis of unmerged intensities, absorption correction using spherical harmonics |
| $T_{min}$, $T_{max}$ | 0.935, 1.0 |
| No. of measured, independent and observed [$I$ > 2s($I$)] reflections | 282940, 32415, 27629 |
| $R_{int}$ | 0.069 |
| (sin q/l)$_{max}$ (Å$^{-1}$) | 0.856 |

| **Refinement** | |
|---|---|
| $R[F^2 > 2s(F^2)]$, $wR(F^2)$, $S$ | 0.035, 0.077, 1.08 |
| No. of reflections | 32415 |
| No. of parameters | 957 |
| No. of restraints | 933 |
| H-atom | H atoms treated by a mixture of independent and |

| treatment | constrained refinement |
|---|---|
| | $w = 1/[s^2(F_o^2) + (0.0045P)^2 + 72.4676P]$ where $P = (F_o^2 + 2F_c^2)/3$ |
| $D\tilde{n}_{max}$, $D\tilde{n}_{min}$ (e Å$^{-3}$) | 3.77, -2.82 |

Computer programs: GDA - generic data acquisition software, aimless (Evans, P. R. and Murshudov, G. N., 2013) *CCP4* (Winn, M. D. *et al.*, 2011) DIALS 3.11.1-g247d2660a-release (Winter, G. *et al.*, 2018) pointless (Evans, P., 2006) XIA2 3.11.0 (Winter, G., 2010), *SHELXT* 2018/2 (Sheldrick, 2018), *SHELXL* 2018/3 (Sheldrick, 2015), Olex2 1.5 (Dolomanov *et al.*, 2009).

### 11.4 Crystal Images of {K•AsPhBW$_{11}$}

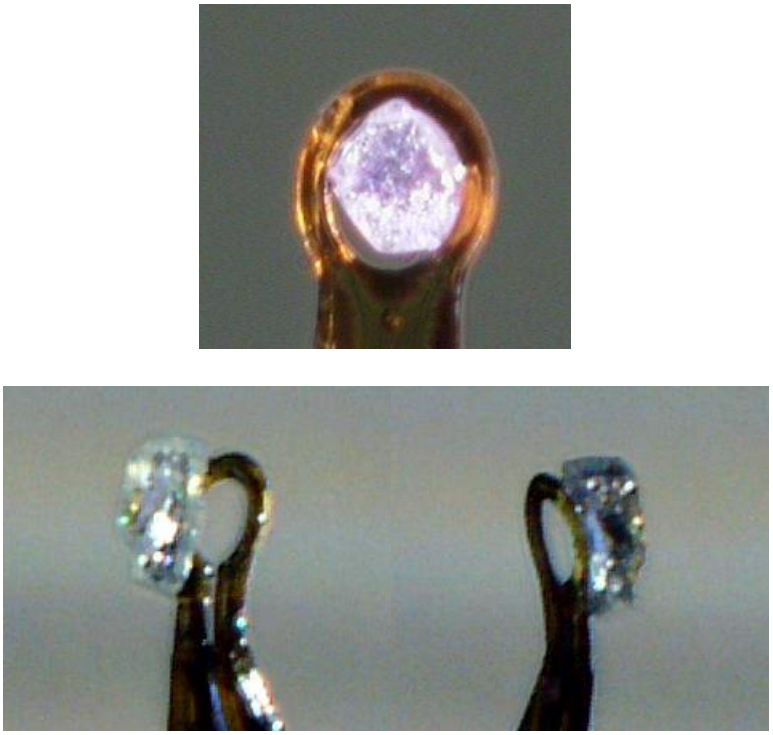


**Figure 74**. Images of a single crystal of {**K•AsPhBW$_{11}$**}. The images shown here are not from the crystal collection used for SCXRD.

## 11.5 Crystal Data and Structure Refinement for {K•PPhBW$_{11}$}

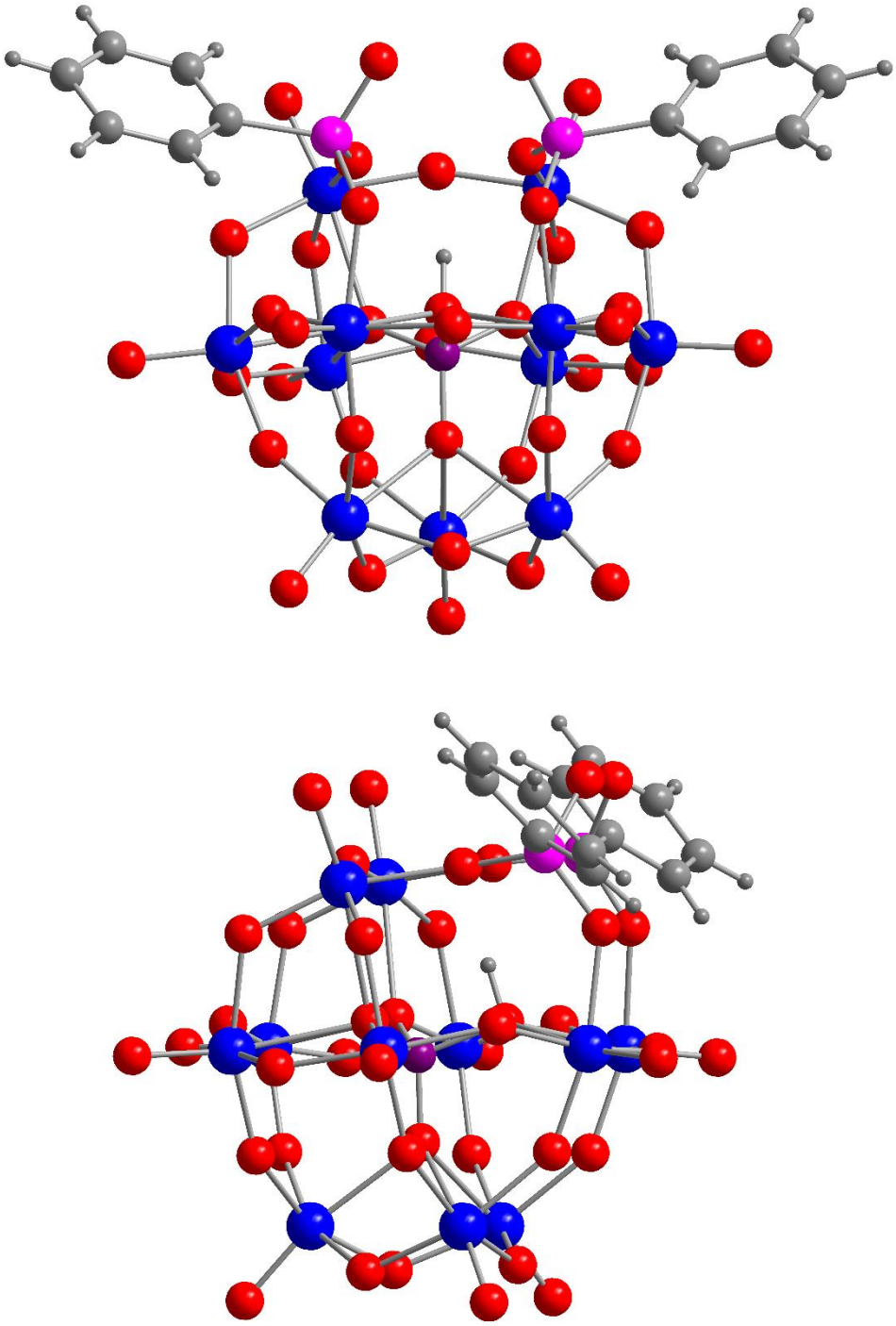


**Figure 75**. Crystal structure of {**K•PPhBW$_{11}$**}. Solvent omitted for clarity.

**Table 17. Experimental details**

| **Crystal data - wkdjlf_d1** | |
|---|---|
| Chemical formula | $C_{18}H_{29}BK_3N_6O_{53}P_2W_{11}\cdot 4[H2O]$ |
| $M_r$ | 3461.93 |
| Crystal system, space group | Monoclinic, $P2_1$ |
| Temperature (K) | 100 |
| *a*, *b*, *c* (Å) | 12.3035 (4), 23.9565 (5), 12.4053 (4) |
| b (°) | 118.757 (4) |
| *V* (Å$^3$) | 3205.49 (19) |
| *Z* | 2 |
| Radiation type | Synchrotron, l = 0.6889 Å |
| m (mm$^{-1}$) | 18.28 |
| Crystal size (mm) | 0.25 × 0.08 × 0.08 × 0.08 (radius) |

| **Data collection** | |
|---|---|
| Diffractometer | Fluid Film Devices |
| Absorption correction | For a sphere<br>*CrysAlis PRO* 1.171.43.63a (Rigaku Oxford Diffraction, 2023) Spherical absorption correction using equivalent radius and absorption coefficient. Empirical absorption correction using spherical harmonics, implemented in SCALE3 ABSPACK scaling algorithm. |
| $T_{min}$, $T_{max}$ | 0.129, 0.167 |
| No. of measured, independent and | 41822, 12893, 12500 |

| | |
|---|---|
| observed [$I > 2s(I)$] reflections | |
| $R_{int}$ | 0.093 |
| $(\sin q/l)_{max}$ ($Å^{-1}$) | 0.625 |

| **Refinement** | |
|---|---|
| $R[F^2 > 2s(F^2)]$, $wR(F^2)$, $S$ | 0.050, 0.118, 1.04 |
| No. of reflections | 12893 |
| No. of parameters | 850 |
| No. of restraints | 1897 |
| H-atom treatment | H atoms treated by a mixture of independent and constrained refinement |
| | $w = 1/[s^2(F_o^2) + (0.0368P)^2 + 108.4183P]$ where $P = (F_o^2 + 2F_c^2)/3$ |
| $Dñ_{max}$, $Dñ_{min}$ ($e Å^{-3}$) | 3.33, -2.36 |
| Absolute structure | Flack x determined using 5237 quotients [(I+)-(I-)]/[(I+)+(I-)] (Parsons, Flack and Wagner, Acta Cryst. B69 (2013) 249-259). |
| Absolute structure parameter | 0.074 (11) |

Computer programs: GDA - generic data acquisition software, *CrysAlis PRO* 1.171.43.63a (Rigaku OD, 2023), *SHELXT* 2018/2 (Sheldrick, 2018), *SHELXL* 2018/3 (Sheldrick, 2015), Olex2 1.5 (Dolomanov *et al.*, 2009).

## 11.6 Crystal Data and Structure Refinement for {$AsPhNH_2BW_{11}$}

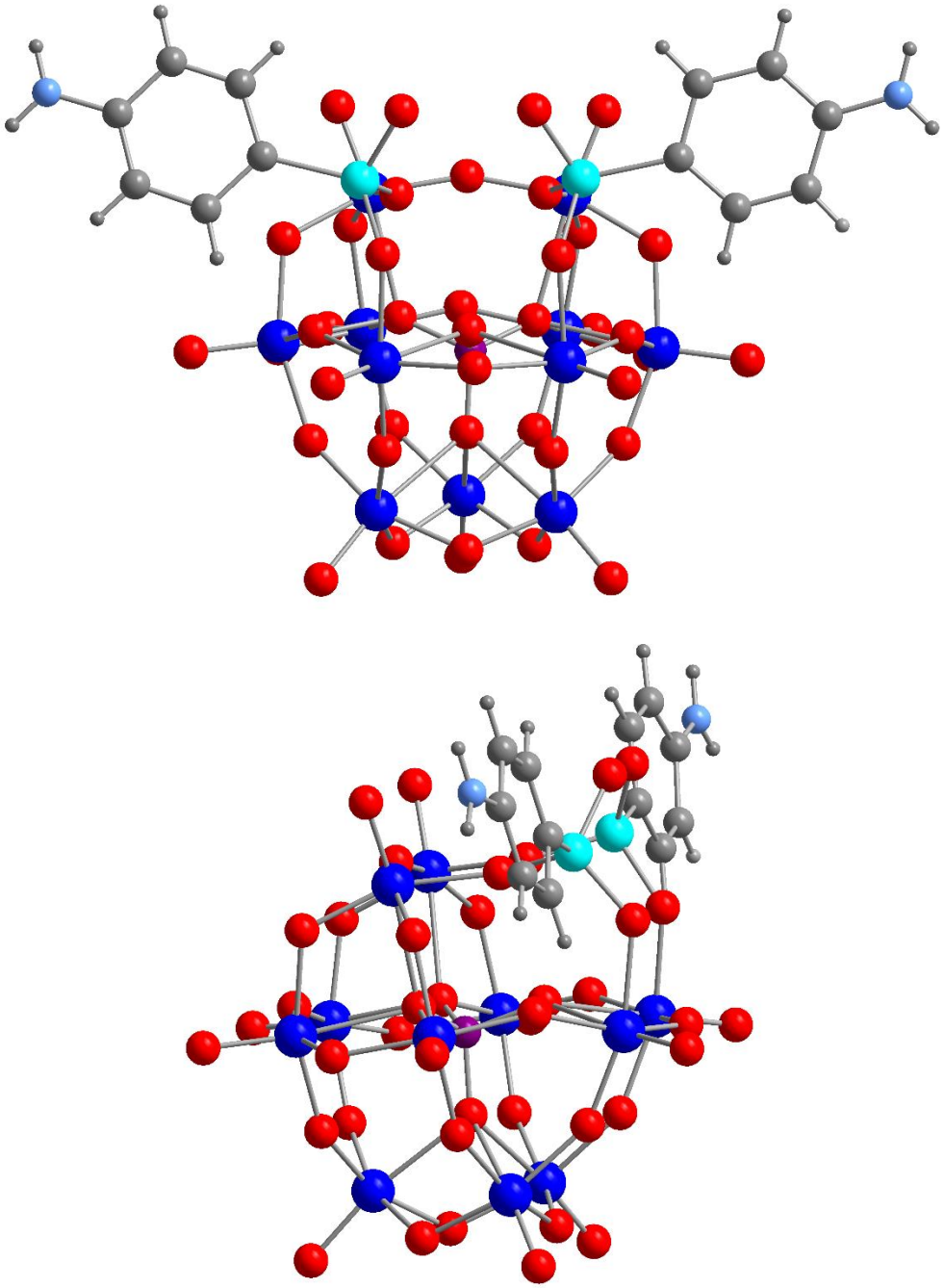


**Figure 76**. Crystal structure of {**$AsPhNH_2BW_{11}$**}. Solvent omitted for clarity.

**Table 18. Experimental details**

| **Crystal data - shelxt_a** | |
|---|---|
| Chemical formula | $C_{12}H_{12}As_2BN_2O_{41}W_{11}\cdot 2.5(C_{16}H_{36}N)\cdot 0.5(C_{15}H_{34}N)\cdot 1.5(C_2H_3N)$ |
| $M_r$ | 3805.17 |
| Crystal system, space group | Triclinic, *P*1 |
| Temperature (K) | 100 |
| *a*, *b*, *c* (Å) | 13.6162 (2), 15.0890 (2), 23.6833 (3) |
| a, b, g (°) | 88.392 (1), 89.469 (1), 87.136 (1) |
| *V* (Å$^3$) | 4857.71 (11) |
| *Z* | 2 |
| Radiation type | synchrotoron, l = 0.6889 Å |
| m (mm$^{-1}$) | 12.53 |

| **Data collection** | |
|---|---|
| Diffractometer | Fluid Film Devices |
| Absorption correction | Empirical (using intensity measurements) *CCP4* 8.0.003: AIMLESS, version 0.7.9 : 10/06/22 Scaling & analysis of unmerged intensities, absorption correction using spherical harmonics |
| No. of measured, independent and observed [*I* > 2s(*I*)] reflections | 64807, 35619, 29337 |
| $R_{int}$ | 0.049 |
| $(\sin q/l)_{max}$ (Å$^{-1}$) | 0.617 |

| **Refinement** | |
|---|---|
| $R[F^2 > 2s(F^2)]$, $wR(F^2)$, *S* | 0.046, 0.118, 1.04 |
| No. of reflections | 35619 |

| | |
|---|---|
| No. of parameters | 2236 |
| No. of restraints | 4656 |
| H-atom treatment | H-atom parameters constrained |
| $D\rho_{max}$, $D\rho_{min}$ (e Å$^{-3}$) | 4.60, -2.24 |
| Absolute structure | Flack x determined using 11435 quotients [(I+)-(I-)]/[(I+)+(I-)] (Parsons, Flack and Wagner, Acta Cryst. B69 (2013) 249-259). |
| Absolute structure parameter | 0.022 (7) |

Computer programs: GDA - generic data acquisition software, aimless (Evans, P. R. and Murshudov, G. N., 2013) *CCP4* (Winn, M. D. *et al.*, 2011) DIALS 3.11.1-g247d2660a-release (Winter, G. *et al.*, 2018) pointless (Evans, P., 2006) XIA2 3.11.0 (Winter, G., 2010), *SHELXT* 2018/2 (Sheldrick, 2018), *SHELXL* 2018/3 (Sheldrick, 2015), Olex2 1.5 (Dolomanov *et al.*, 2009).

### 11.7 Crystal Images of {$AsPhNH_2BW_{11}$}

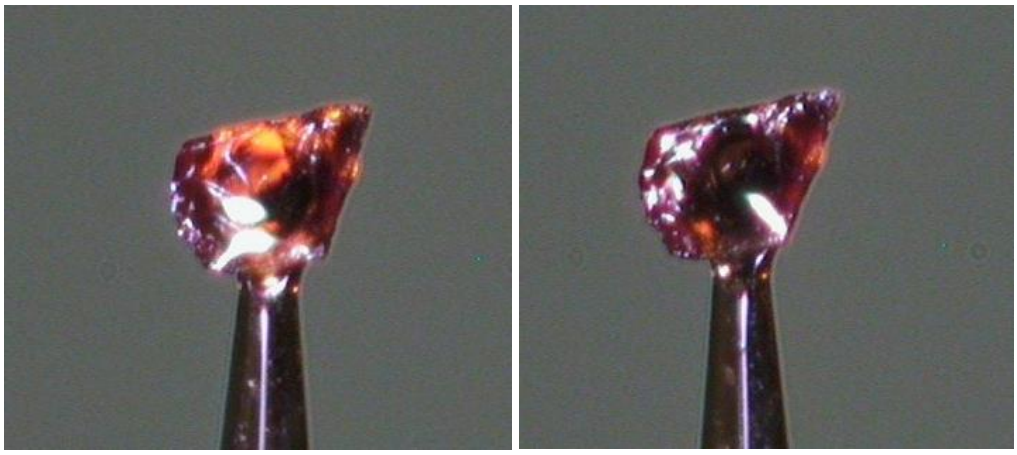


**Figure 77**. Crystal images of **$AsPhNH_2BW_{11}$**.

## 11.8 Frontier Orbital Estimations

**Table 19.** POM Frontier Orbital Estimations using Onset Reduction Potentials.

| Entry | POM | CV – red (V) | UV-Vis abs (nm) | UV-Vis abs (eV) | UV-Vis Corrected Optical Gap (eV) | LUMO Energy (eV) | HOMO Energy (eV) |
|---|---|---|---|---|---|---|---|
| 1 | TBADT | –1.1976 | 394.91 | 3.1400 | 4.3018 | –3.411 | –7.713 |
| 2 | **$P_2W_{18}$** | –0.8742 | 402.72 | 3.0791 | 4.2184 | –3.786 | –8.004 |
| 3 | **$PPhP_2W_{17}$** | –0.4925 | 406.77 | 3.0484 | 4.1764 | –4.229 | –8.405 |
| 4 | **$AsPhP_2W_{17}$** | –0.5535 | 408.39 | 3.0363 | 4.1598 | –4.158 | –8.318 |
| 5 | **$AsPhNO_2P_2W_{17}$** | –0.5029 | 409.08 | 3.0312 | 4.1527 | –4.217 | –8.369 |
| 6 | **$AsPhNH_2P_2W_{17}$** | –0.5874 | 408.41 | 3.0362 | 4.1596 | –4.119 | –8.278 |
| 7 | **$SiPhP_2W_{17}$** | –0.9087 | 410.15 | 3.0233 | 4.1419 | –3.746 | –7.888 |
| 8 | **$PW_{12}$** | –0.6021 | 363.42 | 3.4121 | 4.6745 | –4.102 | –8.776 |
| 9 | **$PMo_{12}$** | –0.1711 | 446.65 | 2.7762 | 3.8034 | –4.602 | –8.405 |
| 10 | **$SiW_{12}$** | –1.0604 | 359.18 | 3.4523 | 4.7296 | –3.570 | –8.300 |

**Table 20.** POM Frontier Orbital Estimations using $E_{mid}$ Potentials.

| Entry | POM | CV – $E_{mid}$ (V) | LUMO Energy (eV) | HOMO Energy (eV) |
|---|---|---|---|---|
| 1 | TBADT | –1.184 | –3.427 | –7.728 |
| 2 | **$P_2W_{18}$** | –1.195 | –3.806 | –8.025 |
| 3 | **$PPhP_2W_{17}$** | –0.481 | –4.243 | –8.419 |
| 4 | **$AsPhP_2W_{17}$** | –0.540 | –4.173 | –8.333 |
| 5 | **$AsPhNO_2P_2W_{17}$** | –0.490 | –4.232 | –8.384 |
| 6 | **$AsPhNH_2P_2W_{17}$** | –0.658 | –4.037 | –8.196 |
| 7 | **$SiPhP_2W_{17}$** | –0.982 | –3.662 | –7.803 |
| 8 | **$PW_{12}$** | –0.582 | –4.125 | –8.799 |
| 9 | **$PMo_{12}$** | –0.241 | –4.520 | –8.324 |
| 10 | **$SiW_{12}$** | –1.131 | –3.488 | –8.218 |